

JULIUS-MAXIMILIANS-UNIVERSITÄT WÜRZBURG
FAKULTÄT FÜR PHYSIK UND ASTRONOMIE
LEHRSTUHL FÜR ASTRONOMIE

MASTER THESIS

VLBI and Multiband-Variability Study
of the γ -ray Blazar 4C+01.28

Author
Florian Rösch

Supervisor
Prof. Dr. Matthias Kadler



ASTRO WÜRZBURG

*A thesis submitted in fulfillment of the requirements
for the degree of Master of Science
in the group of*

Prof. Dr. Matthias Kadler

Chair of Astronomy

Zusammenfassung

Blazare gehören zu den hellsten Objekten des Universums. Als Unterklasse von radio-lauten aktiven Galaxienkernen (AGN), emittieren sie Strahlung im kompletten elektromagnetischen Spektrum von Radiofrequenzen bis hin zu hochenergetischer γ -Strahlung und weisen relativistische Jets auf, die man sich als stark kollimierte Plasmaströme vorstellen kann. Um die Struktur und die physikalischen Eigenschaften dieser Jets zu untersuchen, kann die Methode der Very Long Baseline Interferometry (VLBI) verwendet werden, bei der mehrere Radioteleskope zu einem Netzwerk zusammengefasst werden, was zu sehr hohen Winkelauflösungen führt.

Im Energiebereich der γ -Strahlung stellen Blazare die größte Population innerhalb der extragalaktischen Quellen dar. Allerdings ist noch nicht klar in welcher Region, innerhalb des AGN, diese γ -Strahlung entsteht. Auf der einen Seite zeigt die γ -Strahlung von vielen Blazaren eine hohe Variabilität auf kurzen Zeitskalen auf, was auf eine kompakte Emissionsregion innerhalb der sogenannten Broad Line Region (BLR) hinweist, die sich bis zu einer Distanz von ungefähr einem Parsec um das supermassive schwarze Loch im Zentrum des AGN befindet. Deshalb wird die Entstehung der γ -Strahlung oft durch inverse Compton-Streuung von BLR-Photonen erklärt. Auf der anderen Seite zeigen VLBI-Beobachtungen neu entstandene Jetkomponenten, deren Ausstoßung aus dem Radiokern mit dem Auftreten von hellen Radio- und γ -Strahlenausbrüchen in Verbindung gebracht werden kann. In Kombination mit Korrelationsanalysen zwischen γ -Strahlenlichtkurven und Radiolichtkurven, weist dies auf eine Emissionsregion hin, die sich außerhalb der BLR befindet.

Der Blazar 4C+01.28 ist eine helle und sehr variable Radio- und γ -Strahlenquelle. In beiden Energiebändern wird eine hohe Variabilität auf Zeitskalen von Tagen bis Jahren beobachtet. Deshalb eignet sich 4C+01.28 gut dazu, um die Lage der Emissionsregion der γ -Strahlung innerhalb der Quelle zu untersuchen.

Zu diesem Zweck wurde die Parsec-Skalenstruktur des Jets von 4C+01.28 untersucht. Dafür wurden Radiodaten verwendet, die mit dem Very Long Baseline Array (VLBA) bei einer Frequenz von 43 GHz während einer Periode von ungefähr neun Jahren von April 2009 bis April 2018 beobachtet wurden. Es wurden zwei helle und kompakte neu entstandene Jetkomponenten gefunden, die mit dem Auftreten von hellen Radio- bzw. γ -Strahlenausbrüchen in Verbindung gebracht werden können. Eine Kinematikanalyse der VLBA-Beobachtungen ergab eine maximale scheinbare Jetgeschwindigkeit von $\beta_{\text{app}} = 19.0 \pm 3.3$ und eine obere Schranke für den Beobachtungswinkel von $\phi \lesssim 5^\circ$.

Außerdem wurden die γ -Strahlenlichtkurve von 4C+01.28, gemessen mit *Fermi*/LAT, und verschiedene Radiolichtkurven von 4C+01.28, beobachtet bei unterschiedlichen Ra-

diolfrequenzen mit dem Atacama Large Millimeter/submillimeter Array (ALMA), dem Submillimeter Array (SMA) bzw. dem Owens Valley Radio Observatory (OVRO), untersucht. Eine Korrelationsanalyse zwischen der γ -Strahlenlichtkurve und den verschiedenen Radiolichtkurven ergab positive Zeitdifferenzen zwischen den Lichtkurven.

Durch die Kombination der Ergebnisse der Kinematikanalyse und der Korrelationsanalyse kann das Auftreten der Radio- bzw. γ -Strahlenausbrüche, die von den untersuchten Lichtkurven gezeigt werden, mit einem Modell, in dem diese Ausbrüche entstehen, wenn eine Jetkomponente die Emissionsregion der γ -Strahlung bzw. die Kernregionen der verschiedenen Radiofrequenzen durchquert, beschrieben werden. Mit diesem Modell konnte eine untere Schranke der Lage der Emissionsregion der γ -Strahlung, bezogen auf den Fußpunkt des Jets, von $r_\gamma \gtrsim 6$ pc bestimmt werden.

Abstract

Blazars are among the brightest objects in the sky. As a subclass of radio-loud Active Galactic Nuclei (AGN), they emit radiation throughout the entire electromagnetic spectrum from radio frequencies up to high γ -ray energies and feature relativistic jets that are thought to be highly collimated plasma streams. To study the inner structure and physical properties of these jets, a method called Very Long Baseline Interferometry (VLBI) can be used, in which an array of radio telescopes is built, leading to a very high angular resolution.

At γ -ray energies, blazars depict the largest population of extragalactic sources. However, the location of the γ -ray emitting region is still unclear. On the one hand side, a lot of blazars show γ -ray variability on short time scales that indicates a compact emission region located within the broad line region (BLR) which is located at distances $\lesssim 1$ pc from the supermassive black hole (SMBH) representing the central engine of the AGN. Therefore, the γ -ray emission is generally explained by inverse Compton scattering of BLR photons. On the other hand, using VLBI observations, newly ejected jet components were found that seem to be associated with bright radio and γ -ray outbursts. Together with cross-correlation analyses between γ -ray light curves and radio light curves, this indicates a location of the γ -ray emitting region beyond the BLR.

The blazar 4C+01.28 is a bright and very variable radio and γ -ray emitter. At both energy bands, high-amplitude variability is observed on time scales of days to years. Therefore, 4C+01.28 is a good target for studying the location of the γ -ray emitting region.

For this purpose, the parsec-scale jet structure of 4C+01.28 was studied, using radio data observed by the Very Long Baseline Array (VLBA) at 43 GHz over a period of around nine years from April 2009 until April 2018. Two bright and compact newly ejected jet components were found that seem to be associated with bright outbursts, shown in the *Fermi*/LAT γ -ray light curve and in different radio light curves, respectively. A kinematic analysis of these VLBA observations leads to a maximum apparent jet speed of $\beta_{\text{app}} = 19.0 \pm 3.3$ and an upper limit of the viewing angle of $\phi \lesssim 5^\circ$.

Furthermore, the 14-day binned γ -ray light curve of 4C+01.28 measured with *Fermi*/LAT and different radio light curves of 4C+01.28 observed at several frequencies with the Atacama Large Millimeter/submillimeter Array (ALMA), the Submillimeter Array (SMA) and the Owens Valley Radio Observatory (OVRO) respectively, were investigated. A cross-correlation analysis between the γ -ray light curve and the different radio light curves results in positive time lags, meaning that the radio light curves lag the *Fermi*/LAT γ -ray light curve.

Combining the results of the kinematic analysis and the cross-correlation analysis, the occurrence of the outbursts shown in the investigated light curves can be described by using a model in which these outbursts become observable when a jet component passes through the γ -ray emitting region and the core region of different radio frequencies, respectively. Using this model, a lower limit of the location of the γ -ray emitting region with respect to the jet base was calculated to be $r_\gamma \gtrsim 6$ pc.

Contents

Zusammenfassung	i
Abstract	iii
1. Motivation	3
2. Scientific Context	5
2.1. Active Galactic Nuclei	5
2.1.1. Classification and Unification	6
2.1.2. Emission Processes	12
2.1.3. The Physics of Jets in AGN	17
2.1.4. The γ -ray Emitting Region	24
2.2. Very Long Baseline Interferometry	26
2.2.1. The Two-Element Interferometer	26
2.2.2. Interferometry with Arrays	30
2.2.3. The Very Long Baseline Array	32
2.2.4. Analysis of VLBI Data	34
2.3. Cross-Correlation Function	37
2.3.1. Discrete Cross-Correlation Function	37
2.3.2. Interpolated Cross-Correlation Function	38
3. Presenting 4C+01.28	39
3.1. Previous Radio Observations	39
3.2. Previous Kinematic Analyses	40
4. VLBA Observations of 4C+01.28	45
4.1. Imaging and Model-fitting	46
4.2. Kinematic Analysis	49
4.3. Jet Geometry	59
5. Multiband Variability Analysis	61
5.1. Light Curves at Different Frequencies	61
5.2. Cross-Correlation Analysis	65

6. Discussion	69
6.1. Kinematic Analysis	69
6.1.1. Jet Orientation	73
6.1.2. Location of the 43 GHz Core	74
6.2. Interpretation of the Time Lags	75
6.2.1. Core Shift	77
6.2.2. Location of the γ -ray Emitting Region	78
6.2.3. Location of the Radio Cores at Different Frequencies	81
6.3. The Overall Picture	82
7. Conclusion and Outlook	87
A. (u, v)-Plane Coverages	89
B. Images of 4C+01.28	95
C. Error Analysis of the Ejection Time	101
C.1. Linear Regression	101
C.2. Ejection Time	102
D. Additional Tables	107
Bibliography	157
List of Figures	161
List of Tables	163
Danksagung	165

1. Motivation

Until the 20th century, astronomers were only able to observe the universe in the optical regime of the electromagnetic spectrum. Then, in 1932, Karl Jansky, working at the Bell Telephone Laboratories, identified a steady hiss component in the radio background at a wavelength of 14.6 m, while doing a study of the sources of static affecting trans-Atlantic radio communications. One year later, he inferred that the radiation which produced this hiss component came from the center of the Milky Way Galaxy (Burke & Graham-Smith 2010; Shields 1999). Nowadays, this discovery is seen as the birth of the science of radio astronomy (Burke & Graham-Smith 2010), even though several radio engineers began to be interested in radio astronomy not until the end of World War II (Shields 1999) and its full importance became visible only in the 1950s and 1960s with the discoveries of the 21 cm hydrogen line, the pulsars and the cosmic microwave background (Burke & Graham-Smith 2010).

Another important discovery was made by Allan Sandage in 1960, when he found a stellar object with a faint nebulosity and broad emission lines at unfamiliar wavelengths. Since several other such star-like objects coincident with radio sources were found, such sources became known as quasi-stellar radio sources or quasars. Due to the large redshifts of these quasars, they had to be extragalactic objects and were suspected to lie in the centers of distant galaxies called active galactic nuclei (AGN; Shields 1999). Some of these AGN show so-called radio jets that transport energetic particles from the nuclei to the outer regions which could be hundreds of kiloparsecs away (Beckmann & Shrader 2012; Kembhavi & Narlikar 1999; Schneider 2015). To investigate the inner structure and the physical properties of these jets, radio astronomers use a method called Very Long Baseline Interferometry (VLBI), in which an array of radio telescopes is built, leading to a very high angular resolution (Burke & Graham-Smith 2010; Thompson et al. 2017).

AGN emit radiation throughout the entire electromagnetic spectrum from radio frequencies up to high γ -ray energies. In the case of blazars, a subtype of AGN, this high-energy γ -ray emission shows high-amplitude variability on very short time scales of less than a day (e.g., HESS Collaboration 2010; Jorstad et al. 2013). Furthermore, while the radio emission is thought to be produced by synchrotron radiation from relativistic electrons, the γ -ray emission is widely believed to be produced by inverse Compton scattering of photons by the same relativistic electrons that are responsible for the synchrotron radiation. Therefore, the radio and γ -ray emission are expected to be correlated (Lister et al. 2015). In fact, such correlations between γ -ray light curves and radio light curves were found by Fuhrmann et al. (2014) and Max-Moerbeck et al. (2014),

for example. Furthermore, Jorstad et al. (2001) found newly ejected jet components that seem to be associated with γ -ray outbursts, using VLBI observations.

Moreover, blazars represent the largest population of extragalactic sources in the γ -ray band (Abdo et al. 2009). However, it is not yet clear where this γ -ray emission is produced within the jet. On the one hand side, the flux variability on short time scales indicates a compact emission region located at the central parsec-scale region around the central engine of the AGN. Therefore, the γ -ray emission is generally explained by inverse Compton scattering of UV photons from the broad line region (BLR; Costamante et al. 2018). On the other hand, using VLBI observations, newly ejected jet components were found that seem to be associated with bright radio and γ -ray outbursts (Jorstad et al. 2001). Together with cross-correlation analyses between γ -ray light curves and radio light curves, this indicates a location of the γ -ray emitting region beyond the BLR (e.g., Jorstad et al. 2017; Max-Moerbeck et al. 2014).

The blazar 4C+01.28 is a good target for testing the location of the γ -ray emitting region. VLBI observations at 43 GHz of 4C+01.28 show the ejection of a superluminal jet component that seems to be associated with a bright γ -ray outburst (MacDonald et al. 2017). Furthermore, 4C+01.28 was observed at different radio frequencies. The light curves of these radio observations show high variability in flux density, similar to the γ -ray light curve (see Sect. 5.1). Therefore, the parsec-scale jet structure observed by the Very Long Baseline Array (VLBA) at 43 GHz and the cross-correlation between the γ -ray light curve and the radio light curves observed at different frequencies were studied in this thesis to determine the location of the γ -ray emitting region within the jet of 4C+01.28.

The scientific context of this thesis will be given in Chapt. 2, including information on AGN (Sect. 2.1) and VLBI (Sect. 2.2) as well as a short introduction to the cross-correlation analysis (Sect. 2.3). In Chapt. 3, the blazar 4C+01.28 will be introduced by showing some previous results. After that, the results of the 43 GHz VLBA observations, including a kinematic analysis, and the results of the multiband variability analysis, including the cross-correlation analysis between the γ -ray light curve and the different radio light curves, will be presented in Chapt. 4 and Chapt. 5 respectively. These results will then be discussed in Chapt. 6, leading to a lower limit of the location of the γ -ray emitting region. Finally, the results presented in this thesis will be summarized in Chapt. 7, in which also a short outlook will be given.

Throughout this thesis, a Λ CDM cosmological model with $H_0 = 70 \text{ km s}^{-1} \text{ Mpc}^{-1}$, $\Omega_m = 0.30$ and $\Omega_\Lambda = 0.70$ was used.

2. Scientific Context

In this thesis, the parsec-scale jet structure of the blazar 4C+01.28 was investigated. Furthermore, the cross-correlation between light curves measured at γ -rays and different radio frequencies was analyzed. Therefore, the scientific context concerning these studies is given in this chapter.

Since blazars are a subtype of Active Galactic Nuclei (AGN), Sect. 2.1 will deal with these AGN, especially with blazars. To study the parsec-scale jet structure of 4C+01.28, radio observations were used that were taken by the technique of Very Long Baseline Interferometry (VLBI). Therefore, the aspects of VLBI that are important for this thesis will be discussed in Sect. 2.2. Finally, some important information on the cross-correlation function will be presented in Sect. 2.3.

2.1. Active Galactic Nuclei

While the emission of normal galaxies is dominated by thermal radiation of stars, there are also so-called active galaxies that show significant emission in the total range of the electromagnetic spectrum from radio up to γ -ray energies, overwhelming the stellar emission of the entire galaxy. This emission originates from very small regions at the center of such active galaxies called Active Galactic Nuclei (AGN; e.g., Beckmann & Shrader 2012). These AGN consist of a supermassive black hole (SMBH) as the central engine surrounded by an accretion disk of hot plasma which is formed by the strong gravitational field of the SMBH pulling the surrounding materials inwards (e.g., Kembhavi & Narlikar 1999). AGN can be divided into several subtypes due to their different luminosities, emission line properties and radio-loudnesses. However, these different classes can be united in a so-called unification model (Antonucci 1993; Urry & Padovani 1995). In radio-loud AGN, relativistic jets are present roughly perpendicular to the accretion disk. These jets are most prominent in radio-frequency observations and are believed to be highly collimated plasma outflows launched from the accretion disk (e.g., Beckmann & Shrader 2012).

The continuum radiation of AGN is emitted through elementary processes. While the low frequency emission is dominated by synchrotron radiation, the origin of the high-energy γ -ray emission is still unclear. This γ -ray emission could be produced by inverse Compton scattering or could be explained by hadronic emission models (e.g., Böttcher 2010). Furthermore, it is not clear where the γ -ray emission is produced. The flux variability on short time scales indicates a compact emission region located at

the central parsec-scale region around the SMBH (e.g., Costamante et al. 2018), while multiwavelength observations combined with VLBI observations indicate that the γ -ray emission region is located well beyond the central parsec-scale region (e.g., Jorstad et al. 2017; Max-Moerbeck et al. 2014).

In this section, a brief overview of the physical properties of AGN will be given. Since 4C+01.28 is classified as a blazar, this section deals mainly with blazars. However, for completeness, other important AGN types will also be mentioned very briefly. If no additional references are given, this section is based on the textbooks by Beckmann & Shrader (2012), Kembhavi & Narlikar (1999) and Schneider (2015).

2.1.1. Classification and Unification

As previously mentioned, AGN can be divided into several subtypes due to their different luminosities, emission line properties and radio-loudnesses.

According to Kellermann et al. (1989), the ratio R_{r-o} of the radio flux density S_r to the optical flux density S_o

$$R_{r-o} = \frac{S_r}{S_o} \quad (2.1.1)$$

can be used to distinguish between radio-loud and radio-quiet AGN. For $R_{r-o} > 10$, the AGN is classified as radio-loud, whereas radio-quiet sources show ratios of $0.1 < R_{r-o} < 1$.

The next step towards classifying AGN is to categorize them by their emission line properties. While some AGN only show narrow emission lines, other AGN also show broad emission lines. Together with the different luminosities, this leads to the different classes of objects included in the so-called AGN Zoo. Therefore, the main classes of AGN will be discussed in the following paragraphs.

Seyfert Galaxies

Carl Seyfert (1943) found a class of galaxies with bright, central, point-like cores showing highly ionized emission lines superposed on a normal star-like spectrum. These so-called Seyfert galaxies were the first objects classified as AGN. They are the most common class of AGN that are observed in the local Universe and appear to have the morphology of spiral galaxies. Furthermore, most Seyfert galaxies are typically found to be radio-quiet.

On the basis of their emission line properties, Seyfert galaxies can be further separated into two different classes. While Seyfert type 1 objects show broad Balmer lines with narrow components and narrow forbidden lines, the Balmer and the forbidden lines of Seyfert type 2 objects both show the same narrow width. Furthermore, Seyfert 1 galaxies emit strong continuum emission from the far infrared to the X-ray band, whereas Seyfert 2 galaxies show a weaker continuum.

Radio Galaxies

Radio galaxies are the radio-loud counterparts of Seyfert galaxies. While broad line radio galaxies (BLRG) show broad emission lines and narrow forbidden lines similar to Seyfert 1 galaxies, narrow line radio galaxies (NLRG) have spectra like Seyfert 2 galaxies, showing only narrow emission lines. However, in contrast to Seyfert galaxies, radio galaxies are typically associated with elliptical galaxies.

According to Fanaroff & Riley (1974), radio galaxies can also be subdivided into two so-called Fanaroff-Riley classes by the appearance of their extended radio emission and their different luminosities in addition to the classification based on the emission line properties. While low-luminosity Fanaroff-Riley class I (FR-I) galaxies show bright, dominant nuclei and two broad radio jets ending in plumes, high-luminosity Fanaroff-Riley class II (FR-II) galaxies usually only have weak one-sided jets ending in dominant radio lobes.

Quasars

Quasar is the acronym for quasi-stellar radio source. These sources were first found by radio surveys and appeared as blue stars in optical images. However, only 10 % of quasars are radio-loud; although some objects display the optical properties of quasars, they do not necessarily show strong radio emissions. These radio-quiet objects were called quasi-stellar objects (QSO), while historically the name quasar was used for radio-loud sources. Today the distinction between quasars and QSO is not very much in use.

QSO, or radio-quiet quasars, show optical spectra similar to those of Seyfert galaxies, but they are more luminous. Actually, quasars are the most luminous AGN. While QSO of type 1 show broad and narrow emission lines similar to Seyfert 1 galaxies, QSO of type 2 show only narrow emission lines as can also be seen in Seyfert 2 galaxies.

Radio-loud quasars can be further classified into radio-bright flat-spectrum radio quasars (FSRQ) and steep radio spectrum quasars (SRSQ). Whereas SRSQ are dominated by radio lobe emission, FSRQ show compact radio structures. Furthermore, FSRQ are a sub-class of blazars.

Blazars

Blazars are core dominated, compact radio sources with a flat or inverted spectrum showing emission stretching across the entire electromagnetic spectrum from the radio regime up to very high energies above 1 TeV. In fact, blazars are the largest population of extragalactic objects in the γ -ray band (Abdo et al. 2009). Since blazars are among the brightest AGN, they often outshine the emission of their host galaxies. Therefore, it is usually impossible to identify their host galaxies. Furthermore, blazars show a strong and variable polarization in both the radio and optical domains as well as strong variability in flux density on time scales from years to less than a day, the so-called intraday variability.

Based on their emission line properties and on the luminosity, blazars can be divided into FSRQ and BL Lac objects, named after the prototype source BL Lacertae. While FSRQ exhibit strong emission lines, the emission lines of the less luminous BL Lac objects are absent or weak.

Classified as radio-loud AGN, blazars show relativistic jets that are observable throughout the entire electromagnetic spectrum, pointing directly at the observer, or very close to the observer's line of sight. Therefore, the emission of blazars is relativistically beamed to higher luminosities due to Doppler boosting (for more details, see Sect. 2.1.3). Furthermore, VLBI observations reveal jet features moving with apparent superluminal speeds downstream along the jet. This apparent superluminal motion can be explained by a projection effect which will be discussed in more detail in Sect. 2.1.3.

As mention before, blazars emit radiation throughout the entire electromagnetic spectrum. Therefore, their spectral energy distribution (SED), in which the flux density or the luminosity is plotted with respect to the frequency, is of special interest. These SEDs show a characteristic double-hump structure, which is shown for the blazar 4C+01.28 as an example in Fig. 2.1 (Abdo et al. 2010). While the low-frequency peak is dominated by synchrotron emission of relativistic electrons, the origin of the high-energy peak is still unclear, with leptonic and hadronic emission models being discussed (e.g., Böttcher 2010). In leptonic models, the high-energy emission is produced via inverse Comp-

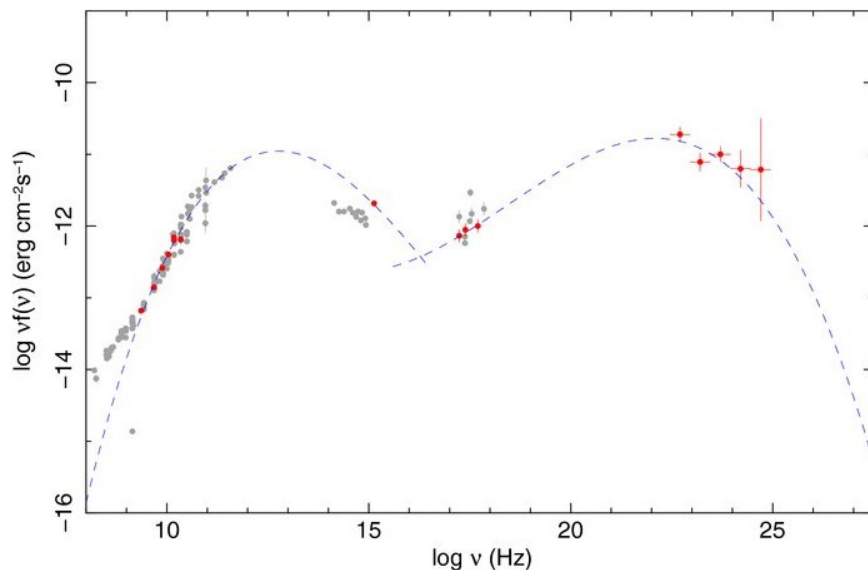


Figure 2.1.: SED of 4C+01.28 showing the characteristic double-hump structure of blazar SEDs. The red points denote quasi-simultaneous data presented by Abdo et al. (2010), while the gray points are non-simultaneous archival data. The dashed lines represent the best fits to the synchrotron and inverse Compton part of the SED. Taken from Abdo et al. (2010).

ton scattering of seed photons by the electrons causing the synchrotron emission (e.g., Maraschi et al. 1992; Dermer et al. 1992; Sikora et al. 1994, 2009; Ghisellini & Tavecchio 2009), whereas in hadronic emission models, the high-energy emission is produced by pion decay into photons and neutrinos (Mannheim 1993). These emission processes will be further discussed in Sect. 2.1.2.

Fossati et al. (1998) divided a sample of 126 blazars into 5 GHz radio luminosity bins and built the averaged SED in each bin by averaging the luminosities at selected frequencies. Later, Donato et al. (2001) added the slope of the X-ray emission of the same 126 blazars to the averaged SEDs. The result is shown in the right panel of Fig. 2.2. One can see that the peak frequencies shift to lower frequencies for increasing luminosity, which is called the blazar sequence. Furthermore, the ratio of the high-energy peak to the low-energy peak increases with increasing frequency. These trends were also found by Ghisellini et al. (2017). They divided blazars into γ -ray luminosity bins and built the averaged SEDs separately for BL Lac, FSRQ and also for all blazars together. While BL Lac objects form a sequence showing smaller peak frequencies with increasing luminosity, FSRQ show approximately the same SED with increasing luminosity but the ratio of the high-energy peak to the low-energy peak increases. Since the high-luminosity bins are populated mostly by FSRQ and the low-luminosity bins are populated mostly by BL

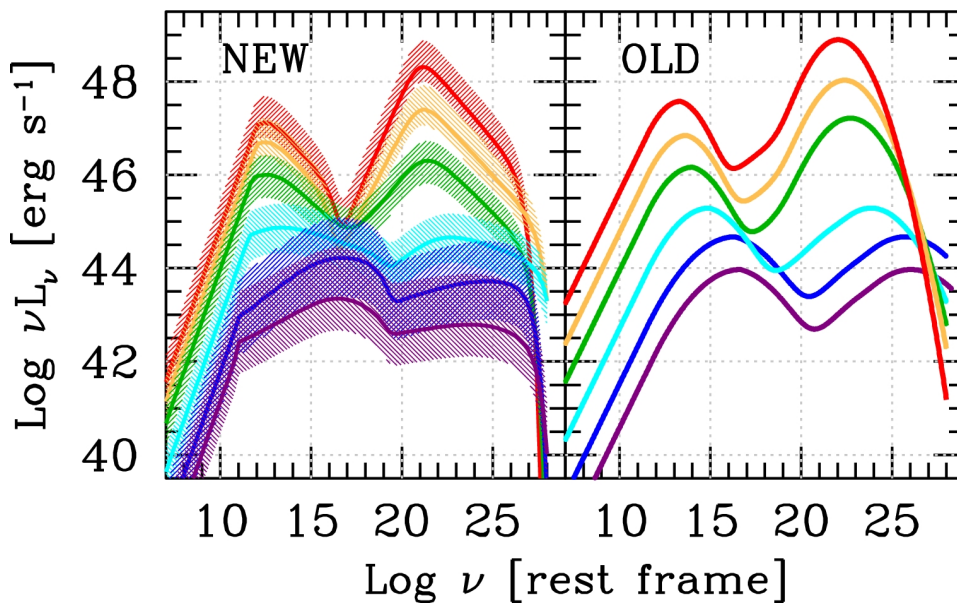


Figure 2.2.: Comparison between the new blazar sequence (left) derived by Ghisellini et al. (2017) dividing blazars into γ -ray luminosity bins and the original one (right) derived by Fossati et al. (1998) and Donato et al. (2001) dividing blazars into 5 GHz radio luminosity bins. Both versions show increasing peak frequencies and dominances of the high-energy peak with increasing luminosity. Taken from Ghisellini et al. (2017).

Lacs, these properties become more prominent for all blazars together, which is shown in the left panel of Fig. 2.2.

Model of Unification

Since all AGN classes mentioned above show many similarities, it can be assumed that the observed characteristics are caused by the same physical processes. Therefore, these AGN classes can be united in a unification model. This model will be summarized in the following section. More detailed information on it can be found in Antonucci (1993) and Urry & Padovani (1995). The concept of this unification model is illustrated in Fig. 2.3.

AGN show bolometric luminosities of $L_{\text{bol}} \sim 10^{41} \text{ erg s}^{-1}$ to $L_{\text{bol}} \sim 10^{48} \text{ erg s}^{-1}$. These high luminosities can only be produced by accretion on a central mass M . The maximum

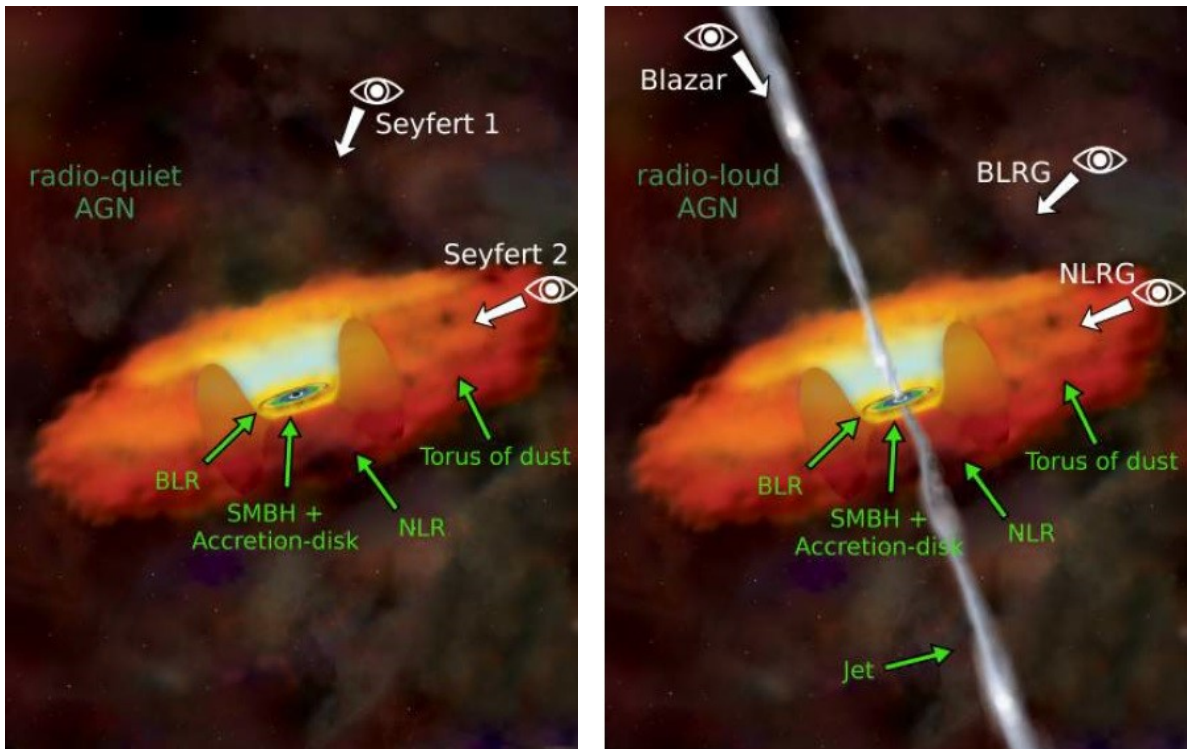


Figure 2.3.: Illustration of the AGN unification model according to Antonucci (1993) and Urry & Padovani (1995). The left panel shows a radio-quiet AGN, while the right panel shows a radio-loud one. An AGN consists of a supermassive black hole (SMBH) surrounded by an accretion disk and a cold dust torus. There are also the broad line region (BLR) and the narrow line region (NLR), producing broad and narrow emission lines, respectively. In radio loud AGN there is also a radio jet nearly perpendicular to the accretion disk. The classification of an AGN depends on the viewing angle. Adapted from NASA/CXC/M.Weiss, edited by Amar Hekalo.

luminosity that can be produced due to accretion is the so-called Eddington luminosity L_{Edd} , which is given by

$$L_{\text{Edd}} = \frac{4\pi GMm_p c}{\sigma_T} = 1.3 \cdot 10^{38} \text{ erg s}^{-1} \frac{M}{M_\odot}, \quad (2.1.2)$$

in which G is the gravitational constant, m_p is the proton mass, c is the speed of light, $\sigma_T \simeq 6.65 \cdot 10^{-25} \text{ cm}^2$ is the Thomson scattering cross-section and M_\odot is the mass of the sun. Therefore, using typical AGN luminosities, one obtains central masses of $M \sim 10^5 M_\odot$ to $10^{10} M_\odot$, leading to the assumption that the central engines of AGN are supermassive black holes (SMBH) surrounded by an accretion disk of hot plasma which is formed by the strong gravitational field of the SMBH pulling the surrounding materials inwards. These disks have radii up to $r \sim 10^{-3} \text{ pc}$ and are surrounded by a cold dust torus located at distances of $r \sim 1 \text{ pc}$ up to a few 10 pc from the SMBH.

Some AGN emit broad emission lines with line widths of 10^3 km s^{-1} to a few 10^4 km s^{-1} . This enormous broadening of the lines can be explained by fast moving clouds of photoionized gas, located in the so-called broad line region (BLR). The BLR is a hot and very dense medium with a particle density of $n \sim 10^9 \text{ cm}^{-3}$ and is located at distances of $r \sim 0.01 \text{ pc}$ to $r \sim 1 \text{ pc}$ from the SMBH. The size of the BLR can be probed by a method called reverberation mapping. This method was used by the Gravity Collaboration (2018) to measure the mean distance of a BLR cloud from the SMBH to be $r_{\text{mean}} = (0.12 \pm 0.03) \text{ pc}$ and the minimum distance of that cloud to be $r_{\text{min}} = (0.03 \pm 0.01) \text{ pc}$ for the quasar 3C 273.

The narrow line region (NLR) is located at distances from the SMBH of $r \sim 100 \text{ pc}$ to $r \sim 1000 \text{ pc}$, consisting of a colder and less dense accumulation of gas clouds compared to the BLR. These gas clouds emit narrow lines with line widths of 400 km s^{-1} to 500 km s^{-1} . The NLR has a particle density of $n \sim 10^3 \text{ cm}^{-3}$ to $n \sim 10^5 \text{ cm}^{-3}$.

In radio-loud AGN there are also relativistic jets roughly perpendicular to the accretion disk, which are thought to be highly collimated plasma outflows launched from the accretion disk.

With the help of this unification model, the characteristics of the different AGN types mentioned above can be explained, assuming that there are basically two types of AGN, namely radio-quiet and radio-loud AGN. For each of these two types there is a range of luminosities leading to the differences between Seyfert galaxies and radio-quiet QSO as well as the Fanaroff-Riley classes. Then, all other differences can be explained by orientation effects.

As one can see in Fig. 2.3, the dust torus will obscure the BLR if an AGN is observed at a large viewing angle, leading to the fact that only narrow emission lines from the NLR are visible. Therefore, in the radio-quiet case, the AGN will be classified as a Seyfert 2 galaxy or a QSO type 2, depending on the luminosity, while in the radio-loud case, the AGN will be classified as an NLRG. At smaller viewing angles, the BLR can also be seen, leading to a classification as Seyfert 1 galaxy or QSO type 1 for radio-quiet

AGN and as BLRG for radio-loud ones. The absent or weak emission lines of BL Lac objects can be explained by the very small viewing angles of these objects. Therefore, the emission of the radio jet, pointing almost directly to the observer, is relativistically beamed to higher luminosities due to Doppler boosting (for more details, see Sect. 2.1.3) and hence outshines the emission lines of the NLR and BLR.

Since the orientation is the only difference between blazars and radio galaxies, one can assume that blazars are simply rotated counterparts of radio galaxies. Therefore, BL Lac objects should be the rotated counterparts of FR-I galaxies, whereas FSRQ are thought to be the rotated counterparts of FR-II galaxies (Urry & Padovani 1995).

All of the different AGN classes mentioned above and their properties are listed in Table 2.1, for a summary of the unification model.

Table 2.1.: Different classes of AGN and their properties. Adapted from Kadler (2015).

Type	Radio Loudness	Emission Lines	Luminosity	Jet?	Radio Morphology
Seyfert 1	radio-quiet	broad, narrow	low	no	none
Seyfert 2	radio-quiet	narrow	low	no	none
QSO type 1	radio-quiet	broad, narrow	high	no	none
QSO type 2	radio-quiet	narrow	high	no	none
BLRG	radio-loud	broad, narrow	low	yes	FR-I
	radio-loud	broad, narrow	high	yes	FR-II
NLRG	radio-loud	narrow	low	yes	FR-I
	radio-loud	narrow	high	yes	FR-II
BL Lac	radio-loud	none	low	yes	compact
FSRQ	radio-loud	broad, narrow	high	yes	compact

2.1.2. Emission Processes

AGN emit radiation throughout the entire electromagnetic spectrum from radio frequencies up to high-energy γ -rays. While the radio emission is thought to be dominated by synchrotron radiation, the origin of the γ -ray emission is still unclear. In leptonic models, the γ -ray emission is produced via inverse Compton scattering (e.g., Maraschi et al. 1992; Dermer et al. 1992; Sikora et al. 1994, 2009; Ghisellini & Tavecchio 2009), whereas in hadronic models, it is produced by pion decay into photons and neutrinos (Mannheim 1993). These different emission processes will be discussed briefly in this section. If no further references are given, this section is based on Beckmann & Shrader (2012). For a more detailed discussion of the leptonic emission models, see Rybicki & Lightman (1985).

Synchrotron Radiation

Synchrotron radiation is emitted when charged particles are accelerated in a magnetic field. Consider a particle with charge $q = Ze$, rest mass m and Lorentz factor $\gamma = \left(1 - \frac{v^2}{c^2}\right)^{-1/2}$ traveling with velocity \vec{v} through a uniform and static magnetic field \vec{B} . Then, the Lorentz force

$$\frac{d}{dt}(\gamma m \vec{v}) = \frac{Ze}{c} (\vec{v} \times \vec{B}) \quad (2.1.3)$$

acts on the particle. Since this force is perpendicular to the velocity of the particle and the magnetic field, v and γ are constant and there is no force acting in the direction of the magnetic field, meaning that the velocity in the direction of the field v_{\parallel} is constant. Therefore, the velocity perpendicular to the magnetic field $v_{\perp} = \sqrt{v^2 - v_{\parallel}^2}$ is also constant. Thus, the particle describes a helical motion with constant pitch angle β between \vec{v} and \vec{B} and Lamor frequency

$$\omega_g = \frac{ZeB}{\gamma mc}. \quad (2.1.4)$$

This acceleration process leads to a total power P of

$$P = \frac{2Z^2 e^2}{3c^3} \gamma^4 \left[\left(\frac{dv_{\perp}}{dt} \right)^2 + \gamma^2 \left(\frac{dv_{\parallel}}{dt} \right)^2 \right]. \quad (2.1.5)$$

Since the acceleration is perpendicular to the velocity, $\frac{dv_{\parallel}}{dt} = 0$, while $\frac{dv_{\perp}}{dt} = \omega_g v_{\perp} = \omega_g v \sin \beta$ due to the circular motion of the particle. This leads to

$$P = \frac{2Z^4 e^4 B^2 \gamma^2 v^2 \sin^2 \beta}{3c^5 m^2}. \quad (2.1.6)$$

Here, one can see that $P \propto m^{-2}$. Therefore, synchrotron radiation is most efficient for electrons and positrons. Hence, in the following the charges will be set to $q = e$, considering only electrons and positrons.

Due to beaming effects, the synchrotron radiation is concentrated in a narrow cone symmetric around \vec{v} with an opening angle $\phi \simeq \gamma^{-1}$. As the electron executes a helical motion around the magnetic field, an observer detects radiation only when this cone points towards the line of sight. Therefore, the observer sees a sequence of pulses with a width much smaller than ω_g . For an ensemble of electrons, the frequency spectrum of this radiation appears to be continuous with a maximum at the critical frequency $\nu_c \propto E^2$, in which E is the energy of the electrons. Then, the power per unit frequency

of the synchrotron emission is given by

$$P(E, \nu) = \frac{\sqrt{3}e^3 B \sin \beta}{mc^2} F(x), \quad (2.1.7)$$

with $x = \frac{\nu}{\nu_c}$ and $F(x) = \frac{\nu}{\nu_c} \int_{\nu/\nu_c}^{\infty} K_{5/3}(\xi) d\xi$, in which $K_{5/3}(\xi)$ is the modified Bessel function of order $\frac{5}{3}$. Now, considering an ensemble of electrons having energies in the interval between E_1 and E_2 , the emitted power as a function of the frequency is given by

$$P(\nu) = \int_{E_1}^{E_2} P(E, \nu) n(E) dE, \quad (2.1.8)$$

in which $n(E) dE$ is the number density of electrons in the energy interval between E and $E + dE$. Assuming that the number density of the electrons is given by a power law, as $n(E) dE = CE^{-p}dE$, in which C is the normalization and p is the power law index and both are constant, the emitted spectrum is given by a simple power law form as

$$P(\nu) \propto \nu^{-\alpha}, \quad (2.1.9)$$

in which $\alpha = \frac{p-1}{2}$ is the spectral index.

This simple power law form is only valid for an optically thin medium. The optical depth τ_ν of a medium through which a photon travels along a typical path from s_0 to s is defined by

$$\tau_\nu(s) = \int_{s_0}^s \alpha_\nu(s') ds', \quad (2.1.10)$$

in which α_ν is the absorption coefficient. When $\tau_\nu > 1$, the medium is said to be optically thick or opaque. Otherwise, the medium is said to be optically thin or transparent, when $\tau_\nu < 1$. In an optically thick medium, low frequency photons interact with electrons and are absorbed, which is called synchrotron self-absorption. In this case, the spectrum rises proportionally to $\nu^{5/2}$, leading to a flux density of

$$S(\nu) \propto \nu^{5/2}. \quad (2.1.11)$$

Note that here, the slope of the spectrum does not depend on the energy distribution of the electrons. The optically thick part of the spectrum only dominates below a critical frequency ν_{sa} at which $\tau_\nu = 1$. At higher frequencies, the medium is optically thin and the spectrum falls with $\nu^{-(p-1)/2}$, leading to a flux density of

$$S(\nu) \propto \nu^{-\frac{p-1}{2}}. \quad (2.1.12)$$

Inverse Compton Scattering

In leptonic models, the high-energy γ -ray emission is thought to be produced by inverse Compton (IC) scattering (e.g., Maraschi et al. 1992; Dermer et al. 1992; Sikora et al. 1994, 2009; Ghisellini & Tavecchio 2009).

Compton scattering is the inelastic scattering of photons by electrons in which a photon transfers energy to an electron. However, if the electrons are moving at relativistic speeds, an electron can transfer energy to a photon, which is called inverse Compton scattering. Let the laboratory frame, in which the scattering event is observed, be L and the rest frame of the relativistic electron be L' , then the energy of the photon in L' is given by

$$h\nu' = \gamma h\nu \left(1 + \frac{v_e}{c} \cos \theta\right), \quad (2.1.13)$$

in which h is the quantum of action, v_e is the speed of the electron in the laboratory frame L , ν and ν' are the frequencies of the photon in the laboratory frame L and in the rest frame of the electron L' , respectively, and θ is the angle between the directions of the photon and of the incoming electron in the laboratory frame L . Since the photon energy is much smaller than the electron energy in the electron's frame L' , $h\nu' \ll m_e c^2$, in which m_e is the mass of the electron, the scattering event can be treated as elastic scattering process. Therefore, in L' , the energy of the photon does not change, meaning that $E'_2 \simeq E'_1$. Transforming this expression back into the laboratory frame L leads to

$$E_2 \simeq \gamma^2 E_1, \quad (2.1.14)$$

in which E_1 and E_2 are the photon energies before and after the scattering process, respectively. Therefore, the photon gains energy proportional to the square of the Lorentz factor γ of the electron. Due to energy conservation, this energy gain is limited to $E_2 \leq E_1 + \gamma m_e c^2$, which leads to the maximum change in photon frequency $\Delta\nu$ of

$$\Delta\nu \leq \frac{\gamma m_e c^2}{h}. \quad (2.1.15)$$

There are two possible IC models to explain the high-energy γ -ray emission in AGN jets. When the seed photons of the IC scattering are provided by the synchrotron emission, this process is called synchrotron self-Compton (SSC) process. Here, synchrotron photons are up-scattered to γ -ray energies by the same electron population responsible for the synchrotron emission (e.g., Maraschi et al. 1992). For this to occur, the plasma has to be optically thick. Since already up-scattered photons can further be up-scattered by the SSC process, this effect is very sensitive to the source brightness and above a certain brightness temperature T_B , the IC losses can cool down the electrons efficiently. According to Kellermann & Pauliny-Toth (1969), this maximum brightness temperature can be determined by the ratio of the IC luminosity L_C to the synchrotron luminosity

L_S . This ratio can be written in terms of the maximum brightness temperature T_{\max} as

$$\frac{L_C}{L_S} \sim \frac{1}{2} \left(\frac{T_{\max}}{10^{12}} \right)^5 \nu_c \left[1 + \frac{1}{2} \left(\frac{T_{\max}}{10^{12}} \right)^5 \nu_c \right], \quad (2.1.16)$$

in which ν_c is the upper cutoff frequency of the radio spectrum in MHz, probably $\nu_c \sim 10^{5\pm 1}$. Therefore, $\frac{L_C}{L_S} < 1$ for $T_{\max} < 10^{11}$ K, but $\frac{L_C}{L_S} \sim \left(\frac{T_{\max}}{10^{11}} \right)^{10}$ for $T_{\max} > 10^{12}$ K, meaning that the energy losses due to IC scattering become catastrophic when the maximum brightness temperature is greater than 10^{12} K. In this case, the brightness temperature decreases to 10^{11} K $\lesssim T_B \lesssim 10^{12}$ K, in which $\frac{L_C}{L_S} \sim 1$, meaning that the IC losses and the synchrotron losses are of the same order (Kellermann & Pauliny-Toth 1969), which is called equipartition (Readhead 1994). While equipartition is a state that holds for many years, IC scattering dominates for $T_B \sim 10^{12}$ K and an emission region will radiate away most of its energy in a time scale of days (Readhead 1994). Therefore, the brightness temperature of $T_B \sim 10^{12}$ K is referred to as the inverse Compton limit. Nevertheless, many sources have brightness temperatures beyond the inverse Compton limit, which can be explained by Doppler boosting, transient nonequilibrium events, coherent emission, emission by relativistic protons, or a combination of these effects (Kovalev et al. 2005).

When the seed photons for the IC scattering are photons from external regions, the IC process is called external Compton (EC) scattering. Here, γ -rays are produced by EC on UV photons inside the BLR (e.g., Sikora et al. 1994), by EC on IR photons between the BLR and the dust torus (e.g., Sikora et al. 2009) and EC on photons from the cosmic microwave background (CMB; e.g., Ghisellini & Tavecchio 2009). Furthermore, the γ -ray emission in broad-line blazars is generally explained as EC on BLR photons so far (Costamante et al. 2018).

Hadronic Emission Models

In hadronic models, the low-frequency emission is also dominated by synchrotron radiation of electrons, while the high-energy emission is produced by hadronic particles. The following description of such models is based on Böttcher (2010). If the threshold for pion production via proton-photon ($p\gamma$) interactions is reached due to the conversion of a significant amount of the jet power into the acceleration of relativistic protons (p), synchrotron-supported pair cascades will develop (Mannheim 1993). For this to occur, magnetic fields of several tens of Gauss are needed, in which also synchrotron radiation of the primary protons and of secondary muons and mesons must be taken into account. The cascades mentioned above can be initiated by different decay processes. They can be induced by photons from the π^0 -decay (" π^0 cascade"), electrons from the $\pi^\pm \rightarrow \mu^\pm \rightarrow e^\pm$ decay (" π^\pm cascade"), p -synchrotron photons (" p -synchrotron cascade"), and μ^- , π^- and K -synchrotron photons (" μ^\pm -synchrotron cascade"). While the " π^0 cascade" and " π^\pm cascade" produce featureless γ -ray spectra, the " p -synchrotron cascade"

and " μ^\pm -synchrotron cascade" produce a two-component γ -ray spectrum.

2.1.3. The Physics of Jets in AGN

As previously mentioned, blazars feature jets that transport energetic particles from the nuclei to the outer regions which could be hundreds of kiloparsecs away. However, the production of these jets has not yet been fully understood, but current jet formation models are mostly based on magnetohydrodynamic (MHD) processes (Camenzind 1993). Blandford & Znajek (1977) developed an MHD jet formation model where the jet is driven by the black hole spin. Here, a magnetosphere around the SMBH is produced via the magnetic field provided by the accretion disk. In this magnetosphere, a plasma can form which can be accelerated via the interaction of the rotating SMBH and the magnetic

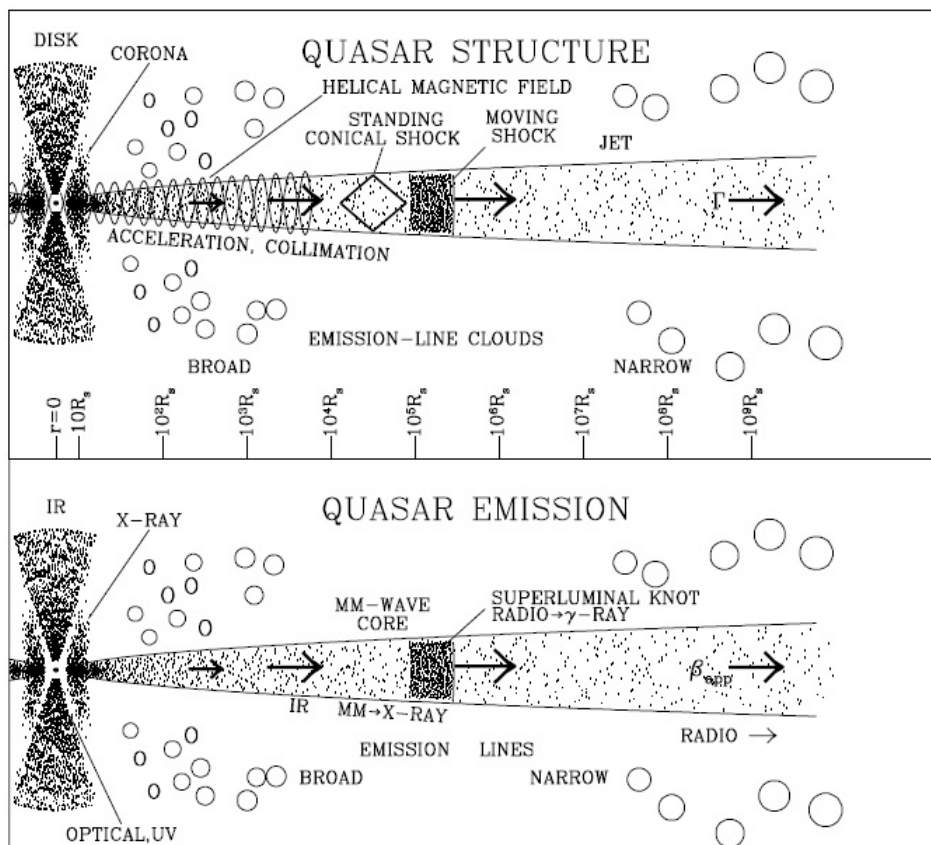


Figure 2.4.: Sketch of a jet in radio-loud AGN showing the structure of the jet (upper panel) and its emission properties (lower panel). The density of dots corresponds to the intensity of the emission. The length scale is given in terms of Schwarzschild radii of the SMBH and is logarithmically in order to cover a wide range of distances from the SMBH. Taken from Marscher (2009).

field. Another different MHD jet formation model, in which the jet is produced by the magnetized rotating accretion disk around the black hole, was developed by Blandford & Payne (1982). Here, the plasma is extracted from the accretion disk by the toroidal component of the magnetic field lines of the disk which is produced due to the rotation of the disk.

The structure of a jet in radio-loud AGN and its emission properties are shown in Fig. 2.4. VLBI observations can be used to study this structure. These observations show several different jet features, namely the radio core, quasi-stationary jet features and superluminal moving jet components (Marscher 2009).

The radio core is the most compact part of a jet and could be located at the transition region between optically thick and thin emission or at a standing conical shock a short distance downstream of this transition region. A third possibility for the appearance of the core is a bend of the jet towards the observer's line of sight. However, this cannot be the main explanation of radio cores, since it is less likely that the jet bends towards the observer than away from the line of sight (Marscher 2009). More detailed information on the radio core is given later in this section.

Quasi-stationary jet features are identified with stationary components or features moving at subluminal apparent speeds. These jet features can be produced by recollimation shocks or jet bending, either because the jet bends towards the line of sight or from the formation of a shock due to the collision of the jet with an interstellar cloud (Marscher 2009).

The most common interpretation of the superluminal jet components are propagating shock waves. These shock waves can be produced when the energy density or velocity of the plasma injected into the jet at its origin irregularly increase (Marscher 2009). The phenomenon of the apparent superluminal motion of these jet components will be explained later in this section.

The Radio Core

If the radio core is the region where the optical depth is near to unity, as mentioned above, the absolute position of the core $r_{c,\nu}$ depends on the frequency ν (Marscher 2009) and is given by

$$r_{c,\nu} \propto \nu^{-\frac{1}{k_r}}, \quad (2.1.17)$$

in which the power law index k_r depends on the spectral index and on the magnetic field and particle density distributions (Königl 1981). Therefore, the location of the radio core shifts upstream towards the central engine with increasing frequency (Marscher 2009), as illustrated in Fig. 2.5.

To measure the core shift effect, the location of the core at different frequencies has to be measured. For this purpose, the separation of moving jet components from the core measured at close epochs observed at different frequencies can be used. Assuming that these moving features are optically thin and therefore do not change their posi-

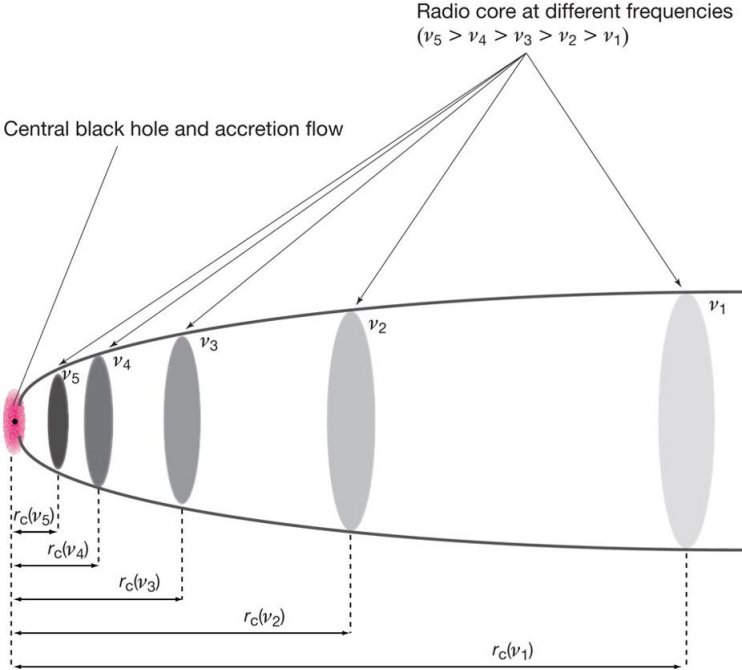


Figure 2.5.: Sketch illustrating the core shift effect. The radio core, represented by the gray ellipses, shifts upstream towards the jet base with increasing frequency. Taken from Hada et al. (2011).

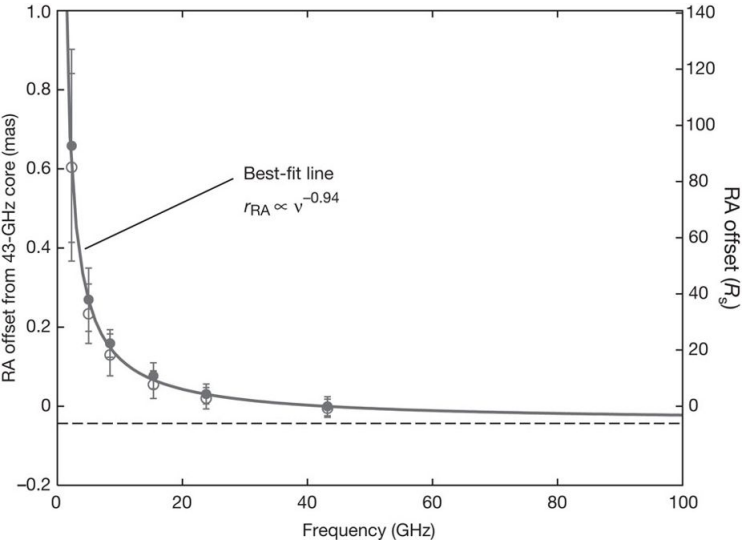


Figure 2.6.: Core shift of M87, measured with quasi-simultaneous radio observations at 2, 5, 8, 15, 22 and 43 GHz. The solid line represents the power law fit. The 43 GHz core is used as reference position. Taken from Hada et al. (2011).

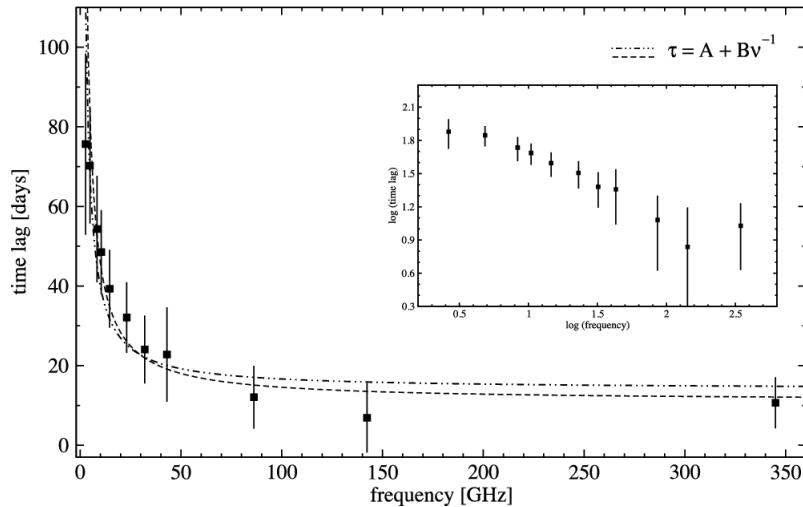


Figure 2.7.: Core shift derived by time lags between γ -ray and radio light curves. Positive time lags denote that the γ -ray light curves lead the radio light curve. The dashed-dotted line represents a fit to all time lags, while the dashed line represents a fit neglecting the time lag of the lowest radio frequency. A double logarithmic representation of the data is given in the inset. Taken from Fuhrmann et al. (2014).

tions, the offset between their separation from the core at different frequencies reflects the frequency dependent core shift (Lobanov 1998). Another method to measure the core shift effect is the phase-referencing technique for quasi-simultaneous multifrequency observations. This technique was used by Hada et al. (2011) to determine the core shift effect of M87, which is shown in Fig. 2.6. Using radio observations at 2, 5, 8, 15, 22 and 43 GHz, they measured the core positions of M87 relative to the reference source M84 and fitted the offset of the different core positions to the 43 GHz core with a power law. They found a power law index of $\frac{1}{k_r} = 0.94 \pm 0.09$, consistent with the model presented by Blandford & Königl (1979) for a freely expanding conical jet in equipartition between magnetic-field energy and jet particle density, in which $k_r = 1$.

Fuhrmann et al. (2014) introduced another method to measure the core shift effect, using time lags between γ -ray and radio light curves derived by a cross-correlation analysis. They performed a source stacking cross-correlation analysis of 54 blazars to determine the time lags between the γ -ray light curve and several radio light curves measured at various frequencies. Assuming that the time lags of radio outbursts observed in the light curves are due to opacity effects and that these outbursts travel at a constant speed, the measured time lags reflect the frequency dependent core shift. Therefore, Fuhrmann et al. (2014) fitted the derived time lags with a power law, plotted in Fig. 2.7, and found a power law index of $\frac{1}{k_r} = 1$, also consistent with Blandford & Königl (1979).

However, this core shift effect is only visible in some compact radio jets but not in others. The latter negative result implies that the core could also be represented by a

standing conical shock through which the turbulent jet plasma passes. Therefore, this result further implies that jets are not only smooth flows punctuated by superluminal components but also contain bright stationary features (Marscher 2009).

Apparent Superluminal Motion

As previously mentioned, VLBI observations show jet components moving outwards along the jet with apparent speeds v higher than the speed of light c . This apparent superluminal motion can be explained by a projection effect.

Consider a single radiating component moving towards an observer along the jet with relativistic speed v and angle ϕ to the line of sight, as illustrated in Fig. 2.8. This component emits signals at the times t_0 and $t_1 = t_0 + \Delta t_{\text{emit}}$ that reach the observer at later times $t'_0 = t_0 + \frac{a+b}{c}$ and $t'_1 = t_1 + \frac{b}{c}$ due to the photon travel distances $a + b$ and b respectively. Furthermore, during the time Δt_{emit} the component moves the distance $a = v\Delta t_{\text{emit}} \cos \phi$ in the direction of the observer. Therefore, the time interval Δt_{obs} , in which the emitted signals arrive at the observer, is given by

$$\Delta t_{\text{obs}} = t'_1 - t'_0 = \Delta t_{\text{emit}} - \frac{a}{c} = \left(1 - \frac{v}{c} \cos \phi\right) \Delta t_{\text{emit}}. \quad (2.1.18)$$

In addition, the projected distance Δx_{app} the component travels in the plane of sky

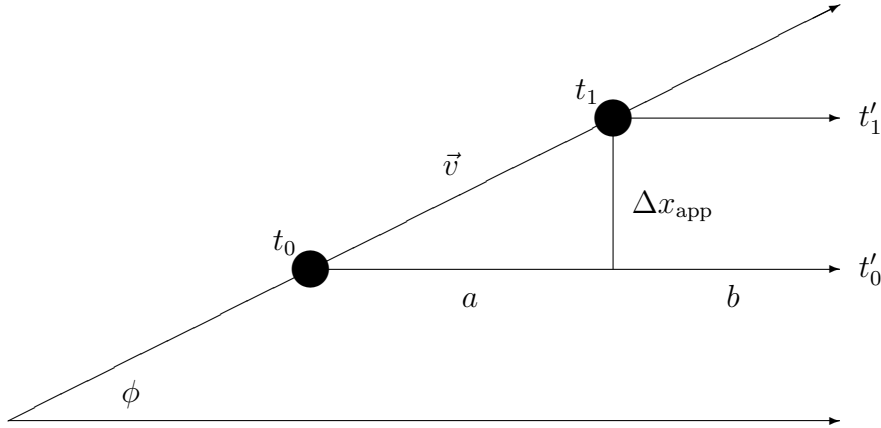


Figure 2.8.: Sketch of a jet component moving at relativistic speed v along the jet with angle ϕ to the line of sight. Signals are emitted at times t_0 and t_1 , respectively. These signals arrive at the observer at later times t'_0 and t'_1 , because of the photon travel distances $a + b$ and b , respectively.

is given by $\Delta x_{\text{app}} = v\Delta t_{\text{emit}} \sin \phi$, leading to the apparent speed v_{app} of

$$v_{\text{app}} = \frac{\Delta x_{\text{app}}}{\Delta t_{\text{obs}}} = \frac{v \sin \phi}{1 - \frac{v}{c} \cos \phi}. \quad (2.1.19)$$

Therefore, for large intrinsic speeds $\beta = \frac{v}{c}$ and small viewing angles ϕ to the line of sight, the observed apparent speed v_{app} can be faster than the speed of light.

Using $\beta_{\text{app}} = \frac{v_{\text{app}}}{c}$, Equation (2.1.19) can be rewritten as

$$\beta_{\text{app}} = \frac{\beta \sin \phi}{1 - \beta \cos \phi}. \quad (2.1.20)$$

Chodorowski (2005) pointed out that Equation (2.1.20) is only valid for nearby sources. For distant sources, the apparent speed also depends on the redshift z . Specifically, because the source moves away from the observer with the Hubble velocity v_{H} due to the expansion of the universe, it is reduced by a factor of $1 + z$. The following explanation is adapted from Chodorowski (2005). Since the apparent distance Δx_{app} , corresponding to the angle $\Delta\theta$ on the sky, depends on the angular diameter distance D_{A} by $\Delta x_{\text{app}} = \Delta\theta D_{\text{A}}$, the apparent speed of the moving jet component is given by

$$\beta_{\text{app}} = \frac{\mu D_{\text{A}}}{c}, \quad (2.1.21)$$

in which $\mu = \frac{\Delta\theta}{\Delta t_{\text{obs}}}$ is the measured proper motion of the component. Furthermore, the angular diameter distance D_{A} depends on the redshift and the luminosity distance D_{L} by

$$D_{\text{A}} = \frac{D_{\text{L}}}{(1 + z)^2}. \quad (2.1.22)$$

Therefore, the apparent speed of the jet can be calculated as

$$\beta_{\text{app}} = \frac{\mu}{c} \cdot \frac{D_{\text{L}}}{(1 + z)^2}, \quad (2.1.23)$$

in which the expansion of the universe has already been included. This dependence of β_{app} on the redshift has to be eliminated by multiplying a factor of $1 + z$ to determine the internal parameters of the source, namely the intrinsic speed β and the viewing angle ϕ . This means that the measured β_{app} must be corrected by a factor of $1 + z$ in order to use Equation (2.1.20) for further calculations. Therefore, the corrected apparent speed is given by

$$\beta_{\text{app}} = \frac{\mu}{c} \cdot \frac{D_{\text{L}}}{1 + z}. \quad (2.1.24)$$

To determine the luminosity distance, a cosmological model with $H_0 = 70 \text{ km s}^{-1} \text{ Mpc}^{-1}$, $\Omega_{\text{m}} = 0.30$ and $\Omega_{\Lambda} = 0.70$ was used in this thesis.

Relativistic Beaming and Doppler Boosting

Since the jets of blazars point into the direction of the observer, or very close to the observer's line of sight, the observed flux density of these sources is relativistically beamed to higher levels, due to Doppler boosting. To describe this effect, an expression of the Doppler factor has to be obtained. If ν_{obs} is the observed frequency in the observer-frame and ν_{emit} is the emitted frequency in the rest-frame of the source, the Doppler factor δ is given by

$$\delta = \frac{\nu_{\text{obs}}}{\nu_{\text{emit}}} = \frac{1}{\gamma(1 - \beta \cos \phi)} = \frac{\sqrt{1 - \beta^2}}{1 - \beta \cos \phi}, \quad (2.1.25)$$

in which $\gamma = \frac{1}{\sqrt{1 - \beta^2}}$ is the Lorentz factor, β is the jet speed in units of the speed of light and ϕ is the viewing angle.

Since it can be shown that $S(\nu)\nu^{-3}$ is a Lorentz invariant, in which $S(\nu)$ is the flux density at frequency ν (Rybicki & Lightman 1985), for a source with power law spectrum $S(\nu) \propto \nu^{-\alpha}$, follows

$$S_{\text{obs}}(\nu_{\text{obs}}) = \delta^{3+\alpha} S_{\text{emit}}(\nu_{\text{obs}}), \quad (2.1.26)$$

in which S_{emit} is the emitted flux density in the rest-frame of the source, S_{obs} is the observed flux density in the observer-frame and α is the spectral index. However, if the source is located at redshift z , the Doppler factor has to be reduced by a factor of $1 + z$, leading to

$$S_{\text{obs}}(\nu_{\text{obs}}) = \left(\frac{\delta}{1 + z} \right)^{3+\alpha} S_{\text{emit}}(\nu_{\text{obs}}). \quad (2.1.27)$$

Now consider a two-sided jet at redshift z in which a jet component moves towards the observer and a counterjet component moves away from the observer with the same speeds and emitted flux densities as well as angles ϕ and $\pi + \phi$ to the line of sight, respectively. The flux density of the jet component is beamed to higher values, while the flux density of the counterjet component is beamed to lower values, according to Equations (2.1.25) and (2.1.27). Therefore, the jets of blazars mostly appear to be one-sided, which can be explained by this Doppler boosting effect.

Furthermore, since the brightness temperature $T_{\text{B}} \propto S(\nu)$, the brightness temperature of a source located at the redshift z is also effected by Doppler boosting. Therefore, one obtains

$$T_{\text{B,obs}} = \left(\frac{\delta}{1 + z} \right)^3 T'_{\text{B}}, \quad (2.1.28)$$

in which $T_{\text{B,obs}} \propto S_{\text{obs}}(\nu_{\text{obs}})$ is the observed brightness temperature in the observer-frame and $T'_{\text{B}} \propto S_{\text{emit}}(\nu_{\text{emit}})$ is the brightness temperature in the rest-frame of the source (Kembhavi & Narlikar 1999). Thus, the brightness temperature can exceed the inverse Compton limit, due to Doppler boosting.

2.1.4. The γ -ray Emitting Region

Blazars emit radiation throughout the entire electromagnetic spectrum from radio frequencies up to high γ -ray energies. This high-energy γ -ray emission shows high-amplitude variability on very short time scales of less than a day (e.g., HESS Collaboration 2010; Jorstad et al. 2013). Furthermore, as already discussed in Sect. 2.1.2, the radio emission is thought to be produced by synchrotron radiation from relativistic electrons, whereas the γ -ray emission is widely believed to be produced by inverse Compton scattering of photons by the same relativistic electrons that are responsible for the synchrotron radiation. Therefore, the radio and γ -ray emission are expected to be correlated (Lister et al. 2015). In fact, such correlations between γ -ray light curves and radio light curves were found by Fuhrmann et al. (2014) and Max-Moerbeck et al. (2014), for example.

Moreover, blazars represent the largest population of extragalactic objects in the γ -ray band (Abdo et al. 2009). However, the exact location of the γ -ray emitting region is still unclear. On the one hand side, the γ -ray emission in broad-line blazars is generally explained by EC on BLR photons (Costamante et al. 2018). Furthermore, the frequently observed intraday variability of the γ -ray emission of blazars indicates a compact emission region near the central engine (Costamante et al. 2018), because the size R of this region is linked to the minimum variability time scale t_{\min} by

$$R < ct_{\min} \frac{\delta}{1+z}, \quad (2.1.29)$$

in which δ is the Doppler factor, c is the speed of light and z is redshift (Sbarrato et al. 2011). However, the same BLR photons used for EC become targets for the $\gamma - \gamma \rightarrow e^{\pm}$ process, leading to a strong cut-off in the γ -ray spectrum above ~ 20 GeV. Therefore, no emission at Very High Energies (VHE) ≥ 100 GeV should be detectable, since the maximum of the $\gamma - \gamma$ absorption is at around 100 GeV to 200 GeV (Costamante et al. 2018). Nevertheless, such VHE emission was observed from the FSRQ 4C+21.35 (Aleksić et al. 2011), for example. Furthermore, Costamante et al. (2018) found no evidence for the expected BLR absorption by analyzing γ -ray spectra of 106 broad-line blazars and concluded that the γ -ray emitting region should be located outside the BLR.

On the other hand, multiwavelength observations combined with VLBI observations indicate a γ -ray emitting region located well beyond the BLR. Jorstad et al. (2001) found a connection between γ -ray outbursts and ejections of superluminal jet components from the radio core that places the γ -ray emitting region several parsecs downstream of the central engine. Furthermore, Fuhrmann et al. (2014) presented a stacked cross-correlation analysis between radio light curves measured at various frequencies and γ -ray light curves of 54 blazars and found that the γ -ray light curves lead the radio light curves, meaning that the γ -ray emitting region should be located upstream of the radio cores. They also found that the γ -ray emitting region of the quasar 3C 454.3 is located at the outer edge of the BLR or beyond at a distance of ~ 0.8 pc to ~ 1.6 pc

from the SMBH. Similar results were found by Max-Moerbeck et al. (2014) using a cross-correlation analysis between 15 GHz OVRO and γ -ray light curves. They found locations of the γ -ray emitting region far beyond the BLR at distances from the SMBH of (12 ± 9) pc for the blazar PKS 1502+106 and $\geq (15 \pm 8)$ pc for the blazar AO 0235+164.

2.2. Very Long Baseline Interferometry

Since the Earth's atmosphere is only transparent in the optical and the radio regime, radio astronomy plays a very important role in investigating the universe. To study the parsec-scale structure and the physical properties of AGN jets, radio astronomers developed a method called Very Long Baseline Interferometry (VLBI), in which an array of radio telescopes leads to a very high angular resolution (Burke & Graham-Smith 2010; Thompson et al. 2017). Since, the angular resolution θ of a single radio telescope is given by

$$\theta \approx 1.22 \frac{\lambda}{D}, \quad (2.2.1)$$

in which λ is the observational wavelength and D is the diameter of the telescope (Carroll & Ostlie 2014), the diameter of the telescope has to be increased to improve the angular resolution of an observation at a given wavelength. This can be done by synchronizing multiple radio telescopes in an array; the diameter then is given by the longest baseline between the reflection centers of two telescopes of this array. In the case of VLBI arrays, very long baselines of thousands of kilometers are implemented to reach very high angular resolutions (Burke & Graham-Smith 2010; Thompson et al. 2017). In this section the observational technique of VLBI will be introduced. If no other references are given, this section will be based on the textbooks by Burke & Graham-Smith (2010) and Thompson et al. (2017).

2.2.1. The Two-Element Interferometer

The simplest array of radio telescopes consists of two identical antennas. Therefore, the concept of radio interferometry will be discussed at first for this so-called two-element interferometer (see Fig. 2.9), based on the explanation of Clark (1999) if no other references are given.

Consider a radio source at location \vec{R} that causes a time-variable electric field $\vec{E}(\vec{R}, t)$. This electric field propagates through space and can be detected by a radio telescope at location \vec{r} . If the time interval of this varying field is finite, its magnitude can be expressed by the real part of a Fourier series in which only the exponentials are time dependent. Then, the Fourier coefficients $\vec{E}_\nu(\vec{R})$ of the electric field $\vec{E}(\vec{R}, t)$ can be used for the further calculations. These coefficients are called quasi-monochromatic components and are complex quantities. Using these coefficients, one can determine the electric field at location \vec{r} to be

$$\vec{E}_\nu(\vec{r}) = \int \int \int P_\nu(\vec{R}, \vec{r}) \vec{E}_\nu(\vec{R}) dx dy dz, \quad (2.2.2)$$

in which $P_\nu(\vec{R}, \vec{r})$ describes the influences of the electric field at \vec{R} on the electric field

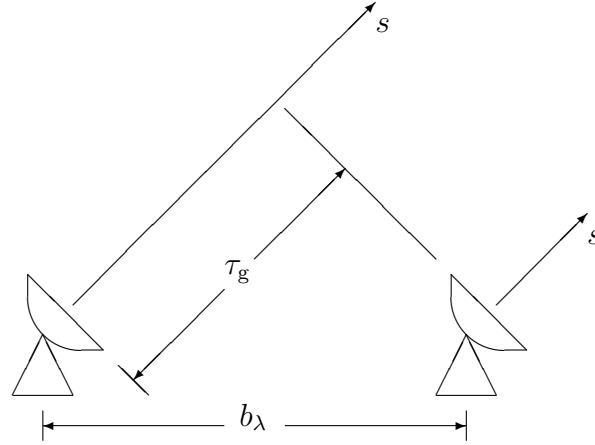


Figure 2.9.: Two-element interferometer, consisting of two identical radio telescopes. Adapted from Burke & Graham-Smith (2010).

at \vec{r} and is called the propagator.

At this point, some assumptions are introduced to simplify the calculations. At first, all polarization phenomena can be ignored, meaning that the electric field can be treated as a scalar field. Furthermore, it is assumed that the source of interest is far away, meaning that it is impossible to describe the structure of the emitting region in the third dimension. Therefore, one can only observe the surface brightness $\varepsilon_\nu(\vec{R})$ of the source, distributed on the surface of a celestial sphere in the distance $|\vec{R}|$ from the observer. The third assumption is that the space within this celestial sphere is empty, leading to a simple form for the propagator in Equation (2.2.2). With these three assumptions, Equation (2.2.2) can be rewritten as

$$\vec{E}_\nu(\vec{r}) = \int \varepsilon_\nu(\vec{R}) \frac{e^{2\pi i\nu|\vec{R}-\vec{r}|/c}}{|\vec{R}-\vec{r}|} dS, \quad (2.2.3)$$

in which dS is the element of surface area on the celestial sphere.

With Equation (2.2.3), the so-called spatial coherence function $V_\nu(\vec{r}_1, \vec{r}_2)$ can be calculated as the correlation of the field at \vec{r}_1 and the field at \vec{r}_2 , which is defined as the expectation value $\langle E_\nu(\vec{r}_1) E_\nu^*(\vec{r}_2) \rangle$, in which the asterisk indicates the complex conjugate. Using Equation (2.2.3), one obtains

$$V_\nu(\vec{r}_1, \vec{r}_2) = \left\langle \int \int \varepsilon_\nu(\vec{R}_1) \varepsilon_\nu^*(\vec{R}_2) \frac{e^{2\pi i\nu|\vec{R}_1-\vec{r}_1|/c}}{|\vec{R}_1-\vec{r}_1|} \frac{e^{-2\pi i\nu|\vec{R}_2-\vec{r}_2|/c}}{|\vec{R}_2-\vec{r}_2|} dS_1 dS_2 \right\rangle. \quad (2.2.4)$$

Furthermore, assuming that the radiation from astronomical objects is not spatially coherent, meaning that $\langle \varepsilon_\nu(\vec{R}_1) \varepsilon_\nu^*(\vec{R}_2) \rangle = 0$ for $\vec{R}_1 \neq \vec{R}_2$, Equation (2.2.4) becomes

$$V_\nu(\vec{r}_1, \vec{r}_2) = \int \left\langle \left| \varepsilon_\nu(\vec{R}) \right|^2 \right\rangle \left| \vec{R} \right|^2 \frac{e^{2\pi i \nu |\vec{R}-\vec{r}_1|/c} e^{-2\pi i \nu |\vec{R}-\vec{r}_2|/c}}{\left| \vec{R}-\vec{r}_1 \right| \left| \vec{R}-\vec{r}_2 \right|} dS. \quad (2.2.5)$$

Moreover, writing \vec{s} for the unit vector $\frac{\vec{R}}{|\vec{R}|}$ and $I_\nu(\vec{s})$ for the observed intensity $\left\langle \left| \varepsilon_\nu(\vec{R}) \right|^2 \right\rangle \left| \vec{R} \right|^2$ and assuming $\vec{R} \gg \vec{r}_i$, which is equivalent to the second simplifying assumption presented above and leads to the fact that terms of the order $\left| \frac{\vec{r}_i}{\vec{R}} \right|$ can be neglected and $dS = \left| \vec{R} \right|^2 d\Omega$, Equation (2.2.5) becomes

$$V_\nu(\vec{r}_1, \vec{r}_2) = \int I_\nu(\vec{s}) e^{-2\pi i \nu \vec{s}(\vec{r}_1 - \vec{r}_2)/c} d\Omega. \quad (2.2.6)$$

This spatial coherence function is the quantity that is measured by a radio interferometer. Furthermore, the intensity distribution $I_\nu(\vec{s})$, in which an observer is interested, can be deduced by measuring $V_\nu(\vec{r}_1, \vec{r}_2)$ and performing a Fourier inversion. For this purpose, there are two possibilities to simplify Equation (2.2.6). Before explaining these two possibilities, it is useful to introduce convenient coordinate systems. While the vectors \vec{r}_i are described in the (u, v, w) -system, the vector \vec{s} is described in the (l, m, n) -system, which leads to $d\Omega = \frac{dldm}{n} = \frac{dldm}{\sqrt{1-l^2-m^2}}$.

The first way to simplify Equation (2.2.6) is to assume that the two telescopes are coplanar. Then, the baseline, measured in terms of the wavelength λ , is given by $\vec{b}_\lambda = \vec{r}_1 - \vec{r}_2 = \lambda(u, v, 0)^T$ (see Fig. 2.9), while $\vec{s} = (l, m, \sqrt{1-l^2-m^2})^T$. Therefore, Equation (2.2.6) can be rewritten as

$$V_\nu(u, v, w \equiv 0) = \int \int I_\nu(l, m) \frac{e^{-2\pi i (ul+vm)}}{\sqrt{1-l^2-m^2}} dldm, \quad (2.2.7)$$

in which the spatial coherence function $V_\nu(u, v, w \equiv 0)$ is the Fourier transform of the modified intensity $\frac{I_\nu(l, m)}{\sqrt{1-l^2-m^2}}$.

The second way to simplify Equation (2.2.6) is to assume that all of the radiation comes from a small area of the celestial sphere. Let \vec{s} and \vec{s}_0 be unit vectors and $\vec{s} = \vec{s}_0 + \vec{\sigma}$, in which $\vec{\sigma}$ is a small vector, then these assumptions imply that

$$\begin{aligned} 1 = \vec{s}_0^2 = \vec{s}^2 &= \vec{s}_0^2 + 2\vec{s}_0\vec{\sigma} + \vec{\sigma}^2 \approx 1 + 2\vec{s}_0\vec{\sigma} \\ &\Rightarrow \vec{s}_0\vec{\sigma} = 0 \end{aligned}$$

$$\Rightarrow \vec{s}_0 \perp \vec{\sigma}.$$

Introducing a special coordinate system again such that $\vec{s}_0 = (0, 0, 1)^T$, Equation (2.2.6) becomes

$$V'_\nu(u, v, w) = e^{-2\pi i w} \int \int I_\nu(l, m) e^{-2\pi i (ul+vm)} dl dm. \quad (2.2.8)$$

Here, the baseline is given by $\vec{b}_\lambda = \lambda(u, v, w)^T$. Furthermore, the exponential factor in front of the integral in Equation (2.2.8) can be absorbed into the left hand side by $V_\nu(u, v, w) = e^{2\pi i w} V'_\nu(u, v, w)$, which then is independent of w and leads to

$$V_\nu(u, v) = \int \int I_\nu(l, m) e^{-2\pi i (ul+vm)} dl dm. \quad (2.2.9)$$

This function $V_\nu(u, v)$ is the coherence function relative to the direction \vec{s}_0 , which is called the phase tracking center. This phase tracking center \vec{s}_0 is defined by the condition $\tau_g = \tau_i$. If the telescope at location \vec{r}_1 is chosen as reference antenna, the electric field will arrive at the second telescope at location \vec{r}_2 delayed by the geometrical time delay $\tau_g = \frac{\vec{b}\vec{s}}{c}$ (see Fig. 2.9). Furthermore, an additional instrumental time delay τ_i can be inserted to equalize the signal delay, which then defines the phase tracking center \vec{s}_0 (Burke & Graham-Smith 2010).

Equation (2.2.9) is a Fourier transform. Therefore, the direct inversion is given by

$$I_\nu(l, m) = \int \int V_\nu(u, v) e^{2\pi i (ul+vm)} du dv. \quad (2.2.10)$$

However, in practice, the coherence function $V_\nu(u, v)$ is only sampled at specific points, which can be described by a sampling function $S_\nu(u, v)$ that is zero where no data have been taken and one where data have been taken. Therefore, Equation (2.2.10) becomes

$$I_\nu^D(l, m) = \int \int V_\nu(u, v) S_\nu(u, v) e^{2\pi i (ul+vm)} du dv. \quad (2.2.11)$$

which is often referred to as the dirty image. Defining the so-called dirty beam B^D , which is also known as synthesized beam or point spread function, to be

$$B^D(l, m) = \int \int S_\nu(u, v) e^{2\pi i (ul+vm)} du dv, \quad (2.2.12)$$

one can see in Equation (2.2.11), that the dirty image I^D is the true intensity distribution I convolved with the dirty beam B^D .

Finally, an additional factor $A_\nu(\vec{s})$ describing the sensitivity of the radio telescopes

as a function of direction has to be included in Equation (2.2.9), leading to

$$V(u, v) = \int \int A_\nu(l, m) I_\nu(l, m) e^{-2\pi i(ul+vm)} dl dm. \quad (2.2.13)$$

This so-called complex visibility $V(u, v)$ is therefore given by the convolution of the coherence function $V_\nu(u, v)$ and the primary beam B^P , which is given by

$$B^P(u, v) = \int \int A_\nu(l, m) e^{-2\pi i(ul+vm)} dl dm \quad (2.2.14)$$

and is also known as normalized reception pattern of the interferometer elements.

To summarize, the measured quantity in radio interferometry is the complex visibility $V(u, v)$, which is the convolution of the primary beam B^P and the coherence function $V_\nu(u, v)$. This coherence function is the Fourier transform of the so-called dirty image I^D , which is the true intensity distribution I convolved with the dirty beam B^D . Therefore, to compute the real intensity distribution, the dirty image has to be deconvolved. This deconvolution process will be discussed in more detail in Sect. 2.2.4.

2.2.2. Interferometry with Arrays

An array of radio telescopes consists of multiple two-element interferometer. For an array with N elements there exist $N(N-1)/2$ baselines b_{ij} that observe visibilities \hat{V}_{ij} , which are related to the true visibilities V_{ij} by

$$\hat{V}_{ij} = g_i g_j^* V_{ij}, \quad (2.2.15)$$

in which g_i and g_j are the complex gain factors of the array elements i and j . These gain factors include the effects of the atmospheric paths to the telescopes and instrumental effects. Therefore, to determine the true visibilities V_{ij} , these gain factors have to be computed, which can be done by using observations of calibrator sources. However, this calibration procedure yields a lot of redundant information and very big data sets which can be optimized by using the so-called closure relations. These closure relations will be discussed here, based on Cornwell & Fomalont (1999) and Cornwell (1989).

Using the phase part of Equation (2.2.15), one obtains

$$\hat{\theta}_{ij} = \theta_{ij} + \phi_i - \phi_j, \quad (2.2.16)$$

in which $\hat{\theta}_{ij}$ is the measured phase, θ_{ij} is the true phase and ϕ_i is the phase error associated with the i -th telescope. Furthermore, let the sum of the measured phases around a loop of three baselines be defined by

$$\hat{C}_{ijk} = \hat{\theta}_{ij} + \hat{\theta}_{jk} + \hat{\theta}_{ki}, \quad (2.2.17)$$

in which \hat{C}_{ijk} is called the closure phase. Moreover, Equation (2.2.17) is also valid for the true phases, leading to

$$C_{ijk} = \theta_{ij} + \theta_{jk} + \theta_{ki}. \quad (2.2.18)$$

Therefore, the observed and true sums are equal, which is shown by

$$\begin{aligned} \hat{C}_{ijk} &= \hat{\theta}_{ij} + \hat{\theta}_{jk} + \hat{\theta}_{ki} \\ &= \theta_{ij} + \phi_i - \phi_j + \theta_{jk} + \phi_j - \phi_k + \theta_{ki} + \phi_k - \phi_i \\ &= \theta_{ij} + \theta_{jk} + \theta_{ki} \\ &= C_{ijk}. \end{aligned} \quad (2.2.19)$$

This shows that a closure phase can be computed that is independent of the phase errors of the individual telescopes. Similarly, a closure amplitude A_{ijkl} can be defined for a loop of four telescopes to be

$$A_{ijkl} = \frac{|\hat{V}_{ij}| |\hat{V}_{kl}|}{|\hat{V}_{ik}| |\hat{V}_{jl}|}. \quad (2.2.20)$$

Here, the amplitudes of the complex gain factors cancel out, so that the observed closure amplitude equals the true closure amplitude, similar to the closure phases.

The closure phases can be used for self-calibration by allowing only corrections to the measured visibility phases that do not alter the closure phases. One advantage of this method is that the closure phases do not have to be calculated explicitly or stored. Furthermore, receiver noise can be treated by choosing the telescope phases ϕ_i to minimize the mean square differences S between the observed visibilities V_{ij}^{obs} and the visibilities V_{ij}^{mod} , which are predicted by a model and are modified by the unknown telescope phases:

$$S = \sum_{i,j} w_{ij} |V_{ij}^{\text{obs}} - e^{i\phi_i} e^{-i\phi_j} V_{ij}^{\text{mod}}|^2, \quad (2.2.21)$$

in which w_{ij} is a weighting factor that can be used to favor baselines b_{ij} which show good signal-to-noise ratios (SNR). Once the telescope phases ϕ_i that minimize S are found, they can be used for the calibration of nearby objects (Cornwell 1989).

As already mention in Sect. 2.2.1, the observed visibility V_{ij} is only sampled at specific points on the (u, v) -plane. For a single two-element interferometer, this visibility $V(u, v)$ appears as two points opposite to each other on the (u, v) -plane, which can be explained due to the fact that one two-element interferometer offers two anti-parallel baseline vectors. Here, the distance of these two points to the origin of the (u, v) -plane correspond to the length of the baseline. Therefore, large arrays consisting of several telescopes are used to sample as many values of the visibility function as possible. Furthermore, the rotation of the Earth can also be used for this purpose. This is called Earth rotation synthesis or aperture synthesis. During an extended observation period,

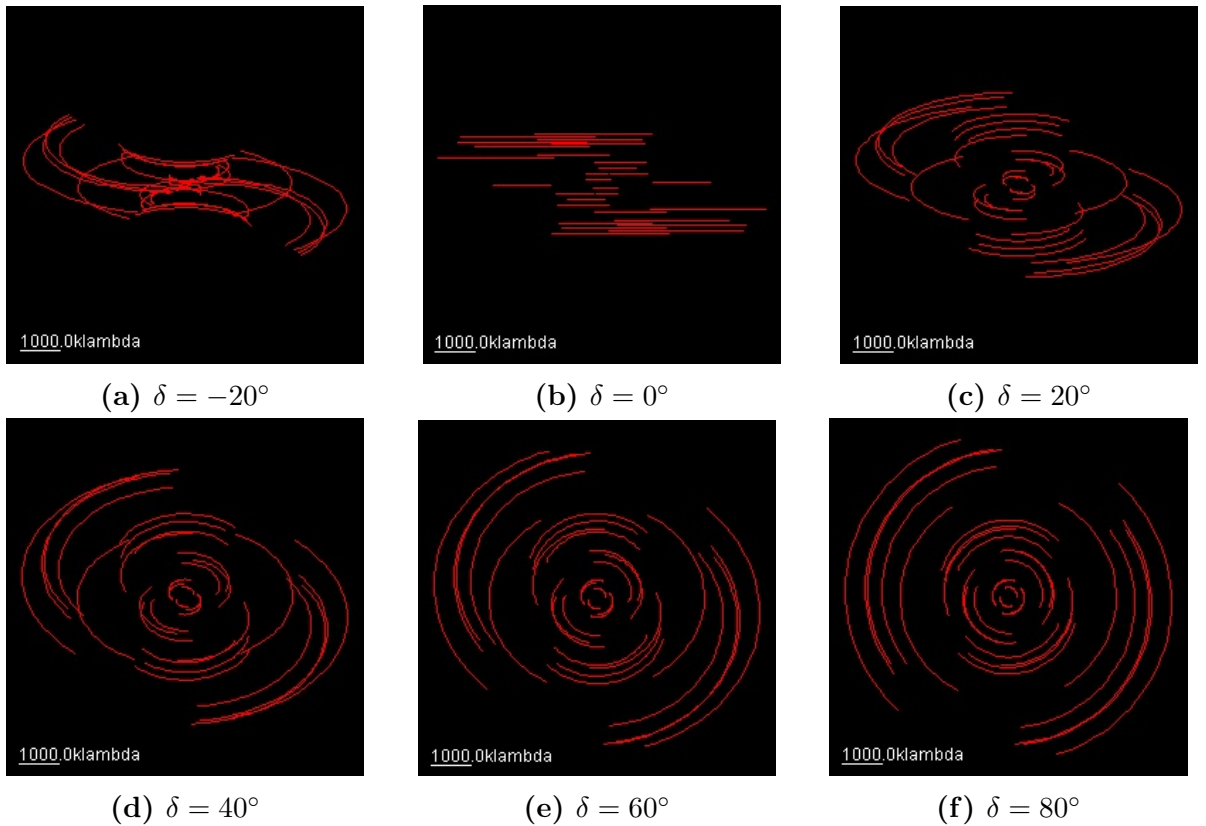


Figure 2.10.: (u, v) -plane coverages of the MERLIN array for eight-hour tracking observations at different declinations δ . The plots were made with the Virtual Radio Interferometer (VRI)(<http://www.narrabri.atnf.csiro.au/astronomy/vri.html>).

the rotation of the Earth changes the orientation of the two-element interferometer baselines with respect to the observed source. Therefore, these baselines produce arcs on the (u, v) -plane. The effect of this aperture synthesis is shown in Fig. 2.10, in which (u, v) -plane coverages of the MERLIN array are plotted for eight-hour tracking observations at different declinations δ . One can see that the synthesis effect is strongest at large declinations, leading to circles on the (u, v) -plane for $\delta = 90^\circ$. For smaller declinations the circles become ellipses, while for $\delta = 0^\circ$ the circles become straight lines.

2.2.3. The Very Long Baseline Array

One example of such a VLBI array is the Very Long Baseline Array (VLBA). The following information on the VLBA was taken from the National Radio Astronomy Observatory (NRAO) website¹.

¹<https://science.nrao.edu/facilities/vlba>

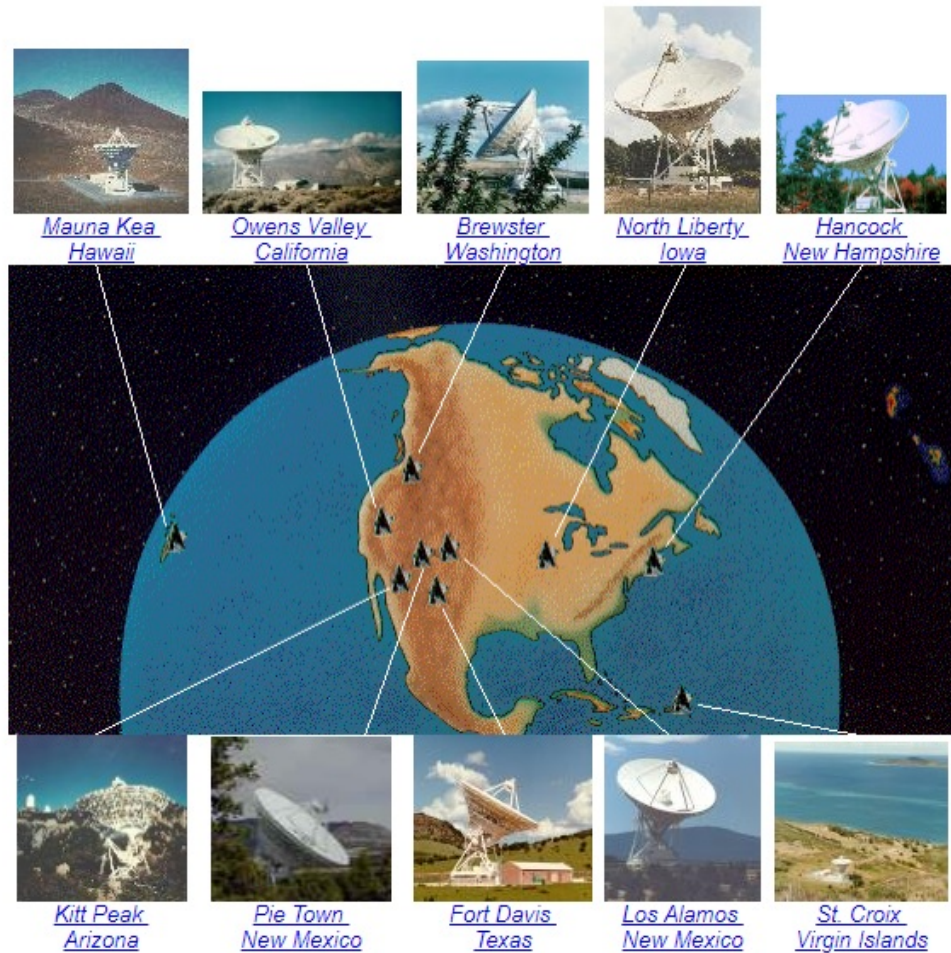


Figure 2.11.: The Very Long Baseline Array consisting of 10 identical telescopes. Taken from NRAO (<http://www.vlba.nrao.edu/sites/>).

The VLBA consists of 10 identical telescopes with diameters of 25 m that are spread across the USA and located at Brewster, Washington (BR), Fort Davis, Texas (FD), Hancock, New Hampshire (HN), Kitt Peak, Arizona (KP), Los Alamos, New Mexico (LA), Mauna Kea, Hawaii (MK), North Liberty, Iowa (NL), Owens Valley, California (OV), Pie Town, New Mexico (PT) and St. Croix, Virgin Islands (SC). The locations of the individual telescopes are shown in Fig. 2.11. The telescopes build baselines from 200 km up to the largest baseline of 8600 km between the telescopes located at Mauna Kea, Hawaii and St. Croix, Virgin Islands. The VLBA observes at frequencies of 312 MHz to 96 GHz subdivided into nine discrete bands plus two narrow sub-gigahertz bands. It can be used to observe radio sources with brightness temperatures higher than $\sim 10^5$ K.

2.2.4. Analysis of VLBI Data

As previously discussed in Sect. 2.2.2, the visibility data observed with a VLBI array have to be calibrated, as the first step in analyzing VLBI data. This initial amplitude and phase calibration can for example be performed using the Astronomical Image Processing System (AIPS) provided by the NRAO. Since this calibration process was not part of this thesis, no further information on AIPS will be given here. Nevertheless, more information on the calibration process can be found for example in Cotton (1995) and Diamond (1995).

In Sect. 2.2.1, it was shown that the measured visibility V^{obs} of a source is the Fourier transform of the measured intensity I^{D} , which is the convolution of the true intensity I with the synthesized beam B^{D} . Therefore, the measured intensity has to be deconvolved to obtain the true intensity distribution of the observed source. This deconvolution process will be discussed in this section.

The observed visibility is given by

$$V^{\text{obs}}(u, v) = S(u, v) w(u, v) V(u, v), \quad (2.2.22)$$

in which $S(u, v)$ is the sampling function introduced in Sect. 2.2.1, $V(u, v)$ is the true visibility and $w(u, v)$ is a weighting factor (Thompson et al. 2017). To obtain the best SNR, the visibilities should be weighted inversely as their variances, meaning that the weighting factors $w(u, v)$ should be inversely proportional to these variances. If the averaging time is the same for all data points, these variances and therefore also the weighting factors should all be the same, which is known as natural weighting. Otherwise, the data can also be weighted by a factor that is inversely related to the area density of the data in the (u, v) -plane, which is called uniform weighting. While natural weighting provides higher sensitivity, uniform weighting provides higher resolution (Thompson et al. 2017).

As mentioned above, the visibility V^{obs} is the Fourier transform of the so-called dirty image I^{D} , which is the convolution of the true intensity I with the dirty beam B^{D} . Therefore, to obtain the true intensity of a source, the dirty image has to be deconvolved. One method to perform this deconvolution is the so-called CLEAN algorithm introduced by Högbom (1974). This algorithm works as follows.

1. Compute the dirty image I^{D} and the dirty beam B^{D} by Fourier transformation of the measured visibility $V^{\text{obs}}(u, v)$ and the weighted sampling function $w(u, v) S(u, v)$, respectively.
2. Find the point with highest intensity in the image. For this purpose, it is useful to specify an area within the image by setting CLEAN windows. Then, multiply the dirty beam B^{D} with the peak intensity and a loop gain and subtract it from the image at the position of this point. Furthermore, record the position and

amplitude of the removed point by inserting a δ -function into a CLEAN model.

3. Repeat the procedure of step 2 iteratively until all significant source structure has been removed from the image.
4. Convolve the δ -functions with a idealized CLEAN beam that usually is a Gaussian with a half-amplitude width equal to that of the dirty beam.
5. Add all removed components into the CLEAN image.

This CLEAN algorithm can be combined with self-calibration (see Sect. 2.2.2), which then is called hybrid imaging or mapping. In general, Equation (2.2.21) can be written as

$$S = \sum_{ij} w_{ij} |V_{ij}^{\text{obs}} - g_i g_j^* V_{ij}^{\text{mod}}|^2, \quad (2.2.23)$$

in which g_i and g_j are the complex gain factors of the i -th and j -th telescopes, respectively (Thompson et al. 2017). This Equation (2.2.23) can also be written as

$$S = \sum_{ij} w_{ij} |V_{ij}^{\text{mod}}|^2 |X_{ij} - g_i g_j^*|^2, \quad (2.2.24)$$

in which X_{ij} is given by

$$X_{ij} = \frac{V_{ij}^{\text{obs}}}{V_{ij}^{\text{mod}}} \quad (2.2.25)$$

and can be used to determine the gain factors by minimizing S in a way that does not alter the closure relations. Using this formalism, the CLEAN algorithm combined with self-calibration works in the following way (Thompson et al. 2017):

1. Produce an initial CLEAN image.
2. Compute the X_{ij} factors for each visibility integration period.
3. Compute the gain factors for each integration period.
4. Calibrate the measured visibility values using the gain factors.
5. Build a new CLEAN image.
6. Check for convergence and go back to step 2 if necessary.

The difference mapping algorithm implemented in the program DIFMAP (Shepherd 1997), in which the CLEAN algorithm is combined with self-calibration in amplitude and phase, was used for the deconvolution process in this thesis. Following the explanations given in the DIFMAP-cookbook², this process was started with a point source model at the

²<ftp://ftp.astro.caltech.edu/pub/difmap/>

map center. Then, several **CLEAN** steps, each followed by a phase self-calibration, were performed until a new **CLEAN** model was found that best fit the data. After that, an amplitude self-calibration over the complete observation time was performed. This process was repeated with ever decreasing time intervals for the amplitude self-calibration, leading to a final **CLEAN** image. After removing all **CLEAN** components, this image was model-fitted by elliptical 2D Gaussian components, producing a model that can be used to study the kinematics of the source.

To produce plots and to analyze the time evolution and kinematics of 4C+01.28, the Interactive Spectral Interpretation System (**ISIS**) (Houck & DeNicola 2000) was used.

2.3. Cross-Correlation Function

In order to search for correlations between γ -ray and radio light curves, a cross-correlation analysis was performed. The Cross-Correlation Function (CCF) for two discrete and evenly sampled light curves, $x(t_i)$ and $y(t_i)$, as a function of the time lag τ is given by

$$CCF(\tau) = \frac{1}{N} \sum_{i=1}^N \frac{[x(t_i) - \bar{x}][y(t_i - \tau) - \bar{y}]}{\sigma_x \sigma_y}, \quad (2.3.1)$$

in which \bar{x} , σ_x and \bar{y} , σ_y are the mean values and the standard deviations of $x(t_i)$ and $y(t_i)$, respectively (Fuhrmann et al. 2014). This function can only be computed if $x(t_i)$ and $y(t_i)$ are sampled by a discrete set of points which are separated by a constant spacing $\Delta t = t_{i+1} - t_i$ for all values $1 \leq i \leq N - 1$ (Edelson & Krolik 1988; White & Peterson 1994). In this case, the CCF is well defined for any $\tau = m\Delta t$, since there are $N - m$ points t_i such that $t_i - \tau$ is also in the data set, at least so long as $N - m \gg 1$. However, astronomical data are mostly unevenly sampled, so that there are no values of τ such that t_i and $t_i - \tau$ are both in the data set for more than one t_i (Edelson & Krolik 1988). To avoid this problem, two different methods are commonly used, namely the Discrete Cross-Correlation Function (DCF), introduced by Edelson & Krolik (1988), as well as the Interpolated Cross-Correlation Function (ICF), in which the light curves are interpolated and resampled to achieve evenly sampled light curves (White & Peterson 1994). These two methods will be discussed in further detail in Sects. 2.3.1 and 2.3.2, respectively.

2.3.1. Discrete Cross-Correlation Function

To compute the CCF for two unevenly sampled data sets $x(t_i)$ and $y(t_j)$, Edelson & Krolik (1988) introduced the so-called Discrete Cross-Correlation Function (DCF) which is defined in the following manner. At first, the set of unbinned discrete correlations of all measured pairs $(x(t_i), y(t_j))$, associated with the pairwise lag $\Delta t_{ij} = t_j - t_i$, is computed to be

$$UDCF_{ij} = \frac{[x(t_i) - \bar{x}][y(t_j) - \bar{y}]}{\sqrt{(\sigma_x^2 - e_x^2)(\sigma_y^2 - e_y^2)}}, \quad (2.3.2)$$

in which e_x and e_y are the measurement errors associated with the data sets $x(t_i)$ and $y(t_j)$, respectively. Binning this result in time and averaging over the M pairs for which $\tau - \frac{\Delta\tau}{2} \leq \Delta t_{ij} < \tau + \frac{\Delta\tau}{2}$ leads to

$$DCF(\tau) = \frac{1}{M} \sum UDCF_{ij}, \quad (2.3.3)$$

with the uncertainty given by

$$\sigma_{DCF(\tau)} = \frac{1}{M-1} \sqrt{\sum [UDCF_{ij} - DCF(\tau)]^2}. \quad (2.3.4)$$

Note that it will be necessary to replace $M-1$ in the denominator of Equation (2.3.4) by $\sqrt{(M-1)(M'-1)}$, if the $UDCF_{ij}$ within a single bin show mutual correlations. Here, M' denotes the number of uncorrelated $UDCF$ values within the bin, which is given by the number of different measurement times t_i for the data set $x(t_i)$.

2.3.2. Interpolated Cross-Correlation Function

Another method to compute the CCF of two unevenly sampled data sets $x(t_i)$ and $y(t_j)$ is the so-called Interpolated Cross-Correlation Function (ICF). In this thesis, the ICF method introduced by White & Peterson (1994) was used, in which the CCF was computed twice and the results were averaged. In the first pass, each measured data point of $x(t_i)$ was paired with interpolated values of $y(t_i - \tau)$. In the second pass, the measured points of $y(t_j)$ were paired with interpolated values of $x(t_j + \tau)$. For this purpose, a piecewise linear interpolation was used.

To determine the uncertainties of the time lags τ derived by the ICF, the method introduced by Peterson et al. (1998) was used in this thesis. The following explanation of this method is based on Peterson et al. (1998). There are two principal sources of uncertainties in cross-correlation time lags, namely flux uncertainties in the individual measurements and uncertainties associated with the sampling rate of the light curves. The uncertainties in the fluxes can easily be assessed by Monte Carlo (MC) simulations. For this purpose, each flux measurement is modified statistically independent of each of the others by random Gaussian deviates based on the individual uncertainties of the fluxes, which is referred to as "flux randomization" (FR). The uncertainties associated with the sampling rate can be assessed by drawing randomly selected data points from the data set. Therefore, each MC realization is based on a randomly chosen subset of the original data set, leading to the term "random subset selection" (RSS). In order to consider both sources of uncertainties, the FR and RSS methods can be combined in one single MC simulation. Multiple such MC simulations then build up a cross-correlation peak distribution, so that the uncertainty of the time lag τ can be computed as the standard deviation of the time lags at which this simulated ICF peaks are located.

3. Presenting 4C+01.28

4C+01.28 (also known as 1055+018, J1058+015 and J1058+0133) was first classified as a blazar by Impey & Tapia (1990). However, its further classification is not really clear. While some authors (e.g., Fuhrmann et al. 2014; Jorstad et al. 2017; Max-Moerbeck et al. 2014) identified 4C+01.28 as a BL Lac object due to its optical properties, others (e.g., Lister et al. 1998, 2019; Murphy et al. 1993; Pushkarev et al. 2009) classified it as a highly polarized quasar based on its radio properties.

4C+01.28 has a redshift of $z = 0.89$ (Jorstad et al. 2017). At this distance $1 \text{ mas} = 7.77 \text{ pc}$, using a cosmological model with $H_0 = 70 \text{ km s}^{-1} \text{ Mpc}^{-1}$, $\Omega_m = 0.30$ and $\Omega_\Lambda = 0.70$.

4C+01.28 has also been the subject of extensive multifrequency radio observations. The light curves of these observations show high variability in flux density with outbursts occurring every 1-2 years (Lister et al. 1998). Such behavior can also be seen in the *Fermi*/LAT γ -ray light curve that will be presented in Sect. 5.1. Furthermore, VLBA observations at 43 GHz of 4C+01.28 show the ejection of a superluminal jet component that seems to be associated with a bright γ -ray outburst (MacDonald et al. 2017). Therefore, 4C+01.28 is a good target to determine the location of the γ -ray emitting region.

3.1. Previous Radio Observations

Attridge et al. (1999) presented images of 4C+01.28, taken at 5 GHz with the VLBA plus a single Very Large Array (VLA) antenna. A polarized flux density image of this study shows that the jet of 4C+01.28 consists of two distinct parts, namely a spine, containing several jet components, in which the magnetic field is perpendicular to the jet axis and a boundary layer, called the sheath, in which the magnetic field is parallel to the jet axis. This spine-sheath polarization structure was later confirmed by Pushkarev et al. (2005) using VSOP observations at 1.6 GHz and 5 GHz. A 5 GHz polarized flux density image is shown in Fig. 3.1. This image was observed with the ground-array, consisting of the VLBA plus the 100 m Effelsberg antenna. Attridge et al. (1999) interpreted this two-component polarization structure to be caused by transverse shocks that dominate within the jet spine and lead to a magnetic field perpendicular to the jet axis, as well as interactions between the jet and the surrounding medium, resulting in the longitudinal magnetic field of the sheath. Otherwise, Pushkarev et al. (2005) interpreted the spine-sheath structure to be caused by a helical or toroidal magnetic field associated with the

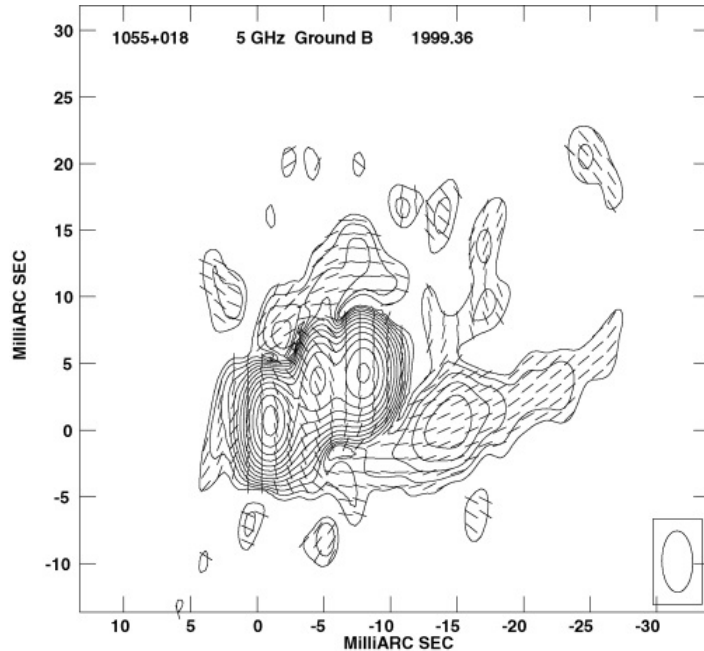


Figure 3.1.: Polarized intensity image of 4C+01.28, taken at 5 GHz with the VLBA plus the 100 m Effelsberg antenna. The superposed sticks show the orientation of the magnetic field. The ellipse in the bottom right corner corresponds to the beam. The contours begin at $0.5 \text{ mJy beam}^{-1}$ and increase by a factor of $\sqrt{2}$. Taken from Pushkarev et al. (2005).

jet.

Furthermore, these 5 GHz observations show a typical core-jet structure with a bright unresolved component to the east and a jet to the west-northwest (Attridge et al. 1999). This core-jet structure can also be seen in VLBA images taken at 15 GHz (Lister et al. 2018) and 43 GHz (Jorstad et al. 2017). However, on kiloparsec scales, 4C+01.28 appears as an FR II radio source, showing hot spots to the north and south of the core and a jet to the south connecting the core and the southern hot spot (Murphy et al. 1993). An image of this kiloparsec-scale structure taken with the VLA at 1.64 GHz and presented by Murphy et al. (1993) is shown in Fig. 3.2. Therefore, there is a significant misalignment of the jet orientation of 4C+01.28 between the parsec and kiloparsec scales (Attridge et al. 1999).

3.2. Previous Kinematic Analyses

4C+01.28 was monitored with the VLBA at 15 GHz as part of the MOJAVE sample and at 43 GHz. Jorstad et al. (2017) presented a kinematic analysis of these 43 GHz VLBA observations, taken from April 2009 to January 2013. In Fig. 3.3, the distance of the jet

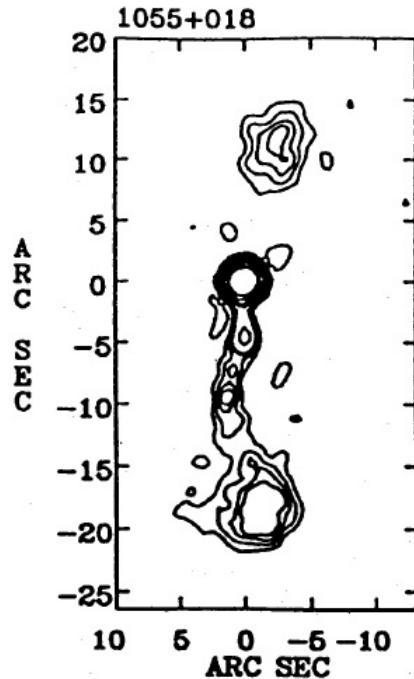


Figure 3.2.: 1.64 GHz VLA image of 4C+01.28. The contours are given by $(-4, -3, -2, -1, 1, 2, 3, 4, 8, 16, 32, \dots, 512)$ mJy beam^{-1} and the beam is given by $1.36 \text{ arcsec} \times 1.31 \text{ arcsec}$ at -30.5° . Taken from Murphy et al. (1993).

component to the core component is plotted with respect to the observation time. The obtained speeds of the different jet components are listed in Table 3.1. One can see, that 4C+01.28 possesses a quasi-stationary component A1 ($\mu < 2\sigma$) which is close to the core. Furthermore, Jorstad et al. (2017) detected a superluminal jet component B1 that appeared in the second half of 2009. Behind this component, a so-called trailing feature b1 was formed, showing the slowest apparent speed. Moreover, another jet component C1, that is not plotted in Fig. 3.3, was observed beyond 1 mas from the core. Jorstad et al. (2017) also determined the mean viewing angle of 4C+01.28 to be $\phi = (2.7 \pm 0.9)^\circ$, using the apparent speeds of the jet components and the Doppler factors derived from the variability of the light curves of these components.

A kinematic analysis of the 15 GHz VLBA observations taken from July 1995 to October 2012 was presented by Lister et al. (2019). They performed a simple vector motion fit and an acceleration fit. The results of the vector fit are listed in Table 3.2, while the results of the acceleration fit are listed in Table 3.3. In Fig. 3.4, the distance of the jet components to the core component is plotted with respect to the observation time. One can see, that Lister et al. (2019) identified two components (3 and 4), that show significant accelerated ($\dot{\mu} > 3\sigma$) and non-radial motion, meaning that their velocity

vectors did not point back to the core location within the uncertainties. Component 5 shows a significant inward motion with a slow pattern speed. Furthermore, Pushkarev et al. (2009) used the 15 GHz VLBA observations to determine the viewing angle of 4C+01.28 to be $\phi = 4.4^\circ$.

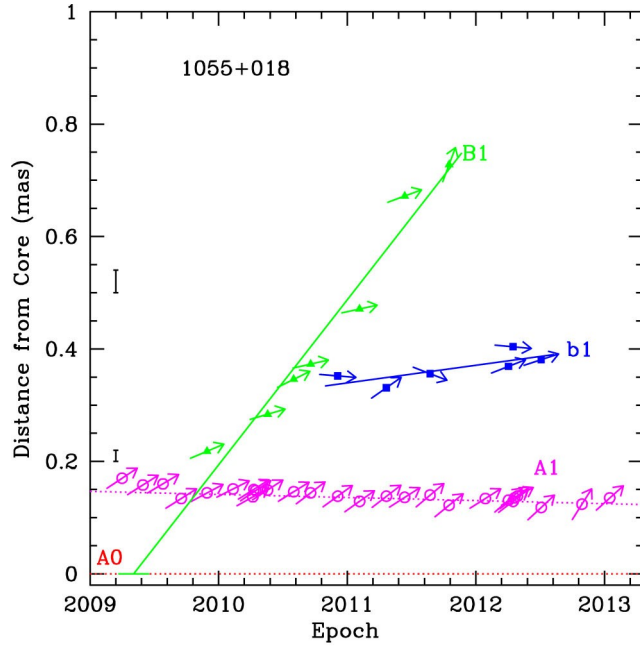


Figure 3.3.: Kinematic analysis of 43 GHz VLBA observations of 4C+01.28. The distance of the jet components to the core component is plotted with respect to the observation time. The lines represent a vector fit. Taken from Jorstad et al. (2017).

Table 3.1.: Mean distances and apparent speeds of the different jet components of a previous kinematic analysis of 43 GHz VLBA observations of 4C+01.28. Adapted from Jorstad et al. (2017).

Component	$\langle R \rangle$ [mas]	μ [mas yr ⁻¹]	β_{app} [c]
(1)	(2)	(3)	(4)
A1	0.14 ± 0.01	0.012 ± 0.008	0.59 ± 0.39
B1	0.44 ± 0.19	0.294 ± 0.027	14.14 ± 1.32
b1	0.37 ± 0.03	0.053 ± 0.025	2.53 ± 1.21
C1	1.75 ± 0.16	0.147 ± 0.006	7.05 ± 0.28

Note: Col.(1): Component ID; Col.(2): Mean distance of the jet component to the core component; Col.(3): Proper motion of the jet component; Col.(4): Apparent speed of the jet component in units of the speed of light (corrected by the redshift and computed using a cosmological model with $H_0 = 70 \text{ km s}^{-1} \text{ Mpc}^{-1}$, $\Omega_m = 0.30$ and $\Omega_\Lambda = 0.70$).

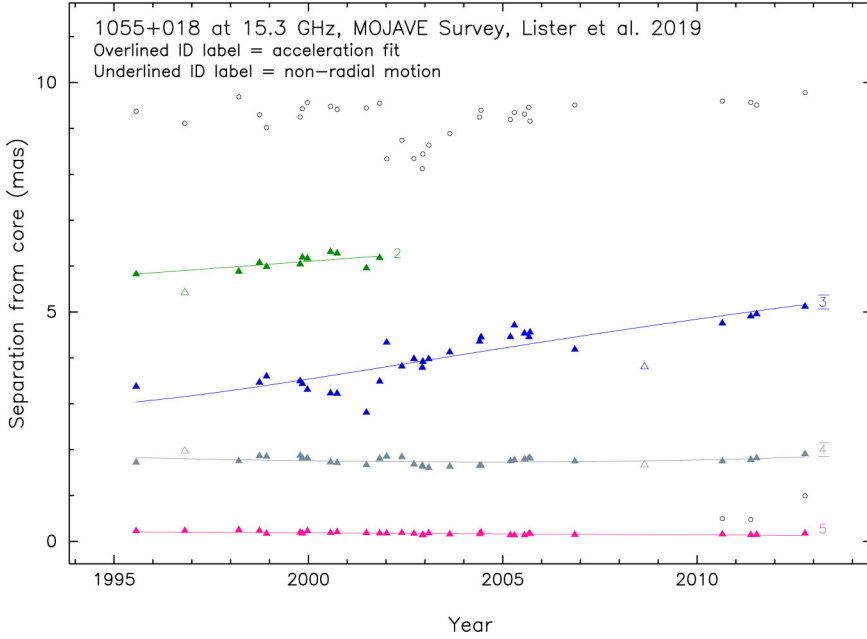


Figure 3.4.: Kinematic analysis of 15 GHz VLBA observations of 4C+01.28. The distance of the jet components to the core component is plotted with respect to the observation time. The lines represent the vector and acceleration fit, respectively. Taken from Lister et al. (2019).

Table 3.2.: Mean distances and apparent speeds of the different jet components of a previous vector fit kinematic analysis of 15 GHz VLBA observations of 4C+01.28. Adapted from Lister et al. (2019).

Component	$\langle R \rangle$ [mas]	μ [$\mu\text{as yr}^{-1}$]	β_{app} [c]
(1)	(2)	(3)	(4)
2	6.08	78 ± 42	3.8 ± 2.0
3 ^a	4.01	145 ± 14	6.98 ± 0.68
4 ^a	1.75	27.8 ± 5.1	1.34 ± 0.25
5 ^b	0.17	5.0 ± 1.8	0.241 ± 0.085

Note: Col.(1): Component ID; Col.(2): Mean distance of the jet component to the core component; Col.(3): Proper motion of the jet component; Col.(4): Apparent speed of the jet component in units of the speed of light (corrected by the redshift and computed using a cosmological model with $H_0 = 71 \text{ km s}^{-1} \text{ Mpc}^{-1}$, $\Omega_m = 0.27$ and $\Omega_\Lambda = 0.73$).

a: significant non-radial motion

b: slow pattern motion

Table 3.3.: Apparent speeds and accelerations of the different jet components of a previous acceleration fit kinematic analysis of 15 GHz VLBA observations of 4C+01.28. Adapted from Lister et al. (2019).

Component	μ [$\mu\text{as yr}^{-1}$]	β_{app} [c]	$\dot{\mu}$ [$\mu\text{as yr}^{-2}$]
(1)	(2)	(3)	(4)
2	84 ± 35	4.0 ± 1.7	74 ± 30
3 ^{ab}	150 ± 14	7.24 ± 0.66	13.8 ± 4.5
4 ^{ab}	25.7 ± 5.2	1.24 ± 0.25	4.5 ± 1.5
5 ^c	5.4 ± 1.7	0.258 ± 0.081	1.37 ± 0.52

Note: Col.(1): Component ID; Col.(2): Proper motion of the jet component; Col.(3): Apparent speed of the jet component in units of the speed of light (corrected by the redshift and computed using a cosmological model with $H_0 = 71 \text{ km s}^{-1} \text{ Mpc}^{-1}$, $\Omega_m = 0.27$ and $\Omega_\Lambda = 0.73$); Col.(4): Acceleration of the jet components.

a: significant accelerated motion

b: significant non-radial motion

c: significant inward motion

4. VLBA Observations of 4C+01.28

To study the parsec-scale jet structure of 4C+01.28, radio data from the Boston University (BU) Blazar Monitoring Program¹ were investigated. These BU-data, observed with the VLBA at 43 GHz over a period of around nine years from April 2009 until April 2018, had already been calibrated and imaged by the BU-group. Information on the calibration and imaging process can be found for example in Jorstad et al. (2005) and Jorstad et al. (2017).

The (u, v) -plane coverages of all observations are shown in Appendix A. One can see that most of the (u, v) -plane coverages look very similar to each other and show baselines up to $\sim 1300 M\lambda$, leading to angular resolutions of ~ 0.194 mas. Only five (u, v) -plane coverages differ from the other significantly. In these five epochs, one of the telescopes that provide the longest baselines, namely the telescopes located at Mauna Kea, Hawaii, and St. Croix, Virgin Islands, was not included in the array.

During the observations on November 28, 2009 (Fig. A.1e), April 7, 2010 (Fig. A.2a), and August 23, 2011 (Fig. A.3a), the Mauna Kea telescope was not included in the array. Therefore, these three (u, v) -plane coverages show only baselines up to $\sim 800 M\lambda$, which leads to a worse resolution of ~ 0.315 mas and a larger beam size (see Fig. B.1e, Fig. B.2a and Fig. B.3b).

In contrast, the (u, v) -plane coverages of the November 6, 2017 (Fig. A.5j) and February 17, 2018 (Fig. A.6a) epochs show baselines up to $\sim 1100 M\lambda$ but a lack of data in the northwest-southeast direction, which leads to an even worse resolution of ~ 0.699 mas and a large beam size in this direction (see Fig. B.6e). This is due to the fact that in these two observations, the St. Croix telescope was not part of the array. In addition to the St. Croix telescope, the Brewster telescope was also missing in the array in the November 6, 2017 epoch. Therefore, the (u, v) -plane coverage of this epoch (Fig. A.5j) shows even less data into the northwest-southeast direction compared to the February 17, 2018 epoch (Fig. A.6a). This leads to the worst resolution of all 48 epochs of ~ 1.12 mas and the largest beam size in the northwest-southeast direction (see Fig. B.6d).

The array configurations and the parameters of the individual beams for all 48 epochs are listed in Table D.1 together with the image parameters.

¹<http://www.bu.edu/blazars/VLBAproject.html>

4.1. Imaging and Model-fitting

As mentioned above, the calibration and imaging process of the investigated VLBA observations had already been performed by the BU-group. However, the publicly available CLEAN-maps are all shifted in coordinates and restored by the same beam. Therefore, new CLEAN-images of all 48 epochs were produced by loading the CLEAN-models and the uniformly weighted, fully calibrated visibility files provided by the BU-group into DIFMAP. While most of these images show one bright feature at the center and a faint jet in the north-western direction, two new bright jet features emerged in August 2015 and August 2017, moving along the jet (see the figures presented in Appendix B). Furthermore, there are also six epochs that show relatively bright features in the northern direction which can not be seen in the other 42 epochs. The images of these six epochs

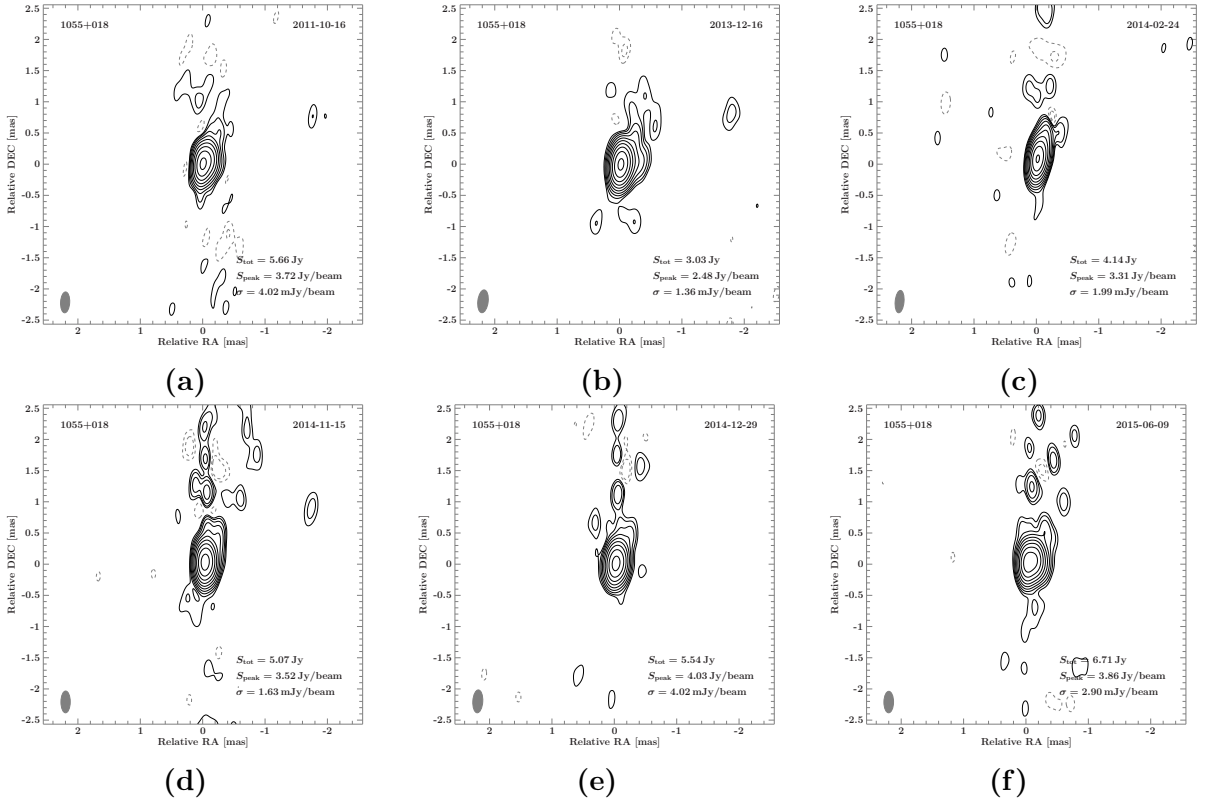


Figure 4.1.: Uniformly weighted 43 GHz VLBA total intensity images of 4C+01.28, showing features in the northern direction that are not seen in the other 42 images of the observation period. S_{tot} is the total integrated flux density, S_{peak} is the highest flux density per beam and σ is the noise level. The gray ellipse in the bottom left corner corresponds to the beam. The contours begin at 3σ and increase logarithmically by a factor of 2.

are plotted in Fig. 4.1.

In an attempt to improve them, the visibility files of these six epochs were loaded into DIFMAP with uniform weighting, to produce new CLEAN-models. For this purpose, the CLEAN windows were only set in the north-western direction of the jet. By performing several CLEAN steps, each followed by a phase self-calibration, new models were constructed that fit the data best. Then, an amplitude self-calibration over the complete observation time was performed. This procedure was repeated with ever decreasing time intervals for the amplitude self-calibration of 180 s, 60 s, 20 s, 5 s, 1 s and 0 s, producing new improved images after a final deep CLEAN of the entire map.

These new images are plotted in Fig. 4.2. One can see that these new images are more comparable to these of the other 42 epochs than the images produced by the BU-group and also show one bright feature and a faint jet into the north-western direction.

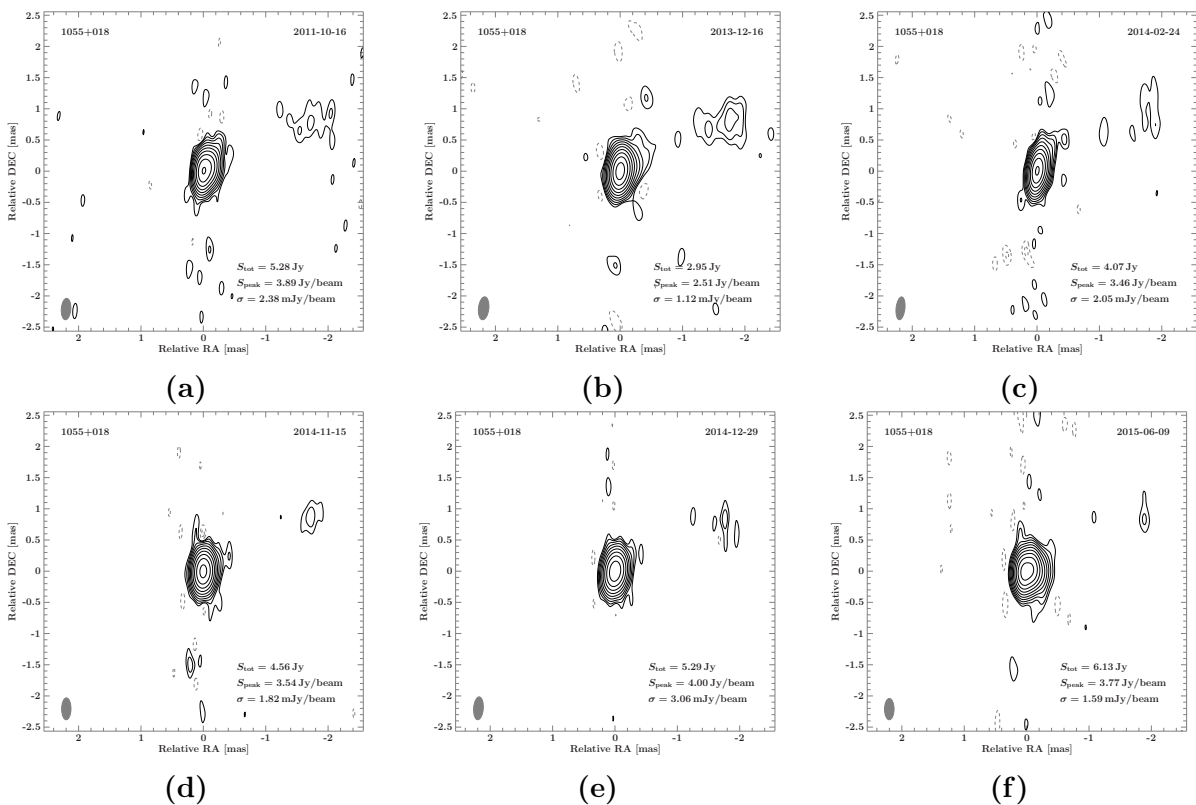


Figure 4.2.: Newly calibrated and cleaned uniformly weighted 43 GHz VLBA total intensity images of 4C+01.28, showing the same epochs as shown in Fig. 4.1. These images are more comparable to the other images of the observation period than those plotted in Fig. 4.1. S_{tot} is the total integrated flux density, S_{peak} is the highest flux density per beam and σ is the noise level. The gray ellipse in the bottom left corner corresponds to the beam. The contours begin at 3σ and increase logarithmically by a factor of 2.

The images of all 48 epochs, including the six new images, are plotted in the figures shown in Appendix B as well as in Fig. 4.3 until Fig. 4.5. The image parameters of all 48 epochs, including the six new images, are listed in Table D.1, together with the array configurations and the parameters of the individual beams.

To study the time evolution of the parsec-scale jet structure of 4C+01.28, the fully calibrated visibility files of all 48 epochs were loaded into DIFMAP, with uniform weighting, and model-fitted by 2D Gaussian components. While the core components were fitted with elliptical Gaussians, the jet components were fitted using circular Gaussians. The important parameters of the fitted Gaussian components, such as the flux density, the positional coordinates and the full width at half maximum (FWHM) of the major and minor axes are listed in Table D.2.

In some cases, the fitted components may not be resolved, meaning that the fitted size of these Gaussians is too small. Therefore, the lowest resolvable size a_{lim} of a Gaussian component was computed to check whether the fitted components were resolved or unresolved. This resolution limit is given by

$$a_{\text{lim}} = 2^{2-\beta/2} b_{\psi} \sqrt{\frac{\ln 2}{\pi} \ln \left(\frac{SNR}{SNR - 1} \right)}, \quad (4.1.1)$$

in which b_{ψ} is the FWHM of the beam size along an arbitrary position angle ψ , SNR is the signal-to-noise ratio and $\beta = 0$ for uniform weighting (for natural weighting $\beta = 2$) (Lobanov 2005). Here, $SNR = \frac{S_{\text{comp}}}{\sigma_{\text{comp}}}$, where S_{comp} is the flux density of the fitted Gaussian component and σ_{comp} is the noise level of the area that is occupied by this component. Note that the resolution limit can be significantly smaller than the beam size, due to its dependence on the SNR (Kovalev et al. 2005).

Using Equation (4.1.1), the resolution limits for all jet and core components of all 48 epochs were computed. Here, the major axes of the corresponding beams were used as b_{ψ} for the circular Gaussian jet components, while for the elliptical Gaussian core components, b_{ψ} was measured as the FWHM of the beam size along the position angle of the corresponding major and minor axes of the fitted core component respectively, which leads to resolution limits for both axes respectively. Whenever a fitted axis was smaller than the corresponding resolution limit, the component was considered to be unresolved. These unresolved axes were set to the corresponding resolution limit. With that method, it was found that only seven circular jet components and two elliptical core components were unresolved, but here only the minor axes of these two components were unresolved, while all major axes of all 48 core components were resolved.

Another important parameter of the fitted Gaussian components is their brightness temperature T_{B} which can be calculated by

$$T_{\text{B}} = \frac{2 \ln 2}{\pi k_{\text{B}}} \frac{S \lambda^2 (1+z)}{a_{\text{maj}} a_{\text{min}}}, \quad (4.1.2)$$

in which S is the flux density of the Gaussian component, a_{maj} and a_{min} are the FWHM of the major and minor axes of the Gaussian component, λ is the wavelength of observation, z is the redshift and k_B is the Boltzmann constant (Kovalev et al. 2005).

Using Equation (4.1.2), with $\lambda = \frac{c}{\nu}$, in which c is the speed of light and $\nu = 43$ GHz is the frequency of observation, and the values given in Table D.2, the brightness temperatures of all jet and core components were calculated. For unresolved components, the resolution limits were used which leads to lower limits of the brightness temperatures in these cases. The obtained brightness temperatures are also listed in Table D.2, together with the other important parameters of the fitted Gaussian components.

4.2. Kinematic Analysis

To analyze the motion of the jet components, their position relative to the core component was studied. Their time evolution is shown in Fig. 4.3 to Fig. 4.5, in which the fitted Gaussian components are plotted above the uniformly weighted images of all 48 epochs with respect to the observation time. In the beginning of the observation period, the images show one bright feature at the core region and a faint jet in the north-western direction that could be identified as component S1 (see Fig. 4.3 and Fig. 4.4). One can see that the bright feature at the core region could mostly be fitted with three components. The easternmost and mostly brightest component of these three components was identified as core component C. While the component next to C could clearly be identified as jet component S2, it was difficult to identify the third one properly. In August 2015, a new bright and compact jet component appeared (see Fig. 4.5a) that could be identified as component J4 and tracked back until April 2015 (see Fig. 4.4b). Finally, in August 2017, another new jet component emerged (see Fig. 4.5b) that was detected for the first time in February 2017 and could be identified as component J5.

The speeds of the jet components were fitted by linear regression of their distance to the core component d using the following equation:

$$d(t) = d_{\text{mid}} + \mu(t - t_{\text{mid}}),$$

in which $t_{\text{mid}} = (t_{\text{max}} + t_{\text{min}})/2$ is the midpoint of observation, d_{mid} is the distance of the jet component to the core component at t_{mid} and μ is the proper motion. For the uncertainties of the distances, the semi major axes of the corresponding components were used. As already mentioned above, at the beginning of the observation period, 4C+01.28 shows a faint jet component S1 and a bright feature at the core region, that could mostly be fitted with three components. While the easternmost component was identified as core component C and the component next to C could clearly be identified as component S2, it was difficult to identify the third one properly. Therefore, different kinematic models were considered.

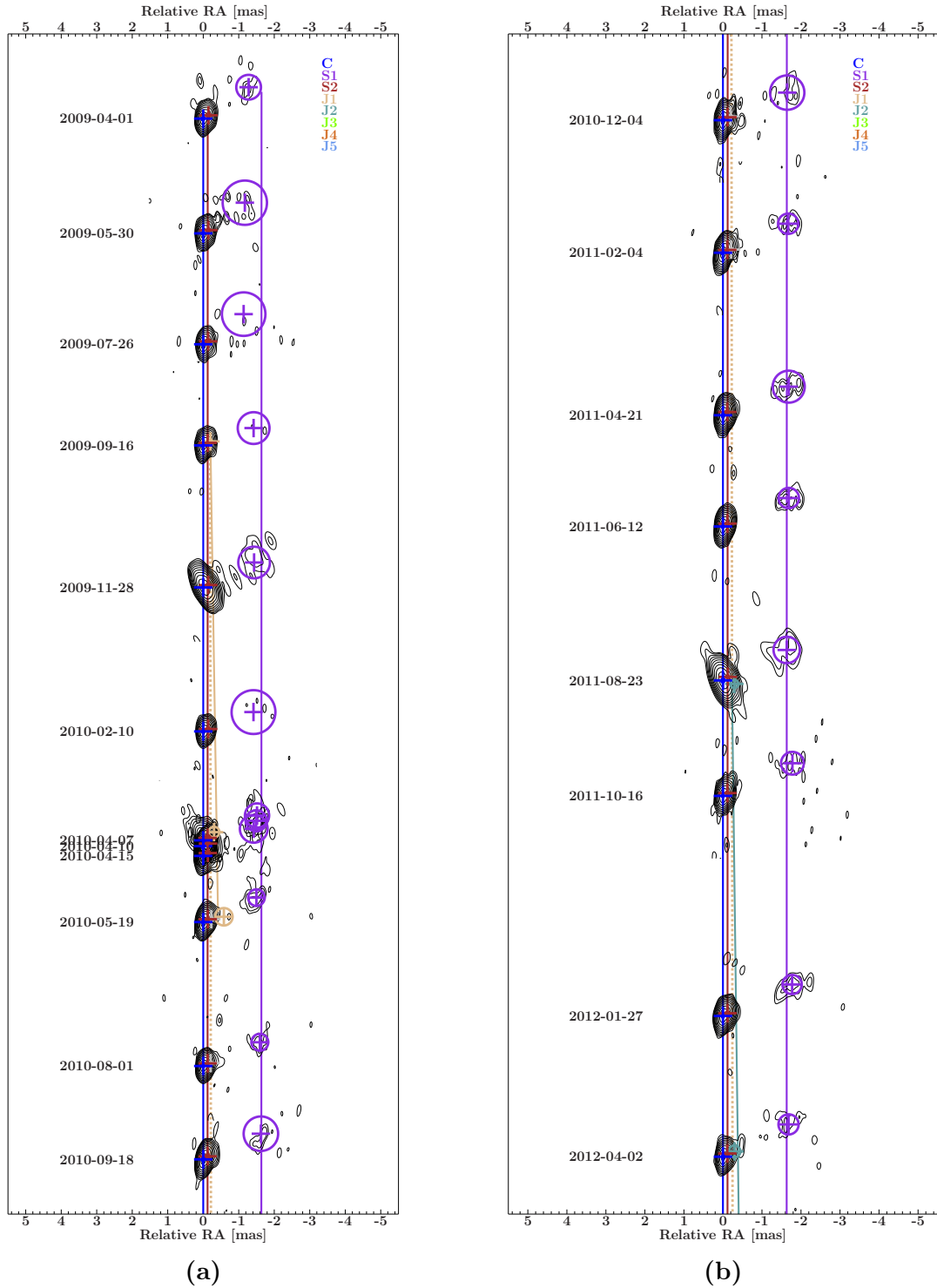


Figure 4.3.: Time evolution of the components' position relative to the position of the core component. The solid lines, representing kinematic model 2, and the dashed line, representing kinematic model 1, were fitted by linear regression of the distance as a function of the time using all 48 epochs. The contours begin at 3σ and increase logarithmically by a factor of 2.

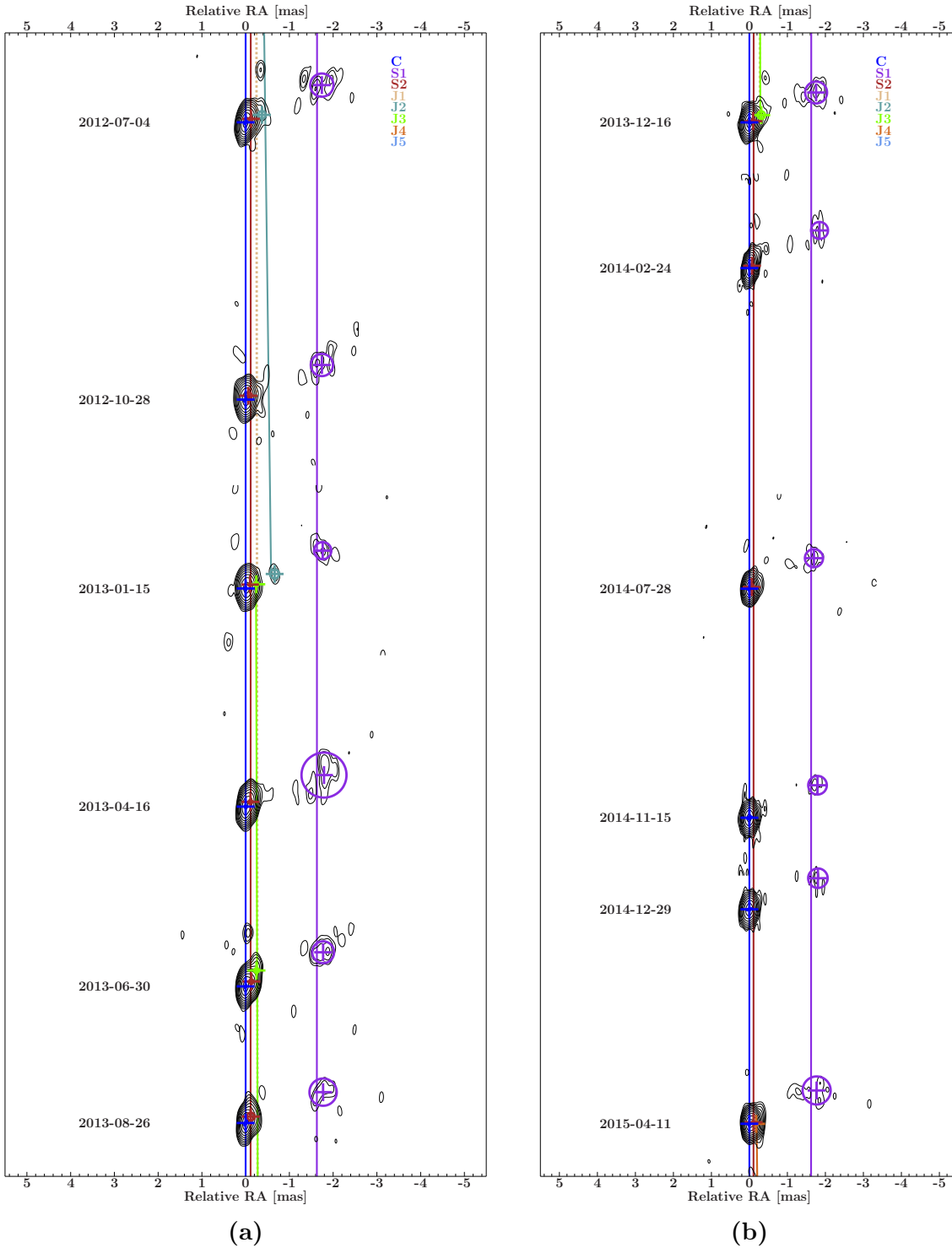


Figure 4.4.: Time evolution of the components' position relative to the position of the core component. The solid lines, representing kinematic model 2, and the dashed line, representing kinematic model 1, were fitted by linear regression of the distance as a function of the time using all 48 epochs. The contours begin at 3σ and increase logarithmically by a factor of 2.

4. VLBA Observations of 4C+01.28

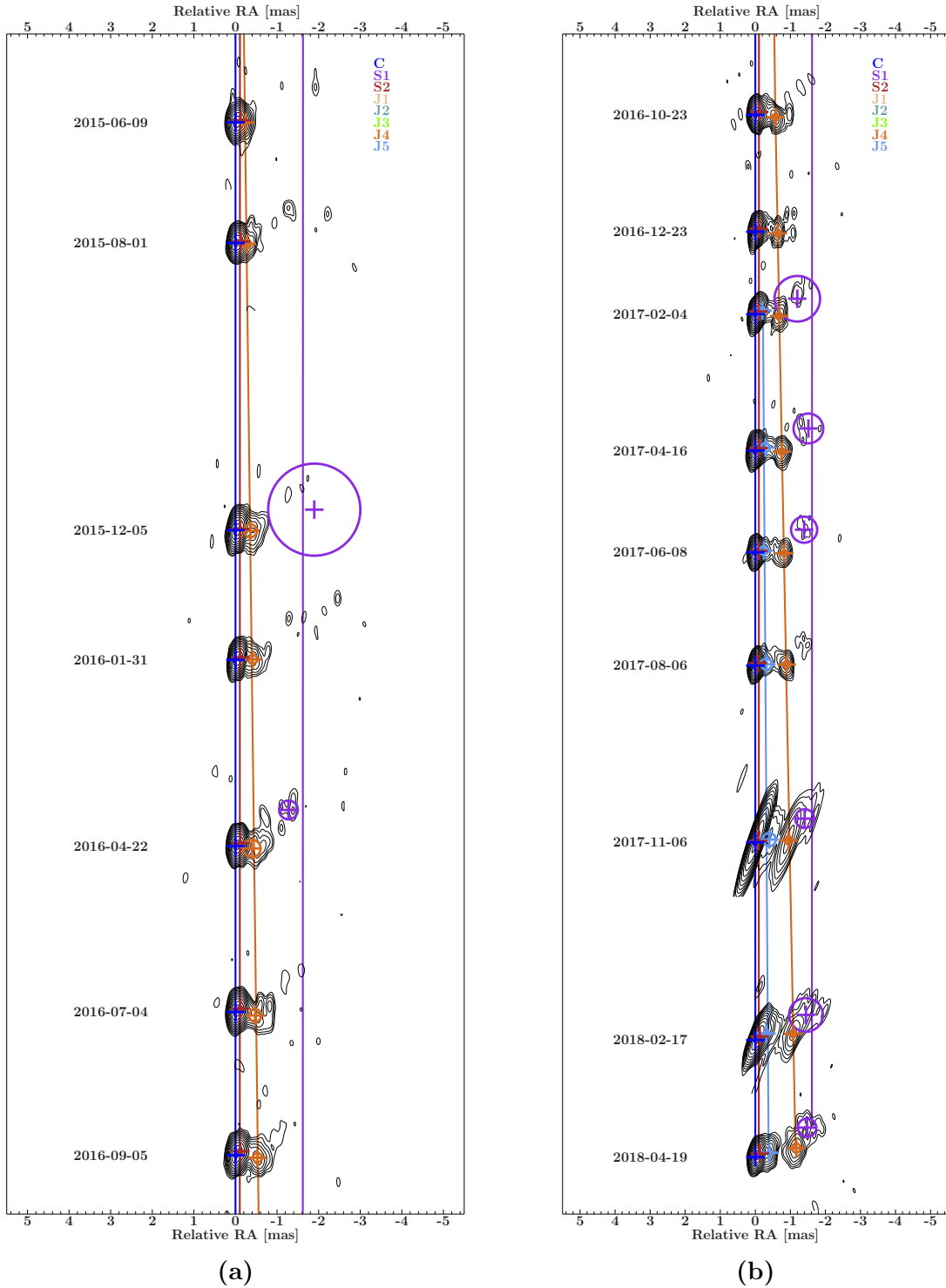


Figure 4.5.: Time evolution of the components' position relative to the position of the core component. The solid lines, representing kinematic model 2 and the accelerated model for component J4, respectively, were fitted by linear regression of the distance as a function of the time using all 48 epochs. The contours begin at 3σ and increase logarithmically by a factor of 2.

Kinematic Model 1

In kinematic model 1, shown in Fig. 4.6, the second component within the bright feature was identified as the same jet component J1 during the complete observation period, showing a very low speed compared to the speeds of the other jet components J4 and J5, representing the newly ejected bright jet feature and the other newly ejected jet component at the end of the observation period. All calculated speeds of the jet components of this kinematic model are listed in Table 4.1 together with the reduced χ^2 values of the fit. The apparent speeds β_{app} were corrected by the redshift and computed using a cosmological model with $H_0 = 70 \text{ km s}^{-1} \text{ Mpc}^{-1}$, $\Omega_m = 0.30$ and $\Omega_\Lambda = 0.70$. With this model, apparent speeds up to $\beta_{\text{app}} \approx 15$ for component J4 were calculated.

Table 4.1.: Apparent speed and ejection time of the different jet components of kinematic model 1.

Component	μ [mas yr ⁻¹]	β_{app} [c]	t_0 [yr]	χ_{red}^2
(1)	(2)	(3)	(4)	(5)
S1	0.001 ± 0.020	0.03 ± 0.95	—	0.33
S2	-0.0033 ± 0.0020	-0.157 ± 0.094	—	0.20
J1	0.041 ± 0.013	1.97 ± 0.61	2004.9 ± 2.0	1.18
J4	0.303 ± 0.021	14.50 ± 0.99	2014.71 ± 0.14	0.20
J5	0.144 ± 0.076	6.9 ± 3.6	2015.5 ± 1.2	0.071

Note: Col.(1): Component ID; Col.(2): Proper motion of the jet component; Col.(3): Apparent speed of the jet component in units of the speed of light (corrected by the redshift and computed using a cosmological model with $H_0 = 70 \text{ km s}^{-1} \text{ Mpc}^{-1}$, $\Omega_m = 0.30$ and $\Omega_\Lambda = 0.70$); Col.(4): ejection time of the component; Col.(5): reduced χ^2 value of the fit. Due to the conservatively calculated uncertainties of the data points, it can be that $\chi_{\text{red}}^2 < 1$. In these cases, the uncertainties of the data points are greater than the mean deviation of these data points from the best fit.

Using the same classification method that had already been used by Jorstad et al. (2017), jet components with detections at ≥ 10 epochs and proper motion $\mu < 2\sigma$ were classified as stationary features, whereas all other jet components were classified as moving jet features. Stationary jet components were labeled with S, moving jet components were labeled with J and the core components were labeled with C. Therefore, S1 and S2 were considered to be stationary jet components, although the speed of S2 seems to be negative.

Figure 4.6 also shows the flux density of the components, the relative uncertainties of which were estimated to be 5%. One can see that the flux density of the different components shows high variability. While the flux density of component S2 shows similar behaviour to that of the core component, the flux density of S1 varies around a constant flux value, which is why these components were identified as S1. Component J1 was

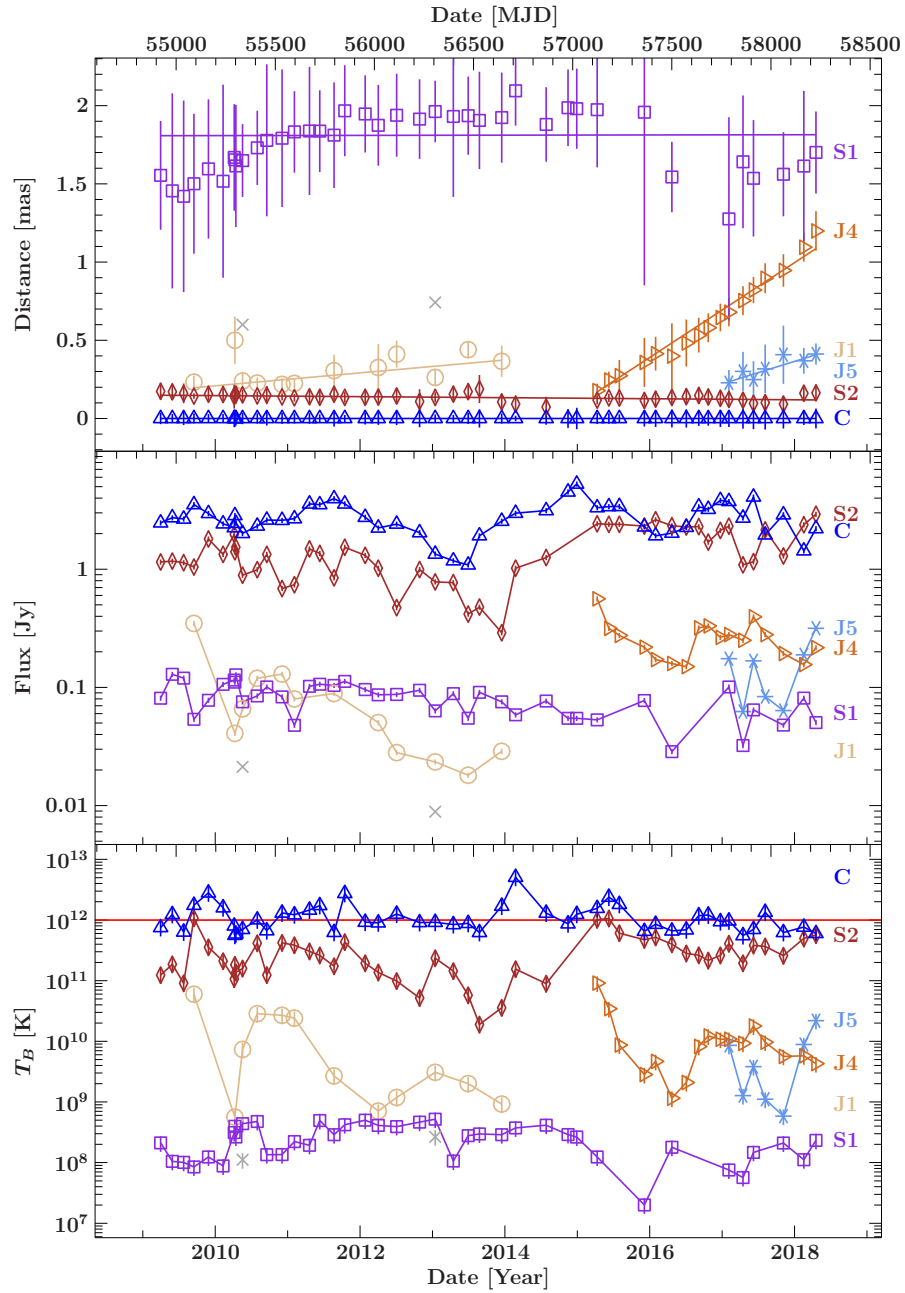


Figure 4.6.: Kinematic model 1. Upper panel: Distance of the jet components relative to the core component plotted over time. The lines were fitted via linear regression and their gradients represent the speed of the corresponding component. Middle panel: Flux density of the components plotted over time. Lower panel: Brightness temperature of the components plotted over time. The red line corresponds to the inverse Compton limit (see Sect. 2.1.2). At all panels the lower time axes are given in years, while the upper time axes are given in mjd.

only detected until December 2013. As one can see in Fig. 4.6, its flux density decreased until that date. In fact, in 2013, it showed the lowest flux density value of all identified components. Therefore, J1 seems to be too faint in order to detect it in later epochs.

Furthermore, the brightness temperature of the components are also plotted in Fig. 4.6. Here, the uncertainties were calculated with the Gaussian law of error propagation, using relative uncertainties of 5 % for the flux density and 20 % for the major and minor axes, respectively. One can see that the brightness temperatures of all jet components are below the inverse Compton limit (see Sect. 2.1.2), represented by the horizontal red line in the lower panel of Fig. 4.6, within the uncertainties. Only the brightness temperature of the core component is sometimes significantly above this limit. However, these high temperatures should be no problem since they hold up only for short time scales, which is discussed in more detail in Sect. 2.1.2.

Moreover, the ejection times of the moving jet components were determined as that point where the separation of the corresponding jet component to the core component equals zero. More information on the calculation of these ejection times, especially regarding their uncertainties estimated by Equation (C.2.12), can be found in Appendix C. The calculated ejection times are also listed in Table 4.1. It was found that the new bright features were ejected in ≈ 2014.71 (J4) and in ≈ 2015.5 (J5).

Kinematic Model 2

In kinematic model 2, component J1 of kinematic model 1 (see Fig. 4.6) was divided into three different components, J1, J2 and J3, that show speeds comparable to the speeds of the other jet components J4 and J5, representing the newly ejected bright jet feature and the other newly ejected jet component at the end of the observation period. This model is presented in Fig. 4.7. One can see that the flux densities of the components J1 and J2 decreased rapidly, so that the components J1 and J2 could only be detected in three and four epochs, respectively. Component J3 only has a low flux density and therefore could only be seen in three epochs. However, there should be at least five identifications of one component at different epochs to compute its speed properly via linear regression (e.g., Lister et al. 2009). Therefore, the computed speeds of the components J1, J2 and J3 are not sufficiently constrained. The calculated speeds of the other jet components of this kinematic model are listed in Table 4.2. With this model, apparent speeds up to $\beta_{\text{app}} \approx 15$ for component J4 were calculated, although the maximal speed of $\beta_{\text{app}} \approx 24$ was measured for component J1, but this is not sufficiently constrained.

Furthermore, the ejection times of the moving jet components were also computed for this kinematic model and are listed in Table 4.2. Note that the ejection times of the components J1, J2 and J3 are also not sufficiently constrained and therefore not listed in Table 4.2, similar to the speeds of these components.

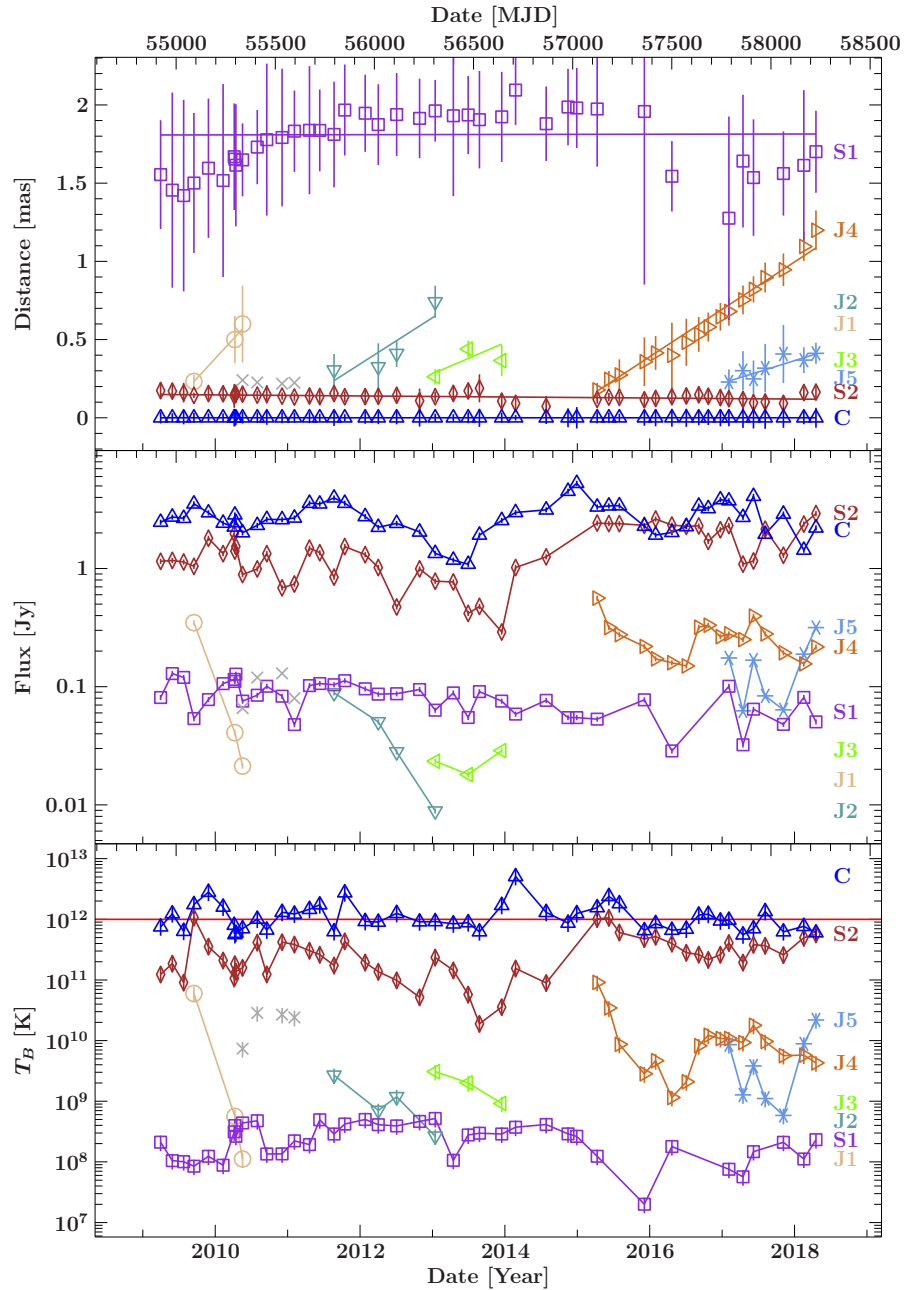


Figure 4.7.: Kinematic model 2. Upper panel: Distance of the jet components relative to the core component plotted over time. The lines were fitted via linear regression and their gradients represent the speed of the corresponding component. Component J1 of kinematic model 1 (see Fig. 4.6) was split into three components (J1, J2, J3) showing speeds that are more comparable to the speeds of the components J4 and J5. Middle panel: Flux density of the components plotted over time. Lower panel: Brightness temperature of the components plotted over time. The red line corresponds to the inverse Compton limit (see Sect. 2.1.2). At all panels the lower time axes are given in years, while the upper time axes are given in mjd.

Table 4.2.: Apparent speed and ejection time of the different jet components of kinematic model 2.

Component	μ [mas yr ⁻¹]	β_{app} [c]	t_0 [yr]	χ_{red}^2
(1)	(2)	(3)	(4)	(5)
S1	0.001 ± 0.020	0.03 ± 0.95	—	0.33
S2	-0.0033 ± 0.0020	-0.157 ± 0.094	—	0.20
J4	0.303 ± 0.021	14.50 ± 0.99	2014.71 ± 0.14	0.20
J5	0.144 ± 0.076	6.9 ± 3.6	2015.5 ± 1.2	0.071

Note: Col.(1): Component ID; Col.(2): Proper motion of the jet component; Col.(3): Apparent speed of the jet component in units of the speed of light (corrected by the redshift and computed using a cosmological model with $H_0 = 70 \text{ km s}^{-1} \text{ Mpc}^{-1}$, $\Omega_m = 0.30$ and $\Omega_\Lambda = 0.70$); Col.(4): ejection time of the component; Col.(5): reduced χ^2 value of the fit. Due to the conservatively calculated uncertainties of the data points, it can be that $\chi_{\text{red}}^2 < 1$. In these cases, the uncertainties of the data points are greater than the mean deviation of these data points from the best fit.

Accelerated Kinematic Model for Component J4

Looking at the upper panels of Fig. 4.6 and Fig. 4.7, one can see that component J4 seems to accelerate. Therefore, an accelerated kinematic model was considered for this component. For this purpose, the distance to the core component was fitted by linear regression for distances $d \lesssim 0.6 \text{ mas}$ and by another linear regression for distances $d \gtrsim 0.6 \text{ mas}$. This accelerated kinematic model is plotted in Fig. 4.8. Here, as for the time evolution plots shown in Fig. 4.3 to Fig. 4.5, the lines represent the fits of kinematic model 2 and the accelerated kinematic model for component J4 respectively, while the dashed line represents the fit of component J1 of kinematic model 1.

Furthermore, the ejection time of component J4 was computed, using the same formalism as for the other two kinematic models which is explained in more detail in Appendix C. For this purpose, the parameters derived from the first linear regression for distances $d \lesssim 0.6 \text{ mas}$ were used. To illustrate the ejection times of the moving jet components, the lines in Fig. 4.8 were extrapolated to the point of intersection with the core component.

The proper motions, apparent speeds, reduced χ^2 values and the ejection time derived using the accelerated kinematic model for component J4 are listed in Table 4.3. Looking at the reduced χ^2 values², one can see that these of the accelerated kinematic model, with $\chi_{\text{red}}^2 = 0.039$ for $d \lesssim 0.6 \text{ mas}$ and $\chi_{\text{red}}^2 = 0.037$ for $d \gtrsim 0.6 \text{ mas}$, are much smaller than those of the other two kinematic models with $\chi_{\text{red}}^2 = 0.20$. This means that the fit

²Due to the conservatively calculated uncertainties of the data points, it can be that $\chi_{\text{red}}^2 < 1$. In these cases, the uncertainties of the data points are greater than the mean deviation of these data points from the best fit.

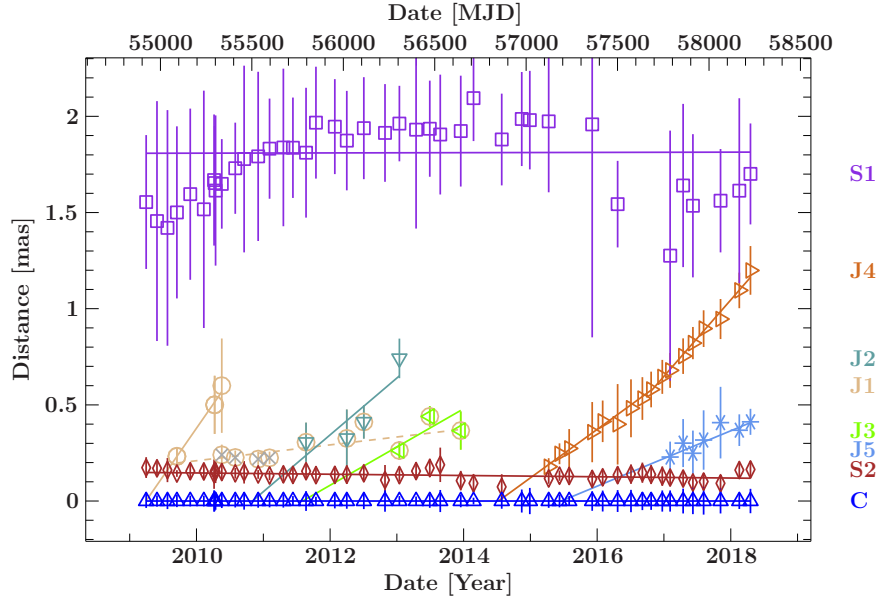


Figure 4.8.: Distance of the jet components relative to the core component plotted over time. The solid lines, representing kinematic model 2 and the accelerated model for component J4, respectively, and the dashed line, representing component J1 for kinematic model 1, were fitted via linear regression and their gradients represent the speed of the corresponding component. Component J4 was fitted by two separated linear regressions.

Table 4.3.: Apparent speeds and ejection time of component J4, derived from the accelerated kinematic model for this component.

d [mas]	μ [mas yr ⁻¹]	β_{app} [c]	t_0 [yr]	χ_{red}^2
(1)	(2)	(3)	(4)	(5)
$\lesssim 0.6$	0.252 ± 0.051	12.1 ± 2.4	2014.52 ± 0.26	0.039
$\gtrsim 0.6$	0.397 ± 0.069	19.0 ± 3.3	—	0.037

Note: Col.(1): Distance to the core component; Col.(2): Proper motion of the jet component; Col.(3): Apparent speed of the jet component in units of the speed of light (corrected by the redshift and computed using a cosmological model with $H_0 = 70 \text{ km s}^{-1} \text{ Mpc}^{-1}$, $\Omega_m = 0.30$ and $\Omega_\Lambda = 0.70$); Col.(4): ejection time of the component; Col.(5): reduced χ^2 value of the fit. Due to the conservatively calculated uncertainties of the data points, it can be that $\chi_{\text{red}}^2 < 1$. In these cases, the uncertainties of the data points are greater than the mean deviation of these data points from the best fit.

of the accelerated kinematic model is much better than that of the other two kinematic models. Therefore, the speeds and ejection time of the accelerated kinematic model are used in the following for all further calculations.

With this model, apparent speeds up to $\beta_{\text{app}} \approx 19$ for component J4 were calculated. Furthermore, it was found that component J4 was ejected in ≈ 2014.52 , which is ≈ 0.2 years earlier than the ejection time computed with the fit of kinematic model 1 and kinematic model 2, respectively (≈ 2014.71).

4.3. Jet Geometry

Using a model in which the diameter D of the jet at the distance d can be described by a power law $D \propto d^l$, the geometry of the jet is given by the power law index l . For a conical jet, $l = 1$, while $l < 0$ for a collimated jet. Furthermore, $l > 0$ can be interpreted as a decelerating jet (Kadler et al. 2004).

To study the geometry of the jet of 4C+01.28, a model was used in which the diameter of the jet at the distance d of a jet component is given by the major axis of this component. Hence, the major axes of the fitted jet components are plotted double logarithmically as a function of their distance to the core component in Fig. 4.9. Here, the uncertainties were estimated by 20% of the major axis of the corresponding component.

To estimate the power law index l , the logarithm of the major axes were fitted by linear regression with respect to the logarithm of the distances, which is represented by

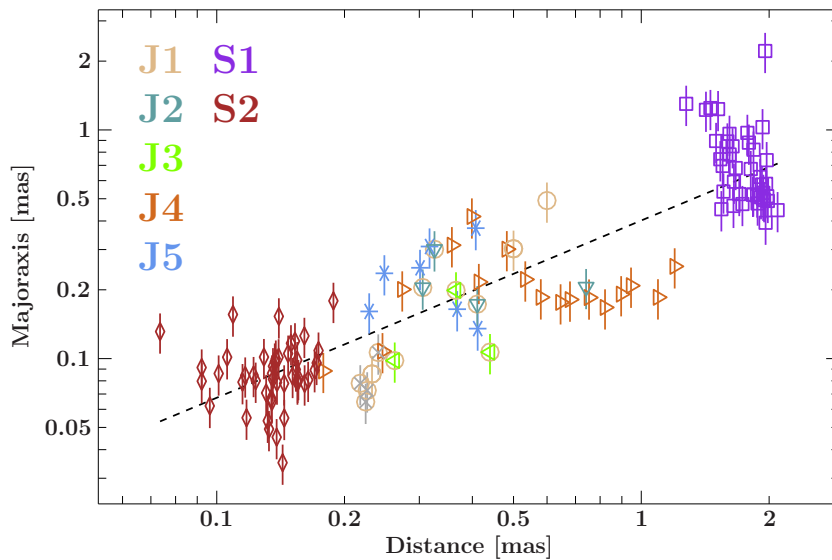


Figure 4.9.: Major axes of the jet components plotted double logarithmically as a function of the distance to the core component. The dashed line was fitted via linear regression and its gradient corresponds to the power law index of the jet diameter.

the dashed line in Fig. 4.9. With this method, one obtains

$$l = 0.775 \pm 0.016,$$
$$C = (0.4016 \pm 0.0090) \text{ mas}^{1-l},$$
$$\chi_{\text{red}}^2 = 4.41,$$

in which C is the constant of proportionality.

One can see that the power law index l is not consistent with unity, even within an uncertainty of 3σ . Therefore, the jet of 4C+01.28 is not conical.

5. Multiband Variability Analysis

4C+01.28 was also observed at other radio frequencies and at γ -ray energies. Therefore, the γ -ray light curve measured by the Large Area Telescope on board of the *Fermi* Gamma-ray Space Telescope (*Fermi*/LAT) and several radio light curves measured at different frequencies are studied in this Chapter.

5.1. Light Curves at Different Frequencies

Fermi/LAT γ -ray Light Curve

The following information on *Fermi*/LAT is adapted from Atwood et al. (2009). *Fermi*/LAT was built to measure the arrival time, energy and direction of γ -rays in the energy range from 20 MeV to more than 300 GeV. It consists of a tracking section with 36 silicon strip detectors, tracking charged particles, and 16 layers of tungsten foil that provide the conversion of γ -rays to electron-positron pairs. Furthermore, a calorimeter composed of CsI crystals is arranged beneath the tracker to determine the γ -ray energy. To eliminate charged-particle background events, an anticoincidence detector around the tracker is used. More detailed information on *Fermi*/LAT can be found in Atwood et al. (2009).

A 14-day binned *Fermi*/LAT light curve of 4C+01.28, measured at 0.1 GeV to 300 GeV, was produced by Michael Kreter and is shown in Fig. 5.1. The data are listed in Table D.3. One can see that the γ -ray flux shows high variability with prominent bright outbursts in 2011, 2014 and 2015 and a prominent flux minimum in 2013.

ALMA Light Curves

The Atacama Large Millimeter/submillimeter Array (ALMA) is located at the Chajnantor plateau of the Chilean Andes at an altitude of 5000 m and consists of a large array of 12 m antennas and a compact array of twelve 7 m and four 12 m antennas. While the telescopes of the large 12 m array can be placed in different locations on the plateau, which leads to baselines up to 16 km, the antennas of the compact array stay mostly in a fixed configuration. ALMA can observe at a wide frequency range that is divided into different bands, ranging from band 3, starting at 84 GHz, to band 10, ending at ~ 950 GHz. The information on ALMA was taken from the ALMA Science Portal¹.

¹<https://almascience.eso.org/>

Since 4C+01.28 was used as a calibrator source for ALMA observations, data of 4C+01.28 measured at band 3 (84 – 116 GHz), band 6 (211 – 275 GHz) and band 7 (275 – 373 GHz) were available at the ALMA Calibrator Source Catalogue². These data were downloaded. The ALMA-band 3 data are listed in Table D.4, the ALMA-band 6 data are listed in Table D.5 and the ALMA-band 7 data are listed in Table D.6. The light curves of all three bands are plotted in Fig. 5.1. One can see that the flux densities of all three ALMA light curves show high variability, similar to the *Fermi*/LAT γ -ray light curve. Furthermore, the ALMA light curves show a three-hump structure with flux density peaks in 2014, 2015 and 2017 and a prominent flux density minimum in 2013, as can also be seen in the γ -ray light curve.

Due to the wide frequency ranges of the different bands, the flux densities of the individual light curves were not measured at the same frequency. Therefore, the mean frequencies ν , with uncertainties given by the standard deviation, were computed for all three bands respectively. For ALMA-band 3 one obtains

$$\nu = (97.0 \pm 6.2) \text{ GHz},$$

for ALMA-band 6 one obtains

$$\nu = (232.5 \pm 2.4) \text{ GHz}$$

and for ALMA-band 7 one obtains

$$\nu = (341.9 \pm 8.5) \text{ GHz}.$$

These mean frequencies were used in the following for the further calculations.

SMA Light Curve

The Submillimeter Array (SMA) is located at Mauna Kea in Hawaii and consists of eight radio antennas with diameters of 6 m, that can be arranged in configurations with baselines up to 509 m. It observes at frequencies from 180 GHz to 418 GHz. The information on SMA was taken from the SMA Observer Center³.

Since 4C+01.28 was used as a calibrator source for SMA observations, data taken at the 1 mm band were available at the Submillimeter Calibrator List⁴. These data were downloaded and are listed in Table D.7. The light curve, plotted in Fig. 5.1, also shows high variability of the flux density and similar behavior to the other *Fermi*/LAT γ -ray and ALMA light curves with a prominent flux density minimum in 2013 and a three-hump structure with flux density peaks in 2014, 2015 and 2017. Furthermore, the

²<https://almascience.eso.org/sc/>

³<http://sma1.sma.hawaii.edu/smaoc.html>

⁴<http://sma1.sma.hawaii.edu/callist/callist.html>

behavior of the SMA light curve before the minimum in 2013 is also very similar to that of the *Fermi*/LAT γ -ray light curve.

Similar as for the ALMA observations, the SMA measurements were taken at different frequencies within the 1 mm band. Therefore, the mean frequency ν , with uncertainty given by the standard deviation, was also computed here, leading to

$$\nu = (226.9 \pm 8.5) \text{ GHz.}$$

This mean frequency was used in the following for the further calculations, similar to those of the ALMA light curves.

OVRO Light Curve

4C+01.28 is also part of the Owens Vally Radio Observatory (OVRO) blazar monitoring program that has been monitored a large sample of 1158 likely γ -ray-loud blazars with the OVRO 40 m telescope at 15 GHz about twice per week since 2007 (Richards et al. 2011). The resulting flux density measurements are publicly available at the program website⁵, from which the data for 4C+01.28 were downloaded. More detailed information on the OVRO blazar monitoring program can be found in Richards et al. (2011).

The OVRO data are listed in Table D.8 and the corresponding light curve is plotted in Fig. 5.1. One can see that the flux density shows also high variability, similar to the other light curves. Furthermore, the OVRO light curve shows a minimum in flux density in 2013 and a three-hump structure with peaks in 2014, 2015 and 2017, as can also be seen in the other light curves. Moreover, the behavior of the OVRO light curve before the minimum in 2013 is very similar to those of the *Fermi*/LAT γ -ray and the SMA light curves.

VLBA Light Curve

Figure 5.1 also shows a light curve measured by the VLBA at 43 GHz. Here, the total flux densities of the BU-data derived in this thesis and listed in Table D.1 are plotted with relative uncertainties of 5%. One can see that this light curve also shows high variability in the flux density, similar to the other light curves. It also shows a minimum of the flux density in 2013 and two peaks in 2015 and 2017, as can be seen in the other light curves. However, the peak in 2014 was not observed, which can be explained by the worse sampling rate of around every two months, compared to the other observations. Furthermore, the behavior of the VLBA light curve before the minimum in 2013 is also very similar to those of the *Fermi*/LAT γ -ray, SMA and OVRO light curves.

⁵<http://www.astro.caltech.edu/ovroblazars>

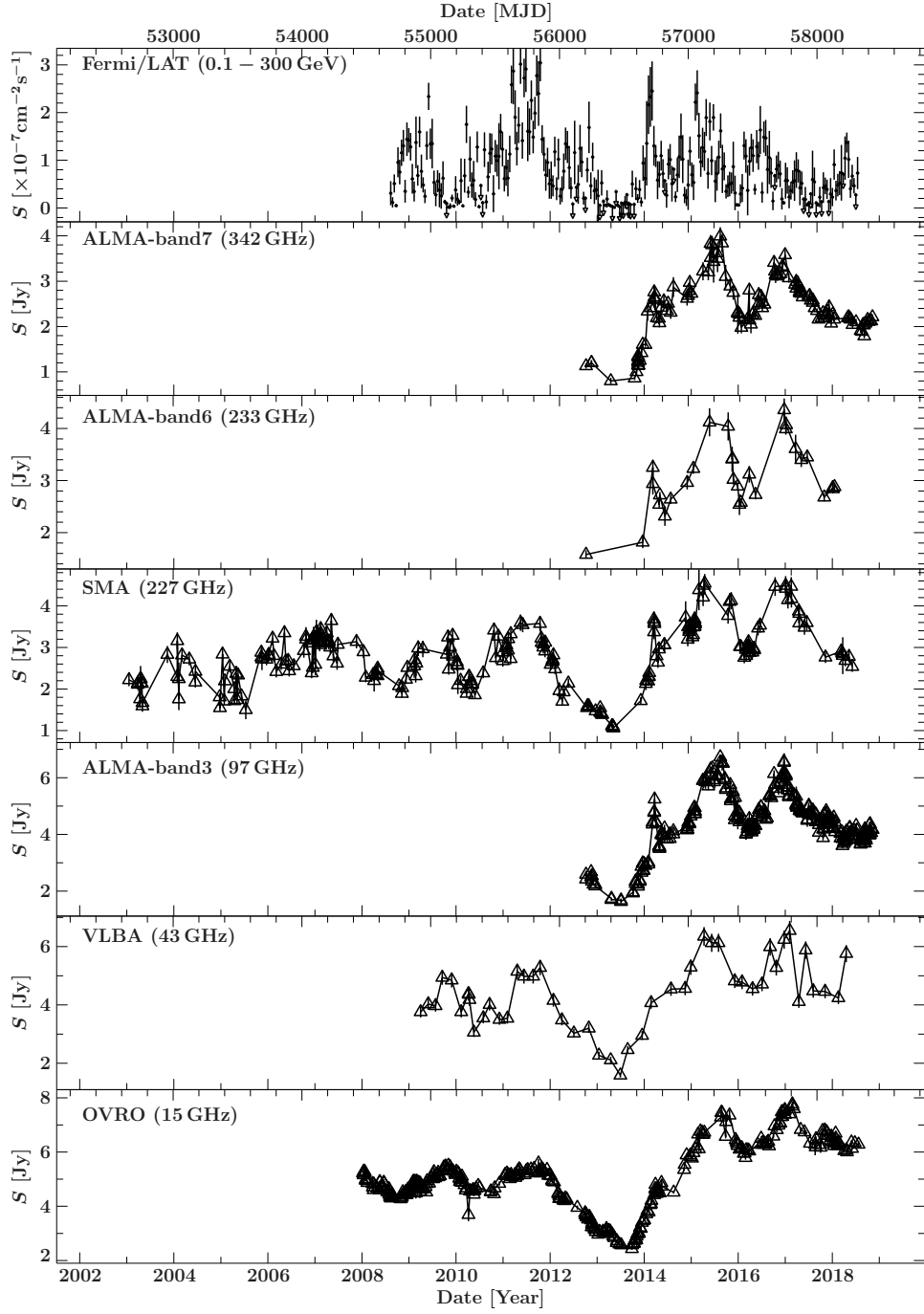


Figure 5.1.: 14-day binned γ -ray and radio light curves observed by *Fermi*/LAT, ALMA, SMA and OVRO (data are listed in Appendix D) and the total flux density VLBA light curve (data are listed in Table D.1), showing similar variability behavior. The given frequencies are the mean values of the observation frequencies of the individual light curves. At all panels the lower time axes are given in years, while the upper time axes are given in mjd.

5.2. Cross-Correlation Analysis

As already mentioned in Sect. 5.1, the light curves plotted in Fig. 5.1 all show similar behavior. Therefore, one can assume that the *Fermi*/LAT γ -ray and the various radio light curves are correlated. To test this assumption, a cross-correlation analysis was performed between the *Fermi*/LAT γ -ray light curve and the radio light curves measured by ALMA (band 3 and band 7 only), SMA and OVRO, respectively. The ALMA-band 6 and VLBA light curves were neglected in this study, because of their poor sampling rate, compared to the other radio observations.

Due to the unevenly sampled radio light curves, two different methods were used for the cross-correlation analysis, namely the Discrete Cross-Correlation Function (DCF, see also Sect. 2.3.1) according to Edelson & Krolik (1988) as well as the Interpolated Cross-Correlation Function (ICF, see also Sect. 2.3.2) according to White & Peterson (1994), combined with the method introduced by Peterson et al. (1998) to compute the uncertainties of the time lags derived by the ICF. Furthermore, some measurements of the 14 day binned *Fermi*/LAT γ -ray light curve are only upper limits, denoted by the arrows in the γ -ray light curve shown in Fig. 5.1. These upper limits were neglected for the analysis. Nevertheless, the analysis was also performed with these upper limits included in the γ -ray light curve, to test the effect of neglecting them, but there were no significant differences in both cases. Therefore, only the results without the upper limits are presented here, similar to the cross-correlation analysis presented in Max-Moerbeck et al. (2014).

The results of the cross-correlation analysis are shown in Fig. 5.2, in which the correlation-coefficients are plotted as a function of the time lag. Here, the bin size for the DCF was chosen to be the averaged sampling time of both light curves, while the bin size for the ICF was chosen to be half of that computed for the DCF. While the coefficients derived by the DCF are plotted in red, those derived by the ICF are plotted in black. One can see that both methods provide comparable results for the correlation between the γ -ray light curve and the individual radio light curves. Furthermore, both cross-correlation functions between the γ -ray light curve and the two different ALMA light curves, respectively (Fig. 5.2a and Fig. 5.2c), show their maximum peaks at positive time lags, which means that the γ -ray light curve leads the radio light curves. Otherwise, the cross-correlation function between the γ -ray light curve and the SMA light curve (Fig. 5.2b) as well as the cross-correlation function between the γ -ray light curve and the OVRO light curve (Fig. 5.2d) show a three-hump structure with the first peaks located at negative time lags for both different radio light curves, which would mean that the γ -ray light curve lags the radio light curves. The other two peaks are located at positive time lags for both different radio light curves. While the third peaks are located at unphysically large time lags, the time lags of the second peaks are comparable to the time lags derived by the cross-correlation between the γ -ray light curve and both ALMA light curves, respectively. Therefore, the time lags of these second peaks were used in the following for the further calculations.

As one can see in Fig. 5.2c, the ICF between the γ -ray light curve and the ALMA-band 3 light curve shows a maximal correlation coefficient of $r_{\text{corr}} = 0.390$ at a time lag of $\tau_{\gamma,\nu} = (191 \pm 43)$ d, while the DCF between these two light curves shows a maximal correlation coefficient of $r_{\text{corr}} = 0.424 \pm 0.071$ at a time lag of $\tau_{\gamma,\nu} = 197.2$ d. These two time lags and correlation coefficients correspond very well to each other, respectively.

The ICF between the γ -ray light curve and the ALMA-band 7 light curve (see Fig. 5.2a) results in a peak correlation coefficient of $r_{\text{corr}} = 0.450$ at a time lag of $\tau_{\gamma,\nu} = (108 \pm 52)$ d. With the DCF between these two light curves, the peak is $r_{\text{corr}} = 0.477 \pm 0.079$ at a time lag of $\tau_{\gamma,\nu} = 247.5$ d. This time lag is much greater than that

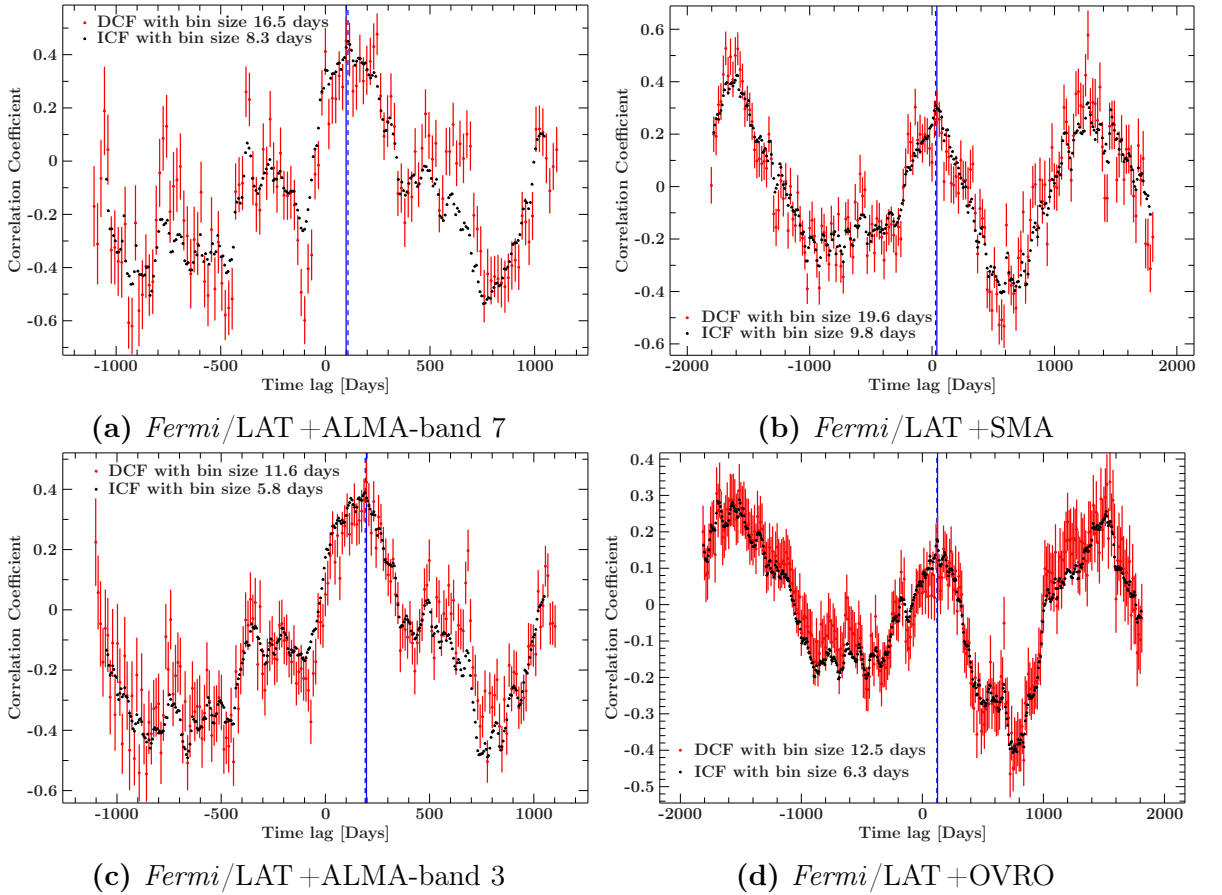


Figure 5.2.: Cross-correlation coefficients between *Fermi*/LAT γ -ray and four radio light curves, observed by ALMA, SMA and OVRO at different frequencies, plotted over the time lag. The bin size for the DCF was chosen to be the averaged sampling time of both light curves, while the bin size for the ICF was chosen to be half of that computed for the DCF. Positive time lags mean that the radio light curve lags the *Fermi*/LAT γ -ray light curve. The DCF and ICF time lags that are used for further calculations are marked with solid and dashed blue lines, respectively.

derived by the ICF, but the DCF shows another peak of $r_{\text{corr}} = 0.452 \pm 0.085$ at a time lag of $\tau_{\gamma,\nu} = 99.0$ d, which is more similar to the correlation coefficient and time lag obtained by the ICF. Therefore, the values of the second peak of the DCF were used for the further calculations.

The cross-correlation function between the γ -ray light curve and the SMA light curve is plotted in Fig. 5.2b and shows a three-hump structure, as always mentioned above. While for the ICF the maximal correlation coefficient of $r_{\text{corr}} = 0.424$ is located at a time lag of $\tau_{\gamma,\nu} = (-1597 \pm 624)$ d, for the DCF the maximal correlation coefficient of $r_{\text{corr}} = 0.578 \pm 0.094$ is located at a time lag of $\tau_{\gamma,\nu} = 1274.0$ d. These two different peaks can be explained by the symmetry of the two light curves around the flux minimum in 2013 (see Fig. 5.1). While the correlation between the part of the SMA light curve lying before the minimum in 2013 and the part of the γ -ray light curve lying after the minimum in 2013 leads to the maximum of the ICF at the negative time lag, the correlation between the part of the SMA light curve lying after the minimum in 2013 and the part of the γ -ray light curve lying before the minimum in 2013 leads to the maximum of the DCF at the positive time lag. However, both cross-correlation functions show a third peak, representing the correlation of the total light curves. For the ICF, this peak correlation coefficient of $r_{\text{corr}} = 0.309$ is located at a time lag of $\tau_{\gamma,\nu} = (29 \pm 29)$ d. With the DCF this peak correlation coefficient is $r_{\text{corr}} = 0.301 \pm 0.068$ at a time lag of $\tau_{\gamma,\nu} = 39.2$ d. These two time lags are more similar to those derived by the cross-correlation between the γ -ray light curve and the two ALMA light curves, respectively. Therefore, the time lags of this third peak are used for the further calculations.

The cross-correlation function between the γ -ray light curve and the OVRO light curve is plotted in Fig. 5.2d and shows a similar structure to that between the γ -ray light curve and the SMA light curve. Here, the ICF results in a maximal correlation coefficient of $r_{\text{corr}} = 0.288$ at a time lag of $\tau_{\gamma,\nu} = (-1512 \pm 1316)$ d. With the DCF, the maximum is $r_{\text{corr}} = 0.337 \pm 0.080$ at a time lag of $\tau_{\gamma,\nu} = 1550.0$ d. These two different peaks can also be explained by the symmetry of the two light curves around the flux minimum in 2013 (see Fig. 5.1), similar as for the cross-correlation between the γ -ray light curve and the SMA light curve. However, both cross-correlation functions show a third peak, as can also be seen in the cross-correlation functions between the γ -ray light curve and the SMA light curve. For the ICF, this peak correlation coefficient of $r_{\text{corr}} = 0.179$ is located at a time lag of $\tau_{\gamma,\nu} = (120 \pm 50)$ d, while for the DCF, this peak correlation coefficient is $r_{\text{corr}} = 0.178 \pm 0.065$ at a time lag of $\tau_{\gamma,\nu} = 125.0$ d. Similar to the cross-correlation between the γ -ray light curve and the SMA light curve, these two time lags are more comparable to those derived by the cross-correlation between the γ -ray light curve and the two ALMA light curves, respectively. Therefore, the time lags of this third peak are also used for the further calculations.

The derived time lags and cross-correlation coefficients that are used for the further calculations and discussions are listed in Table 5.1.

Table 5.1.: Cross-correlation coefficients and time lags derived by the ICF and DCF between the *Fermi*/LAT γ -ray light curve and four radio light curves observed at different frequencies, respectively.

Radio light curve	ν [GHz]	r_{corr}	$\tau_{\gamma,\nu}$ [d]
(1)	(2)	(3)	(4)
DCF:			
ALMA-band 7	341.9 ± 8.5	0.452 ± 0.085	99.0
SMA	226.9 ± 8.5	0.301 ± 0.068	39.2
ALMA-band 3	97.0 ± 6.2	0.424 ± 0.071	197.2
OVRO	15	0.178 ± 0.065	125.0
ICF:			
ALMA-band 7	341.9 ± 8.5	0.450	108 ± 52
SMA	226.9 ± 8.5	0.309	29 ± 29
ALMA-band 3	97.0 ± 6.2	0.390	191 ± 43
OVRO	15	0.179	120 ± 50

Note: Col.(1): Radio light curve; Col.(2): Mean frequency of the radio light curve; Col.(3): Peak cross-correlation coefficient; Col.(4): Time lag corresponding to the peak cross-correlation coefficient.

6. Discussion

Studying 48 epochs of VLBA observations of 4C+01.28 taken at 43 GHz, two newly ejected jet features were found that seem to be associated with prominent outbursts in the *Fermi*/LAT γ -ray light curve and in several radio light curves observed at different frequencies by ALMA, SMA and OVRO respectively. To illustrate that, the ejection times derived in Sect. 4.2 are plotted as vertical dashed lines in Fig. 6.1, together with the different γ -ray and radio light curves. While the solid lines in the lower panel represent the components of kinematic model 2 and the accelerated kinematic model for component J4 respectively, the dashed line represents component J1 of the kinematic model 1. The orange and blue bands represent the 1σ uncertainties of the ejection times of the components J4 (orange) and J5 (blue). For the components J1, J2 and J3, no error bands are plotted because the ejection times of these three components are not sufficiently constrained.

Concentrating on the two newly ejected jet features represented by the components J4 and J5, one can see in Fig. 6.1 that these components were ejected after two prominent outbursts in the γ -ray light curve. Considering the positive time lags derived by the cross-correlation analysis between the γ -ray light curve and four radio light curves observed at different frequencies (see Sect. 5.2), the prominent γ -ray outburst in 2014 can be associated with the ejection of component J4, while the ejection of component J5 can be associated with the γ -ray outburst in 2015.

Therefore, using a model in which the outbursts in the different γ -ray and radio light curves were produced when a newly ejected jet component passed through the γ -ray emitting region and through the radio core at different frequencies respectively, one can compute the location of the γ -ray emitting region and the locations of the different radio cores, using the speeds derived by the kinematic analysis presented in Sect. 4.2 and the time lags obtained by the cross-correlation analysis presented in Sect. 5.2. This will be discussed in the following sections.

6.1. Kinematic Analysis

Before computing the location of the γ -ray emitting region, the results of the kinematic analysis presented in Sect. 4.2 will be compared to those of previous kinematic analyses. Jorstad et al. (2017) have already analyzed the structural time evolution of 4C+01.28 using the same data that were investigated in this thesis, but only observations until January 2013 (see also Sect. 3.2). The results of their study are plotted in Fig. 6.2

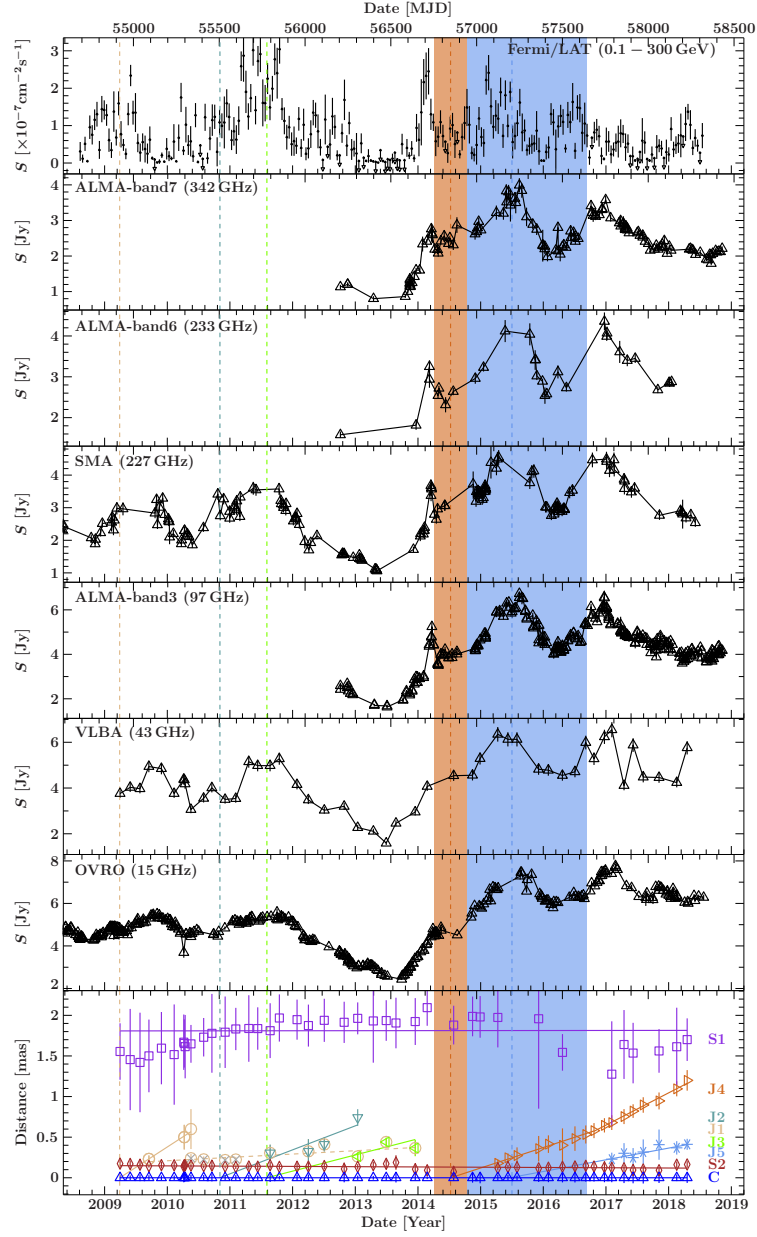


Figure 6.1.: 14-day binned γ -ray and radio light curves observed by *Fermi*/LAT, ALMA, SMA and OVRO, total flux VLBA light curve and the distance of the jet components relative to the core component plotted over time. The solid lines in the lower panel represent kinematic model 2 and the accelerated model for component J4, respectively, while the dashed line in the lower panel represents component J1 of the kinematic model 1. The vertical dashed lines represent the ejection times of the jet components. The orange and blue bands represent the 1σ uncertainties of the ejection times of the components J4 (orange) and J5 (blue). The ejection of the components J4 and J5 seems to be associated with prominent γ -ray and radio outbursts. The given frequencies are the mean values of the observation frequencies of the individual light curves. At all panels the lower time axes are given in years, while the upper time axes are given in mjd.

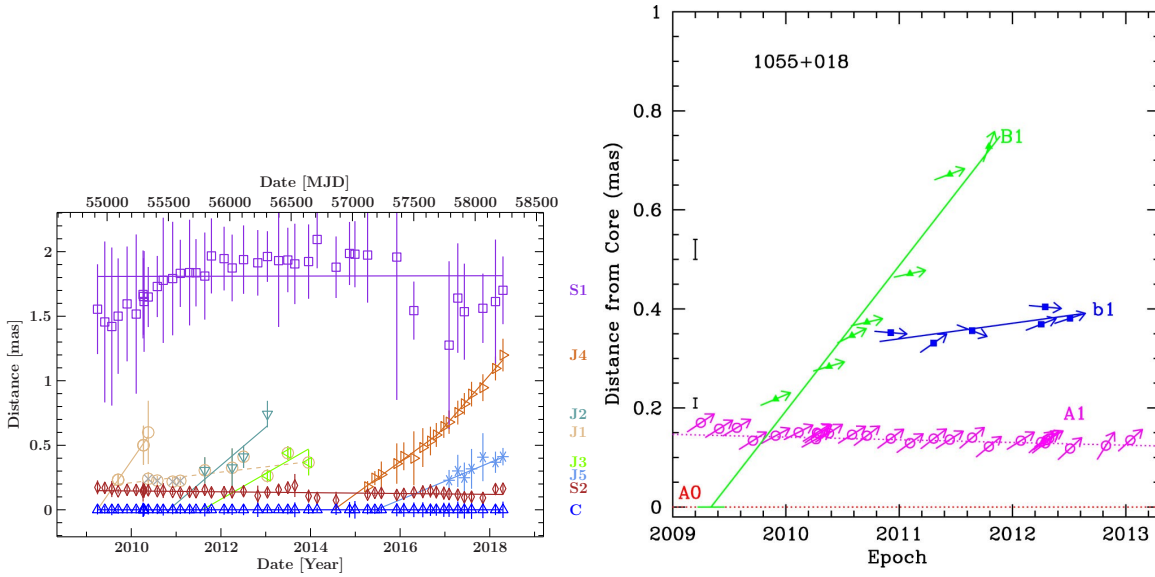


Figure 6.2.: Comparison of the kinematic analysis presented in this thesis with the kinematic analysis of 43 GHz VLBA observations presented by Jorstad et al. (2017). Left panel: Distance of the jet components relative to the core component derived in this thesis plotted over time. The solid lines represent kinematic model 2 and the accelerated model for component J4, respectively, while the dashed line represents component J1 of the kinematic model 1. Right panel: Distance of the jet components relative to the core component plotted over time taken from Jorstad et al. (2017). The solid lines represent a vector fit.

together with the results of the kinematic analysis presented in Sect. 4.2 for comparison. The left panel of Fig. 6.2 shows the distance of the jet components presented in this thesis with respect to the core component as a function of the observation time. Here, all three kinematic models are included. While the solid lines represents the fits of kinematic model 2 and the accelerated model for component J4, the dashed line represents the fit for component J1 of kinematic model 1. In the right panel of Fig. 6.2 the distance of the jet components relative to the core component are plotted over time, according to Jorstad et al. (2017).

One can see that Jorstad et al. (2017) also found a stationary feature A1 with an absolute value of the proper motion of $\mu = (0.012 \pm 0.008) \text{ mas yr}^{-1}$ that shows an inward motion. This component A1 is very similar to the jet component S2 with an absolute value of the proper motion of $\mu = (0.0033 \pm 0.0020) \text{ mas yr}^{-1}$ that also shows an inward motion. Furthermore, Jorstad et al. (2017) found two other components, the moving jet feature B1 and a so-called trailing feature b1 that seems to have formed behind B1. These two components seem to be a combination of kinematic models 1 and 2 developed within the scope of this thesis. While the proper motion

of component B1 of $\mu = (0.294 \pm 0.027) \text{ mas yr}^{-1}$ corresponds to the proper motions of all three components J1, J2 and J3 of kinematic model 2 with $\mu \sim 0.50 \text{ mas yr}^{-1}$, $\mu \sim 0.30 \text{ mas yr}^{-1}$ and $\mu \sim 0.20 \text{ mas yr}^{-1}$ respectively, the proper motion of component b1 of $\mu = (0.053 \pm 0.025) \text{ mas yr}^{-1}$ coincides with that of component J1 of kinematic model 1 with $\mu = (0.041 \pm 0.013) \text{ mas yr}^{-1}$. Note that all these components are located within one bright feature, together with the core component and component S2 (A1). Therefore, it is difficult to fit and identify these components properly, which could explain the differences in the kinematic analysis presented in this thesis and that presented in Jorstad et al. (2017). Due to the unclear identification of these components, they were neglected for further calculations. However, Jorstad et al. (2017) suggested that a new superluminal jet component might be ejected in 2011, because of a long-lasting outburst shown in the light curves. This jet feature could be represented by component J3 of kinematic model 2, as can be seen in Fig. 6.1. Moreover, Jorstad et al. (2017) found another moving jet component C1 at a mean distance with respect to the core component of $(1.75 \pm 0.16) \text{ mas}$ that is not plotted in the right panel of Fig. 6.2. Due to this mean distance to the core component, C1 should correspond to the stationary jet component S1 of the kinematic analysis presented in this thesis, but C1 shows a proper motion of $\mu = (0.147 \pm 0.006) \text{ mas yr}^{-1}$ that is much faster than that of S1 with $\mu = (0.001 \pm 0.020) \text{ mas yr}^{-1}$. However, the left panel of Fig. 6.2 shows that the distance to the core component of component S1 increases in the first half of the observational period. Therefore, the proper motion of S1 should be much faster and hence comparable to that of component C1, if only data of this period were taken into account.

To conclude, the kinematic analysis presented in this thesis corresponds very well to the kinematic analysis presented by Jorstad et al. (2017). While the stationary components S1 and S2 of the kinematic analysis presented in Sect. 4.2 correspond to the components A1 and C1 of the study presented by Jorstad et al. (2017), respectively, the components B1 and b1 of the analysis presented by Jorstad et al. (2017) seem to be a combination of kinematic models 1 and 2 developed within the scope of this thesis.

4C+01.28 was also observed in the MOJAVE sample. These observations were taken with the VLBA at 15 GHz during a period of more than 17 years from July 1995 to October 2012. A kinematic analysis based on these MOJAVE observations was presented in Lister et al. (2019), in which the distance of the jet components relative to the core component was fitted with a non-accelerating vector fit and also with a constant acceleration fit (see also Sect. 3.2). The results of this study are plotted in Fig. 6.3. One can see that the MOJAVE data plotted in Fig. 6.3 show two components, 4 and 5, at distances to the core component of 1.75 mas and 0.17 mas respectively, that correspond to the stationary components S1 and S2 of the kinematic analysis presented in this thesis and plotted in the left panel of Fig. 6.2. Furthermore, the speeds of the components 4 and 5 of the MOJAVE data correspond to the speeds of the components S1 and S2, especially for the acceleration fit. While the acceleration fit of component 5 of the MOJAVE data shows a significant inward motion with an absolute value of the

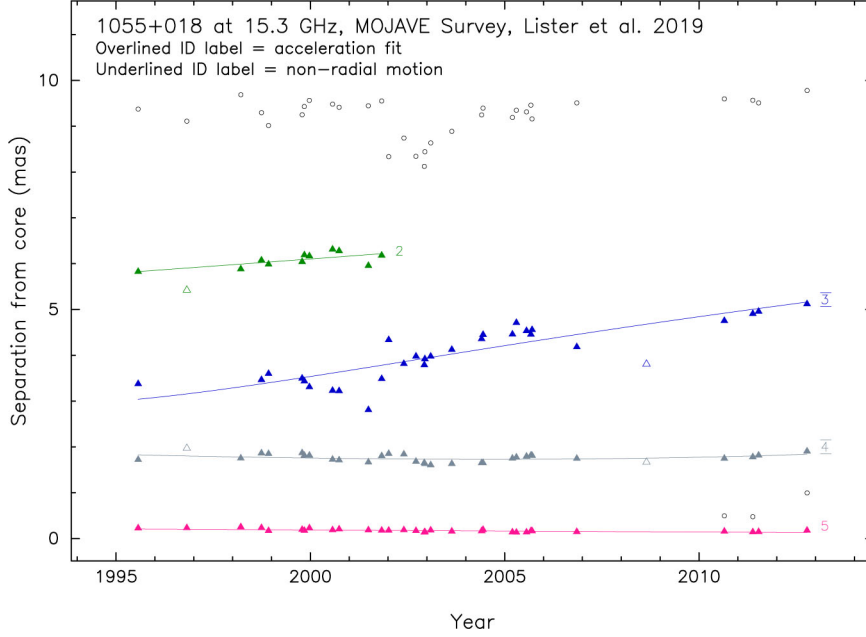


Figure 6.3.: Kinematic analysis of 15 GHz VLBA observations of 4C+01.28. The distance of the jet components to the core component is plotted with respect to the observation time. The lines represent the vector and acceleration fit, respectively. Taken from Lister et al. (2019).

proper motion of $\mu = (0.0054 \pm 0.0017) \text{ mas yr}^{-1}$ that is very similar to the absolute value of the proper motion of component S2 of $\mu = (0.0033 \pm 0.0020) \text{ mas yr}^{-1}$ derived by the kinematic analysis presented in Sect. 4.2, the acceleration fit of component 4 leads to a proper motion of $\mu = (0.0257 \pm 0.0052) \text{ mas yr}^{-1}$ that coincide with the proper motion of component S1 of $\mu = (0.001 \pm 0.020) \text{ mas yr}^{-1}$ derived by the kinematic analysis presented in this thesis. Therefore, the stationary jet components S1 and S2 of the kinematic analysis presented in Sect. 4.2 also correspond to the jet components 4 and 5 of the kinematic analysis of the 15 GHz MOJAVE data presented in Lister et al. (2019).

6.1.1. Jet Orientation

To calculate the de-projected distance between the location of the γ -ray emitting region and the jet base, the viewing angle ϕ of the jet has to be computed. For this purpose, Equation (2.1.20) can be used. However, there are two unknown variables in this equation, namely the jet speed β and the viewing angle ϕ . Therefore, only an upper limit on the viewing angle ϕ can be estimated by setting $\beta = 1$ and solving Equation (2.1.20) for ϕ , which leads to

$$\phi \leq \arccos \left(\frac{\beta_{\text{app,max}}^2 - 1}{\beta_{\text{app,max}}^2 + 1} \right), \quad (6.1.1)$$

in which $\beta_{\text{app, max}}$ is the largest possible apparent jet speed.

As already discussed, the jet components J1, J2 and J3 should be neglected for the calculation of the viewing angle because of their unclear identification. Furthermore, their apparent speeds derived by kinematic model 2 are not sufficiently constrained (see Sect. 4.2). Therefore, the largest possible apparent speed within the 1σ uncertainties is $\beta_{\text{app, max}} = 22.3$ derived by the accelerated kinematic model for component J4. Using this value for $\beta_{\text{app, max}}$ together with Equation (6.1.1), one obtains the upper limit of the viewing angle to be

$$\phi \lesssim 5^\circ.$$

This upper limit of the viewing angle is similar to the typical viewing angle for blazar jets of $\phi < 5^\circ$ derived by Jorstad et al. (2017). Furthermore, it is consistent to other estimates of the viewing angle of 4C+01.28. While Jorstad et al. (2017) determined the viewing angle of 4C+01.28 to be $\phi = (2.7 \pm 0.9)^\circ$, using 43 GHz VLBA observations, Pushkarev et al. (2009) used 15 GHz VLBA observations to determine the viewing angle of 4C+01.28 to be $\phi = 4.4^\circ$. Both values coincide with the upper limit of the viewing angle of $\phi \lesssim 5^\circ$ determined in this thesis.

6.1.2. Location of the 43 GHz Core

Another important quantity that is needed to compute the location of the γ -ray emitting region is the apparent distance of the 43 GHz core to the jet base $r_{\text{c, 43, app}}$ (see Fig. 6.4). To determine this apparent distance, the jet geometry studied in Sect. 4.3 can be used. One can use a model in which the diameter D of the jet is given by a power law: $D \propto d^l$, in which d is the distance and l is the power law index (Kadler et al. 2004). Solving this relation for the apparent distance of the 43 GHz core yields

$$r_{\text{c, 43, app}} = \left(\frac{a_{\text{maj, core}}}{C} \right)^{\frac{1}{l}}, \quad (6.1.2)$$

in which $a_{\text{maj, core}}$ is the major axis of the core component representing the jet diameter at distance $r_{\text{c, 43, app}}$ and C is the constant of proportionality. While C and l have already been determined by the study of the jet geometry presented in Sect. 4.3, $a_{\text{maj, core}}$ has not yet been estimated. As previously mentioned in Sect. 4.1, only the minor axes of two core components are unresolved but all major axes of all 48 core components are resolved. Therefore, $a_{\text{maj, core}}$ was calculated as the mean value of the major axes of all 48 core components, leading to $a_{\text{maj, core}} = (0.087 \pm 0.028)$ mas.

Since C and l are not statistically independent of each other, a similar method as presented in Appendix C was used to calculate the uncertainty $\sigma_{r_{\text{c, 43, app}}}$ of the apparent

distance $r_{c,43,\text{app}}$, leading to

$$\sigma_{r_{c,43,\text{app}}}^2 = \left(\frac{\sigma_{a_{\text{maj,core}}}}{a_{\text{maj,core}}}\right)^2 + \left(\frac{\sigma_C}{C}\right)^2 + (\sigma_l \cdot \ln r_{c,43,\text{app}})^2 - 0.4 \cdot \ln r_{c,43,\text{app}} \frac{\sum_{i=1}^N \ln d_i}{N \cdot \sum_{i=1}^N (\ln d_i)^2 - \left(\sum_{i=1}^N \ln d_i\right)^2}, \quad (6.1.3)$$

in which $\sigma_{a_{\text{maj,core}}}$, σ_C and σ_l are the uncertainties of $a_{\text{maj,core}}$, C and l , respectively, N is the number of jet components that were used for the analysis of the jet geometry presented in Sect. 4.3 and d_i is the distance of the i -th jet component.

Using a model in which the entire jet can be approximated by the geometry derived in Sect. 4.3, one can calculate the apparent distance of the 43 GHz core with respect to the jet base $r_{c,43,\text{app}}$ (see Fig. 6.4). Using Equation (6.1.2) and Equation (6.1.3) together with $l = 0.775 \pm 0.016$ and $C = (0.4016 \pm 0.0090) \text{ mas}^{1-l}$ derived in Sect. 4.3 and $a_{\text{maj,core}} = (0.087 \pm 0.028) \text{ mas}$, one obtains

$$r_{c,43,\text{app}} = (0.139 \pm 0.057) \text{ mas}.$$

6.2. Interpretation of the Time Lags

The positive time lags derived by the cross-correlation analysis between the *Fermi*/LAT γ -ray light curve and several radio light curves presented in Sect. 5.2 show that the γ -ray light curve leads the radio light curves. Therefore, the location of the γ -ray emitting region can be computed by using a formalism similar to that presented by Max-Moerbeck et al. (2014). Here, a model is used in which the radio and γ -ray activity shown in the light curves is produced by a moving emission region. This region corresponds to a jet component observed with VLBI and moves downstream along the jet. While the γ -ray outburst becomes visible when this jet component crosses the γ -ray emitting region at distance r_γ from the jet base, the radio outbursts become observable when the component passes through the core region of different frequencies ν at distance $r_{c,\nu}$ from the jet base, which is illustrated in Fig. 6.4. Here, one can see that the location of the γ -ray emitting region r_γ can be estimated using the location of the radio core $r_{c,\nu}$ at frequency ν and the distance between these two locations $r_{\gamma,\nu}$, leading to

$$r_\gamma = r_{c,\nu} - r_{\gamma,\nu}, \quad (6.2.1)$$

in which $r_{\gamma,\nu}$ is given by

$$r_{\gamma,\nu} = \mu \cdot \tau_{\gamma,\nu}, \quad (6.2.2)$$

in which μ is the proper motion of the jet component occurring the outbursts and $\tau_{\gamma,\nu}$ is the time lag between the γ -ray light curve and the radio light curve taken at frequency

ν .

Since only the apparent location of the 43 GHz core $r_{c,43,\text{app}}$ could be determined in Sect. 6.1.2, Equation (6.2.1) changes to

$$r_{\gamma,\text{app}} = r_{c,43,\text{app}} - \mu \cdot \tau_{\gamma,43}, \quad (6.2.3)$$

in which $r_{\gamma,\text{app}}$ is the apparent location of the γ -ray emitting region and $\tau_{\gamma,43}$ is the time lag between the γ -ray light curve and the 43 GHz radio light curve. However, this time lag was not determined in the cross-correlation analysis presented in Sect. 5.2. Therefore, the core shift was used to compute a term representing the time lag $\tau_{\gamma,43}$, which is discussed in the following section.

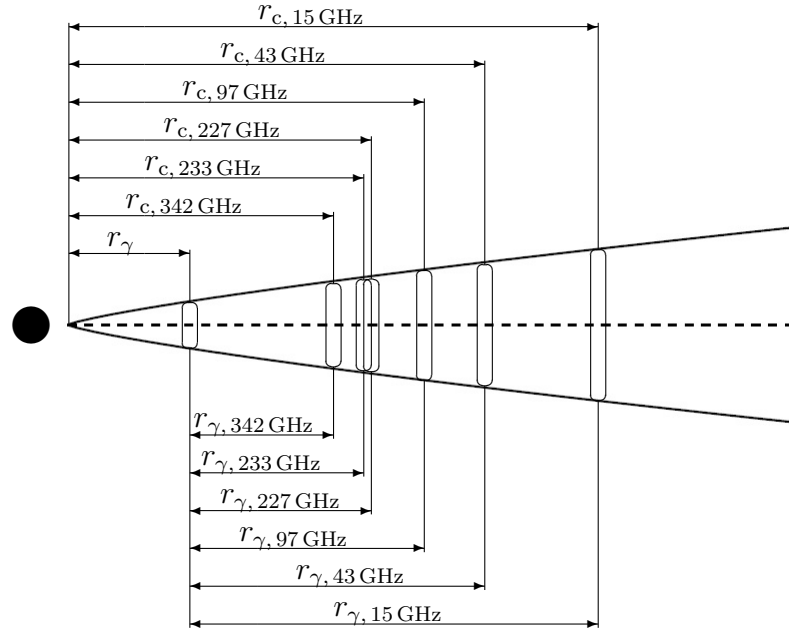


Figure 6.4.: Sketch of a jet, illustrating the core shift with respect to the γ -ray emitting region. The black circle in front of the jet represents the black hole and the ovals within the jet represent the core components at different frequencies. The location of the core component moves further downstream with decreasing frequency. r_{γ} denotes the location of the γ -ray emitting region with respect to the jet base, $r_{c,\nu}$ denotes the location of the core component at frequency ν with respect to the jet base and $r_{\gamma,\nu}$ denotes the distance between the core component at frequency ν and the γ -ray emitting region.

6.2.1. Core Shift

The location of the radio core $r_{c,\nu}$, where the optical depth become one, shifts according to Equation (2.1.17) (Königl 1981). This core shift is illustrated in Fig. 6.4. Using a model in which the outbursts shown by the light curves plotted in Fig. 5.1 and Fig. 6.1 were also due to opacity effects, one can investigate the core shift using the time lags derived by a cross-correlation analysis between γ -ray and several radio light curves measured at different frequencies (Fuhrmann et al. 2014).

Using Equation (6.2.1) and Equation (6.2.2) to calculate the location of the radio core in Equation (2.1.17), one obtains $r_{c,\nu} = r_\gamma + \mu \cdot \tau_{\gamma,\nu} \propto \nu^{-\frac{1}{k_r}}$, in which $-\frac{1}{k_r}$ is the power law index representing the core shift. Furthermore, setting $r_\gamma = 0$, meaning that the location of the γ -ray emitting region is used as reference position, and using a model in which the jet component producing the γ -ray and radio outbursts traveled at a constant speed through the region of the jet where the radio cores and the γ -ray emitting region are located, one obtains

$$\tau_{\gamma,\nu} \propto \nu^{-\frac{1}{k_r}}. \quad (6.2.4)$$

Therefore, the time lags listed in Table 5.1 are plotted double logarithmically as a function of the frequency in Fig. 6.5 to determine the power law index $-\frac{1}{k_r}$ via linear regression. For this purpose, the time lags derived by the DCF (red triangles in Fig. 6.5)

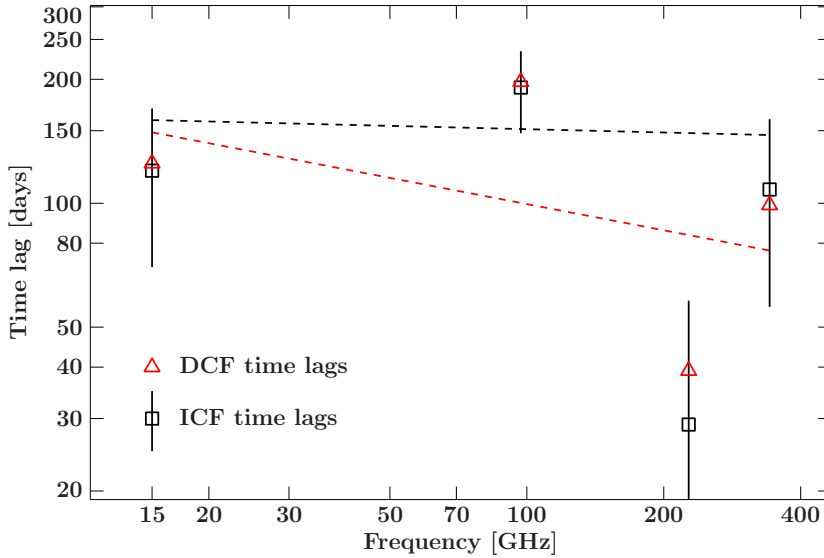


Figure 6.5.: The time lags derived from the DCF and the ICF are plotted double logarithmically as a function of frequency to obtain an estimate of the power law index $-\frac{1}{k_r}$ representing the core shift. The red and black dashed lines were fitted by linear regression using only the DCF time lags and the ICF time lags, respectively. Their gradients represent the power law index.

were fitted separately, as well as the time lags obtained by the ICF (black squares in Fig. 6.5). While the fit of the DCF time lags is plotted as a red dashed line, the fit of the time lags derived by the ICF is plotted as a black dashed line in Fig. 6.5.

With this method, by fitting the time lags of the DCF, one obtains

$$-\frac{1}{k_r} = -0.21 \pm 0.31,$$

$$\chi_{\text{red}}^2 = 1.00$$

for the power law index. Otherwise, derived by fitting the time lags of the ICF, one obtains

$$-\frac{1}{k_r} = -0.03 \pm 0.44,$$

$$\chi_{\text{red}}^2 = 2.29.$$

One can see that both values of $-\frac{1}{k_r}$ are consistent with each other within their uncertainties. Therefore, the weighted mean of $-\frac{1}{k_r}$ was computed to be

$$-\frac{1}{k_r} = -0.15 \pm 0.25.$$

Using this weighted mean value for $-\frac{1}{k_r}$, one obtains $k_r = 7 \pm 11$, which is much greater than the expected value of $k_r = 1$ for a freely expanding jet in equipartition between magnetic-field energy and jet particle density (Blandford & Königl 1979). However, $k_r = 7 \pm 11$ is consistent with unity within its uncertainty. Furthermore, k_r can reach 2.5 in regions with steep pressure gradients and can become even larger in the presence of external density gradients and foreground free-free absorption (Lobanov 1998).

Knowing the power law index $-\frac{1}{k_r}$ of the core shift, one can use Equation (6.2.4) to determine a term representing the time lag between the γ -ray light curve and the 43 GHz radio light curve. Building ratios of the time lags, one obtains

$$\tau_{\gamma, 43} = \tau_{\gamma, \nu} \left(\frac{43 \text{ GHz}}{\nu} \right)^{-\frac{1}{k_r}}. \quad (6.2.5)$$

Now, Equation (6.2.5) can be used to compute the apparent location of the γ -ray emitting region, which will be discussed in the next section.

6.2.2. Location of the γ -ray Emitting Region

Using a model in which the γ -ray and radio outbursts shown in the light curves plotted in Fig. 5.1 and Fig. 6.1 are produced via a moving jet component passing through the radio core and γ -ray emitting region respectively, the apparent location of these regions can be computed using the time lags between the γ -ray and the radio light curves derived

in Sect. 5.2 and the apparent speed of the jet component derived in Sect. 4.2. For this purpose, Equation (6.2.3) can be used. Inserting Equation (6.2.5) into Equation (6.2.3), one obtains

$$r_{\gamma, \text{app}} = r_{c, 43, \text{app}} - \mu \cdot \tau_{\gamma, \nu} \left(\frac{43 \text{ GHz}}{\nu} \right)^{-\frac{1}{k_r}}. \quad (6.2.6)$$

Since there are two jet components with different apparent speeds that seem to be associated with two prominent outbursts shown in the different γ -ray and radio light curves, it is not clear which proper motion μ should be used for the calculation of the location of the γ -ray emitting region. Therefore, the radio light curves that were investigated in the cross-correlation analysis presented in Sect. 5.2 are plotted in Fig. 6.6, shifted by the time lags derived by the DCF and ICF, respectively. Here, the red bands mark the duration of the two prominent γ -ray outbursts in 2014 and 2015. For both

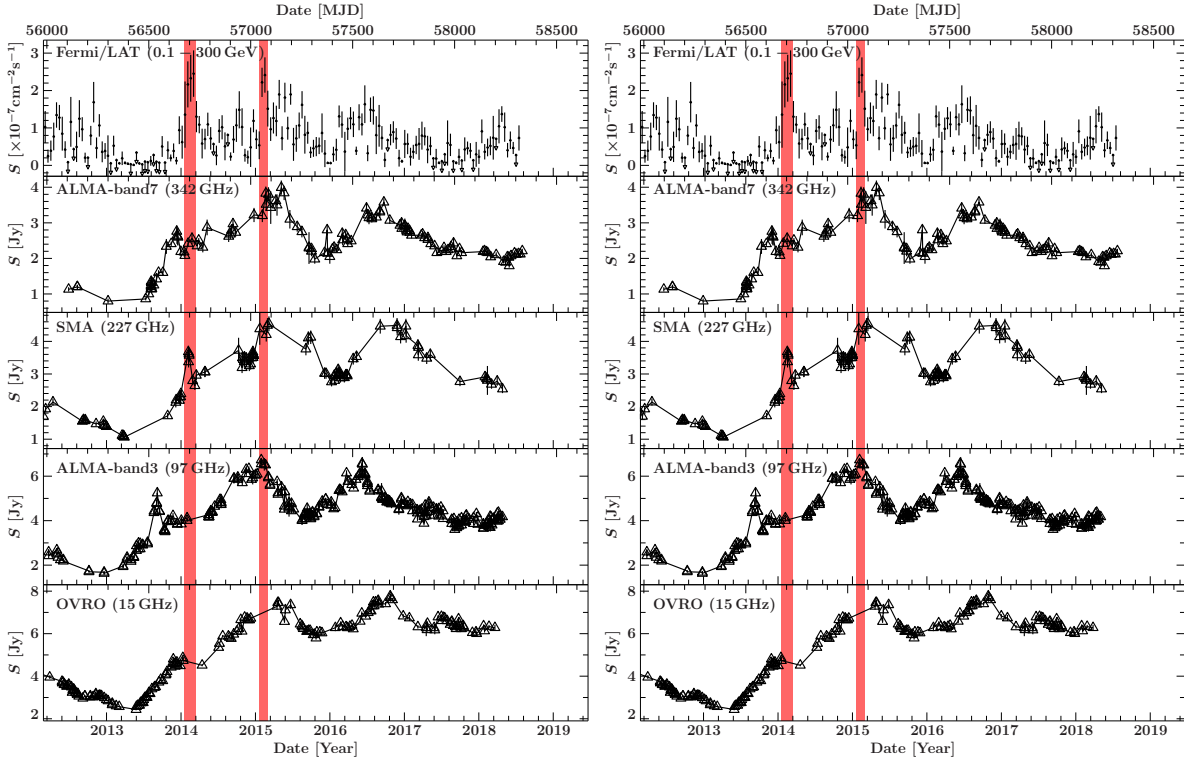


Figure 6.6.: 14-day binned γ -ray and radio light curves observed by *Fermi*/LAT, ALMA, SMA and OVRO. The radio light curves are shifted by the time lags derived in Sect. 5.2 by the DCF (left panel) and ICF (right panel), respectively. The red bands mark the duration of the two prominent γ -ray outbursts in 2014 and 2015. The cross-correlation seems to be driven by the outburst in 2015. The given frequencies are the mean values of the observation frequencies of the individual light curves. At all panels the lower time axes are given in years, while the upper time axes are given in mjd.

methods, one can see that only the peak of the shifted SMA light curve lies within the first red band corresponding to the first γ -ray outburst in 2014, while the peaks of all other shifted radio light curves do not lie within this red band. Otherwise, the second red band corresponding to the second γ -ray outburst in 2015 can be associated with peaks of all shifted radio light curves, leading to a model in which the cross-correlation is driven by the second outburst in 2015. As can be seen in Fig. 6.1, this outburst seems to be associated with the moving jet component J5. Therefore, the proper motion of $\mu = (0.144 \pm 0.076)$ mas yr $^{-1}$ of component J5 was used to compute the apparent location of the γ -ray emitting region.

Using Equation (6.2.6), together with $r_{c,43,\text{app}} = (0.139 \pm 0.057)$ mas derived in Sect. 6.1.2, $\mu = (0.144 \pm 0.076)$ mas yr $^{-1}$, as well as the time lags $\tau_{\gamma,\nu}$ and the frequencies ν listed in Table 6.1, the apparent location of the γ -ray emitting region was computed for both cross-correlation methods and all radio light curves that were studied in the cross-correlation analysis presented in Sect. 5.2. Whenever DCF time lags were used for the calculation, $-\frac{1}{k_r} = -0.21 \pm 0.31$ derived in Sect. 6.2.1 by the DCF time lags was used for this purpose. Otherwise, $-\frac{1}{k_r} = -0.03 \pm 0.44$ derived in Sect. 6.2.1 by the ICF time lags was used. All different values for the apparent location of the γ -ray emitting region are listed in Table 6.1.

One can see that all values for $r_{\gamma,\text{app}}$ listed in Table 6.1 are consistent with each other

Table 6.1.: Apparent location of the γ -ray emitting region computed by the different DCF and ICF time lags between the *Fermi*/LAT γ -ray light curve and different radio light curves measured at different frequencies.

Radio light curve	ν [GHz]	r_{corr}	$\tau_{\gamma,\nu}$ [d]	$r_{\gamma,\text{app}}$ [mas]
(1)	(2)	(3)	(4)	(5)
DCF:				
ALMA-band 7	341.9 ± 8.5	0.452 ± 0.085	99.0	0.079 ± 0.076
SMA	226.9 ± 8.5	0.301 ± 0.068	39.2	0.117 ± 0.059
ALMA-band 3	97.0 ± 6.2	0.424 ± 0.071	197.2	0.047 ± 0.078
OVRO	15	0.178 ± 0.065	125.0	0.099 ± 0.062
ICF:				
ALMA-band 7	341.9 ± 8.5	0.450	108 ± 52	0.094 ± 0.077
SMA	226.9 ± 8.5	0.309	29 ± 29	0.127 ± 0.059
ALMA-band 3	97.0 ± 6.2	0.390	191 ± 43	0.062 ± 0.077
OVRO	15	0.179	120 ± 50	0.093 ± 0.068

Note: Col.(1): Radio light curve; Col.(2): Mean frequency of the radio light curve; Col.(3): Peak cross-correlation coefficient; Col.(4): Time lag corresponding to the peak cross-correlation coefficient; Col.(5): Apparent location of the γ -ray emitting region.

within their uncertainties. Therefore, the weighted mean of the apparent location of the γ -ray emitting region was computed to be

$$r_{\gamma, \text{app}} = 0.095 \pm 0.024 \text{ mas.}$$

At a redshift of $z = 0.89$ (Jorstad et al. 2017), this is equal to

$$r_{\gamma, \text{app}} = 0.74 \pm 0.19 \text{ pc,}$$

using a cosmological model with $H_0 = 70 \text{ km s}^{-1} \text{ Mpc}^{-1}$, $\Omega_m = 0.30$ and $\Omega_\Lambda = 0.70$.

To determine the de-projected location of the γ -ray emitting region r_γ , the viewing angle ϕ of the jet can be used, leading to

$$r_\gamma = \frac{r_{\gamma, \text{app}}}{\sin \phi}. \quad (6.2.7)$$

Since in Sect. 6.1.1 only an upper limit of the viewing angle could be estimated, only a lower limit on the location of the γ -ray emitting region could be computed. Using the upper limit of the viewing angle of $\phi \lesssim 5^\circ$ derived in Sect. 6.1.1 and the smallest possible value for the apparent location of the γ -ray emitting region of $r_{\gamma, \text{app}} = 0.55 \text{ pc}$, one obtains

$$r_\gamma \gtrsim 6 \text{ pc,}$$

which is far beyond the BLR. Note that this de-projected location of the γ -ray emitting region is only the distance between this region and the jet base but not the distance between the γ -ray emitting region and the SMBH representing the central engine of the blazar. However, the distance between the jet base and the central SMBH should be very small compared to the location of the γ -ray emitting region and may therefore be neglected.

The value of the de-projected location of the γ -ray emitting region of $r_\gamma \gtrsim 6 \text{ pc}$ corresponds to values presented by Max-Moerbeck et al. (2014) for the AGN AO 0235+164 with $r_\gamma \geq (15 \pm 8) \text{ pc}$ and PKS 1502+106 with $r_\gamma = (12 \pm 9) \text{ pc}$.

Furthermore, to calculate the crossing time when the jet component producing the γ -ray outburst passes through the γ -ray emitting region, the relative distance Δr between the γ -ray emitting region and the 43 GHz core has to be computed via $\Delta r = r_{\gamma, \text{app}} - r_{c, 43, \text{app}}$, leading to $\Delta r = (-0.044 \pm 0.062) \text{ mas}$.

6.2.3. Location of the Radio Cores at Different Frequencies

In Sect. 6.2.1, it was shown that $r_{\gamma, \nu} = r_{c, \nu, \text{app}} - r_{\gamma, \text{app}} \propto \nu^{-\frac{1}{k_r}}$. Using this relation and building ratios, one can compute the apparent locations of the different radio cores at different frequencies $r_{c, \nu, \text{app}}$ and the relative distances $\Delta r = r_{c, \nu, \text{app}} - r_{c, 43, \text{app}}$ between

these locations and the location of the 43 GHz core to be

$$r_{c,\nu,\text{app}} = (r_{c,43,\text{app}} - r_{\gamma,\text{app}}) \cdot \left(\frac{\nu}{43 \text{ GHz}} \right)^{-\frac{1}{k_r}} + r_{\gamma,\text{app}}, \quad (6.2.8)$$

$$\Delta r = (r_{c,43,\text{app}} - r_{\gamma,\text{app}}) \cdot \left(\frac{\nu}{43 \text{ GHz}} \right)^{-\frac{1}{k_r}} + r_{\gamma,\text{app}} - r_{c,43,\text{app}}. \quad (6.2.9)$$

To calculate the apparent locations of the different radio cores at different frequencies $r_{c,\nu,\text{app}}$ and the relative distances Δr , the weighted mean values of the location of the γ -ray emitting region of $r_{\gamma,\text{app}} = 0.095 \pm 0.024 \text{ mas}$ derived in Sect. 6.2.2 and of the power law index of the core shift of $-\frac{1}{k_r} = -0.15 \pm 0.25$ derived in Sect. 6.2.1 were used. All computed values of $r_{c,\nu,\text{app}}$ and Δr are listed in Table 6.2.

Table 6.2.: Apparent locations of the different radio cores at different frequencies and the relative distances between these locations and the location of the 43 GHz core.

Radio light curve	ν [GHz]	$r_{c,\nu,\text{app}}$ [mas]	Δr [mas]
(1)	(2)	(3)	(4)
ALMA-band 7	341.9 ± 8.5	0.127 ± 0.045	-0.012 ± 0.024
ALMA-band 6	232.5 ± 2.4	0.129 ± 0.047	-0.010 ± 0.020
SMA	226.9 ± 8.5	0.129 ± 0.047	-0.010 ± 0.020
ALMA-band 3	97.0 ± 6.2	0.134 ± 0.051	-0.005 ± 0.011
VLBA	43	0.139 ± 0.057	0
OVRO	15	0.147 ± 0.068	0.008 ± 0.017

Note: Col.(1): Radio light curve; Col.(2): Mean frequency of the radio light curve; Col.(3): Apparent location of the radio core at frequency ν ; Col.(4): Relative distance between the radio cores at different frequencies and the 43 GHz core.

6.3. The Overall Picture

As mentioned before, in this thesis the radio and γ -ray activity shown in the light curves plotted in Fig. 5.1 and Fig. 6.1 is described by using a model in which this activity was produced by jet components that move downstream along the jet. Furthermore, within this model, two prominent γ -ray outbursts became observable when the jet components J4 and J5 passed through the γ -ray emitting region, while the corresponding radio outbursts became visible when these two jet components crossed the different radio core regions. To test this model, the crossing time t of these two components was computed as the point at which the separation of the corresponding jet component to the 43 GHz core equals the relative distance Δr between the location of the 43 GHz core and the locations

of the γ -ray emitting region and the different radio core regions, respectively. More information on the calculation of these crossing times, especially on their uncertainties estimated by Equation (C.2.15), can be found in Appendix C. All calculated crossing times are listed in Table 6.3 and plotted in Fig. 6.7 as vertical dashed lines, together with the different γ -ray and radio light curves. Here, the orange dashed lines correspond to component J4, while the blue dashed lines correspond to component J5. Furthermore, the orange and blue bands represent the 1σ uncertainties of the crossing times of J4 and J5, respectively.

In Fig. 6.7, one can see that the bright outbursts of the individual light curves in 2014 correspond to the crossing times of component J4 within 3σ , while the bright outbursts of the individual light curves in 2015 coincide with the crossing times of component J5 even within 1σ . However, component J4 seems to cross the γ -ray emitting region and the different radio core regions too late to produce the prominent outbursts of the individual light curves in 2014. Nevertheless, this could be explained by the accelerated model of this jet component. Due to this accelerated motion of component J4, it is not clear at which time this component passed through the γ -ray emitting and radio core regions respectively, because this accelerated motion was approximated by two linear fits (see Sect. 4.2). Otherwise, the crossing times of component J4 are consistent with the prominent outbursts shown in the different light curves in 2014 within 3σ . Furthermore, the crossing times of component J5 correspond to the prominent outbursts shown in the different light curves in 2015. Therefore, the model used in this thesis is confirmed.

To conclude, in Fig. 6.7, it was shown that the radio and γ -ray activity shown in the light curves were produced by the moving jet components J4 and J5 that travel

Table 6.3.: Crossing times at which the moving jet components J4 and J5 passed through the γ -ray emitting region and the different radio core regions.

Light curve	ν	Δr	$t(\text{J4})$	$t(\text{J5})$
(1)	[GHz] (2)	[mas] (3)	[yr] (4)	[yr] (5)
<i>Fermi</i> /LAT γ -ray		-0.044 ± 0.062	2014.34 ± 0.38	2015.2 ± 1.5
ALMA-band 7	341.9 ± 8.5	-0.012 ± 0.024	2014.47 ± 0.28	2015.4 ± 1.3
ALMA-band 6	232.5 ± 2.4	-0.010 ± 0.020	2014.48 ± 0.28	2015.4 ± 1.3
SMA	226.9 ± 8.5	-0.010 ± 0.020	2014.48 ± 0.28	2015.4 ± 1.3
ALMA-band 3	97.0 ± 6.2	-0.005 ± 0.011	2014.50 ± 0.26	2015.4 ± 1.3
VLBA	43	0	2014.52 ± 0.26	2015.5 ± 1.2
OVRO	15	0.008 ± 0.017	2014.55 ± 0.26	2015.5 ± 1.2

Note: Col.(1): Light curve; Col.(2): Mean frequency of the radio light curve; Col.(3): Relative distance between the radio cores at different frequencies and the 43 GHz core; Col.(4): Crossing times of component J4; Col.(5) Crossing times of component J5.

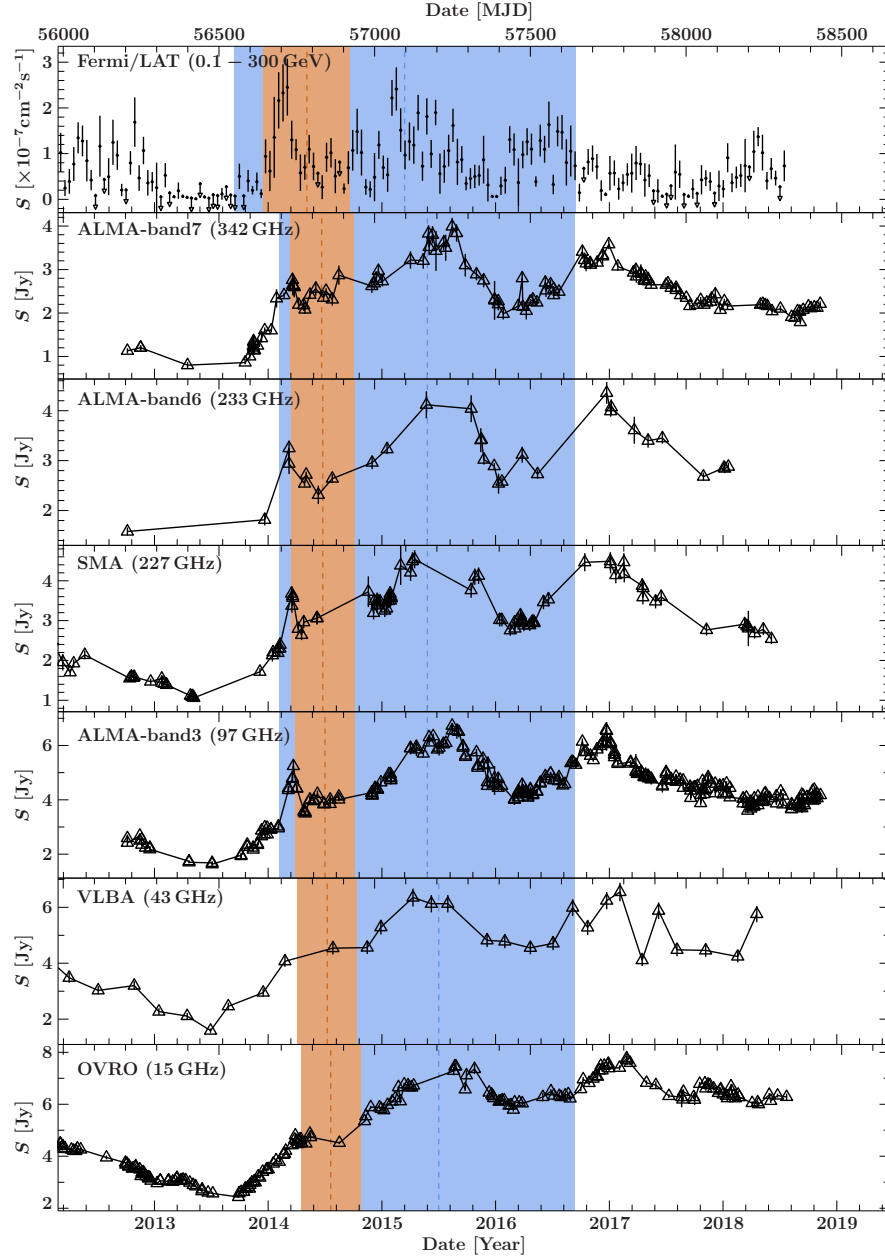


Figure 6.7.: 14-day binned γ -ray and radio fluxes observed by *Fermi*/LAT, ALMA, SMA and OVRO, respectively and the total fluxes observed by the VLBA plotted over time. The vertical dashed lines represent the crossing times of the jet components J4 (orange) and J5 (blue), when these two components passed through the core regions of the given frequencies and the γ -ray emitting region, respectively. The orange and blue bands represent the 1σ uncertainties of the crossing times of the components J4 (orange) and J5 (blue). The crossing times correspond to the occurrence of bright outbursts shown by the individual light curves in 2014 and 2015. The given frequencies are the mean values of the observation frequencies of the individual light curves. At all panels the lower time axes are given in years, while the upper time axes are given in mjd.

downstream along the jet. It is particularly visible for component J5 that the calculated crossing times coincide with the prominent radio and γ -ray outbursts in 2015. This γ -ray outburst was produced when component J5 passed through the γ -ray emitting region at a distance of $r_\gamma \gtrsim 6$ pc from the jet base. Further downstream in the jet, J5 crossed the different core regions, producing the outbursts shown by the different radio light curves measured at different frequencies. After passing through the 43 GHz core, J5 appeared as a newly ejected jet feature in the 43 GHz VLBA observations presented in Sect. 4.1 and could therefore be tracked to compute its apparent speed to be $\beta_{\text{app}} = 6.9 \pm 3.6$.

7. Conclusion and Outlook

This thesis studied the structural time evolution of 4C+01.28 by investigating 48 epochs of 4C+01.28 which were observed with the VLBA at 43 GHz over a period of around nine years from April 2009 until April 2018. It was found that two new prominent jet features, J4 and J5, were ejected in 2014.52 ± 0.26 and 2015.5 ± 1.2 , respectively. While component J5 shows a non-accelerated motion with an apparent speed of $\beta_{app} = 6.9 \pm 3.6$, the motion of component J4 seems to be accelerated. Therefore, its separation to the core was fitted with two linear regressions leading to speeds of $\beta_{app} = 12.1 \pm 2.4$ for separations $\lesssim 0.6$ and $\beta_{app} = 19.0 \pm 3.3$ for separations $\gtrsim 0.6$. Using these values, an upper limit of the viewing angle of the jet was calculated to be $\phi \lesssim 5^\circ$, using the fastest possible jet speed shown by component J4. This upper limit of the viewing angle is similar to the typical viewing angle of blazars of $\phi < 5^\circ$ derived by Jorstad et al. (2017). Furthermore, it also corresponds to other estimates of the viewing angle of 4C+01.28 of $\phi = (2.7 \pm 0.9)^\circ$ (Jorstad et al. 2017) and $\phi = 4.4^\circ$ (Pushkarev et al. 2009).

4C+01.28 was also observed at γ -ray energies by *Fermi*/LAT and at other radio frequencies by ALMA, SMA and OVRO, respectively. The several light curves of these observations all show similar behavior with prominent outbursts in 2014 and 2015. Therefore, a cross-correlation analysis was performed between the *Fermi*/LAT γ -ray light curve and four radio light curves observed at different frequencies, resulting in positive time lags, which means that the γ -ray light curve leads the radio light curves. Hence, these positive time lags indicate that the γ -ray emitting region is located upstream of the different radio cores within the jet which is in agreement with the result of a source stacking cross-correlation analysis of 54 blazars presented by Fuhrmann et al. (2014). They also found positive time lags between γ -ray light curves and radio light curves and therefore concluded that the γ -ray emitting region is located upstream of the 3 mm radio core.

Combining the results of the kinematic analysis of the 43 GHz VLBA observations with those of the cross-correlation analysis, the newly ejected jet components J4 and J5 seem to be associated with the prominent outbursts shown by the different light curves in 2014 and 2015. Using a model in which these outbursts were produced when the components J4 and J5 passed through the γ -ray emitting region and the different radio cores, respectively, the location of the γ -ray emitting region with respect to the jet base was calculated to be $r_\gamma \gtrsim 6$ pc. This lower limit of the location of the γ -ray emitting region corresponds to values presented by Max-Moerbeck et al. (2014) for the AGN AO 0235+164 with $r_\gamma \geq (15 \pm 8)$ pc and PKS 1502+106 with $r_\gamma = (12 \pm 9)$ pc. Furthermore, given the typical BLR radii of $\lesssim 1$ pc (Fuhrmann et al. 2014), the γ -ray

emitting region of 4C+01.28 is located far beyond the BLR. A similar result was also found by Costamante et al. (2018). These authors found no evidence for the expected $\gamma - \gamma \rightarrow e^\pm$ absorption within the BLR by analyzing γ -ray spectra of 106 blazars and therefore concluded that the γ -ray emitting region should be located outside the BLR. Therefore, external Compton (EC) scattering on optical-UV photons from the BLR (e.g., Sikora et al. 1994), which is generally used to explain the γ -ray emission (Costamante et al. 2018), can be ruled out as the main γ -ray production mechanism. However, alternatively to EC on BLR photons, the γ -ray emission could be produced via synchrotron self-Compton (SSC) scattering (e.g., Maraschi et al. 1992) or EC on IR photons from the dusty torus (e.g., Sikora et al. 2009).

Finally, to test the model that was developed in this thesis to calculate the γ -ray emitting region, the crossing times of the components J4 and J5 were calculated as the point at which the separation of the corresponding jet component to the 43 GHz core equals the relative distance between the location of the 43 GHz core and the locations of the γ -ray emitting region and the different radio core regions, respectively. While the crossing times of component J5 correspond very well to prominent radio and γ -ray outbursts in 2015, component J4 seems to cross the γ -ray emitting region and the different radio core regions too late to produce the prominent outbursts of the individual light curves in 2014. Nevertheless, this could be explained by the accelerated model of this jet component. Due to this accelerated motion of component J4, it is not clear at which time this component passed through the γ -ray emitting and radio core regions respectively, because this accelerated motion was approximated by two linear fits. However, the crossing times of component J4 correspond to the prominent outbursts shown in the different light curves in 2014 within 3σ .

To obtain a better estimate of the crossing times of component J4, observations of 4C+01.28, taken by the Global Millimeter VLBI Array (GMVA) at 43 GHz and 86 GHz in October 2014 and May 2015, should be included in this analysis. Since the observation taken in October 2014 was very close to the ejection of component J4 (≈ 2014.52), this epoch could help to improve the computation of the ejection time and the crossing times, respectively. Furthermore, the GMVA observations at 86 GHz should provide more detailed information on the inner jet structure of 4C+01.28, which could also help for the calculation of the crossing times. In addition, further VLBA observations of 4C+01.28 at 43 GHz provided by the BU-group should be included in the kinematic analysis to reduce the uncertainties of the ejection time and the crossing times of component J5, respectively.

A. (u, v) -Plane Coverages

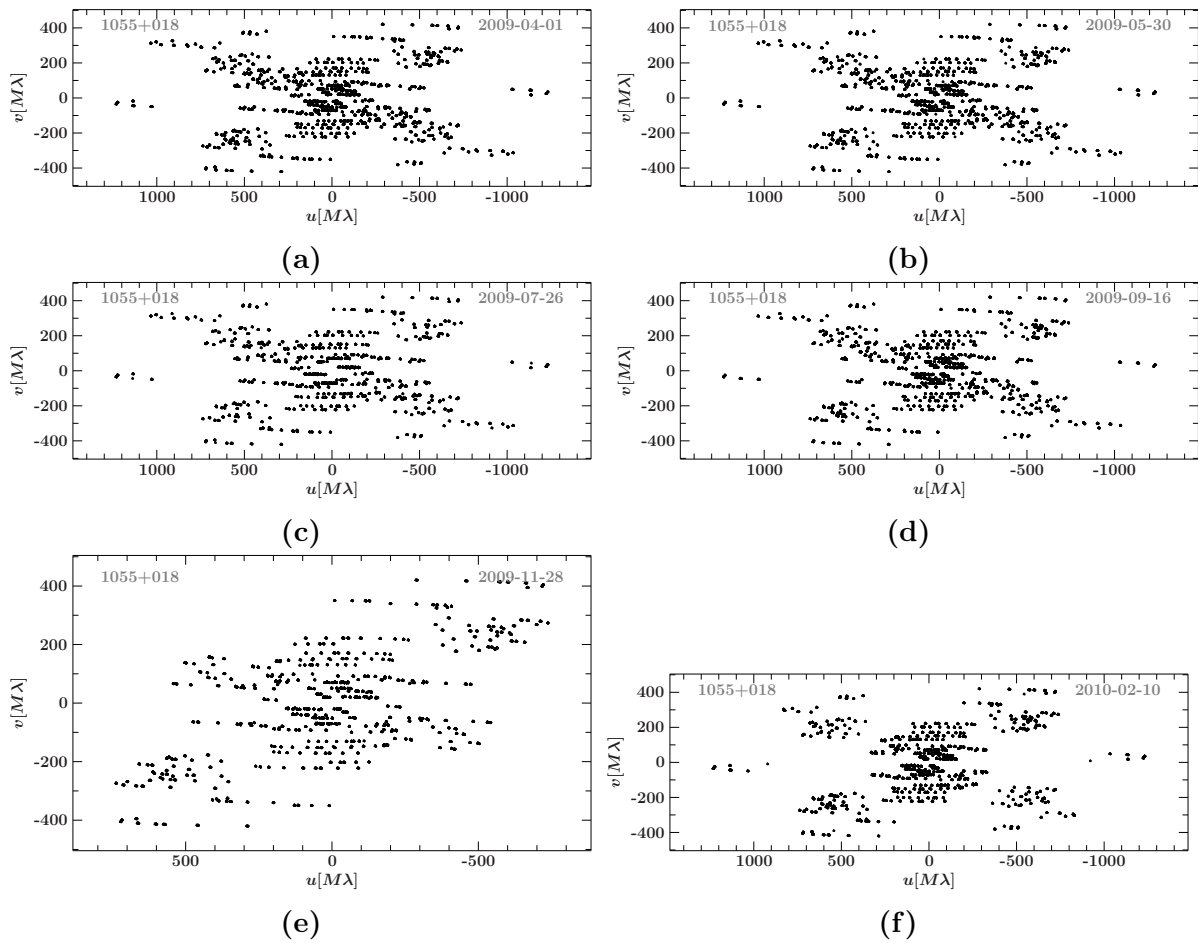


Figure A.1.: (u, v) -Plane Coverages of 4C+01.28 taken with the VLBA at 43 GHz between April 2009 and February 2010.

A. (u, v) -Plane Coverages

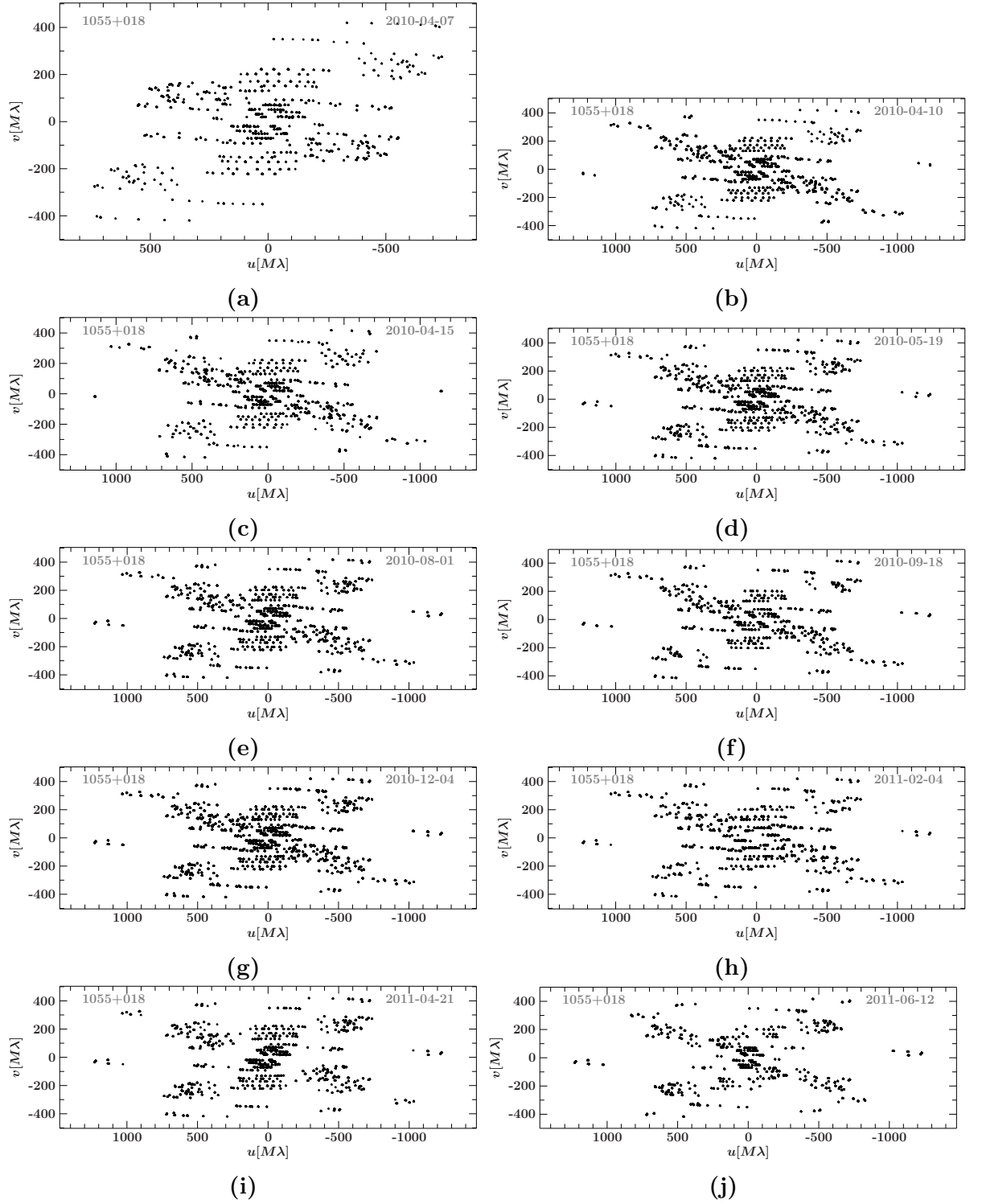


Figure A.2.: (u, v) -Plane Coverages of 4C+01.28 taken with the VLBA at 43 GHz between April 2010 and June 2010.

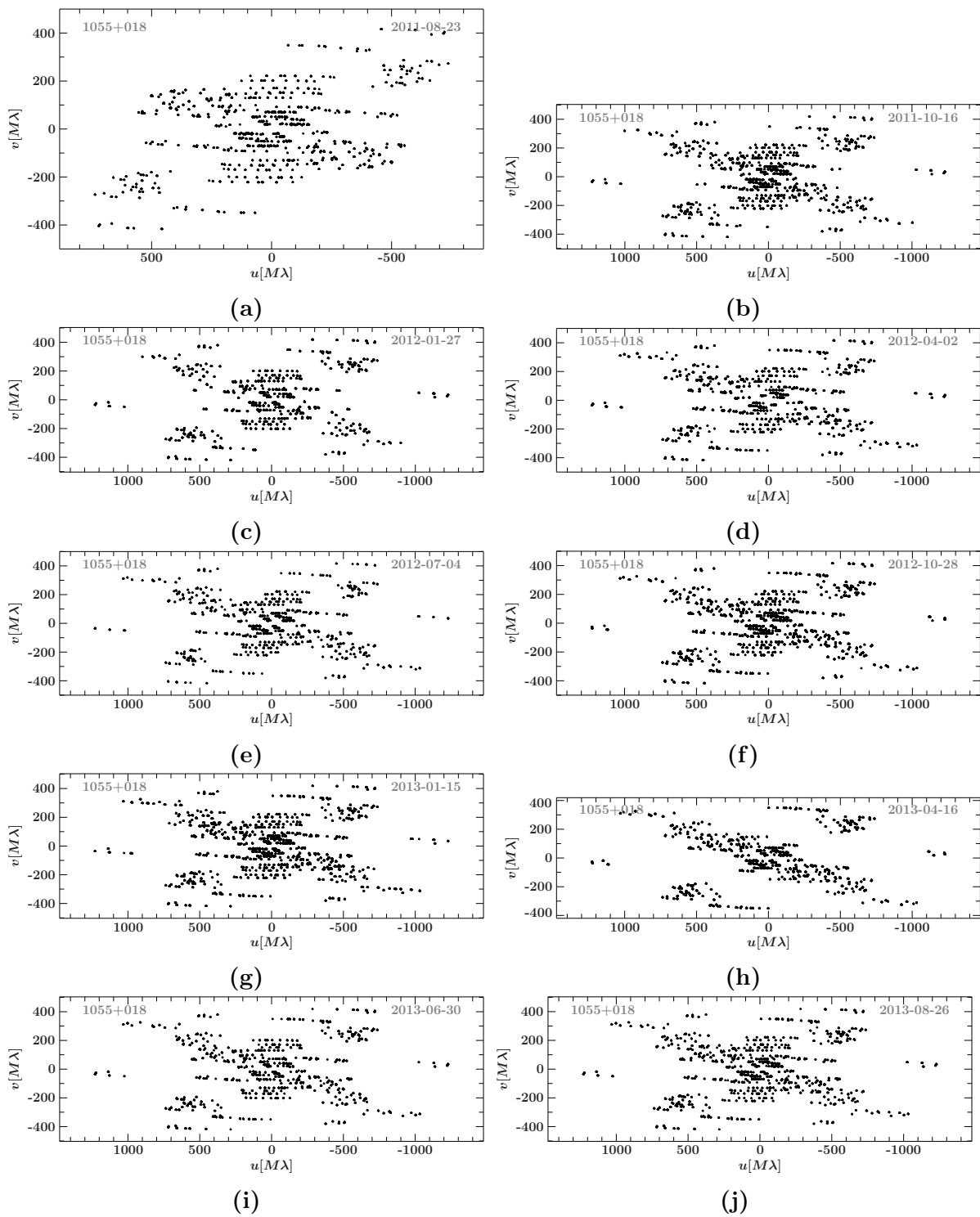


Figure A.3.: (u, v) -Plane Coverages of 4C+01.28 taken with the VLBA at 43 GHz between August 2011 and August 2013.

A. (u, v) -Plane Coverages

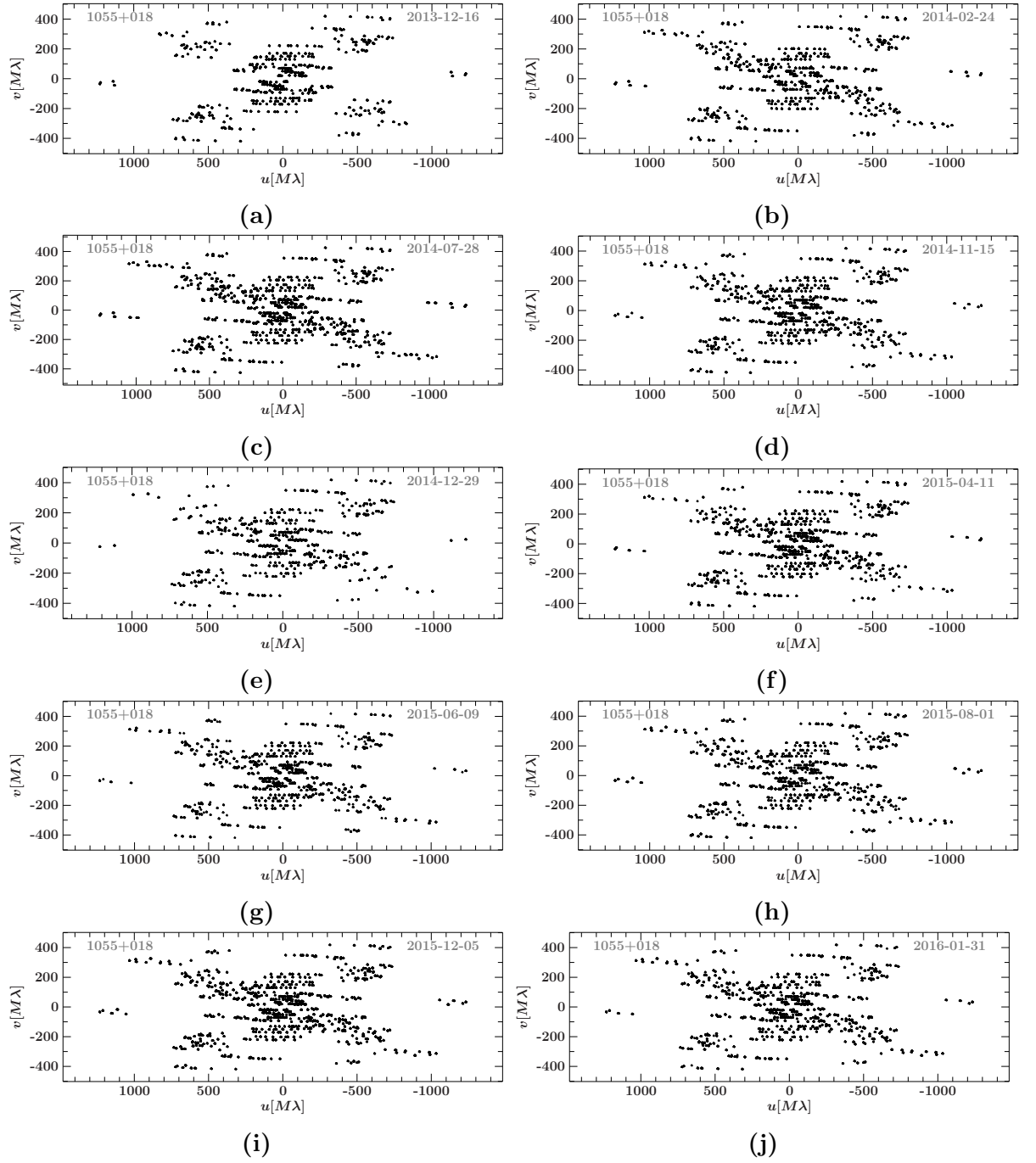


Figure A.4.: (u, v) -Plane Coverages of 4C+01.28 taken with the VLBA at 43 GHz between December 2013 and January 2016.

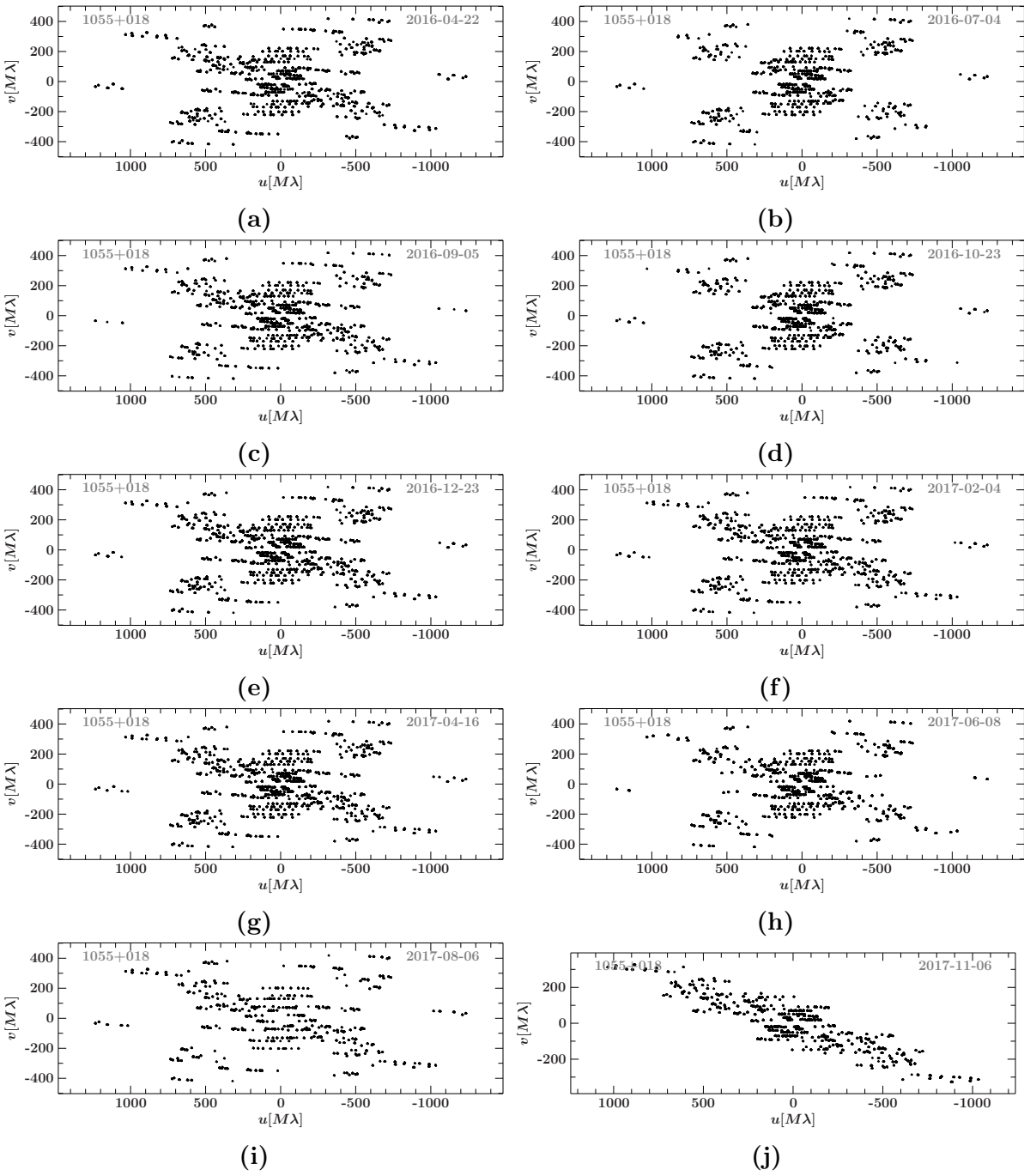


Figure A.5.: (u, v) -Plane Coverages of 4C+01.28 taken with the VLBA at 43 GHz between April 2016 and November 2017.

A. (u, v) -Plane Coverages

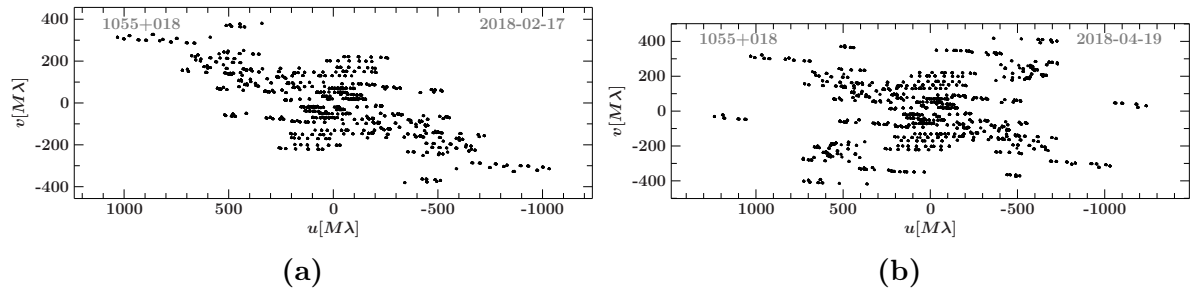


Figure A.6.: (u, v) -Plane Coverages of 4C+01.28 taken with the VLBA at 43 GHz between February 2018 and April 2018.

B. Images of 4C+01.28

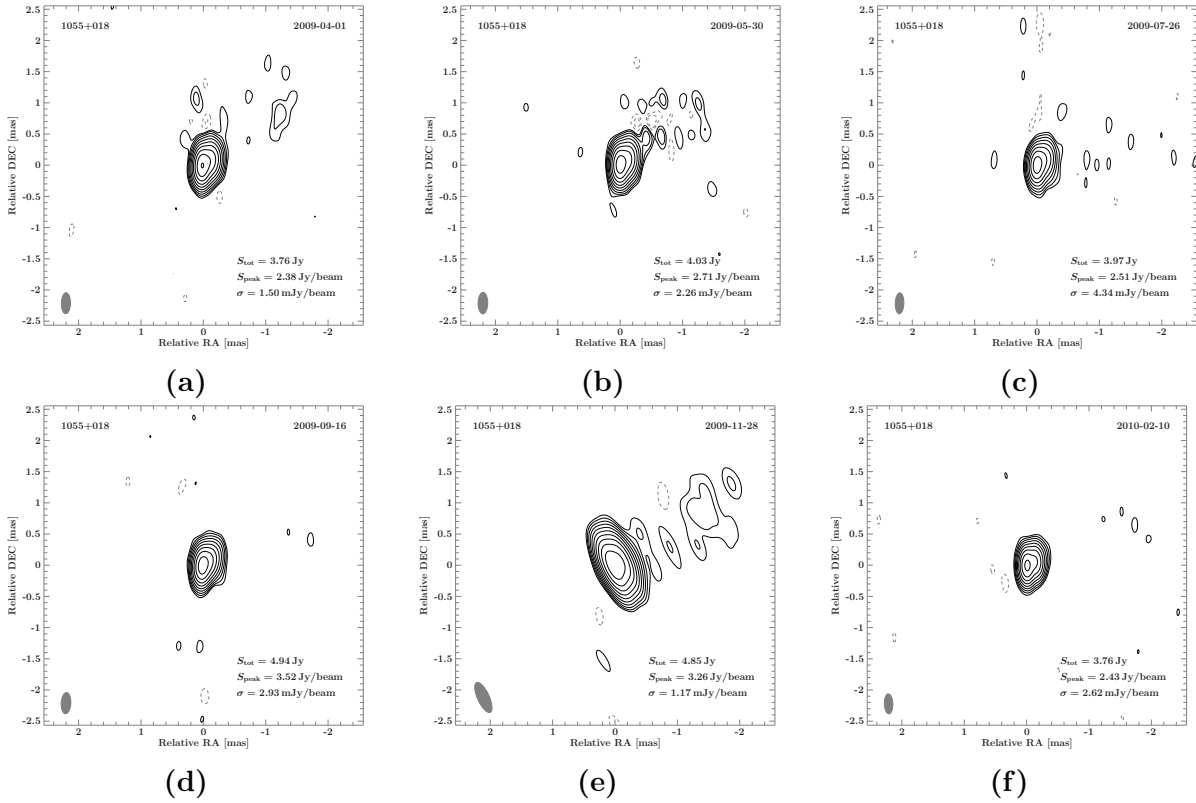


Figure B.1.: Uniformly weighted 43 GHz VLBA total intensity images of 4C+01.28 between April 2009 and February 2010. S_{tot} is the total integrated flux density, S_{peak} is the highest flux density per beam and σ is the noise level. The gray ellipse in the bottom left corner corresponds to the beam. The contours begin at 3σ and increase logarithmically by a factor of 2.

B. Images of 4C+01.28

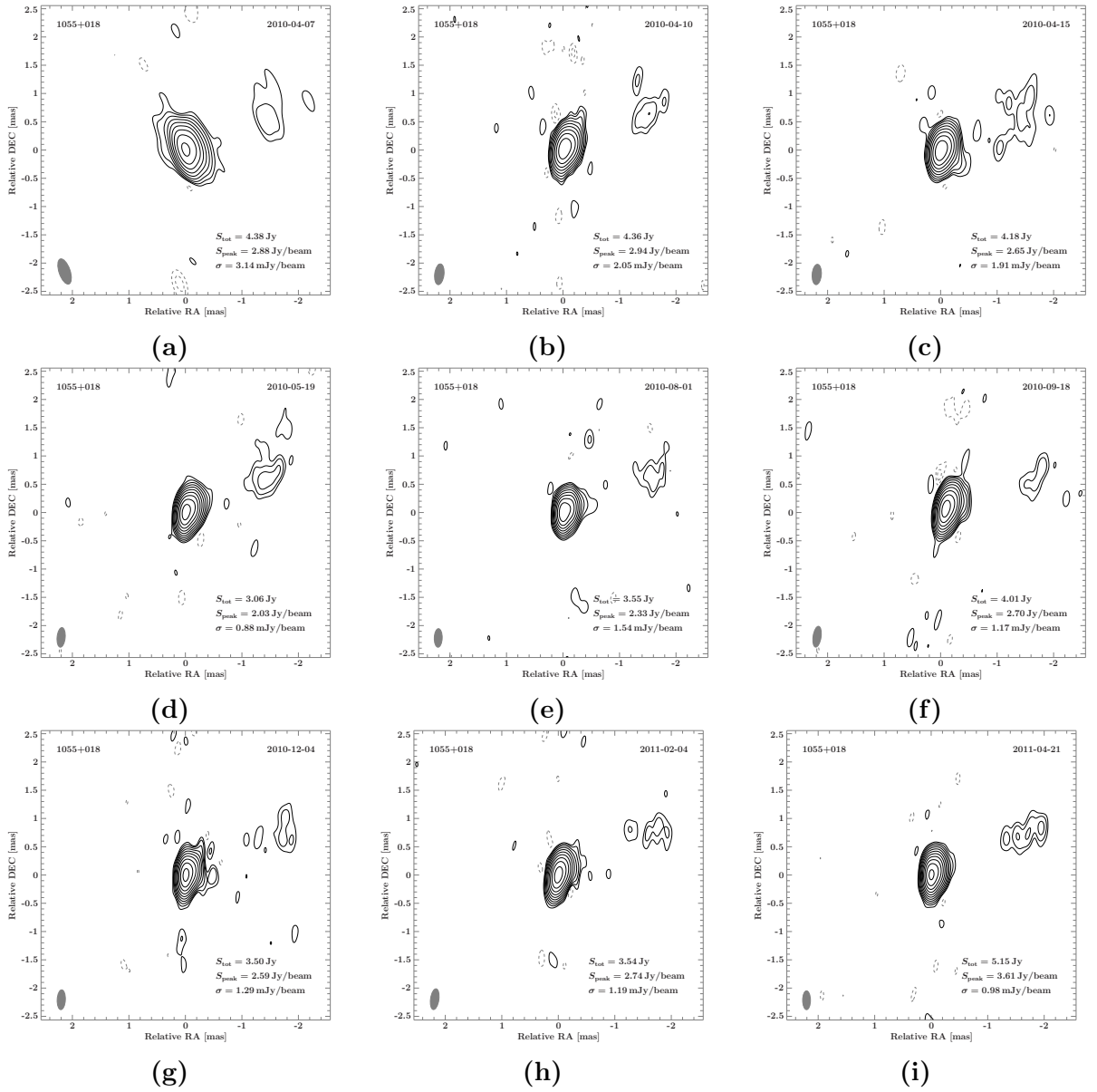


Figure B.2.: Uniformly weighted 43 GHz VLBA total intensity images of 4C+01.28 between April 2010 and April 2011. S_{tot} is the total integrated flux density, S_{peak} is the highest flux density per beam and σ is the noise level. The gray ellipse in the bottom left corner corresponds to the beam. The contours begin at 3σ and increase logarithmically by a factor of 2.

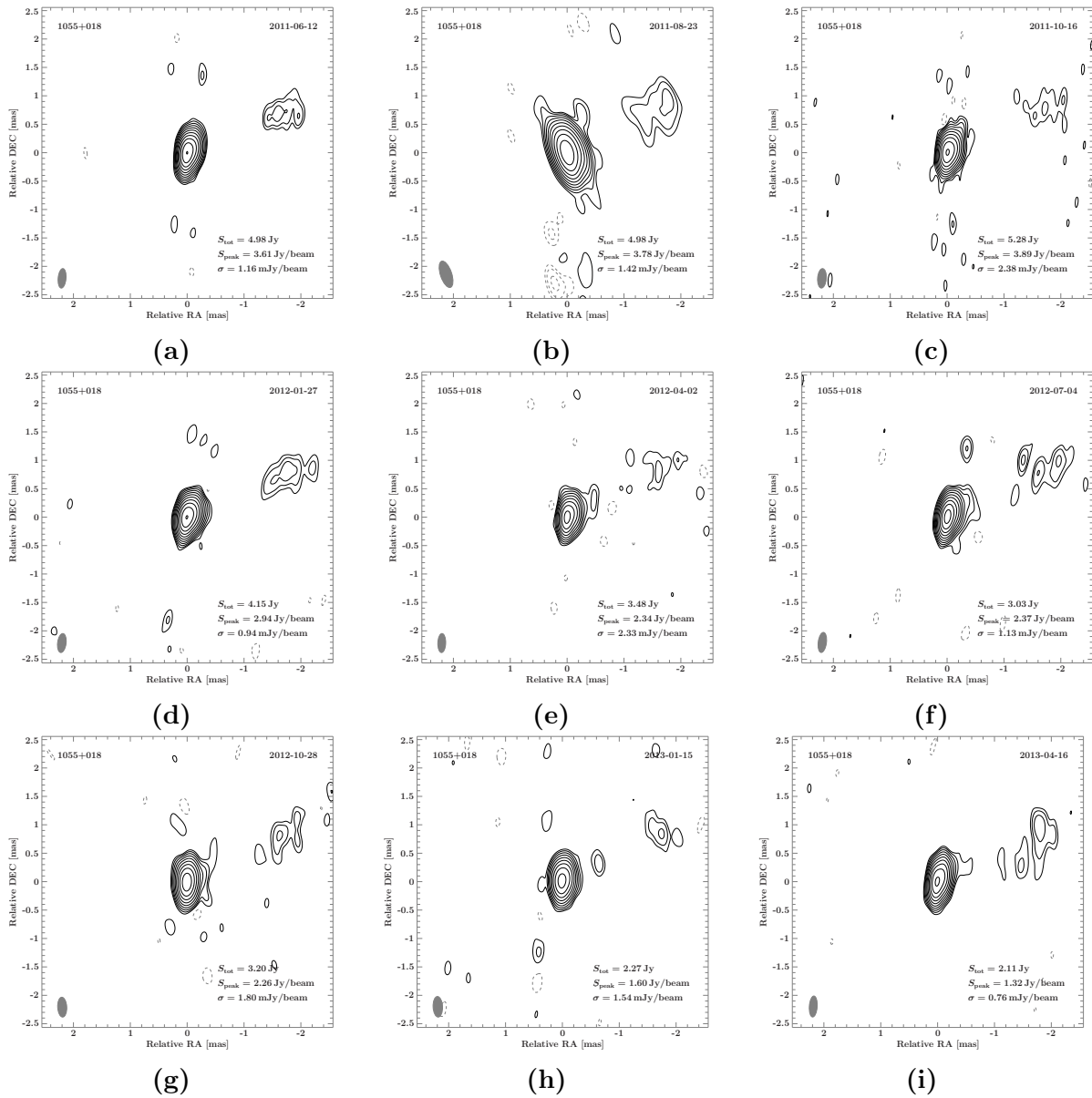


Figure B.3.: Uniformly weighted 43 GHz VLBA total intensity images of 4C+01.28 between June 2011 and April 2013. S_{tot} is the total integrated flux density, S_{peak} is the highest flux density per beam and σ is the noise level. The gray ellipse in the bottom left corner corresponds to the beam. The contours begin at 3σ and increase logarithmically by a factor of 2.

B. Images of 4C+01.28

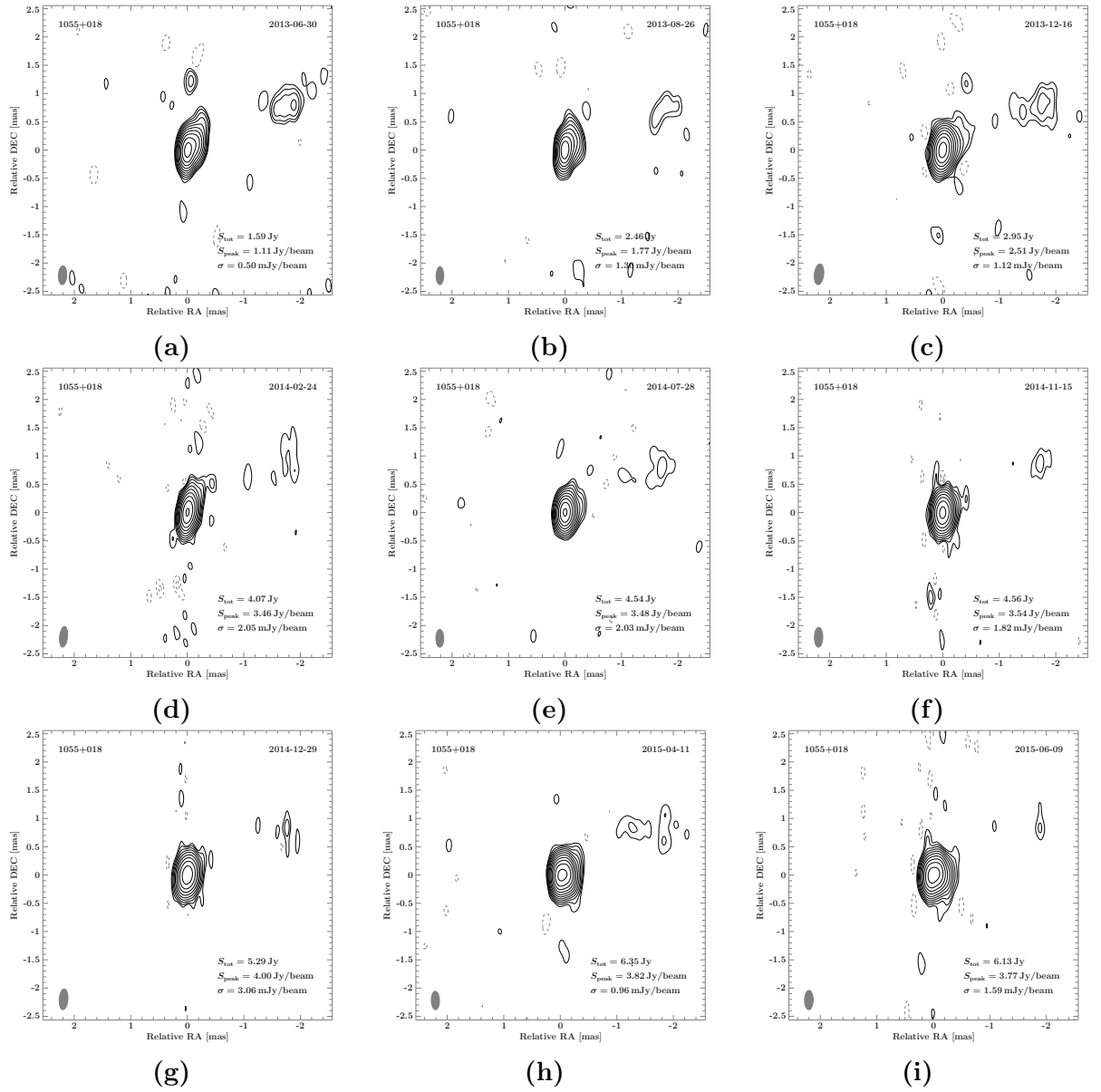


Figure B.4.: Uniformly weighted 43 GHz VLBA total intensity images of 4C+01.28 between June 2013 and June 2015. S_{tot} is the total integrated flux density, S_{peak} is the highest flux density per beam and σ is the noise level. The gray ellipse in the bottom left corner corresponds to the beam. The contours begin at 3σ and increase logarithmically by a factor of 2.

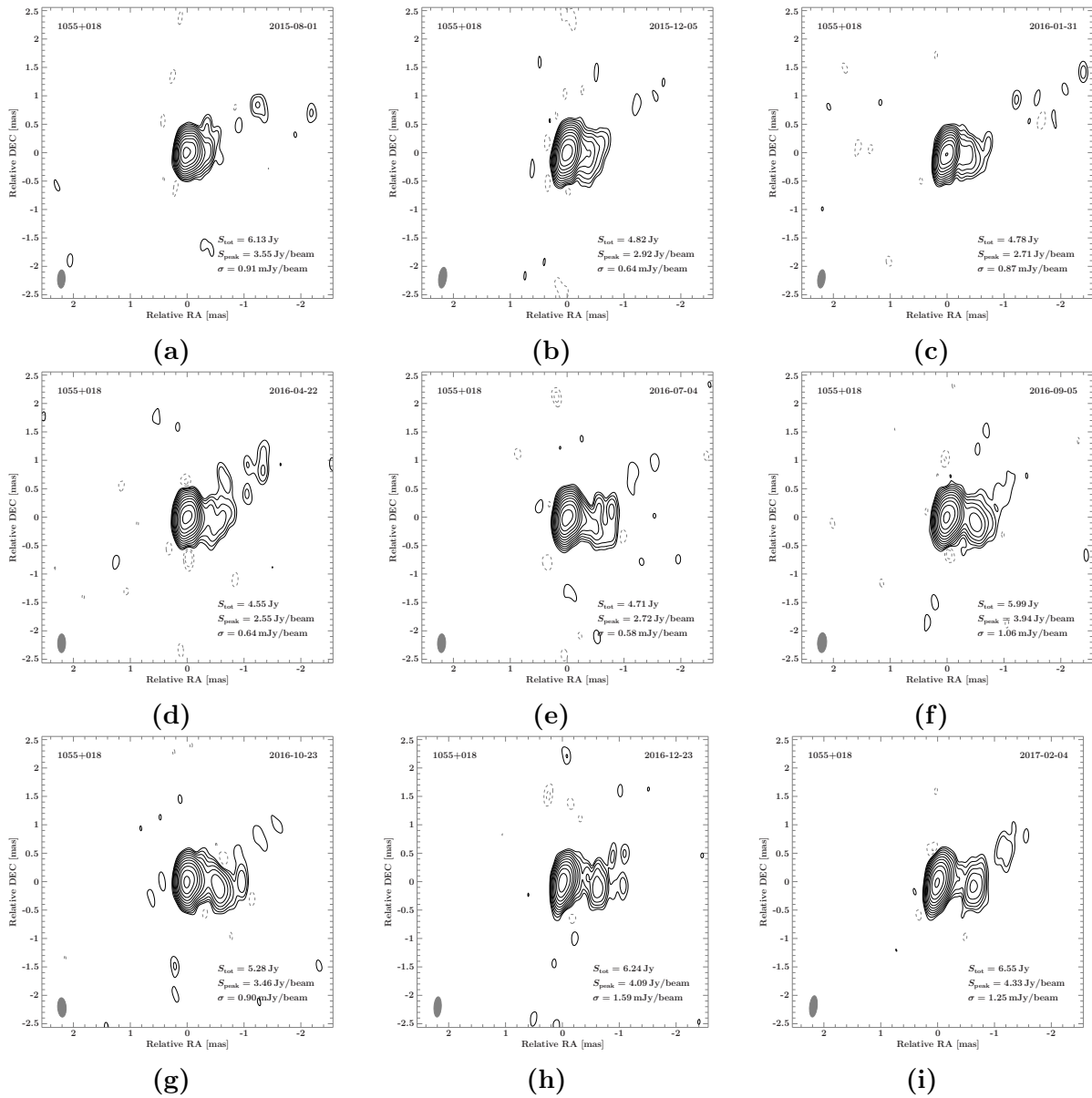


Figure B.5.: Uniformly weighted 43 GHz VLBA total intensity images of 4C+01.28 between August 2015 and February 2017. S_{tot} is the total integrated flux density, S_{peak} is the highest flux density per beam and σ is the noise level. The gray ellipse in the bottom left corner corresponds to the beam. The contours begin at 3σ and increase logarithmically by a factor of 2.

B. Images of 4C+01.28

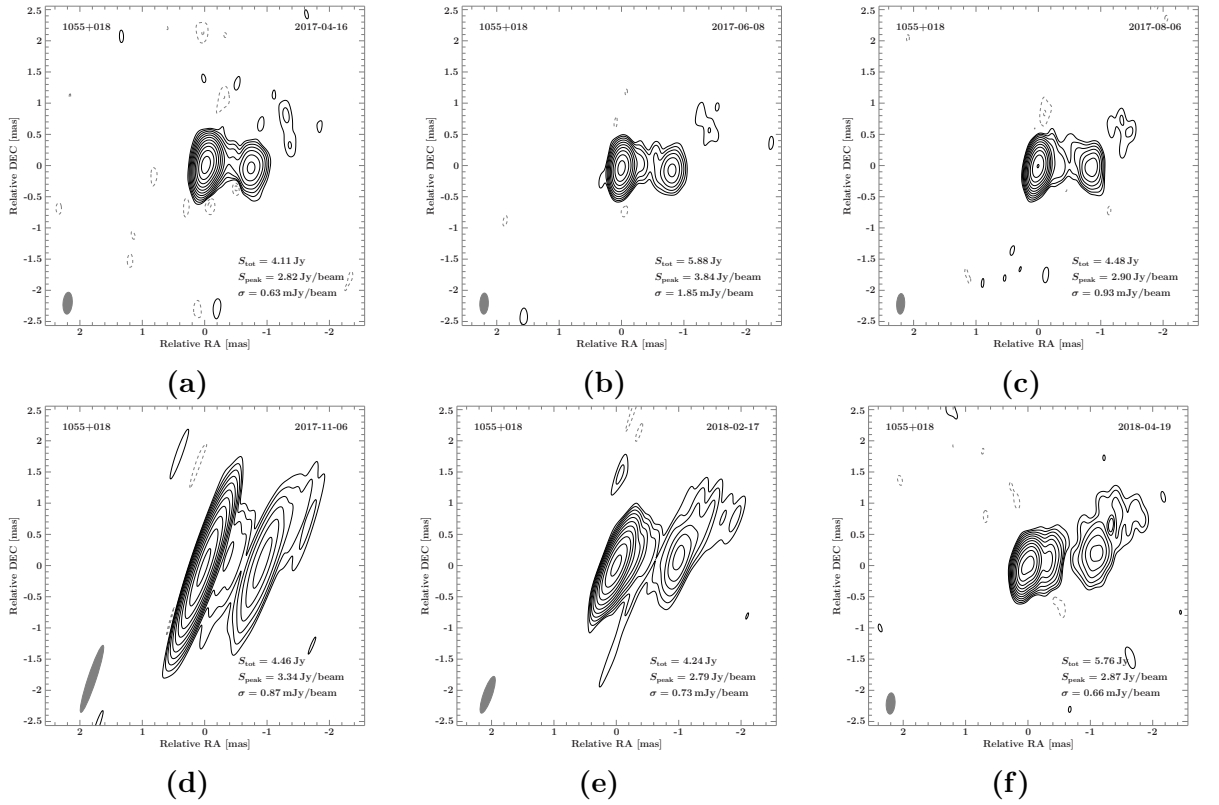


Figure B.6.: Uniformly weighted 43 GHz VLBA total intensity images of 4C+01.28 between April 2017 and April 2018. S_{tot} is the total integrated flux density, S_{peak} is the highest flux density per beam and σ is the noise level. The gray ellipse in the bottom left corner corresponds to the beam. The contours begin at 3σ and increase logarithmically by a factor of 2.

C. Error Analysis of the Ejection Time

To calculate the speed and the ejection time of the jet components, linear regression of the component's distance to the core component with respect to the observation time is used.

C.1. Linear Regression

Two linearly connected physical variables x and y can be expressed by

$$y = a + bx, \quad (\text{C.1.1})$$

in which a and b are constant (Taylor 1988).

If measured values x_i and y_i did not have uncertainties, these measured points would all lie on the line given by Equation (C.1.1). However, in practice, there are uncertainties leading to the fact that these points deviate from this line (Taylor 1988). Assuming that the uncertainties of the x_i are negligibly small compared to the uncertainties of the y_i , then the deviation of each data point Δy_i is given by

$$\Delta y_i = y_i - y(x_i) = y_i - a - bx_i, \quad (\text{C.1.2})$$

which leads to

$$\chi^2 = \sum_{i=1}^N \left[\frac{y_i - y(x_i)}{\sigma_i} \right]^2 = \sum_{i=1}^N \left[\frac{y_i - a - bx_i}{\sigma_i} \right]^2, \quad (\text{C.1.3})$$

in which σ_i denotes the uncertainty of the corresponding y_i (Kießling 2013).

The following derivation is based on Kießling (2013). To calculate the values of a and b , the deviations Δy_i or rather the χ^2 -value must be minimized, leading to the following system of equations (C.1.4)

$$\begin{aligned} \frac{\partial}{\partial a} \chi^2 &= 0, \\ \frac{\partial}{\partial b} \chi^2 &= 0, \end{aligned}$$

$$\begin{aligned} \Rightarrow \sum_{i=1}^N \frac{y_i}{\sigma_i^2} &= a \sum_{i=1}^N \frac{1}{\sigma_i^2} + b \sum_{i=1}^N \frac{x_i}{\sigma_i^2}, \\ \sum_{i=1}^N \frac{x_i y_i}{\sigma_i^2} &= a \sum_{i=1}^N \frac{x_i}{\sigma_i^2} + b \sum_{i=1}^N \frac{x_i^2}{\sigma_i^2}. \end{aligned} \quad (\text{C.1.4})$$

Solving this system of equations (C.1.4) one obtains

$$a = \frac{1}{\Delta} \left(\sum_{i=1}^N \frac{y_i}{\sigma_i^2} \sum_{i=1}^N \frac{x_i^2}{\sigma_i^2} - \sum_{i=1}^N \frac{x_i}{\sigma_i^2} \sum_{i=1}^N \frac{x_i y_i}{\sigma_i^2} \right), \quad (\text{C.1.5})$$

$$b = \frac{1}{\Delta} \left(\sum_{i=1}^N \frac{1}{\sigma_i^2} \sum_{i=1}^N \frac{x_i y_i}{\sigma_i^2} - \sum_{i=1}^N \frac{x_i}{\sigma_i^2} \sum_{i=1}^N \frac{y_i}{\sigma_i^2} \right), \quad (\text{C.1.6})$$

$$\Delta = \sum_{i=1}^N \frac{1}{\sigma_i^2} \sum_{i=1}^N \frac{x_i^2}{\sigma_i^2} - \left(\sum_{i=1}^N \frac{x_i}{\sigma_i^2} \right)^2. \quad (\text{C.1.7})$$

If the y_i , or rather the σ_i , are statistically independent, the uncertainties σ_a and σ_b of a and b can be determined via the Gaussian law of error propagation

$$\sigma_z^2 = \sum_{k=1}^N \left[\sigma_k^2 \left(\frac{\partial z}{\partial y_k} \right)^2 \right], \quad (\text{C.1.8})$$

leading to

$$\sigma_a^2 = \frac{1}{\Delta} \sum_{i=1}^N \frac{x_i^2}{\sigma_i^2}, \quad (\text{C.1.9})$$

$$\sigma_b^2 = \frac{1}{\Delta} \sum_{i=1}^N \frac{1}{\sigma_i^2}, \quad (\text{C.1.10})$$

in which Δ is also given by Equation (C.1.7).

C.2. Ejection Time

In this thesis, the distance of the jet component to the core component y is linearly connected to the observation time t . Therefore, Equation (C.1.1) changes to

$$y = a + b(t - t_{\text{mid}}), \quad (\text{C.2.1})$$

in which $t_{\text{mid}} = (t_{\text{max}} + t_{\text{min}}) / 2$ is the mid point of observation.

After computing the constants a and b via linear regression, the ejection time t_0 can be calculated by setting $y = 0$, which leads to

$$t_0 = -\frac{a}{b} + t_{\text{mid}}, \quad (\text{C.2.2})$$

with the uncertainty σ_{t_0} , estimated with the Gaussian law of error propagation given by Equation (C.1.8), of

$$\sigma_{t_0}^2 = \sigma_a^2 \left(\frac{\partial t_0}{\partial a} \right)^2 + \sigma_b^2 \left(\frac{\partial t_0}{\partial b} \right)^2 = \left(\frac{\sigma_a}{b} \right)^2 + \left(\frac{a\sigma_b}{b^2} \right)^2. \quad (\text{C.2.3})$$

However, this uncertainty is overestimated because a and b are generally not independent of each other (Taylor 1988). They both depend on y_i and σ_i (see Equations (C.1.5) and (C.1.6)). Furthermore, the uncertainties σ_a and σ_b are not statistically independent, because they both depend on the uncertainties σ_i (see Equations (C.1.9) and (C.1.10)), and the Gaussian law of error propagation (Equation (C.1.8)) may only be used for statistically independent uncertainties. Therefore, the ejection time given by Equation (C.2.2) is expressed in terms of y_i and σ_i using the Equations (C.1.5) and (C.1.6)

$$t_0 = -\frac{\frac{1}{\Delta} \left(\sum_{i=1}^N \frac{y_i}{\sigma_i^2} \sum_{i=1}^N \frac{x_i^2}{\sigma_i^2} - \sum_{i=1}^N \frac{x_i}{\sigma_i^2} \sum_{i=1}^N \frac{x_i y_i}{\sigma_i^2} \right)}{\frac{1}{\Delta} \left(\sum_{i=1}^N \frac{1}{\sigma_i^2} \sum_{i=1}^N \frac{x_i y_i}{\sigma_i^2} - \sum_{i=1}^N \frac{x_i}{\sigma_i^2} \sum_{i=1}^N \frac{y_i}{\sigma_i^2} \right)} + t_{\text{mid}}, \quad (\text{C.2.4})$$

with $x_i = t_i - t_{\text{mid}}$. Now, Equation (C.2.4) only depends on statistically independent quantities and the Gaussian law of error propagation can be used to compute the uncertainty of the ejection time. With Equation (C.1.8) one obtains

$$\sigma_{t_0}^2 = \sum_{k=1}^N \left[\sigma_k^2 \left(\frac{\partial t_0}{\partial y_k} \right)^2 \right]. \quad (\text{C.2.5})$$

At first, the derivation $\frac{\partial t_0}{\partial y_k}$ is computed to be

$$\begin{aligned} \frac{\partial t_0}{\partial y_k} &= \frac{\partial t_0}{\partial a} \frac{\partial a}{\partial y_k} + \frac{\partial t_0}{\partial b} \frac{\partial b}{\partial y_k} \\ &= -\frac{1}{b} \frac{1}{\Delta} \left(\frac{1}{\sigma_k^2} \sum_{i=1}^N \frac{x_i^2}{\sigma_i^2} - \frac{x_k}{\sigma_k^2} \sum_{i=1}^N \frac{x_i}{\sigma_i^2} \right) + \frac{a}{b^2} \frac{1}{\Delta} \left(\frac{x_k}{\sigma_k^2} \sum_{i=1}^N \frac{1}{\sigma_i^2} - \frac{1}{\sigma_k^2} \sum_{i=1}^N \frac{x_i}{\sigma_i^2} \right). \end{aligned} \quad (\text{C.2.6})$$

Inserting Equation (C.2.6) into Equation (C.2.5) leads to

$$\begin{aligned}
 \sigma_{t_0}^2 &= \sum_{k=1}^N \left\{ \sigma_k^2 \left[-\frac{1}{b} \frac{1}{\Delta} \left(\frac{1}{\sigma_k^2} \sum_{i=1}^N \frac{x_i^2}{\sigma_i^2} - \frac{x_k}{\sigma_k^2} \sum_{i=1}^N \frac{x_i}{\sigma_i^2} \right) + \frac{a}{b^2} \frac{1}{\Delta} \left(\frac{x_k}{\sigma_k^2} \sum_{i=1}^N \frac{1}{\sigma_i^2} - \frac{1}{\sigma_k^2} \sum_{i=1}^N \frac{x_i}{\sigma_i^2} \right) \right]^2 \right\} \\
 &= \frac{1}{b^2} \frac{1}{\Delta^2} \left[\sum_{k=1}^N \frac{1}{\sigma_k^2} \left(\sum_{i=1}^N \frac{x_i^2}{\sigma_i^2} \right)^2 - 2 \sum_{k=1}^N \frac{x_k}{\sigma_k^2} \sum_{i=1}^N \frac{x_i^2}{\sigma_i^2} \sum_{i=1}^N \frac{x_i}{\sigma_i^2} + \sum_{k=1}^N \frac{x_k^2}{\sigma_k^2} \left(\sum_{i=1}^N \frac{x_i}{\sigma_i^2} \right)^2 \right] \\
 &\quad - 2 \frac{a}{b^3} \frac{1}{\Delta^2} \left[\sum_{k=1}^N \frac{x_k}{\sigma_k^2} \sum_{i=1}^N \frac{x_i^2}{\sigma_i^2} \sum_{i=1}^N \frac{1}{\sigma_i^2} - \sum_{k=1}^N \frac{1}{\sigma_k^2} \sum_{i=1}^N \frac{x_i^2}{\sigma_i^2} \sum_{i=1}^N \frac{x_i}{\sigma_i^2} \right] \\
 &\quad - 2 \frac{a}{b^3} \frac{1}{\Delta^2} \left[\sum_{k=1}^N \frac{x_k}{\sigma_k^2} \left(\sum_{i=1}^N \frac{x_i}{\sigma_i^2} \right)^2 - \sum_{k=1}^N \frac{x_k^2}{\sigma_k^2} \sum_{i=1}^N \frac{x_i}{\sigma_i^2} \sum_{i=1}^N \frac{1}{\sigma_i^2} \right] \\
 &\quad + \frac{a^2}{b^4} \frac{1}{\Delta^2} \left[\sum_{k=1}^N \frac{x_k^2}{\sigma_k^2} \left(\sum_{i=1}^N \frac{1}{\sigma_i^2} \right)^2 - 2 \sum_{k=1}^N \frac{x_k}{\sigma_k^2} \sum_{i=1}^N \frac{1}{\sigma_i^2} \sum_{i=1}^N \frac{x_i}{\sigma_i^2} + \sum_{k=1}^N \frac{1}{\sigma_k^2} \left(\sum_{i=1}^N \frac{x_i}{\sigma_i^2} \right)^2 \right].
 \end{aligned} \tag{C.2.7}$$

Since i and k both run from 1 to N , it is essential that

$$\sum_{i=1}^N \frac{x_i}{\sigma_i^2} = \sum_{k=1}^N \frac{x_k}{\sigma_k^2}, \quad \sum_{i=1}^N \frac{x_i^2}{\sigma_i^2} = \sum_{k=1}^N \frac{x_k^2}{\sigma_k^2}, \quad \sum_{i=1}^N \frac{1}{\sigma_i^2} = \sum_{k=1}^N \frac{1}{\sigma_k^2}.$$

Therefore, Equation (C.2.7) can be simplified to

$$\begin{aligned}
 \sigma_{t_0}^2 &= \frac{1}{b^2} \frac{1}{\Delta^2} \left[\sum_{k=1}^N \frac{1}{\sigma_k^2} \left(\sum_{i=1}^N \frac{x_i^2}{\sigma_i^2} \right)^2 - \sum_{k=1}^N \frac{x_k^2}{\sigma_k^2} \left(\sum_{i=1}^N \frac{x_i}{\sigma_i^2} \right)^2 \right] \\
 &\quad - 2 \frac{a}{b^3} \frac{1}{\Delta^2} \left[- \sum_{k=1}^N \frac{x_k^2}{\sigma_k^2} \sum_{i=1}^N \frac{x_i}{\sigma_i^2} \sum_{i=1}^N \frac{1}{\sigma_i^2} + \left(\sum_{i=1}^N \frac{x_i}{\sigma_i^2} \right)^3 \right] \\
 &\quad + \frac{a^2}{b^4} \frac{1}{\Delta^2} \left[\sum_{k=1}^N \frac{x_k^2}{\sigma_k^2} \left(\sum_{i=1}^N \frac{1}{\sigma_i^2} \right)^2 - \sum_{k=1}^N \frac{1}{\sigma_k^2} \left(\sum_{i=1}^N \frac{x_i}{\sigma_i^2} \right)^2 \right],
 \end{aligned} \tag{C.2.8}$$

in which one sum of the three terms in squared brackets can be factored out of each of

these three terms respectively, leading to

$$\begin{aligned}
 \sigma_{t_0}^2 &= \frac{1}{b^2} \frac{1}{\Delta^2} \sum_{i=1}^N \frac{x_i^2}{\sigma_i^2} \left[\sum_{k=1}^N \frac{1}{\sigma_k^2} \sum_{i=1}^N \frac{x_i^2}{\sigma_i^2} - \left(\sum_{i=1}^N \frac{x_i}{\sigma_i^2} \right)^2 \right] \\
 &\quad - 2 \frac{a}{b^3} \frac{1}{\Delta^2} \sum_{i=1}^N \frac{x_i}{\sigma_i^2} \left[- \sum_{k=1}^N \frac{x_k^2}{\sigma_k^2} \sum_{i=1}^N \frac{1}{\sigma_i^2} + \left(\sum_{i=1}^N \frac{x_i}{\sigma_i^2} \right)^2 \right] \\
 &\quad + \frac{a^2}{b^4} \frac{1}{\Delta^2} \sum_{i=1}^N \frac{1}{\sigma_i^2} \left[\sum_{k=1}^N \frac{x_k^2}{\sigma_k^2} \sum_{i=1}^N \frac{1}{\sigma_i^2} - \left(\sum_{i=1}^N \frac{x_i}{\sigma_i^2} \right)^2 \right].
 \end{aligned} \tag{C.2.9}$$

With Equation (C.1.7), one can see that the three terms in squared brackets in Equation (C.2.9) are equal to Δ or, in case of the second one, to $-\Delta$. As such, Equation (C.2.9) can further be simplified to

$$\sigma_{t_0}^2 = \frac{1}{b^2} \frac{1}{\Delta} \sum_{i=1}^N \frac{x_i^2}{\sigma_i^2} + 2 \frac{a}{b^3} \frac{1}{\Delta} \sum_{i=1}^N \frac{x_i}{\sigma_i^2} + \frac{a^2}{b^4} \frac{1}{\Delta} \sum_{i=1}^N \frac{1}{\sigma_i^2}. \tag{C.2.10}$$

Using Equations (C.1.9) and (C.1.10), Equation (C.2.10) can be written as

$$\begin{aligned}
 \sigma_{t_0}^2 &= \frac{\sigma_a^2}{b^2} + 2 \frac{a}{b^3} \frac{1}{\Delta} \sum_{i=1}^N \frac{x_i}{\sigma_i^2} + \frac{a^2 \sigma_b^2}{b^4} \\
 &= \left(\frac{\sigma_a}{b} \right)^2 + \left(\frac{a \sigma_b}{b^2} \right)^2 + 2 \frac{a}{b^3} \frac{1}{\Delta} \sum_{i=1}^N \frac{x_i}{\sigma_i^2}.
 \end{aligned} \tag{C.2.11}$$

One can see that Equation (C.2.11) is equal to Equation (C.2.3) plus an additional third term, that describes the correlation between a and b . Therefore, this third term will be investigated in the following passage.

Since here y_i denotes the distance of a jet component to the core component, only positive y -values are present. Furthermore, the y -axis ($x = 0$) is shifted to the midpoint of observation ($x = t - t_{\text{mid}}$) meaning that a must always be positive. Moreover, using a model in which the jet diameter D can be described by a power law $D \propto y^l$ (Kadler et al. 2004), the major axis of the different jet components should grow with increasing distance y . Since the uncertainties σ_i of the measured distances y_i are given by the semi major axis of the corresponding jet component, the uncertainties σ_i also rise with increasing distances y_i . Thus, if b is positive, the uncertainties σ_i increase with growing observation time, meaning that for $x_i < 0$ ($t_i < t_{\text{mid}}$), σ_i is less than for $x_i > 0$ ($t_i > t_{\text{mid}}$). Therefore, for $x_i < 0$, the absolute value of $\sum_{i=1}^N \frac{x_i}{\sigma_i^2}$ is greater than for $x_i > 0$, leading to the fact that the total sum $\sum_{i=1}^N \frac{x_i}{\sigma_i^2}$ must be negative. Otherwise, if b is negative, the

uncertainties σ_i decrease with growing observation time. Hence, for $x_i < 0$, σ_i is greater than for $x_i > 0$, meaning that for $x_i < 0$ the absolute value of $\sum_{i=1}^N \frac{x_i}{\sigma_i^2}$ is less than for $x_i > 0$ and the total sum $\sum_{i=1}^N \frac{x_i}{\sigma_i^2}$ must be positive. Summing up, the third term in Equation (C.2.11) must always be negative, because either b or $\sum_{i=1}^N \frac{x_i}{\sigma_i^2}$ must be negative, while all other quantities that are included in this third term are always positive. Hence, the third term of Equation (C.2.11) reduces the overestimated uncertainty calculated by Equation (C.2.3).

Therefore, the uncertainty σ_{t_0} of the ejection time t_0 is given by

$$\sigma_{t_0} = \sqrt{\left(\frac{\sigma_a}{b}\right)^2 + \left(\frac{a\sigma_b}{b^2}\right)^2 + 2\frac{a}{b^3} \frac{1}{\Delta} \sum_{i=1}^N \frac{x_i}{\sigma_i^2}}, \quad (\text{C.2.12})$$

in which $x_i = t_i - t_{\text{mid}}$ and Δ is given by Equation (C.1.7).

This formalism can also be used to calculate the uncertainty of the crossing time t , the point at which the line computed by linear regression passes through a line parallel to $y = 0$ at distance $y = \Delta r$. In this case, the crossing time t is given by

$$t = \frac{\Delta r - a}{b} + t_{\text{mid}}. \quad (\text{C.2.13})$$

Therefore, using the Gaussian law of error propagation, one obtains

$$\sigma_t^2 = \left(\frac{\partial t}{\partial \Delta r}\right)^2 \sigma_{\Delta r}^2 + \sum_{k=1}^N \left[\sigma_k^2 \left(\frac{\partial z}{\partial y_k}\right)^2 \right], \quad (\text{C.2.14})$$

which finally, using a similar calculation as for the uncertainty of the ejection time explained above, leads to the uncertainty σ_t of the crossing time t to be

$$\sigma_t = \sqrt{\left(\frac{\sigma_{\Delta r} + \sigma_a}{b}\right)^2 + \left(\frac{(a - \Delta r)\sigma_b}{b^2}\right)^2 + 2\frac{a - \Delta r}{b^3} \frac{1}{\Delta} \sum_{i=1}^N \frac{x_i}{\sigma_i^2}}, \quad (\text{C.2.15})$$

in which $x_i = t_i - t_{\text{mid}}$ and Δ is given by Equation (C.1.7).

D. Additional Tables

Table D.1.: Image parameters of the uniformly weighted 43 GHz VLBA observations.

Date YYYY-MM-DD (1)	Array (2)	S_{tot} [Jy] (3)	S_{peak} [Jy/beam] (4)	σ_{rms} [mJy/beam] (5)	b_{maj} [mas] (6)	b_{min} [mas] (7)	P.A. [deg] (8)
2009-04-02	BR, FD, HN, KP, LA, MK, NL, OV, PT, SC	3.76	2.38	1.50	0.338	0.145	-1.07
2009-05-30	BR, FD, HN, KP, LA, MK, NL, OV, PT, SC	4.03	2.71	2.26	0.343	0.153	-0.412
2009-07-26	BR, FD, HN, KP, LA, MK, NL, OV, SC	3.97	2.51	4.34	0.336	0.138	-1.85
2009-09-16	BR, FD, HN, KP, LA, MK, NL, OV, PT, SC	4.94	3.52	2.93	0.341	0.153	-3.03
2009-11-28	BR, FD, HN, KP, LA, NL, OV, PT, SC	4.85	3.26	1.17	0.524	0.188	24.7
2010-02-11	BR, FD, KP, LA, MK, NL, OV, PT, SC	3.76	2.43	2.62	0.319	0.136	2.04
2010-04-07	BR, FD, HN, KP, LA, NL, OV, PT, SC	4.38	2.88	3.14	0.467	0.195	19.0
2010-04-10	BR, FD, HN, KP, LA, MK, NL, OV, PT, SC	4.36	2.94	2.05	0.368	0.164	-6.83
2010-04-16	BR, FD, HN, KP, LA, MK, NL, OV, PT, SC	4.18	2.65	1.91	0.361	0.162	-4.52
2010-05-19	BR, FD, HN, KP, LA, MK, NL, OV, PT, SC	3.06	2.03	0.88	0.347	0.142	-5.37
2010-08-01	BR, FD, HN, KP, LA, MK, NL, OV, PT, SC	3.55	2.33	1.54	0.327	0.139	-1.64
2010-09-18	BR, FD, HN, KP, LA, MK, NL, OV, PT, SC	4.01	2.70	1.17	0.371	0.140	-8.4
2010-12-04	BR, FD, HN, KP, LA, MK, NL, OV, PT, SC	3.50	2.59	1.29	0.350	0.143	-2.78
2011-02-05	BR, FD, HN, KP, LA, MK, NL, OV, SC	3.54	2.74	1.19	0.370	0.147	-7.96
2011-04-21	BR, FD, HN, KP, LA, MK, OV, PT, SC	5.15	3.61	0.98	0.333	0.138	0.202
2011-06-12	BR, FD, HN, KP, LA, MK, NL, PT, SC	4.98	3.61	1.16	0.343	0.138	-5.09

Continued on next page.

Table D.1 – continued from previous page

Date YYYY-MM-DD (1)	Array (2)	S_{tot} [Jy] (3)	S_{peak} [Jy/beam] (4)	σ_{rms} [mJy/beam] (5)	b_{maj} [mas] (6)	b_{min} [mas] (7)	P.A. [deg] (8)
2011-08-23	BR, FD, HN, KP, LA, NL, OV, PT, SC	4.98	3.78	1.42	0.485	0.195	18.6
2011-10-16	BR, FD, HN, KP, LA, MK, NL, OV, PT, SC	5.28	3.89	2.38	0.343	0.152	-4.11
2012-01-27	BR, HN, KP, LA, MK, NL, OV, PT, SC	4.15	2.94	0.94	0.335	0.149	-7.09
2012-04-03	BR, FD, HN, KP, LA, MK, NL, OV, PT, SC	3.48	2.34	2.33	0.334	0.137	-1.75
2012-07-04	BR, FD, HN, KP, LA, MK, NL, OV, PT, SC	3.03	2.37	1.13	0.355	0.144	-7.29
2012-10-28	BR, FD, HN, KP, LA, MK, NL, OV, PT, SC	3.20	2.26	1.80	0.348	0.159	2.96
2013-01-15	BR, FD, HN, KP, LA, MK, NL, OV, PT, SC	2.27	1.60	1.54	0.361	0.165	2.63
2013-04-17	BR, FD, HN, KP, LA, MK, NL, OV, PT, SC	2.11	1.32	0.76	0.370	0.137	-3.81
2013-06-30	BR, HN, KP, LA, MK, NL, OV, PT, SC	1.59	1.11	0.50	0.333	0.147	-2.78
2013-08-26	BR, FD, HN, KP, LA, MK, NL, OV, PT, SC	2.46	1.77	1.30	0.319	0.134	-0.502
2013-12-16	BR, FD, KP, LA, MK, NL, OV, PT, SC	2.95	2.51	1.12	0.367	0.166	-6.32
2014-02-25	BR, HN, KP, LA, MK, NL, OV, PT, SC	4.07	3.46	2.05	0.367	0.141	-6.26
2014-07-28	BR, FD, HN, KP, LA, MK, NL, OV, PT, SC	4.54	3.48	2.03	0.314	0.139	0.0706
2014-11-15	BR, FD, HN, KP, LA, MK, NL, OV, PT, SC	4.56	3.54	1.82	0.351	0.149	-0.601
2014-12-29	BR, FD, HN, KP, LA, MK, NL, OV, PT, SC	5.29	4.00	3.06	0.367	0.154	-4.10
2015-04-12	BR, FD, HN, KP, LA, MK, NL, OV, PT, SC	6.35	3.82	0.96	0.325	0.143	1.31
2015-06-09	BR, FD, HN, KP, LA, MK, NL, OV, PT, SC	6.13	3.77	1.59	0.341	0.152	-0.303
2015-08-01	BR, FD, HN, KP, LA, MK, NL, OV, PT, SC	6.13	3.55	0.91	0.319	0.132	-2.48
2015-12-05	BR, FD, HN, KP, LA, MK, NL, OV, PT, SC	4.82	2.92	0.64	0.366	0.137	-7.63
2016-02-01	BR, FD, HN, KP, LA, MK, NL, OV, PT, SC	4.78	2.71	0.87	0.323	0.127	-7.57
2016-04-22	BR, FD, HN, KP, LA, MK, NL, OV, PT, SC	4.55	2.55	0.64	0.327	0.138	-0.611

Continued on next page.

Table D.1 – continued from previous page

Date YYYY-MM-DD (1)	Array (2)	S_{tot} [Jy] (3)	S_{peak} [Jy/beam] (4)	σ_{rms} [mJy/beam] (5)	b_{maj} [mas] (6)	b_{min} [mas] (7)	P.A. [deg] (8)
2016-07-04	BR, FD, HN, KP, LA, MK, NL, OV, PT, SC	4.71	2.72	0.58	0.328	0.141	-1.76
2016-09-05	BR, FD, HN, KP, LA, MK, NL, OV, PT, SC	5.99	3.94	1.06	0.347	0.158	-3.31
2016-10-23	BR, FD, HN, KP, LA, MK, NL, OV, PT, SC	5.28	3.46	0.90	0.338	0.148	3.49
2016-12-24	BR, FD, HN, KP, LA, MK, NL, OV, PT, SC	6.24	4.09	1.59	0.355	0.127	-3.70
2017-02-04	BR, FD, HN, KP, LA, MK, NL, OV, PT, SC	6.55	4.33	1.25	0.375	0.132	-6.12
2017-04-17	BR, FD, HN, KP, LA, MK, NL, OV, PT, SC	4.11	2.82	0.63	0.351	0.147	-4.84
2017-06-08	BR, FD, HN, KP, LA, MK, NL, OV, PT, SC	5.88	3.84	1.85	0.338	0.136	-2.27
2017-08-06	BR, FD, HN, KP, LA, MK, NL, OV, SC	4.48	2.90	0.93	0.329	0.128	-3.14
2017-11-07	FD, HN, KP, LA, MK, NL, OV, PT	4.46	3.34	0.87	1.13	0.131	-18.3
2018-02-17	BR, FD, HN, KP, LA, MK, NL, OV, PT	4.24	2.79	0.73	0.621	0.141	-19.3
2018-04-20	BR, FD, HN, KP, LA, MK, NL, OV, PT, SC	5.76	2.87	0.66	0.341	0.141	-4.12

Note: Col.(1): UTC observation date; Col.(2): Array configuration (BR: Brewster, FD: Fort Davis, HN: Hancock, KP: Kitt Peak, LA: Los Alamos, MK: Mauna Kea, NL: North Liberty, OV: Owens Valley, PT: Pie Town, SC: St. Croix); Col.(3): Total flux density; Col.(4): Highest flux density per beam; Col.(5): Noise level; Col.(6): FWHM of the major axis of the beam; Col.(7): FWHM of the minor axis of the beam; Col.(8): Position angle of the major axis of the beam with respect to the beam’s centroid (measured north through east).

D. Additional Tables

Table D.2.: Modelfit parameters of the fitted Gaussian jet components.

S [Jy] (1)	R [mas] (2)	Θ [deg] (3)	a_{maj} [mas] (4)	ratio (5)	P.A. [deg] (6)	T_{B} [K] (7)	ID (8)
2009-04-02:							
2.47	0.02	117.0	0.072	0.81	-27.9	$7.5 \cdot 10^{11}$	C
1.152	0.15	-56.4	0.108	1.00	-156.0	$1.24 \cdot 10^{11}$	S2
0.0810	1.53	-55.2	0.70	1.00	-148.9	$2.11 \cdot 10^8$	S1
2009-05-30:							
2.73	0.01	23.3	0.058	0.82	-37.9	$1.23 \cdot 10^{12}$	C
1.171	0.17	-55.5	0.089	1.00	-143.6	$1.86 \cdot 10^{11}$	S2
0.1291	1.46	-53.3	1.25	1.00	-137.0	$1.05 \cdot 10^8$	S1
2009-07-26:							
2.66	0.01	128.9	0.084	0.75	3.1	$6.3 \cdot 10^{11}$	C
1.136	0.15	-59.4	0.126	1.00	-137.7	$9.1 \cdot 10^{10}$	S2
0.1199	1.41	-53.3	1.23	1.00	-148.7	$1.01 \cdot 10^8$	S1
2009-09-16:							
3.52	0.02	116.4	0.064	0.62	-43.5	$1.75 \cdot 10^{12}$	C
1.045	0.12	-58.6	0.0351	1.00	-139.2	$1.07 \cdot 10^{12}$	S2
0.348	0.21	-60.7	0.086	1.00	-140.2	$6.0 \cdot 10^{10}$	J1
0.0537	1.48	-71.1	0.89	1.00	-149.4	$8.5 \cdot 10^7$	S1
2009-11-28:							
2.96	0.03	106.4	0.056	0.43	-50.1	$2.80 \cdot 10^{12}$	C
1.804	0.12	-61.1	0.080	1.00	-152.7	$3.6 \cdot 10^{11}$	S2
0.0779	1.56	-63.7	0.89	1.00	-143.6	$1.24 \cdot 10^8$	S1
2010-02-11:							
2.42	0.01	-158.2	0.057	0.59	-40.9	$1.59 \cdot 10^{12}$	C
1.338	0.15	-68.0	0.090	1.00	-136.7	$2.10 \cdot 10^{11}$	S2
0.1063	1.52	-69.3	1.23	1.00	-152.0	$8.8 \cdot 10^7$	S1
2010-04-07:							
2.25	0.02	112.1	0.112	0.28*	23.6	$8.0 \cdot 10^{11}$	C
1.972	0.12	-58.8	0.153	1.00	-142.8	$1.06 \cdot 10^{11}$	S2
0.1154	1.65	-65.2	0.68	1.00	-157.7	$3.13 \cdot 10^8$	S1
2010-04-10:							
2.85	0.01	-7.9	0.105	0.58	-13.4	$5.6 \cdot 10^{11}$	C
1.408	0.16	-58.2	0.098	1.00	-149.4	$1.83 \cdot 10^{11}$	S2
0.0408	0.51	-36.9	0.302	1.00	-155.5	$5.6 \cdot 10^8$	J1
0.1108	1.66	-64.0	0.59	1.00	-156.9	$4.0 \cdot 10^8$	S1
2010-04-16:							

Continued on next page.

Table D.2 – continued from previous page

S	R	Θ	a_{maj}	ratio	P.A.	T_{B}	ID
[Jy]	[mas]	[deg]	[mas]		[deg]	[K]	
(1)	(2)	(3)	(4)	(5)	(6)	(7)	(8)
2.45	0.04	141.5	0.091	0.63	-7.8	$5.9 \cdot 10^{11}$	C
1.537	0.12	-63.9	0.119	1.00	-153.8	$1.37 \cdot 10^{11}$	S2
0.1277	1.58	-62.3	0.78	1.00	-168.3	$2.64 \cdot 10^8$	S1
2010-05-19:							
2.01	0.00	129.9	0.073	0.69	-20.8	$7.0 \cdot 10^{11}$	C
0.889	0.15	-58.0	0.084	1.00	-143.5	$1.59 \cdot 10^{11}$	S2
0.0658	0.24	-71.0	0.106	1.00	-158.0	$7.3 \cdot 10^9$	J1/—
0.0213	0.60	-75.7	0.491	1.00	-155.6	$1.11 \cdot 10^8$	—/J1
0.0755	1.65	-65.4	0.466	1.00	-150.1	$4.4 \cdot 10^8$	S1
2010-08-01:							
2.32	0.00	-75.9	0.067	0.65	-17.4	$1.01 \cdot 10^{12}$	C
0.992	0.15	-59.0	0.055	1.00	-154.2	$4.1 \cdot 10^{11}$	S2
0.1196	0.23	-68.6	0.073	1.00	-155.9	$2.86 \cdot 10^{10}$	J1/—
0.0848	1.73	-67.2	0.474	1.00	-145.2	$4.8 \cdot 10^8$	S1
2010-09-18:							
2.61	0.09	-55.5	0.090	0.61	-11.3	$6.7 \cdot 10^{11}$	C
1.336	0.24	-55.0	0.117	1.00	-135.0	$1.24 \cdot 10^{11}$	S2
0.1010	1.87	-65.5	0.97	1.00	-161.9	$1.35 \cdot 10^8$	S1
2010-12-04:							
2.59	0.01	-167.3	0.070	0.51	-24.2	$1.31 \cdot 10^{12}$	C
0.687	0.14	-58.5	0.0454*	1.00	-154.2	$4.2 \cdot 10^{11}$	S2
0.1296	0.22	-65.6	0.078	1.00	-144.0	$2.69 \cdot 10^{10}$	J1/—
0.0831	1.79	-66.9	0.88	1.00	-162.8	$1.35 \cdot 10^8$	S1
2011-02-05:							
2.68	0.01	116.1	0.065	0.65	-38.0	$1.22 \cdot 10^{12}$	C
0.739	0.12	-56.0	0.0492	1.00	-142.9	$3.9 \cdot 10^{11}$	S2
0.0798	0.21	-68.7	0.065*	1.00	-146.3	$2.41 \cdot 10^{10}$	J1/—
0.0478	1.82	-66.0	0.52	1.00	-141.3	$2.23 \cdot 10^8$	S1
2011-04-21:							
3.57	0.01	124.8	0.069	0.65	-24.0	$1.46 \cdot 10^{12}$	C
1.486	0.13	-52.5	0.079	1.00	-141.5	$3.04 \cdot 10^{11}$	S2
0.1021	1.83	-66.5	0.82	1.00	-147.2	$1.93 \cdot 10^8$	S1
2011-06-12:							
3.52	0.02	133.3	0.052	0.96	-85.0	$1.74 \cdot 10^{12}$	C
1.363	0.12	-59.0	0.081	1.00	-144.3	$2.61 \cdot 10^{11}$	S2

Continued on next page.

Table D.2 – continued from previous page

S [Jy] (1)	R [mas] (2)	Θ [deg] (3)	a_{maj} [mas] (4)	ratio (5)	P.A. [deg] (6)	T_{B} [K] (7)	ID (8)
0.1064	1.82	-66.8	0.52	1.00	-146.0	$4.9 \cdot 10^8$	S1
2011-08-23:							
3.96	0.01	112.2	0.103	0.76	-17.9	$6.3 \cdot 10^{11}$	C
0.846	0.14	-52.6	0.079*	1.00	-135.6	$1.73 \cdot 10^{11}$	S2
0.0887	0.29	-108.8	0.204	1.00	-148.8	$2.69 \cdot 10^9$	J1/J2
0.1039	1.80	-64.5	0.68	1.00	-142.6	$2.89 \cdot 10^8$	S1
2011-10-16:							
3.57	0.00	105.5	0.0446	0.82	-33.2	$2.74 \cdot 10^{12}$	C
1.535	0.13	-57.1	0.067	1.00	-142.5	$4.3 \cdot 10^{11}$	S2
0.1125	1.96	-64.8	0.58	1.00	-156.5	$4.2 \cdot 10^8$	S1
2012-01-27:							
2.75	0.02	121.7	0.076	0.65	-5.2	$9.2 \cdot 10^{11}$	C
1.311	0.11	-59.3	0.093	1.00	-141.2	$1.94 \cdot 10^{11}$	S2
0.0960	1.92	-65.6	0.493	1.00	-150.4	$5.0 \cdot 10^8$	S1
2012-04-03:							
2.23	0.02	134.7	0.080	0.49	-13.6	$9.0 \cdot 10^{11}$	C
1.021	0.12	-54.5	0.097	1.00	-146.5	$1.37 \cdot 10^{11}$	S2
0.0504	0.31	-66.6	0.300	1.00	-142.6	$7.1 \cdot 10^8$	J1/J2
0.0866	1.86	-64.0	0.52	1.00	-141.5	$4.1 \cdot 10^8$	S1
2012-07-04:							
2.41	0.01	-17.7	0.083	0.35	-32.0	$1.25 \cdot 10^{12}$	C
0.473	0.15	-55.1	0.078	1.00	-145.0	$9.9 \cdot 10^{10}$	S2
0.0281	0.41	-64.9	0.173	1.00	-160.4	$1.19 \cdot 10^9$	J1/J2
0.0872	1.94	-63.9	0.53	1.00	-152.5	$3.9 \cdot 10^8$	S1
2012-10-28:							
2.04	0.04	151.2	0.112	0.23	-37.7	$9.1 \cdot 10^{11}$	C
0.994	0.07	-38.5	0.156	1.00	-144.5	$5.2 \cdot 10^{10}$	S2
0.0947	1.88	-66.3	0.51	1.00	-163.8	$4.6 \cdot 10^8$	S1
2013-01-15:							
1.344	0.03	104.2	0.052	0.69	22.5	$9.2 \cdot 10^{11}$	C
0.782	0.11	-39.3	0.065	1.00	-170.2	$2.34 \cdot 10^{11}$	S2
0.0234	0.23	-67.2	0.098	1.00	-159.9	$3.09 \cdot 10^9$	J1/J3
0.00888	0.71	-62.8	0.205*	1.00	-177.9	$2.66 \cdot 10^8$	—/J2
0.0633	1.93	-63.6	0.393	1.00	-154.1	$5.2 \cdot 10^8$	S1
2013-04-17:							

Continued on next page.

Table D.2 – continued from previous page

S [Jy] (1)	R [mas] (2)	Θ [deg] (3)	a_{maj} [mas] (4)	ratio (5)	P.A. [deg] (6)	T_{B} [K] (7)	ID (8)
1.180	0.03	128.7	0.0466	0.82	21.3	$8.4 \cdot 10^{11}$	C
0.769	0.13	-44.4	0.082	1.00	-140.7	$1.44 \cdot 10^{11}$	S2
0.0886	1.90	-68.3	1.03	1.00	-157.7	$1.06 \cdot 10^8$	S1
2013-06-30:							
1.088	0.01	-163.0	0.070	0.32	-22.6	$8.8 \cdot 10^{11}$	C
0.417	0.17	-52.3	0.096	1.00	-145.4	$5.8 \cdot 10^{10}$	S2
0.01807	0.43	-35.2	0.107*	1.00	-150.9	$2.01 \cdot 10^9$	J1/J3
0.0549	1.93	-66.5	0.50	1.00	-153.4	$2.78 \cdot 10^8$	S1
2013-08-26:							
1.921	0.01	144.5	0.115	0.29	-23.8	$6.2 \cdot 10^{11}$	C
0.478	0.18	-38.7	0.179	1.00	-143.6	$1.89 \cdot 10^{10}$	S2
0.0909	1.90	-68.4	0.62	1.00	-155.9	$2.97 \cdot 10^8$	S1
2013-12-16:							
2.55	0.01	96.6	0.065	0.46	70.1	$1.70 \cdot 10^{12}$	C
0.290	0.10	-72.2	0.101	1.00	-149.3	$3.6 \cdot 10^{10}$	S2
0.0288	0.36	-58.3	0.199	1.00	-148.8	$9.2 \cdot 10^8$	J1/J3
0.0756	1.92	-65.8	0.58	1.00	-152.2	$2.88 \cdot 10^8$	S1
2014-02-25:							
2.98	0.01	135.6	0.0343	0.63	-44.2	$5.1 \cdot 10^{12}$	C
1.021	0.09	-49.2	0.091	1.00	-145.9	$1.55 \cdot 10^{11}$	S2
0.0586	2.09	-61.8	0.446	1.00	-160.3	$3.7 \cdot 10^8$	S1
2014-07-28:							
3.14	0.01	132.2	0.080	0.46	-38.8	$1.30 \cdot 10^{12}$	C
1.256	0.06	-54.6	0.131	1.00	-139.2	$8.9 \cdot 10^{10}$	S2
0.0767	1.87	-64.8	0.477	1.00	-149.7	$4.1 \cdot 10^8$	S1
2014-11-15:							
4.51	0.00	-157.3	0.120	0.46	-71.8	$8.7 \cdot 10^{11}$	C
0.0547	1.99	-64.6	0.489	1.00	-149.8	$2.90 \cdot 10^8$	S1
2014-12-29:							
5.26	0.00	-105.4	0.137	0.29*	-77.1	$1.24 \cdot 10^{12}$	C
0.0547	1.98	-65.6	0.51	1.00	-164.1	$2.64 \cdot 10^8$	S1
2015-04-12:							
3.32	0.02	145.6	0.071	0.54	-43.6	$1.56 \cdot 10^{12}$	C
2.43	0.10	-77.0	0.055	1.00	-154.1	$1.01 \cdot 10^{12}$	S2
0.562	0.17	-95.5	0.088	1.00	-137.6	$9.1 \cdot 10^{10}$	J4

Continued on next page.

Table D.2 – continued from previous page

S [Jy] (1)	R [mas] (2)	Θ [deg] (3)	a_{maj} [mas] (4)	ratio (5)	P.A. [deg] (6)	T_{B} [K] (7)	ID (8)
0.0532	1.96	-63.9	0.74	1.00	-176.1	$1.24 \cdot 10^8$	S1
2015-06-09:							
3.39	0.04	114.1	0.066	0.41	-57.0	$2.38 \cdot 10^{12}$	C
2.40	0.09	-70.4	0.053	1.00	-142.5	$1.06 \cdot 10^{12}$	S2
0.316	0.21	-96.6	0.108	1.00	-144.0	$3.5 \cdot 10^{10}$	J4
2015-08-01:							
3.40	0.04	99.7	0.053	0.84	-69.3	$1.81 \cdot 10^{12}$	C
2.40	0.09	-70.4	0.071	1.00	-149.3	$6.1 \cdot 10^{11}$	S2
0.276	0.24	-96.2	0.201	1.00	-142.3	$8.7 \cdot 10^9$	J4
2015-12-05:							
2.28	0.05	104.7	0.102	0.43	-13.4	$6.5 \cdot 10^{11}$	C
2.32	0.06	-76.1	0.079	1.00	-144.9	$4.7 \cdot 10^{11}$	S2
0.219	0.31	-95.5	0.313	1.00	-144.2	$2.83 \cdot 10^9$	J4
0.0775	1.91	-75.4	2.21	1.00	-163.2	$2.00 \cdot 10^7$	S1
2016-02-01:							
1.920	0.09	134.7	0.109	0.24	-13.2	$8.5 \cdot 10^{11}$	C
2.62	0.05	-103.1	0.080	1.00	-144.9	$5.2 \cdot 10^{11}$	S2
0.1721	0.35	-98.7	0.216	1.00	-144.2	$4.7 \cdot 10^9$	J4
2016-04-22:							
2.02	0.07	123.0	0.114	0.30	-7.1	$6.6 \cdot 10^{11}$	C
2.34	0.07	-59.5	0.086	1.00	-144.9	$4.0 \cdot 10^{11}$	S2
0.1594	0.35	-104.8	0.418	1.00	-133.7	$1.15 \cdot 10^9$	J4
0.0286	1.48	-55.6	0.450	1.00	-169.7	$1.79 \cdot 10^8$	S1
2016-07-04:							
2.26	0.06	133.8	0.116	0.31	-11.3	$6.9 \cdot 10^{11}$	C
2.28	0.08	-63.4	0.101	1.00	-143.8	$2.81 \cdot 10^{11}$	S2
0.1497	0.45	-106.3	0.301	1.00	-147.7	$2.09 \cdot 10^9$	J4
2016-09-05:							
3.38	0.04	131.0	0.094	0.41	-15.2	$1.18 \cdot 10^{12}$	C
2.29	0.11	-51.7	0.105	1.00	-150.9	$2.63 \cdot 10^{11}$	S2
0.319	0.51	-100.2	0.222	1.00	-141.8	$8.2 \cdot 10^9$	J4
2016-10-23:							
3.22	0.03	134.4	0.093	0.39	-11.2	$1.21 \cdot 10^{12}$	C
1.696	0.11	-54.8	0.100	1.00	-139.0	$2.15 \cdot 10^{11}$	S2
0.332	0.56	-98.8	0.185	1.00	-150.3	$1.22 \cdot 10^{10}$	J4

Continued on next page.

Table D.2 – continued from previous page

S	R	Θ	a_{maj}	ratio	P.A.	T_{B}	ID
[Jy]	[mas]	[deg]	[mas]		[deg]	[K]	
(1)	(2)	(3)	(4)	(5)	(6)	(7)	(8)
2016-12-24:							
3.82	0.04	160.0	0.110	0.43	-18.6	$9.4 \cdot 10^{11}$	C
2.13	0.09	-60.4	0.102	1.00	-155.1	$2.62 \cdot 10^{11}$	S2
0.265	0.64	-98.0	0.176	1.00	-150.0	$1.08 \cdot 10^{10}$	J4
2017-02-04:							
3.75	0.05	143.3	0.110	0.41	-19.5	$9.7 \cdot 10^{11}$	C
2.31	0.07	-58.7	0.085	1.00	-153.7	$4.1 \cdot 10^{11}$	S2
0.1750	0.18	-70.1	0.161	1.00	-168.0	$8.6 \cdot 10^9$	J5
0.280	0.65	-98.2	0.181	1.00	-158.3	$1.08 \cdot 10^{10}$	J4
0.1009	1.23	-71.1	1.30	1.00	-163.9	$7.6 \cdot 10^7$	S1
2017-04-17:							
2.71	0.01	179.2	0.130	0.37	-27.2	$5.5 \cdot 10^{11}$	C
1.089	0.11	-56.7	0.084	1.00	-153.2	$1.94 \cdot 10^{11}$	S2
0.0625	0.30	-75.1	0.249	1.00	-154.7	$1.27 \cdot 10^9$	J5
0.251	0.75	-92.8	0.185	1.00	-157.8	$9.3 \cdot 10^9$	J4
0.0322	1.64	-67.6	0.85	1.00	-160.7	$5.7 \cdot 10^7$	S1
2017-06-08:							
4.09	0.05	162.8	0.137	0.39	-28.3	$7.0 \cdot 10^{11}$	C
1.158	0.08	-98.3	0.062	1.00	-153.9	$3.8 \cdot 10^{11}$	S2
0.1678	0.23	-89.3	0.236	1.00	-152.8	$3.8 \cdot 10^9$	J5
0.395	0.81	-95.4	0.167	1.00	-154.4	$1.79 \cdot 10^{10}$	J4
0.0645	1.50	-66.5	0.74	1.00	-144.5	$1.47 \cdot 10^8$	S1
2017-08-06:							
1.953	0.07	141.9	0.141	0.09	-31.5	$1.34 \cdot 10^{12}$	C
2.15	0.04	-56.9	0.086	1.00	-156.8	$3.7 \cdot 10^{11}$	S2
0.0836	0.27	-92.3	0.309	1.00	-155.3	$1.11 \cdot 10^9$	J5
0.280	0.85	-91.5	0.191	1.00	-158.3	$9.7 \cdot 10^9$	J4
2017-11-07:							
2.89	0.05	140.9	0.129	0.35	-43.4	$6.2 \cdot 10^{11}$	C
1.294	0.05	-94.3	0.080*	1.00	-148.0	$2.58 \cdot 10^{11}$	S2
0.0637	0.37	-84.4	0.372	1.00	-157.4	$5.8 \cdot 10^8$	J5
0.1934	0.91	-89.2	0.208*	1.00	-166.9	$5.6 \cdot 10^9$	J4
0.0480	1.51	-65.2	0.54	1.00	-149.2	$2.10 \cdot 10^8$	S1
2018-02-17:							
1.431	0.11	130.1	0.083	0.35	-34.3	$7.6 \cdot 10^{11}$	C

Continued on next page.

Table D.2 – continued from previous page

S	R	Θ	a_{maj}	ratio	P.A.	T_{B}	ID
[Jy]	[mas]	[deg]	[mas]		[deg]	[K]	
(1)	(2)	(3)	(4)	(5)	(6)	(7)	(8)
2.38	0.06	-51.9	0.078	1.00	-154.7	$5.0 \cdot 10^{11}$	S2
0.1888	0.27	-64.0	0.164	1.00	-155.4	$8.8 \cdot 10^9$	J5
0.1559	1.01	-83.7	0.185	1.00	-148.3	$5.8 \cdot 10^9$	J4
0.0812	1.51	-64.6	0.96	1.00	-166.6	$1.11 \cdot 10^8$	S1
2018-04-20:							
2.21	0.10	130.0	0.126	0.29	-16.9	$6.0 \cdot 10^{11}$	C
2.92	0.06	-54.0	0.081	1.00	-154.1	$5.7 \cdot 10^{11}$	S2
0.317	0.32	-79.6	0.135	1.00	-146.6	$2.19 \cdot 10^{10}$	J5
0.217	1.11	-79.8	0.253	1.00	-132.8	$4.3 \cdot 10^9$	J4
0.0504	1.60	-60.9	0.52	1.00	-145.7	$2.32 \cdot 10^8$	S1

Note: Col.(1): Flux density of the component; Col.(2): Angular distance of the component with respect to the designated phase center; Col.(3): Position angle of the component's centroid with respect to the designated phase center (measured north through east); Col.(4): FWHM of the major axis of the fitted Gaussian component; Col.(5): Ratio of the component's minor axis to major axis; Col.(6): Position angle of the component's major axis with respect to the centroid of the component (measured north through east); Col.(7): Brightness temperature of the component; Col.(8): Identification of the component, C denotes the core component, S denotes stationary jet features and J denotes moving jet features (if two IDs are given, the first one corresponds to kinematic model 1 and the second one corresponds to kinematic model 2). Values labeled with * were not resolved and therefore set to the given resolution limit. The brightness temperatures of these components are lower limits.

Table D.3.: 14-day binned γ -ray data, measured at 0.1 – 300 GeV with *Fermi*/LAT. Produced by Michael Kreter.

Time [MJD] (1)	σ_{Time} [days] (2)	S [$\text{cm}^{-2}\text{s}^{-1}$] (3)	σ_S [$\text{cm}^{-2}\text{s}^{-1}$] (4)
54689.6552778	7.0	$3.09402551627 \cdot 10^{-8}$	$2.52425220455 \cdot 10^{-8}$
54703.6552778	7.0	$1.17682191429 \cdot 10^{-8}$	$1.08411161491 \cdot 10^{-8}$
54717.6552778	7.0	$5.13336258524 \cdot 10^{-8}$	$1.89956504234 \cdot 10^{-8}$
54731.6552778	7.0	$4.93981109025 \cdot 10^{-9}$	$2.74331828562 \cdot 10^{-9}$
54745.6552778	7.0	$9.57162476493 \cdot 10^{-8}$	$3.14402920206 \cdot 10^{-8}$
54759.6552778	7.0	$7.54419842072 \cdot 10^{-8}$	$2.5857092201 \cdot 10^{-8}$
54773.6552778	7.0	$1.15722152719 \cdot 10^{-7}$	$2.76358110105 \cdot 10^{-8}$
54787.6552778	7.0	$1.30497486029 \cdot 10^{-7}$	$3.30720124366 \cdot 10^{-8}$
54801.6552778	7.0	$3.49935622256 \cdot 10^{-8}$	$2.39661420084 \cdot 10^{-8}$
54815.6552778	7.0	$1.44104216371 \cdot 10^{-7}$	$3.52100083752 \cdot 10^{-8}$
54829.6552778	7.0	$1.41935538327 \cdot 10^{-7}$	$2.57040183922 \cdot 10^{-8}$
54843.6552778	7.0	$1.2836382068 \cdot 10^{-7}$	$2.88981498054 \cdot 10^{-8}$
54857.6552778	7.0	$6.11640112505 \cdot 10^{-8}$	$3.12435808753 \cdot 10^{-8}$
54871.6552778	7.0	$3.46060824196 \cdot 10^{-8}$	$2.10800520522 \cdot 10^{-8}$
54885.6552778	7.0	$1.37610808999 \cdot 10^{-7}$	$5.4026645576 \cdot 10^{-8}$
54899.6552778	7.0	$6.82937813049 \cdot 10^{-8}$	$2.15598420489 \cdot 10^{-8}$
54913.6552778	7.0	$1.59566749327 \cdot 10^{-7}$	$3.21089062952 \cdot 10^{-8}$
54927.6552778	7.0	$7.68563124496 \cdot 10^{-8}$	$3.51473264402 \cdot 10^{-8}$
54941.6552778	7.0	$4.83686592457 \cdot 10^{-8}$	$1.58886080455 \cdot 10^{-8}$
54955.6552778	7.0	$2.46057197832 \cdot 10^{-8}$	$1.44749474306 \cdot 10^{-8}$
54969.6552778	7.0	$1.30846553568 \cdot 10^{-7}$	$2.98833198477 \cdot 10^{-8}$
54983.6552778	7.0	$2.33957372239 \cdot 10^{-7}$	$2.84879531644 \cdot 10^{-8}$
54997.6552778	7.0	$1.34630261285 \cdot 10^{-7}$	$3.18918218324 \cdot 10^{-8}$
55011.6552778	7.0	$1.34944762809 \cdot 10^{-7}$	$5.20180498233 \cdot 10^{-8}$
55025.6552778	7.0	$5.36609625648 \cdot 10^{-8}$	$2.48381509043 \cdot 10^{-8}$
55039.6552778	7.0	$2.78222064602 \cdot 10^{-8}$	$2.42871461734 \cdot 10^{-8}$
55053.6552778	7.0	$5.61545439422 \cdot 10^{-8}$	$2.30469411494 \cdot 10^{-8}$
55067.6552778	7.0	$3.74356580903 \cdot 10^{-8}$	$3.60448272626 \cdot 10^{-8}$
55081.6552778	7.0	$2.5210268637 \cdot 10^{-8}$	$2.69329790008 \cdot 10^{-8}$
55095.6552778	7.0	$6.25364098286 \cdot 10^{-8}$	$3.53471404305 \cdot 10^{-8}$
55109.6552778	7.0	$1.29789478786 \cdot 10^{-8}$	$4.28182374917 \cdot 10^{-9}$
55123.6552778	7.0	$9.52356805349 \cdot 10^{-9}$	0.0
55137.6552778	7.0	$1.42729861588 \cdot 10^{-9}$	$1.0529076758 \cdot 10^{-9}$
55151.6552778	7.0	$3.97452120906 \cdot 10^{-9}$	$6.00709436396 \cdot 10^{-9}$

Continued on next page.

Table D.3 – continued from previous page

Time [MJD] (1)	σ_{Time} [days] (2)	S [$\text{cm}^{-2}\text{s}^{-1}$] (3)	σ_S [$\text{cm}^{-2}\text{s}^{-1}$] (4)
55165.6552778	7.0	$2.0745662039 \cdot 10^{-8}$	$7.3932822395 \cdot 10^{-9}$
55179.6552778	7.0	$3.65371890504 \cdot 10^{-9}$	$2.16379226421 \cdot 10^{-9}$
55193.6552778	7.0	$3.80662501342 \cdot 10^{-8}$	$2.86593215791 \cdot 10^{-8}$
55207.6552778	7.0	$1.82911006231 \cdot 10^{-8}$	$1.32111927593 \cdot 10^{-8}$
55221.6552778	7.0	$1.23432220713 \cdot 10^{-8}$	$4.92433195212 \cdot 10^{-9}$
55235.6552778	7.0	$5.73630608987 \cdot 10^{-8}$	$4.65199510763 \cdot 10^{-8}$
55249.6552778	7.0	$4.52941472135 \cdot 10^{-9}$	$2.16451742871 \cdot 10^{-9}$
55263.6552778	7.0	$6.76449229132 \cdot 10^{-8}$	$3.54433800625 \cdot 10^{-8}$
55277.6552778	7.0	$1.75287147841 \cdot 10^{-7}$	$3.89742695606 \cdot 10^{-8}$
55291.6552778	7.0	$3.32659016768 \cdot 10^{-8}$	$1.20080817161 \cdot 10^{-8}$
55305.6552778	7.0	$1.02544739811 \cdot 10^{-7}$	$4.76033981324 \cdot 10^{-8}$
55319.6552778	7.0	$4.8080239622 \cdot 10^{-8}$	$2.6484107311 \cdot 10^{-8}$
55333.6552778	7.0	$5.81923281342 \cdot 10^{-8}$	$4.05247707813 \cdot 10^{-8}$
55347.6552778	7.0	$1.80062324299 \cdot 10^{-8}$	$1.51328541719 \cdot 10^{-8}$
55361.6552778	7.0	$1.27914738655 \cdot 10^{-7}$	$3.23476268513 \cdot 10^{-8}$
55375.6552778	7.0	$2.73052597152 \cdot 10^{-9}$	$3.23256385869 \cdot 10^{-9}$
55389.6552778	7.0	$4.72341329149 \cdot 10^{-8}$	0.0
55403.6552778	7.0	$1.12877641927 \cdot 10^{-8}$	0.0
55417.6552778	7.0	$1.22239617163 \cdot 10^{-7}$	$3.62589496073 \cdot 10^{-8}$
55431.6552778	7.0	$1.2916969147 \cdot 10^{-8}$	$1.48072752743 \cdot 10^{-8}$
55445.6552778	7.0	$6.55221830388 \cdot 10^{-8}$	$3.13843571393 \cdot 10^{-8}$
55459.6552778	7.0	$1.14699223187 \cdot 10^{-7}$	$4.21104376253 \cdot 10^{-8}$
55473.6552778	7.0	$1.2371287422 \cdot 10^{-7}$	$3.2459794308 \cdot 10^{-8}$
55487.6552778	7.0	$2.98822631371 \cdot 10^{-8}$	$3.88560526469 \cdot 10^{-8}$
55501.6552778	7.0	$1.08951999332 \cdot 10^{-7}$	$3.35179435891 \cdot 10^{-8}$
55515.6552778	7.0	$9.95719132617 \cdot 10^{-8}$	$3.33382414798 \cdot 10^{-8}$
55529.6552778	7.0	$1.08494495631 \cdot 10^{-7}$	$6.9472231696 \cdot 10^{-8}$
55543.6552778	7.0	$1.59824808919 \cdot 10^{-7}$	$3.74998064302 \cdot 10^{-8}$
55557.6552778	7.0	$1.23335218081 \cdot 10^{-7}$	$3.61781157656 \cdot 10^{-8}$
55571.6552778	7.0	$6.16132014371 \cdot 10^{-8}$	$2.71110774204 \cdot 10^{-8}$
55585.6552778	7.0	$8.4806349167 \cdot 10^{-8}$	$3.82115925045 \cdot 10^{-8}$
55599.6552778	7.0	$6.26873545307 \cdot 10^{-8}$	$3.84309230919 \cdot 10^{-8}$
55613.6552778	7.0	$1.13189740506 \cdot 10^{-7}$	$3.8387106388 \cdot 10^{-8}$
55627.6552778	7.0	$2.58804148145 \cdot 10^{-7}$	$3.96845586289 \cdot 10^{-8}$
55641.6552778	7.0	$2.87165830019 \cdot 10^{-7}$	$6.98913801782 \cdot 10^{-8}$

Continued on next page.

Table D.3 – continued from previous page

Time [MJD] (1)	σ_{Time} [days] (2)	S [$\text{cm}^{-2}\text{s}^{-1}$] (3)	σ_S [$\text{cm}^{-2}\text{s}^{-1}$] (4)
55655.6552778	7.0	$1.90298047596 \cdot 10^{-7}$	$5.65705927094 \cdot 10^{-8}$
55669.6552778	7.0	$1.24408996079 \cdot 10^{-7}$	$3.52529053037 \cdot 10^{-8}$
55683.6552778	7.0	$1.7369075845 \cdot 10^{-7}$	$3.76317732565 \cdot 10^{-8}$
55697.6552778	7.0	$3.01860097604 \cdot 10^{-7}$	$4.16615992476 \cdot 10^{-8}$
55711.6552778	7.0	$1.41332397165 \cdot 10^{-7}$	$3.79270603039 \cdot 10^{-8}$
55725.6552778	7.0	$2.72580793623 \cdot 10^{-7}$	$4.0423640562 \cdot 10^{-8}$
55739.6552778	7.0	$2.9153998863 \cdot 10^{-7}$	$4.85424993467 \cdot 10^{-8}$
55753.6552778	7.0	$1.60896117394 \cdot 10^{-7}$	$6.27576271345 \cdot 10^{-8}$
55767.6552778	7.0	$1.59986397553 \cdot 10^{-7}$	$4.86701841023 \cdot 10^{-8}$
55781.6552778	7.0	$2.25810785975 \cdot 10^{-7}$	$4.14816225196 \cdot 10^{-8}$
55795.6552778	7.0	$1.48642067425 \cdot 10^{-7}$	$3.41157457938 \cdot 10^{-8}$
55809.6552778	7.0	$1.98904821777 \cdot 10^{-7}$	$3.39526512221 \cdot 10^{-8}$
55823.6552778	7.0	$2.77502119493 \cdot 10^{-7}$	$4.24450031824 \cdot 10^{-8}$
55837.6552778	7.0	$2.40292675494 \cdot 10^{-7}$	$6.79332011583 \cdot 10^{-8}$
55851.6552778	7.0	$3.04520608803 \cdot 10^{-7}$	$3.88612578868 \cdot 10^{-8}$
55865.6552778	7.0	$1.44321292395 \cdot 10^{-7}$	$2.9461248839 \cdot 10^{-8}$
55879.6552778	7.0	$1.12810336614 \cdot 10^{-7}$	$3.60548488954 \cdot 10^{-8}$
55893.6552778	7.0	$6.91536951792 \cdot 10^{-8}$	$3.31406139916 \cdot 10^{-8}$
55907.6552778	7.0	$9.5629698314 \cdot 10^{-8}$	$3.05346534794 \cdot 10^{-8}$
55921.6552778	7.0	$5.0680622539 \cdot 10^{-8}$	$3.1222733639 \cdot 10^{-8}$
55935.6552778	7.0	$5.8429244147 \cdot 10^{-8}$	$3.91441615268 \cdot 10^{-8}$
55949.6552778	7.0	$4.63750092072 \cdot 10^{-8}$	$2.19048009061 \cdot 10^{-8}$
55963.6552778	7.0	$1.18098079228 \cdot 10^{-7}$	$3.15569637788 \cdot 10^{-8}$
55977.6552778	7.0	$4.03340762585 \cdot 10^{-8}$	$2.3904677747 \cdot 10^{-8}$
55991.6552778	7.0	$1.0245042096 \cdot 10^{-7}$	$4.28276513236 \cdot 10^{-8}$
56005.6552778	7.0	$2.47047742189 \cdot 10^{-8}$	$1.73918960196 \cdot 10^{-8}$
56019.6552778	7.0	$3.93115594086 \cdot 10^{-8}$	$2.69870325425 \cdot 10^{-8}$
56033.6552778	7.0	$7.72348052365 \cdot 10^{-8}$	$3.69277848895 \cdot 10^{-8}$
56047.6552778	7.0	$1.34731316437 \cdot 10^{-7}$	$3.39646874355 \cdot 10^{-8}$
56061.6552778	7.0	$1.27792909483 \cdot 10^{-7}$	$3.36690953982 \cdot 10^{-8}$
56075.6552778	7.0	$8.46911870274 \cdot 10^{-8}$	$4.53335317267 \cdot 10^{-8}$
56089.6552778	7.0	$4.21757792901 \cdot 10^{-8}$	$2.23660473281 \cdot 10^{-8}$
56103.6552778	7.0	$8.48157417591 \cdot 10^{-9}$	0.0
56117.6552778	7.0	$1.16317465649 \cdot 10^{-7}$	$6.66717794394 \cdot 10^{-8}$
56131.6552778	7.0	$4.3532886864 \cdot 10^{-8}$	0.0

Continued on next page.

Table D.3 – continued from previous page

Time [MJD] (1)	σ_{Time} [days] (2)	S [$\text{cm}^{-2}\text{s}^{-1}$] (3)	σ_S [$\text{cm}^{-2}\text{s}^{-1}$] (4)
56145.6552778	7.0	$4.9527755136 \cdot 10^{-8}$	$4.06925318192 \cdot 10^{-8}$
56159.6552778	7.0	$1.24854306429 \cdot 10^{-7}$	$4.93772563547 \cdot 10^{-8}$
56173.6552778	7.0	$9.66030840453 \cdot 10^{-8}$	$3.2180488783 \cdot 10^{-8}$
56187.6552778	7.0	$2.05489538997 \cdot 10^{-8}$	$1.34658671665 \cdot 10^{-8}$
56201.6552778	7.0	$2.06836667748 \cdot 10^{-8}$	0.0
56215.6552778	7.0	$7.97337741163 \cdot 10^{-8}$	$2.57354790499 \cdot 10^{-8}$
56229.6552778	7.0	$1.68932618217 \cdot 10^{-7}$	$5.40434393381 \cdot 10^{-8}$
56243.6552778	7.0	$4.66307780109 \cdot 10^{-8}$	$2.80500120048 \cdot 10^{-8}$
56257.6552778	7.0	$1.06885240599 \cdot 10^{-7}$	$3.00031800855 \cdot 10^{-8}$
56271.6552778	7.0	$3.61103909765 \cdot 10^{-8}$	$2.79127467166 \cdot 10^{-8}$
56285.6552778	7.0	$3.84808233074 \cdot 10^{-8}$	$2.12079240795 \cdot 10^{-8}$
56299.6552778	7.0	$2.5707158691 \cdot 10^{-8}$	$5.45992360232 \cdot 10^{-8}$
56313.6552778	7.0	$5.6258977535 \cdot 10^{-9}$	0.0
56327.6552778	7.0	$5.26716315946 \cdot 10^{-8}$	$2.65440327301 \cdot 10^{-8}$
56341.6552778	7.0	$1.42836335633 \cdot 10^{-8}$	0.0
56355.6552778	7.0	$5.62507295752 \cdot 10^{-9}$	$3.02946088474 \cdot 10^{-9}$
56369.6552778	7.0	$1.88761827885 \cdot 10^{-8}$	$1.8084788604 \cdot 10^{-8}$
56383.6552778	7.0	$6.50203258107 \cdot 10^{-9}$	$3.5845485081 \cdot 10^{-9}$
56397.6552778	7.0	$4.36744811805 \cdot 10^{-9}$	$2.71587704246 \cdot 10^{-9}$
56411.6552778	7.0	$3.00303564598 \cdot 10^{-9}$	0.0
56425.6552778	7.0	$1.19813030215 \cdot 10^{-9}$	$1.26329437986 \cdot 10^{-9}$
56439.6552778	7.0	$3.43373698595 \cdot 10^{-8}$	0.0
56453.6552778	7.0	$5.28049994775 \cdot 10^{-9}$	$3.1795876883 \cdot 10^{-9}$
56467.6552778	7.0	$2.64667655776 \cdot 10^{-9}$	0.0
56481.6552778	7.0	$1.01566324627 \cdot 10^{-8}$	0.0
56495.6552778	7.0	$8.36488516684 \cdot 10^{-9}$	0.0
56509.6552778	7.0	$1.19539927534 \cdot 10^{-8}$	$1.30432419191 \cdot 10^{-8}$
56523.6552778	7.0	$2.78816258406 \cdot 10^{-8}$	0.0
56537.6552778	7.0	$9.8018597458 \cdot 10^{-9}$	0.0
56551.6552778	7.0	$7.28271725787 \cdot 10^{-9}$	0.0
56565.6552778	7.0	$5.03928978068 \cdot 10^{-8}$	$2.7756536236 \cdot 10^{-8}$
56579.6552778	7.0	$7.62082283034 \cdot 10^{-9}$	0.0
56593.6552778	7.0	$4.04499713598 \cdot 10^{-8}$	$2.3790679469 \cdot 10^{-8}$
56607.6552778	7.0	$1.98035684272 \cdot 10^{-8}$	$9.25709175375 \cdot 10^{-9}$
56621.6552778	7.0	$3.87566811808 \cdot 10^{-8}$	$1.97755348523 \cdot 10^{-8}$

Continued on next page.

Table D.3 – continued from previous page

Time [MJD] (1)	σ_{Time} [days] (2)	S [$\text{cm}^{-2}\text{s}^{-1}$] (3)	σ_S [$\text{cm}^{-2}\text{s}^{-1}$] (4)
56635.6552778	7.0	$1.25358365507 \cdot 10^{-8}$	$9.83659325797 \cdot 10^{-9}$
56649.6552778	7.0	$9.40692636138 \cdot 10^{-8}$	$3.71834791969 \cdot 10^{-8}$
56663.6552778	7.0	$6.20511976825 \cdot 10^{-8}$	$4.4052632107 \cdot 10^{-8}$
56677.6552778	7.0	$1.35679966691 \cdot 10^{-7}$	$8.84865009804 \cdot 10^{-8}$
56691.6552778	7.0	$2.16464558956 \cdot 10^{-7}$	$6.16267054407 \cdot 10^{-8}$
56705.6552778	7.0	$2.32981872002 \cdot 10^{-7}$	$6.26714541862 \cdot 10^{-8}$
56719.6552778	7.0	$2.45321606487 \cdot 10^{-7}$	$6.20555501167 \cdot 10^{-8}$
56733.6552778	7.0	$1.30271122925 \cdot 10^{-7}$	$4.17845635479 \cdot 10^{-8}$
56747.6552778	7.0	$1.08894582455 \cdot 10^{-7}$	$2.31264986923 \cdot 10^{-8}$
56761.6552778	7.0	$5.82625868434 \cdot 10^{-8}$	$3.98130790408 \cdot 10^{-8}$
56775.6552778	7.0	$7.02751751532 \cdot 10^{-8}$	$2.75517854981 \cdot 10^{-8}$
56789.6552778	7.0	$1.09653255929 \cdot 10^{-7}$	$3.13023339274 \cdot 10^{-8}$
56803.6552778	7.0	$7.20815975073 \cdot 10^{-8}$	$3.01581232477 \cdot 10^{-8}$
56817.6552778	7.0	$5.71475451194 \cdot 10^{-8}$	0.0
56831.6552778	7.0	$2.66528968148 \cdot 10^{-8}$	$2.61737143462 \cdot 10^{-8}$
56845.6552778	7.0	$9.20172727618 \cdot 10^{-8}$	$3.19566886928 \cdot 10^{-8}$
56859.6552778	7.0	$1.01778318866 \cdot 10^{-7}$	$3.21766317338 \cdot 10^{-8}$
56873.6552778	7.0	$5.08219752495 \cdot 10^{-8}$	$3.72963156693 \cdot 10^{-8}$
56887.6552778	7.0	$8.15356254381 \cdot 10^{-8}$	0.0
56901.6552778	7.0	$2.35047361599 \cdot 10^{-8}$	$1.11720008309 \cdot 10^{-8}$
56915.6552778	7.0	$6.92864476891 \cdot 10^{-8}$	$3.59791125766 \cdot 10^{-8}$
56929.6552778	7.0	$1.07197466374 \cdot 10^{-7}$	$4.45930845822 \cdot 10^{-8}$
56943.6552778	7.0	$1.48481388731 \cdot 10^{-7}$	$4.96233373354 \cdot 10^{-8}$
56957.6552778	7.0	$1.02458447688 \cdot 10^{-7}$	$5.02039762885 \cdot 10^{-8}$
56971.6552778	7.0	$2.7042159193 \cdot 10^{-8}$	$1.7246453354 \cdot 10^{-8}$
56985.6552778	7.0	$2.19492950245 \cdot 10^{-8}$	$1.7687670522 \cdot 10^{-8}$
56999.6552778	7.0	$4.84631211134 \cdot 10^{-8}$	$5.28112200229 \cdot 10^{-8}$
57013.6552778	7.0	$1.19077344391 \cdot 10^{-7}$	$3.06967853239 \cdot 10^{-8}$
57027.6552778	7.0	$6.97700869978 \cdot 10^{-8}$	$2.58144542022 \cdot 10^{-8}$
57041.6552778	7.0	$5.37262176841 \cdot 10^{-8}$	$3.71185255317 \cdot 10^{-8}$
57055.6552778	7.0	$2.21918326895 \cdot 10^{-7}$	$3.91155602221 \cdot 10^{-8}$
57069.6552778	7.0	$2.41454665429 \cdot 10^{-7}$	$4.71927329588 \cdot 10^{-8}$
57083.6552778	7.0	$1.5160670017 \cdot 10^{-7}$	$4.79146963183 \cdot 10^{-8}$
57097.6552778	7.0	$9.69055628486 \cdot 10^{-8}$	$3.17003380813 \cdot 10^{-8}$
57111.6552778	7.0	$1.26663322334 \cdot 10^{-7}$	$4.15264487778 \cdot 10^{-8}$

Continued on next page.

Table D.3 – continued from previous page

Time [MJD] (1)	σ_{Time} [days] (2)	S [$\text{cm}^{-2}\text{s}^{-1}$] (3)	σ_S [$\text{cm}^{-2}\text{s}^{-1}$] (4)
57125.6552778	7.0	$1.18754128881 \cdot 10^{-7}$	$4.0852373129 \cdot 10^{-8}$
57139.6552778	7.0	$1.89629193913 \cdot 10^{-7}$	$3.87644853842 \cdot 10^{-8}$
57153.6552778	7.0	$7.24584922601 \cdot 10^{-8}$	$3.20633802687 \cdot 10^{-8}$
57167.6552778	7.0	$1.81374543597 \cdot 10^{-7}$	$3.96376025588 \cdot 10^{-8}$
57181.6552778	7.0	$9.93899931069 \cdot 10^{-8}$	$3.0630601321 \cdot 10^{-8}$
57195.6552778	7.0	$1.89949372616 \cdot 10^{-7}$	$2.78318616148 \cdot 10^{-8}$
57209.6552778	7.0	$5.62524182363 \cdot 10^{-8}$	$4.41296372956 \cdot 10^{-8}$
57223.6552778	7.0	$7.21691353984 \cdot 10^{-8}$	$3.60080108949 \cdot 10^{-8}$
57237.6552778	7.0	$1.06610784075 \cdot 10^{-7}$	$3.46956390031 \cdot 10^{-8}$
57251.6552778	7.0	$1.61855653418 \cdot 10^{-7}$	$3.64587201793 \cdot 10^{-8}$
57265.6552778	7.0	$8.19035983778 \cdot 10^{-8}$	$5.04990791012 \cdot 10^{-8}$
57279.6552778	7.0	$8.71063325413 \cdot 10^{-8}$	$2.93220564316 \cdot 10^{-8}$
57293.6552778	7.0	$3.47954766284 \cdot 10^{-8}$	$1.50314868009 \cdot 10^{-8}$
57307.6552778	7.0	$4.55900240012 \cdot 10^{-8}$	$2.27522508684 \cdot 10^{-8}$
57321.6552778	7.0	$5.01357323923 \cdot 10^{-8}$	$2.5685771176 \cdot 10^{-8}$
57335.6552778	7.0	$5.22931371018 \cdot 10^{-8}$	$2.21086428586 \cdot 10^{-8}$
57349.6552778	7.0	$8.67031344583 \cdot 10^{-8}$	$5.21092892962 \cdot 10^{-8}$
57363.6552778	7.0	$3.15329489748 \cdot 10^{-8}$	$3.61856420372 \cdot 10^{-8}$
57377.6552778	7.0	$6.51226580658 \cdot 10^{-9}$	$2.63605976237 \cdot 10^{-9}$
57391.6552778	7.0	$6.24114640923 \cdot 10^{-9}$	$2.92659099255 \cdot 10^{-9}$
57405.6552778	7.0	$2.95540157948 \cdot 10^{-8}$	$2.01476225788 \cdot 10^{-8}$
57419.6552778	7.0	$4.18169902089 \cdot 10^{-8}$	$2.94219690069 \cdot 10^{-8}$
57433.6552778	7.0	$1.30896092421 \cdot 10^{-7}$	$2.91520354707 \cdot 10^{-8}$
57447.6552778	7.0	$1.08955106373 \cdot 10^{-7}$	$3.5192608487 \cdot 10^{-8}$
57461.6552778	7.0	$3.692639618 \cdot 10^{-8}$	$5.25958611545 \cdot 10^{-8}$
57475.6552778	7.0	$9.78929535636 \cdot 10^{-8}$	$2.99122739369 \cdot 10^{-8}$
57489.6552778	7.0	$1.26135235956 \cdot 10^{-7}$	$2.96506829427 \cdot 10^{-8}$
57503.6552778	7.0	$1.09868870637 \cdot 10^{-7}$	$3.41896824671 \cdot 10^{-8}$
57517.6552778	7.0	$3.89616564586 \cdot 10^{-8}$	$1.12253615724 \cdot 10^{-8}$
57531.6552778	7.0	$1.28644652625 \cdot 10^{-7}$	$3.48078169757 \cdot 10^{-8}$
57545.6552778	7.0	$1.09544124937 \cdot 10^{-7}$	$2.94140688017 \cdot 10^{-8}$
57559.6552778	7.0	$1.63490458598 \cdot 10^{-7}$	$5.0448975343 \cdot 10^{-8}$
57573.6552778	7.0	$3.25724826704 \cdot 10^{-8}$	$2.14255803998 \cdot 10^{-8}$
57587.6552778	7.0	$1.48619351057 \cdot 10^{-7}$	$3.26573736931 \cdot 10^{-8}$
57601.6552778	7.0	$1.46792985927 \cdot 10^{-7}$	$3.78305586047 \cdot 10^{-8}$

Continued on next page.

Table D.3 – continued from previous page

Time [MJD] (1)	σ_{Time} [days] (2)	S [$\text{cm}^{-2}\text{s}^{-1}$] (3)	σ_S [$\text{cm}^{-2}\text{s}^{-1}$] (4)
57615.6552778	7.0	$8.07447118308 \cdot 10^{-8}$	$5.06126509022 \cdot 10^{-8}$
57629.6552778	7.0	$1.05712951119 \cdot 10^{-7}$	$5.57555272515 \cdot 10^{-8}$
57643.6552778	7.0	$7.3467412042 \cdot 10^{-8}$	$3.14470234869 \cdot 10^{-8}$
57657.6552778	7.0	$1.47672422568 \cdot 10^{-8}$	$1.93792047558 \cdot 10^{-8}$
57671.6552778	7.0	$6.78637753221 \cdot 10^{-8}$	0.0
57685.6552778	7.0	$8.18227133968 \cdot 10^{-8}$	$2.83423663034 \cdot 10^{-8}$
57699.6552778	7.0	$8.91481128683 \cdot 10^{-8}$	$2.86909219389 \cdot 10^{-8}$
57713.6552778	7.0	$7.16895361483 \cdot 10^{-8}$	$2.78289660378 \cdot 10^{-8}$
57727.6552778	7.0	$1.91571887719 \cdot 10^{-8}$	$2.2438742475 \cdot 10^{-8}$
57741.6552778	7.0	$1.10207005042 \cdot 10^{-8}$	$3.89001769141 \cdot 10^{-9}$
57755.6552778	7.0	$5.72363738996 \cdot 10^{-8}$	$3.76226562245 \cdot 10^{-8}$
57769.6552778	7.0	$5.76219076757 \cdot 10^{-8}$	$2.77454615443 \cdot 10^{-8}$
57783.6552778	7.0	$2.31483676295 \cdot 10^{-8}$	$2.38709811901 \cdot 10^{-8}$
57797.6552778	7.0	$3.62588603555 \cdot 10^{-8}$	$1.87602583524 \cdot 10^{-8}$
57811.6552778	7.0	$5.44856699548 \cdot 10^{-8}$	$2.4523163741 \cdot 10^{-8}$
57825.6552778	7.0	$5.73155665981 \cdot 10^{-8}$	$4.25824146932 \cdot 10^{-8}$
57839.6552778	7.0	$7.94942864732 \cdot 10^{-8}$	$3.73751358305 \cdot 10^{-8}$
57853.6552778	7.0	$7.76424196388 \cdot 10^{-8}$	$2.43072290731 \cdot 10^{-8}$
57867.6552778	7.0	$4.23278014382 \cdot 10^{-8}$	$3.6640784041 \cdot 10^{-8}$
57881.6552778	7.0	$5.18638310311 \cdot 10^{-8}$	$2.48220577878 \cdot 10^{-8}$
57895.6552778	7.0	$1.87900593214 \cdot 10^{-8}$	0.0
57909.6552778	7.0	$1.82352883397 \cdot 10^{-8}$	$2.57558492867 \cdot 10^{-8}$
57923.6552778	7.0	$6.73863935236 \cdot 10^{-9}$	$3.41256418122 \cdot 10^{-9}$
57937.6552778	7.0	$1.11824445367 \cdot 10^{-8}$	0.0
57951.6552778	7.0	$2.97266388553 \cdot 10^{-8}$	0.0
57965.6552778	7.0	$5.98095651724 \cdot 10^{-8}$	$6.03605355721 \cdot 10^{-8}$
57979.6552778	7.0	$5.48122458377 \cdot 10^{-8}$	$2.9969990263 \cdot 10^{-8}$
57993.6552778	7.0	$1.08439703621 \cdot 10^{-8}$	0.0
58007.6552778	7.0	$6.81032027316 \cdot 10^{-9}$	$3.82753047231 \cdot 10^{-9}$
58021.6552778	7.0	$2.26938622533 \cdot 10^{-8}$	$2.15144055322 \cdot 10^{-8}$
58035.6552778	7.0	$1.29712301443 \cdot 10^{-8}$	0.0
58049.6552778	7.0	$4.27890394696 \cdot 10^{-8}$	$3.1982921242 \cdot 10^{-8}$
58063.6552778	7.0	$4.62335031638 \cdot 10^{-8}$	$1.7428742924 \cdot 10^{-8}$
58077.6552778	7.0	$3.91357659008 \cdot 10^{-8}$	$2.02399855436 \cdot 10^{-8}$
58091.6552778	7.0	$1.3735496198 \cdot 10^{-8}$	0.0

Continued on next page.

Table D.3 – continued from previous page

Time [MJD] (1)	σ_{Time} [days] (2)	S [$\text{cm}^{-2}\text{s}^{-1}$] (3)	σ_S [$\text{cm}^{-2}\text{s}^{-1}$] (4)
58105.6552778	7.0	$2.93258429407 \cdot 10^{-8}$	$3.32642431991 \cdot 10^{-8}$
58119.6552778	7.0	$2.29555745725 \cdot 10^{-8}$	$1.90318874849 \cdot 10^{-8}$
58133.6552778	7.0	$9.1016481829 \cdot 10^{-8}$	$3.17135659739 \cdot 10^{-8}$
58147.6552778	7.0	$3.64104699541 \cdot 10^{-8}$	$2.05845126533 \cdot 10^{-8}$
58161.6552778	7.0	$4.79353919182 \cdot 10^{-8}$	$2.36835769291 \cdot 10^{-8}$
58175.6552778	7.0	$5.22455988361 \cdot 10^{-8}$	$2.51459312579 \cdot 10^{-8}$
58189.6552778	7.0	$7.38077720111 \cdot 10^{-8}$	$5.84782140048 \cdot 10^{-8}$
58203.6552778	7.0	$7.11077720111 \cdot 10^{-8}$	0.0
58217.6552778	7.0	$1.04515586248 \cdot 10^{-7}$	$4.56125639844 \cdot 10^{-8}$
58231.6552778	7.0	$1.37178809025 \cdot 10^{-7}$	$2.08617022384 \cdot 10^{-8}$
58245.6552778	7.0	$1.02186334909 \cdot 10^{-7}$	$3.91290034778 \cdot 10^{-8}$
58259.6552778	7.0	$4.04972910886 \cdot 10^{-8}$	$1.93301570295 \cdot 10^{-8}$
58273.6552778	7.0	$6.7121985619 \cdot 10^{-8}$	$2.35421055154 \cdot 10^{-8}$
58287.6552778	7.0	$4.65152893627 \cdot 10^{-8}$	$1.6227628692 \cdot 10^{-8}$
58301.6552778	7.0	$2.75862929034 \cdot 10^{-8}$	0.0
58315.6552778	7.0	$7.33011691444 \cdot 10^{-8}$	$3.3734683661 \cdot 10^{-8}$

Note: Col.(1): Midpoint of the individual data bin; Col.(2): Uncertainty of the midpoint given as half of the bin size; Col.(3): γ -ray flux within the individual data bin; Col.(4): Uncertainty of the γ -ray flux (if $\sigma_S = 0.0 \text{ cm}^{-2}\text{s}^{-1}$, the corresponding γ -ray fluxes are only upper limits).

Table D.4.: ALMA-band 3 data, downloaded from <https://almascience.eso.org/sc/> on 16.11.2018.

Date YYYY-MM-DD (1)	Time hh:mm:ss (2)	S [Jy] (3)	σ_S [Jy] (4)	ν [Hz] (5)
2018-11-10	00:00:00.0	4.17	0.07	$1.0349 \cdot 10^{11}$
2018-10-30	00:00:00.0	4.06	0.08	$1.0349 \cdot 10^{11}$
2018-10-30	00:00:00.0	4.21	0.09	$9.146 \cdot 10^{10}$
2018-10-22	00:00:00.0	4.11	0.08	$1.0349 \cdot 10^{11}$
2018-10-21	00:00:00.0	3.99	0.09	$1.0349 \cdot 10^{11}$
2018-10-21	00:00:00.0	4.37	0.09	$9.146 \cdot 10^{10}$
2018-10-16	00:00:00.0	3.97	0.06	$1.0349 \cdot 10^{11}$
2018-10-16	00:00:00.0	4.33	0.09	$9.146 \cdot 10^{10}$
2018-10-11	00:00:00.0	4.04	0.07	$1.0349 \cdot 10^{11}$
2018-09-27	00:00:00.0	4.1	0.1	$9.146 \cdot 10^{10}$
2018-09-20	00:00:00.0	3.8	0.07	$1.0349 \cdot 10^{11}$
2018-09-20	00:00:00.0	4.02	0.08	$9.146 \cdot 10^{10}$
2018-09-15	00:00:00.0	3.87	0.08	$1.0349 \cdot 10^{11}$
2018-09-15	00:00:00.0	4.15	0.1	$9.146 \cdot 10^{10}$
2018-09-11	00:00:00.0	3.69	0.18	$1.0349 \cdot 10^{11}$
2018-09-11	00:00:00.0	4.19	0.08	$9.146 \cdot 10^{10}$
2018-09-04	00:00:00.0	3.79	0.06	$1.0349 \cdot 10^{11}$
2018-09-04	00:00:00.0	4.01	0.11	$9.146 \cdot 10^{10}$
2018-09-04	00:00:00.0	3.74	0.07	$1.0349 \cdot 10^{11}$
2018-09-04	00:00:00.0	3.84	0.08	$9.146 \cdot 10^{10}$
2018-08-28	00:00:00.0	3.91	0.07	$1.0349 \cdot 10^{11}$
2018-08-11	00:00:00.0	3.78	0.03	$1.0349 \cdot 10^{11}$
2018-08-09	00:00:00.0	3.65	0.04	$1.0349 \cdot 10^{11}$
2018-08-09	00:00:00.0	3.84	0.04	$9.146 \cdot 10^{10}$
2018-08-08	00:00:00.0	3.67	0.03	$1.0349 \cdot 10^{11}$
2018-07-12	00:00:00.0	3.83	0.09	$1.0349 \cdot 10^{11}$
2018-07-12	00:00:00.0	4.15	0.1	$9.146 \cdot 10^{10}$
2018-07-05	00:00:00.0	4.31	0.08	$9.146 \cdot 10^{10}$
2018-06-21	00:00:00.0	3.87	0.07	$1.0349 \cdot 10^{11}$
2018-06-21	00:00:00.0	4.13	0.1	$9.146 \cdot 10^{10}$
2018-05-30	00:00:00.0	4.06	0.12	$9.146 \cdot 10^{10}$
2018-05-17	00:00:00.0	4.24	0.09	$9.146 \cdot 10^{10}$
2018-05-14	00:00:00.0	3.95	0.07	$1.0349 \cdot 10^{11}$
2018-05-14	00:00:00.0	4.21	0.09	$9.146 \cdot 10^{10}$

Continued on next page.

Table D.4 – continued from previous page

Date YYYY-MM-DD (1)	Time hh:mm:ss (2)	S [Jy] (3)	σ_S [Jy] (4)	ν [Hz] (5)
2018-05-08	00:00:00.0	3.92	0.07	$1.0349 \cdot 10^{11}$
2018-05-08	00:00:00.0	4.0	0.08	$9.146 \cdot 10^{10}$
2018-04-23	00:00:00.0	3.8	0.09	$1.0349 \cdot 10^{11}$
2018-04-23	00:00:00.0	4.12	0.08	$9.146 \cdot 10^{10}$
2018-04-11	00:00:00.0	3.78	0.08	$1.0349 \cdot 10^{11}$
2018-04-11	00:00:00.0	4.05	0.08	$9.146 \cdot 10^{10}$
2018-04-10	00:00:00.0	3.75	0.08	$1.0349 \cdot 10^{11}$
2018-04-02	00:00:00.0	3.74	0.08	$1.0349 \cdot 10^{11}$
2018-03-31	00:00:00.0	3.93	0.09	$9.146 \cdot 10^{10}$
2018-03-31	00:00:00.0	3.68	0.1	$1.0349 \cdot 10^{11}$
2018-03-31	00:00:00.0	3.87	0.08	$9.146 \cdot 10^{10}$
2018-03-21	00:00:00.0	3.6	0.09	$1.0349 \cdot 10^{11}$
2018-03-21	00:00:00.0	3.85	0.07	$9.146 \cdot 10^{10}$
2018-03-17	00:00:00.0	4.08	0.08	$9.146 \cdot 10^{10}$
2018-03-07	00:00:00.0	4.04	0.07	$9.146 \cdot 10^{10}$
2018-03-06	00:00:00.0	3.87	0.09	$1.0349 \cdot 10^{11}$
2018-03-06	00:00:00.0	4.04	0.08	$9.146 \cdot 10^{10}$
2018-01-23	00:00:00.0	4.09	0.08	$1.0349 \cdot 10^{11}$
2018-01-23	00:00:00.0	4.44	0.08	$9.146 \cdot 10^{10}$
2018-01-12	00:00:00.0	4.25	0.09	$1.0349 \cdot 10^{11}$
2018-01-12	00:00:00.0	4.6	0.09	$9.146 \cdot 10^{10}$
2018-01-01	00:00:00.0	4.2	0.07	$1.0349 \cdot 10^{11}$
2018-01-01	00:00:00.0	4.53	0.09	$9.146 \cdot 10^{10}$
2017-12-21	00:00:00.0	4.47	0.09	$9.146 \cdot 10^{10}$
2017-12-21	00:00:00.0	4.52	0.08	$9.146 \cdot 10^{10}$
2017-12-07	00:00:00.0	4.24	0.1	$1.0349 \cdot 10^{11}$
2017-12-07	00:00:00.0	4.59	0.09	$9.146 \cdot 10^{10}$
2017-11-25	00:00:00.0	4.59	0.08	$9.146 \cdot 10^{10}$
2017-11-14	00:00:00.0	4.74	0.15	$9.146 \cdot 10^{10}$
2017-11-14	00:00:00.0	4.83	0.1	$9.146 \cdot 10^{10}$
2017-11-07	00:00:00.0	4.4	0.17	$9.146 \cdot 10^{10}$
2017-11-01	00:00:00.0	4.21	0.09	$1.0349 \cdot 10^{11}$
2017-11-01	00:00:00.0	4.35	0.09	$9.146 \cdot 10^{10}$
2017-10-27	00:00:00.0	4.35	0.1	$1.0349 \cdot 10^{11}$
2017-10-27	00:00:00.0	4.69	0.11	$9.146 \cdot 10^{10}$

Continued on next page.

Table D.4 – continued from previous page

Date YYYY-MM-DD (1)	Time hh:mm:ss (2)	S [Jy] (3)	σ_S [Jy] (4)	ν [Hz] (5)
2017-10-21	00:00:00.0	3.88	0.09	$1.0349 \cdot 10^{11}$
2017-10-21	00:00:00.0	4.18	0.1	$9.146 \cdot 10^{10}$
2017-10-11	00:00:00.0	4.51	0.09	$9.146 \cdot 10^{10}$
2017-10-03	00:00:00.0	4.46	0.06	$9.146 \cdot 10^{10}$
2017-09-28	00:00:00.0	4.44	0.1	$9.146 \cdot 10^{10}$
2017-09-19	00:00:00.0	4.07	0.08	$1.0349 \cdot 10^{11}$
2017-09-19	00:00:00.0	4.34	0.1	$9.146 \cdot 10^{10}$
2017-09-17	00:00:00.0	4.48	0.14	$1.0349 \cdot 10^{11}$
2017-09-17	00:00:00.0	4.45	0.12	$9.146 \cdot 10^{10}$
2017-08-26	00:00:00.0	4.44	0.1	$1.0349 \cdot 10^{11}$
2017-08-26	00:00:00.0	4.71	0.09	$9.146 \cdot 10^{10}$
2017-08-16	00:00:00.0	4.74	0.12	$9.146 \cdot 10^{10}$
2017-08-03	00:00:00.0	4.66	0.1	$1.0349 \cdot 10^{11}$
2017-08-03	00:00:00.0	4.85	0.1	$9.146 \cdot 10^{10}$
2017-07-18	00:00:00.0	4.7	0.09	$9.146 \cdot 10^{10}$
2017-07-18	00:00:00.0	4.71	0.1	$1.0349 \cdot 10^{11}$
2017-07-18	00:00:00.0	4.76	0.08	$9.146 \cdot 10^{10}$
2017-07-02	00:00:00.0	5.02	0.1	$9.146 \cdot 10^{10}$
2017-07-02	00:00:00.0	4.74	0.07	$1.0349 \cdot 10^{11}$
2017-07-02	00:00:00.0	4.96	0.09	$9.146 \cdot 10^{10}$
2017-06-20	00:00:00.0	4.49	0.22	$1.0349 \cdot 10^{11}$
2017-06-20	00:00:00.0	4.53	0.2	$9.146 \cdot 10^{10}$
2017-05-15	00:00:00.0	4.75	0.19	$1.0349 \cdot 10^{11}$
2017-05-15	00:00:00.0	4.78	0.19	$9.146 \cdot 10^{10}$
2017-05-06	00:00:00.0	4.79	0.09	$1.0349 \cdot 10^{11}$
2017-05-06	00:00:00.0	4.83	0.1	$9.146 \cdot 10^{10}$
2017-05-05	00:00:00.0	4.83	0.1	$1.0349 \cdot 10^{11}$
2017-05-05	00:00:00.0	4.88	0.11	$9.146 \cdot 10^{10}$
2017-04-27	00:00:00.0	4.92	0.14	$1.0349 \cdot 10^{11}$
2017-04-27	00:00:00.0	4.85	0.15	$9.146 \cdot 10^{10}$
2017-04-22	00:00:00.0	4.83	0.13	$1.0349 \cdot 10^{11}$
2017-04-22	00:00:00.0	4.86	0.11	$9.146 \cdot 10^{10}$
2017-04-13	00:00:00.0	5.01	0.25	$1.0349 \cdot 10^{11}$
2017-04-13	00:00:00.0	5.03	0.23	$9.146 \cdot 10^{10}$
2017-04-01	00:00:00.0	4.95	0.07	$1.0349 \cdot 10^{11}$

Continued on next page.

Table D.4 – continued from previous page

Date YYYY-MM-DD (1)	Time hh:mm:ss (2)	S [Jy] (3)	σ_S [Jy] (4)	ν [Hz] (5)
2017-04-01	00:00:00.0	4.98	0.07	$9.146 \cdot 10^{10}$
2017-03-28	00:00:00.0	5.08	0.06	$1.0349 \cdot 10^{11}$
2017-03-28	00:00:00.0	5.02	0.09	$9.146 \cdot 10^{10}$
2017-03-27	00:00:00.0	5.04	0.24	$1.0349 \cdot 10^{11}$
2017-03-27	00:00:00.0	5.34	0.35	$9.146 \cdot 10^{10}$
2017-03-10	00:00:00.0	5.33	0.1	$1.0349 \cdot 10^{11}$
2017-03-10	00:00:00.0	5.39	0.07	$9.146 \cdot 10^{10}$
2017-01-28	00:00:00.0	5.32	0.06	$1.0349 \cdot 10^{11}$
2017-01-28	00:00:00.0	5.37	0.08	$9.146 \cdot 10^{10}$
2017-01-17	00:00:00.0	5.67	0.11	$1.0349 \cdot 10^{11}$
2017-01-17	00:00:00.0	5.66	0.09	$9.146 \cdot 10^{10}$
2017-01-17	00:00:00.0	5.57	0.22	$1.0349 \cdot 10^{11}$
2017-01-17	00:00:00.0	5.76	0.28	$9.146 \cdot 10^{10}$
2017-01-05	00:00:00.0	6.11	0.2	$1.0349 \cdot 10^{11}$
2017-01-05	00:00:00.0	6.05	0.2	$9.146 \cdot 10^{10}$
2017-01-03	00:00:00.0	6.1	0.12	$9.146 \cdot 10^{10}$
2016-12-23	00:00:00.0	6.114	0.306	$1.035 \cdot 10^{11}$
2016-12-23	00:00:00.0	6.534	0.327	$9.15 \cdot 10^{10}$
2016-12-21	00:00:00.0	6.57	0.07	$9.146 \cdot 10^{10}$
2016-12-10	00:00:00.0	6.065	0.303	$9.15 \cdot 10^{10}$
2016-12-10	00:00:00.0	6.12	0.06	$9.146 \cdot 10^{10}$
2016-12-03	00:00:00.0	5.98	0.12	$9.146 \cdot 10^{10}$
2016-11-22	00:00:00.0	5.85	0.26	$9.146 \cdot 10^{10}$
2016-11-10	00:00:00.0	5.46	0.06	$9.146 \cdot 10^{10}$
2016-11-01	00:00:00.0	5.62	0.1	$9.146 \cdot 10^{10}$
2016-10-18	00:00:00.0	5.76	0.11	$9.146 \cdot 10^{10}$
2016-10-13	00:00:00.0	5.76	0.1	$9.146 \cdot 10^{10}$
2016-10-06	00:00:00.0	6.14	0.12	$9.146 \cdot 10^{10}$
2016-09-15	00:00:00.0	5.29	0.12	$9.146 \cdot 10^{10}$
2016-09-07	00:00:00.0	5.37	0.08	$9.146 \cdot 10^{10}$
2016-09-03	00:00:00.0	5.4	0.19	$9.146 \cdot 10^{10}$
2016-08-30	00:00:00.0	5.35	0.19	$9.146 \cdot 10^{10}$
2016-08-11	00:00:00.0	4.58	0.14	$9.146 \cdot 10^{10}$
2016-08-04	00:00:00.0	4.53	0.08	$9.146 \cdot 10^{10}$
2016-07-23	00:00:00.0	4.83	0.18	$9.146 \cdot 10^{10}$

Continued on next page.

Table D.4 – continued from previous page

Date YYYY-MM-DD (1)	Time hh:mm:ss (2)	S [Jy] (3)	σ_S [Jy] (4)	ν [Hz] (5)
2016-07-21	00:00:00.0	4.69	0.23	$1.0349 \cdot 10^{11}$
2016-07-06	00:00:00.0	4.72	0.1	$9.146 \cdot 10^{10}$
2016-06-26	00:00:00.0	4.97	0.06	$1.0349 \cdot 10^{11}$
2016-06-26	00:00:00.0	4.96	0.06	$9.146 \cdot 10^{10}$
2016-06-11	00:00:00.0	4.78	0.15	$9.146 \cdot 10^{10}$
2016-06-09	00:00:00.0	4.87	0.08	$9.146 \cdot 10^{10}$
2016-05-24	00:00:00.0	4.6	0.2	$1.0349 \cdot 10^{11}$
2016-05-24	00:00:00.0	4.63	0.2	$9.146 \cdot 10^{10}$
2016-05-13	00:00:00.0	4.3	0.09	$1.0349 \cdot 10^{11}$
2016-05-13	00:00:00.0	4.32	0.09	$9.146 \cdot 10^{10}$
2016-04-30	00:00:00.0	4.17	0.18	$1.0349 \cdot 10^{11}$
2016-04-30	00:00:00.0	4.21	0.16	$9.146 \cdot 10^{10}$
2016-04-22	00:00:00.0	4.35	0.1	$1.0349 \cdot 10^{11}$
2016-04-22	00:00:00.0	4.39	0.1	$9.146 \cdot 10^{10}$
2016-04-14	00:00:00.0	4.08	0.13	$1.0349 \cdot 10^{11}$
2016-04-14	00:00:00.0	4.12	0.11	$9.146 \cdot 10^{10}$
2016-04-09	00:00:00.0	4.21	0.11	$1.0349 \cdot 10^{11}$
2016-04-09	00:00:00.0	4.27	0.1	$9.146 \cdot 10^{10}$
2016-04-07	00:00:00.0	4.29	0.2	$1.0349 \cdot 10^{11}$
2016-04-07	00:00:00.0	4.3	0.22	$9.146 \cdot 10^{10}$
2016-03-29	00:00:00.0	4.26	0.09	$1.0349 \cdot 10^{11}$
2016-03-29	00:00:00.0	4.32	0.09	$9.146 \cdot 10^{10}$
2016-03-27	00:00:00.0	4.55	0.23	$9.75 \cdot 10^{10}$
2016-03-15	00:00:00.0	4.32	0.15	$9.146 \cdot 10^{10}$
2016-03-15	00:00:00.0	4.29	0.15	$1.0349 \cdot 10^{11}$
2016-03-14	00:00:00.0	4.09	0.07	$1.0349 \cdot 10^{11}$
2016-03-14	00:00:00.0	4.2	0.07	$9.146 \cdot 10^{10}$
2016-03-02	00:00:00.0	4.03	0.2	$1.0349 \cdot 10^{11}$
2016-03-02	00:00:00.0	4.0	0.19	$9.146 \cdot 10^{10}$
2016-01-21	00:00:00.0	4.52	0.19	$9.146 \cdot 10^{10}$
2016-01-10	00:00:00.0	4.44	0.12	$9.146 \cdot 10^{10}$
2016-01-10	00:00:00.0	4.77	0.2	$9.146 \cdot 10^{10}$
2015-12-29	00:00:00.0	4.62	0.4389	$1.035 \cdot 10^{11}$
2015-12-29	00:00:00.0	4.79	0.45505	$9.15 \cdot 10^{10}$
2015-12-28	00:00:00.0	4.57	0.11	$1.0349 \cdot 10^{11}$

Continued on next page.

Table D.4 – continued from previous page

Date YYYY-MM-DD (1)	Time hh:mm:ss (2)	S [Jy] (3)	σ_S [Jy] (4)	ν [Hz] (5)
2015-12-08	00:00:00.0	5.3	0.3	$9.146 \cdot 10^{10}$
2015-12-06	00:00:00.0	4.51	0.14	$1.0349 \cdot 10^{11}$
2015-12-06	00:00:00.0	4.65	0.13	$9.146 \cdot 10^{10}$
2015-11-25	00:00:00.0	5.28	0.09	$9.146 \cdot 10^{10}$
2015-11-22	00:00:00.0	5.51	0.16	$9.146 \cdot 10^{10}$
2015-11-05	00:00:00.0	5.18	0.11	$1.0349 \cdot 10^{11}$
2015-11-05	00:00:00.0	5.25	0.1	$9.146 \cdot 10^{10}$
2015-11-01	00:00:00.0	5.75	0.12	$9.146 \cdot 10^{10}$
2015-09-27	00:00:00.0	5.58	0.08	$1.0349 \cdot 10^{11}$
2015-09-27	00:00:00.0	5.63	0.07	$9.146 \cdot 10^{10}$
2015-09-19	00:00:00.0	5.92	0.13	$1.0349 \cdot 10^{11}$
2015-09-19	00:00:00.0	5.97	0.12	$9.146 \cdot 10^{10}$
2015-09-05	00:00:00.0	6.5	0.2	$9.146 \cdot 10^{10}$
2015-08-30	00:00:00.0	6.53	0.28	$1.0349 \cdot 10^{11}$
2015-08-15	00:00:00.0	6.55	0.09	$1.0349 \cdot 10^{11}$
2015-08-15	00:00:00.0	6.73	0.09	$9.146 \cdot 10^{10}$
2015-07-26	00:00:00.0	6.09	0.12	$1.0349 \cdot 10^{11}$
2015-07-18	00:00:00.0	6.04	0.14	$1.0349 \cdot 10^{11}$
2015-07-18	00:00:00.0	6.06	0.13	$9.146 \cdot 10^{10}$
2015-07-04	00:00:00.0	5.92	0.29	$1.0349 \cdot 10^{11}$
2015-06-28	00:00:00.0	5.85	0.16	$1.0349 \cdot 10^{11}$
2015-06-15	00:00:00.0	6.34	0.1	$9.146 \cdot 10^{10}$
2015-06-02	00:00:00.0	6.11	0.11	$1.0349 \cdot 10^{11}$
2015-06-02	00:00:00.0	6.3	0.1	$9.146 \cdot 10^{10}$
2015-05-14	00:00:00.0	5.7	0.14	$1.0349 \cdot 10^{11}$
2015-04-22	00:00:00.0	5.95	0.21	$1.0349 \cdot 10^{11}$
2015-04-22	00:00:00.0	5.85	0.24	$9.146 \cdot 10^{10}$
2015-04-03	00:00:00.0	5.9	0.23	$1.0349 \cdot 10^{11}$
2015-04-03	00:00:00.0	5.9	0.2	$9.146 \cdot 10^{10}$
2015-01-30	00:00:00.0	4.82	0.14	$1.0349 \cdot 10^{11}$
2015-01-30	00:00:00.0	4.81	0.11	$9.146 \cdot 10^{10}$
2015-01-30	00:00:00.0	4.72	0.16	$1.0349 \cdot 10^{11}$
2015-01-30	00:00:00.0	4.74	0.14	$9.146 \cdot 10^{10}$
2015-01-29	00:00:00.0	4.94	0.21	$9.146 \cdot 10^{10}$
2015-01-24	00:00:00.0	4.94	0.1	$9.146 \cdot 10^{10}$

Continued on next page.

Table D.4 – continued from previous page

Date YYYY-MM-DD (1)	Time hh:mm:ss (2)	S [Jy] (3)	σ_S [Jy] (4)	ν [Hz] (5)
2014-12-29	00:00:00.0	4.64	0.16	$9.146 \cdot 10^{10}$
2014-12-18	00:00:00.0	4.37	0.23	$1.0349 \cdot 10^{11}$
2014-12-18	00:00:00.0	4.4	0.17	$9.146 \cdot 10^{10}$
2014-12-10	00:00:00.0	4.43	0.07	$1.0349 \cdot 10^{11}$
2014-12-10	00:00:00.0	4.37	0.06	$9.146 \cdot 10^{10}$
2014-12-01	00:00:00.0	4.16	0.13	$1.0349 \cdot 10^{11}$
2014-12-01	00:00:00.0	4.18	0.1	$9.146 \cdot 10^{10}$
2014-12-01	00:00:00.0	4.16	0.11	$1.0349 \cdot 10^{11}$
2014-12-01	00:00:00.0	4.18	0.11	$9.146 \cdot 10^{10}$
2014-11-30	00:00:00.0	4.25	0.2	$1.0349 \cdot 10^{11}$
2014-11-30	00:00:00.0	4.27	0.17	$9.146 \cdot 10^{10}$
2014-08-16	00:00:00.0	4.01	0.06	$1.0349 \cdot 10^{11}$
2014-08-16	00:00:00.0	4.12	0.08	$9.146 \cdot 10^{10}$
2014-07-19	00:00:00.0	4.01	0.17	$1.0349 \cdot 10^{11}$
2014-07-19	00:00:00.0	3.85	0.16	$9.146 \cdot 10^{10}$
2014-06-29	00:00:00.0	3.83	0.07	$1.0349 \cdot 10^{11}$
2014-06-29	00:00:00.0	3.86	0.06	$9.146 \cdot 10^{10}$
2014-06-08	00:00:00.0	4.22	0.12	$1.0349 \cdot 10^{11}$
2014-05-28	00:00:00.0	3.95	0.11	$1.0349 \cdot 10^{11}$
2014-05-28	00:00:00.0	3.99	0.12	$9.146 \cdot 10^{10}$
2014-05-15	00:00:00.0	3.98	0.15	$1.0349 \cdot 10^{11}$
2014-05-15	00:00:00.0	4.01	0.13	$9.146 \cdot 10^{10}$
2014-04-30	00:00:00.0	3.5	0.04	$1.0349 \cdot 10^{11}$
2014-04-30	00:00:00.0	3.55	0.04	$9.146 \cdot 10^{10}$
2014-04-26	00:00:00.0	3.54	0.03	$1.0349 \cdot 10^{11}$
2014-04-26	00:00:00.0	3.59	0.03	$9.146 \cdot 10^{10}$
2014-04-03	00:00:00.0	4.43	0.13	$1.0349 \cdot 10^{11}$
2014-04-03	00:00:00.0	4.41	0.13	$9.146 \cdot 10^{10}$
2014-03-23	00:00:00.0	5.2425	0.2	$9.161 \cdot 10^{10}$
2014-03-20	00:00:00.0	4.8	0.12	$1.0349 \cdot 10^{11}$
2014-03-20	00:00:00.0	4.77	0.15	$9.146 \cdot 10^{10}$
2014-03-07	00:00:00.0	4.43	0.09	$1.0349 \cdot 10^{11}$
2014-03-07	00:00:00.0	4.36	0.1	$9.146 \cdot 10^{10}$
2014-02-03	00:00:00.0	3.02	0.08	$1.0349 \cdot 10^{11}$
2014-02-03	00:00:00.0	2.95	0.07	$9.146 \cdot 10^{10}$

Continued on next page.

Table D.4 – continued from previous page

Date YYYY-MM-DD (1)	Time hh:mm:ss (2)	S [Jy] (3)	σ_S [Jy] (4)	ν [Hz] (5)
2014-01-10	00:00:00.0	2.9	0.07	$1.0349 \cdot 10^{11}$
2014-01-10	00:00:00.0	2.92	0.06	$9.146 \cdot 10^{10}$
2013-12-29	00:00:00.0	2.73	0.1	$1.0349 \cdot 10^{11}$
2013-12-29	00:00:00.0	2.97	0.09	$9.146 \cdot 10^{10}$
2013-12-21	00:00:00.0	2.725	0.082	$1.0349 \cdot 10^{11}$
2013-12-21	00:00:00.0	2.986	0.09	$9.146 \cdot 10^{10}$
2013-12-11	00:00:00.0	2.66	0.11	$1.0349 \cdot 10^{11}$
2013-12-11	00:00:00.0	2.87	0.1	$9.146 \cdot 10^{10}$
2013-11-28	00:00:00.0	2.34	0.07	$1.0349 \cdot 10^{11}$
2013-11-28	00:00:00.0	2.38	0.06	$9.146 \cdot 10^{10}$
2013-11-14	00:00:00.0	2.17	0.08	$1.0349 \cdot 10^{11}$
2013-11-14	00:00:00.0	2.24	0.04	$9.146 \cdot 10^{10}$
2013-10-26	00:00:00.0	2.27	0.07	$1.0349 \cdot 10^{11}$
2013-10-26	00:00:00.0	2.35	0.05	$9.146 \cdot 10^{10}$
2013-10-06	00:00:00.0	1.93	0.08	$1.0349 \cdot 10^{11}$
2013-10-06	00:00:00.0	1.96	0.1	$9.146 \cdot 10^{10}$
2013-07-05	00:00:00.0	1.63	0.07	$1.0974 \cdot 10^{11}$
2013-07-05	00:00:00.0	1.68	0.06	$9.821 \cdot 10^{10}$
2013-04-22	00:00:00.0	1.7	0.04	$1.0974 \cdot 10^{11}$
2013-04-22	00:00:00.0	1.74	0.03	$9.821 \cdot 10^{10}$
2012-12-17	00:00:00.0	2.18	0.07	$1.0974 \cdot 10^{11}$
2012-12-17	00:00:00.0	2.24	0.06	$9.821 \cdot 10^{10}$
2012-12-03	00:00:00.0	2.24	0.05	$1.0974 \cdot 10^{11}$
2012-11-21	00:00:00.0	2.35	0.06	$1.0974 \cdot 10^{11}$
2012-11-21	00:00:00.0	2.54	0.05	$9.821 \cdot 10^{10}$
2012-11-15	00:00:00.0	2.5	0.05	$1.0974 \cdot 10^{11}$
2012-11-15	00:00:00.0	2.68	0.03	$9.821 \cdot 10^{10}$
2012-10-06	00:00:00.0	2.42	0.12	$1.0876 \cdot 10^{11}$
2012-10-06	00:00:00.0	2.59	0.13	$9.92 \cdot 10^{10}$

Note: Col.(1): UTC observation date; Col.(2): UTC observation time; Col.(3): Flux density; Col.(4): Uncertainty of the flux density; Col.(5): Observation frequency.

Table D.5.: ALMA-band 6 data, downloaded from <https://almascience.eso.org/sc/> on 16.11.2018.

Date YYYY-MM-DD (1)	Time hh:mm:ss (2)	S [Jy] (3)	σ_S [Jy] (4)	ν [Hz] (5)
2018-01-18	00:00:00.0	2.88	0.08	$2.33 \cdot 10^{11}$
2018-01-06	00:00:00.0	2.84	0.09	$2.33 \cdot 10^{11}$
2018-01-04	00:00:00.0	2.86	0.08	$2.33 \cdot 10^{11}$
2017-10-30	00:00:00.0	2.68	0.08	$2.33 \cdot 10^{11}$
2017-06-20	00:00:00.0	3.45	0.11	$2.33 \cdot 10^{11}$
2017-05-05	00:00:00.0	3.4	0.14	$2.33 \cdot 10^{11}$
2017-03-22	00:00:00.0	3.61	0.27	$2.33 \cdot 10^{11}$
2017-01-07	00:00:00.0	4.07	0.16	$2.33 \cdot 10^{11}$
2017-01-05	00:00:00.0	3.99	0.11	$2.33 \cdot 10^{11}$
2016-12-23	00:00:00.0	4.358	0.218	$2.33 \cdot 10^{11}$
2016-05-15	00:00:00.0	2.73	0.09	$2.33 \cdot 10^{11}$
2016-03-27	00:00:00.0	3.12	0.16	$2.33 \cdot 10^{11}$
2016-01-22	00:00:00.0	2.58	0.08	$2.33 \cdot 10^{11}$
2016-01-11	00:00:00.0	2.54	0.2	$2.33 \cdot 10^{11}$
2015-12-28	00:00:00.0	2.89	0.06	$2.33 \cdot 10^{11}$
2015-11-25	00:00:00.0	3.02	0.1	$2.33 \cdot 10^{11}$
2015-11-17	00:00:00.0	3.42	0.07	$2.33 \cdot 10^{11}$
2015-11-15	00:00:00.0	3.41	0.24	$2.33 \cdot 10^{11}$
2015-10-15	00:00:00.0	4.04	0.27	$2.33 \cdot 10^{11}$
2015-05-24	00:00:00.0	4.12	0.27	$2.33 \cdot 10^{11}$
2015-01-18	00:00:00.0	3.23	0.1	$2.33 \cdot 10^{11}$
2014-12-01	00:00:00.0	2.96	0.13	$2.33 \cdot 10^{11}$
2014-07-26	00:00:00.0	2.64	0.09	$2.33 \cdot 10^{11}$
2014-06-11	00:00:00.0	2.315	0.185	$2.27523 \cdot 10^{11}$
2014-05-03	00:00:00.0	2.72	0.06	$2.33 \cdot 10^{11}$
2014-04-28	00:00:00.0	2.54	0.06	$2.33 \cdot 10^{11}$
2014-03-09	00:00:00.0	2.938	0.206	$2.3521 \cdot 10^{11}$
2014-03-09	00:00:00.0	3.25	0.15	$2.33 \cdot 10^{11}$
2013-12-21	00:00:00.0	1.815	0.113	$2.33 \cdot 10^{11}$
2012-10-06	00:00:00.0	1.58	0.08	$2.21 \cdot 10^{11}$

Note: Col.(1): UTC observation date; Col.(2): UTC observation time; Col.(3): Flux density; Col.(4): Uncertainty of the flux density; Col.(5): Observation frequency.

D. Additional Tables

Table D.6.: ALMA-band 7 data, downloaded from <https://almascience.eso.org/sc/> on 16.11.2018.

Date YYYY-MM-DD (1)	Time hh:mm:ss (2)	S [Jy] (3)	σ_S [Jy] (4)	ν [Hz] (5)
2018-11-09	00:00:00.0	2.21	0.06	$3.4348 \cdot 10^{11}$
2018-10-30	00:00:00.0	2.12	0.06	$3.4348 \cdot 10^{11}$
2018-10-21	00:00:00.0	2.13	0.06	$3.4348 \cdot 10^{11}$
2018-10-10	00:00:00.0	2.11	0.05	$3.4348 \cdot 10^{11}$
2018-10-02	00:00:00.0	2.15	0.05	$3.4348 \cdot 10^{11}$
2018-09-15	00:00:00.0	2.07	0.07	$3.4348 \cdot 10^{11}$
2018-09-06	00:00:00.0	1.79	0.05	$3.4348 \cdot 10^{11}$
2018-09-04	00:00:00.0	2.03	0.05	$3.4348 \cdot 10^{11}$
2018-08-28	00:00:00.0	2.04	0.06	$3.4348 \cdot 10^{11}$
2018-08-19	00:00:00.0	1.89	0.05	$3.4348 \cdot 10^{11}$
2018-08-09	00:00:00.0	1.91	0.05	$3.4348 \cdot 10^{11}$
2018-07-04	00:00:00.0	2.1	0.07	$3.4348 \cdot 10^{11}$
2018-06-07	00:00:00.0	2.04	0.08	$3.4348 \cdot 10^{11}$
2018-05-23	00:00:00.0	2.16	0.05	$3.4348 \cdot 10^{11}$
2018-05-16	00:00:00.0	2.18	0.05	$3.4348 \cdot 10^{11}$
2018-05-08	00:00:00.0	2.21	0.08	$3.4348 \cdot 10^{11}$
2018-05-01	00:00:00.0	2.19	0.06	$3.4348 \cdot 10^{11}$
2018-01-15	00:00:00.0	2.16	0.08	$3.4348 \cdot 10^{11}$
2018-01-05	00:00:00.0	2.27	0.06	$3.4348 \cdot 10^{11}$
2017-12-23	00:00:00.0	2.07	0.06	$3.4348 \cdot 10^{11}$
2017-12-07	00:00:00.0	2.43	0.14	$3.4348 \cdot 10^{11}$
2017-11-25	00:00:00.0	2.33	0.06	$3.4348 \cdot 10^{11}$
2017-11-22	00:00:00.0	2.26	0.07	$3.4348 \cdot 10^{11}$
2017-11-10	00:00:00.0	2.24	0.05	$3.4348 \cdot 10^{11}$
2017-11-01	00:00:00.0	2.19	0.05	$3.4348 \cdot 10^{11}$
2017-10-21	00:00:00.0	2.3	0.07	$3.4348 \cdot 10^{11}$
2017-10-10	00:00:00.0	2.19	0.05	$3.4348 \cdot 10^{11}$
2017-09-16	00:00:00.0	2.16	0.08	$3.4348 \cdot 10^{11}$
2017-09-05	00:00:00.0	2.35	0.05	$3.4348 \cdot 10^{11}$
2017-08-17	00:00:00.0	2.41	0.09	$3.4348 \cdot 10^{11}$
2017-08-03	00:00:00.0	2.53	0.1	$3.4348 \cdot 10^{11}$
2017-08-03	00:00:00.0	2.58	0.08	$3.4348 \cdot 10^{11}$
2017-07-18	00:00:00.0	2.58	0.07	$3.4348 \cdot 10^{11}$
2017-07-08	00:00:00.0	2.68	0.08	$3.4348 \cdot 10^{11}$

Continued on next page.

Table D.6 – continued from previous page

Date YYYY-MM-DD (1)	Time hh:mm:ss (2)	S [Jy] (3)	σ_S [Jy] (4)	ν [Hz] (5)
2017-07-02	00:00:00.0	2.65	0.06	$3.4348 \cdot 10^{11}$
2017-05-15	00:00:00.0	2.65	0.09	$3.4348 \cdot 10^{11}$
2017-05-06	00:00:00.0	2.73	0.07	$3.4348 \cdot 10^{11}$
2017-05-05	00:00:00.0	2.78	0.06	$3.4348 \cdot 10^{11}$
2017-04-27	00:00:00.0	2.84	0.1	$3.4348 \cdot 10^{11}$
2017-04-23	00:00:00.0	2.74	0.05	$3.4348 \cdot 10^{11}$
2017-04-22	00:00:00.0	2.77	0.07	$3.4348 \cdot 10^{11}$
2017-04-13	00:00:00.0	2.9	0.13	$3.4348 \cdot 10^{11}$
2017-04-12	00:00:00.0	2.92	0.2	$3.4348 \cdot 10^{11}$
2017-03-28	00:00:00.0	2.84	0.14	$3.4348 \cdot 10^{11}$
2017-03-27	00:00:00.0	2.99	0.13	$3.4348 \cdot 10^{11}$
2017-03-19	00:00:00.0	2.93	0.16	$3.4348 \cdot 10^{11}$
2017-01-28	00:00:00.0	3.07	0.1	$3.4348 \cdot 10^{11}$
2016-12-30	00:00:00.0	3.58	0.11	$3.4348 \cdot 10^{11}$
2016-12-10	00:00:00.0	3.301	0.165	$3.435 \cdot 10^{11}$
2016-12-10	00:00:00.0	3.33	0.12	$3.4348 \cdot 10^{11}$
2016-11-23	00:00:00.0	3.16	0.09	$3.4348 \cdot 10^{11}$
2016-11-01	00:00:00.0	3.11	0.1	$3.4348 \cdot 10^{11}$
2016-10-31	00:00:00.0	3.15	0.08	$3.4348 \cdot 10^{11}$
2016-10-18	00:00:00.0	3.14	0.18	$3.4348 \cdot 10^{11}$
2016-10-13	00:00:00.0	3.22	0.11	$3.4348 \cdot 10^{11}$
2016-10-06	00:00:00.0	3.41	0.16	$3.4348 \cdot 10^{11}$
2016-07-23	00:00:00.0	2.49	0.09	$3.3746 \cdot 10^{11}$
2016-07-06	00:00:00.0	2.41	0.08	$3.4348 \cdot 10^{11}$
2016-07-06	00:00:00.0	2.55	0.07	$3.4348 \cdot 10^{11}$
2016-06-26	00:00:00.0	2.66	0.11	$3.4348 \cdot 10^{11}$
2016-06-11	00:00:00.0	2.52	0.15	$3.4348 \cdot 10^{11}$
2016-06-09	00:00:00.0	2.7	0.16	$3.4348 \cdot 10^{11}$
2016-05-13	00:00:00.0	2.24	0.07	$3.4348 \cdot 10^{11}$
2016-04-30	00:00:00.0	2.31	0.12	$3.4348 \cdot 10^{11}$
2016-04-22	00:00:00.0	2.26	0.06	$3.4348 \cdot 10^{11}$
2016-04-09	00:00:00.0	2.05	0.2	$3.4348 \cdot 10^{11}$
2016-03-29	00:00:00.0	2.14	0.09	$3.4348 \cdot 10^{11}$
2016-03-27	00:00:00.0	2.8	0.14	$3.43 \cdot 10^{11}$
2016-03-14	00:00:00.0	2.16	0.09	$3.4348 \cdot 10^{11}$

Continued on next page.

Table D.6 – continued from previous page

Date YYYY-MM-DD (1)	Time hh:mm:ss (2)	S [Jy] (3)	σ_S [Jy] (4)	ν [Hz] (5)
2016-01-26	00:00:00.0	1.98	0.13	$3.4348 \cdot 10^{11}$
2016-01-10	00:00:00.0	2.2	0.14	$3.3746 \cdot 10^{11}$
2016-01-10	00:00:00.0	2.27	0.1	$3.3746 \cdot 10^{11}$
2015-12-29	00:00:00.0	2.29	0.44655	$3.435 \cdot 10^{11}$
2015-12-29	00:00:00.0	2.31	0.08	$3.4348 \cdot 10^{11}$
2015-11-24	00:00:00.0	2.75	0.16	$3.4348 \cdot 10^{11}$
2015-11-01	00:00:00.0	2.89	0.14	$3.4348 \cdot 10^{11}$
2015-09-26	00:00:00.0	3.1	0.26	$3.4348 \cdot 10^{11}$
2015-08-29	00:00:00.0	3.84	0.2	$3.4348 \cdot 10^{11}$
2015-08-15	00:00:00.0	3.99	0.2	$3.4348 \cdot 10^{11}$
2015-07-25	00:00:00.0	3.5	0.3	$3.4348 \cdot 10^{11}$
2015-07-19	00:00:00.0	3.62	0.18	$3.4348 \cdot 10^{11}$
2015-06-24	00:00:00.0	3.43	0.46	$3.4348 \cdot 10^{11}$
2015-06-13	00:00:00.0	3.8	0.2	$3.4348 \cdot 10^{11}$
2015-06-02	00:00:00.0	3.52	0.19	$3.4348 \cdot 10^{11}$
2015-05-31	00:00:00.0	3.829	0.191	$3.435 \cdot 10^{11}$
2015-05-14	00:00:00.0	3.2	0.18	$3.4348 \cdot 10^{11}$
2015-04-03	00:00:00.0	3.22	0.2	$3.4348 \cdot 10^{11}$
2015-01-03	00:00:00.0	2.73	0.12	$3.4348 \cdot 10^{11}$
2014-12-21	00:00:00.0	2.97	0.11	$3.4348 \cdot 10^{11}$
2014-12-14	00:00:00.0	2.79	0.15	$3.4348 \cdot 10^{11}$
2014-12-08	00:00:00.0	2.68	0.14	$3.4348 \cdot 10^{11}$
2014-11-30	00:00:00.0	2.62	0.16	$3.4348 \cdot 10^{11}$
2014-08-16	00:00:00.0	2.87	0.22	$3.4348 \cdot 10^{11}$
2014-07-26	00:00:00.0	2.31	0.14	$3.4348 \cdot 10^{11}$
2014-07-06	00:00:00.0	2.51	0.06	$3.4348 \cdot 10^{11}$
2014-06-28	00:00:00.0	2.35	0.09	$3.4348 \cdot 10^{11}$
2014-06-03	00:00:00.0	2.56	0.16	$3.4348 \cdot 10^{11}$
2014-05-15	00:00:00.0	2.42	0.1	$3.4348 \cdot 10^{11}$
2014-04-29	00:00:00.0	2.08	0.1	$3.4348 \cdot 10^{11}$
2014-04-25	00:00:00.0	2.18	0.13	$3.4348 \cdot 10^{11}$
2014-04-09	00:00:00.0	2.19	0.12	$3.4348 \cdot 10^{11}$
2014-03-26	00:00:00.0	2.594	0.233	$3.4403 \cdot 10^{11}$
2014-03-25	00:00:00.0	2.616	0.235	$3.4778 \cdot 10^{11}$
2014-03-21	00:00:00.0	2.646	0.238	$3.4498 \cdot 10^{11}$

Continued on next page.

Table D.6 – continued from previous page

Date YYYY-MM-DD (1)	Time hh:mm:ss (2)	S [Jy] (3)	σ_S [Jy] (4)	ν [Hz] (5)
2014-03-20	00:00:00.0	2.76	0.16	$3.4348 \cdot 10^{11}$
2014-02-21	00:00:00.0	2.41	0.06	$3.4348 \cdot 10^{11}$
2014-01-28	00:00:00.0	2.337	0.21	$3.394 \cdot 10^{11}$
2014-01-11	00:00:00.0	1.6	0.05	$3.4348 \cdot 10^{11}$
2013-12-21	00:00:00.0	1.603	0.064	$3.435 \cdot 10^{11}$
2013-12-11	00:00:00.0	1.42	0.1	$3.4348 \cdot 10^{11}$
2013-11-28	00:00:00.0	1.25	0.08	$3.4348 \cdot 10^{11}$
2013-11-18	00:00:00.0	1.148	0.103	$2.9716 \cdot 10^{11}$
2013-11-17	00:00:00.0	1.137	0.102	$2.9111 \cdot 10^{11}$
2013-11-16	00:00:00.0	1.317	0.145	$3.4498 \cdot 10^{11}$
2013-11-15	00:00:00.0	1.205	0.108	$3.5002 \cdot 10^{11}$
2013-11-15	00:00:00.0	1.35	0.122	$2.9683 \cdot 10^{11}$
2013-11-14	00:00:00.0	1.241	0.112	$2.9741 \cdot 10^{11}$
2013-11-14	00:00:00.0	1.15	0.06	$3.4348 \cdot 10^{11}$
2013-11-03	00:00:00.0	1.0	0.05	$3.4348 \cdot 10^{11}$
2013-10-19	00:00:00.0	0.86	0.04	$3.4348 \cdot 10^{11}$
2013-04-17	00:00:00.0	0.8	0.07	$3.4325 \cdot 10^{11}$
2012-11-18	00:00:00.0	1.2	0.06	$3.4325 \cdot 10^{11}$
2012-11-17	00:00:00.0	1.2	0.05	$3.4325 \cdot 10^{11}$
2012-10-06	00:00:00.0	1.13	0.06	$3.4325 \cdot 10^{11}$

Note: Col.(1): UTC observation date; Col.(2): UTC observation time; Col.(3): Flux density; Col.(4): Uncertainty of the flux density; Col.(5): Observation frequency.

D. Additional Tables

Table D.7.: SMA data, downloaded from sma1.sma.hawaii.edu/callist/callist.html?data=1058%2B015 on 08.11.2018.

Band	Date	Time	ν	S	σ_S
(1)	YYYY-MM-DD	hh:mm	[GHz]	[Jy]	[Jy]
(1)	(2)	(3)	(4)	(5)	(6)
1mm	2003-01-18	06:33	235.60	2.220	0.153
1mm	2003-03-27	05:06	232.00	2.110	0.130
1mm	2003-03-28	05:30	237.50	2.140	0.119
1mm	2003-04-14	04:50	240.00	1.760	0.214
1mm	2003-04-18	04:41	238.00	2.250	0.303
1mm	2003-04-19	06:35	238.00	2.240	0.119
1mm	2003-04-20	07:08	236.00	2.150	0.129
1mm	2003-04-28	04:33	236.00	2.130	0.139
1mm	2003-05-02	03:32	231.70	1.590	0.139
1mm	2003-05-03	02:52	236.20	1.670	0.086
1mm	2003-11-12	05:14	236.00	2.830	0.205
1mm	2004-01-27	08:57	224.75	2.295	0.139
1mm	2004-01-28	07:49	220.57	3.158	0.206
1mm	2004-02-09	06:25	226.30	1.757	0.266
1mm	2004-02-09	06:25	226.30	2.245	0.391
1mm	2004-03-05	07:05	226.30	2.816	0.155
1mm	2004-04-30	05:03	225.08	2.715	0.146
1mm	2004-06-16	01:15	225.52	2.164	0.128
1mm	2004-06-17	04:41	225.59	2.421	0.142
1mm	2004-12-22	05:36	225.52	1.807	0.092
1mm	2004-12-24	16:01	225.52	1.546	0.087
1mm	2005-01-13	09:07	225.56	2.837	0.154
1mm	2005-01-27	07:33	225.50	1.707	0.088
1mm	2005-01-31	12:11	235.47	2.190	0.116
1mm	2005-03-10	13:57	225.56	2.543	0.140
1mm	2005-04-14	06:35	225.55	2.002	0.144
1mm	2005-04-15	09:05	219.80	1.712	0.091
1mm	2005-04-30	03:24	222.18	2.372	0.154
1mm	2005-05-06	05:42	225.52	1.742	0.089
1mm	2005-05-14	02:52	225.36	2.332	0.162
1mm	2005-06-10	04:24	225.48	1.827	0.096
1mm	2005-07-13	05:07	220.02	1.500	0.227
1mm	2005-11-10	17:32	220.57	2.881	0.148
1mm	2005-11-11	14:51	220.55	2.764	0.152

Continued on next page.

Table D.7 – continued from previous page

Band	Date	Time	ν	S	σ_s
(1)	YYYY-MM-DD	hh:mm	[GHz]	[Jy]	[Jy]
	(2)	(3)	(4)	(5)	(6)
1mm	2005-11-15	15:55	221.02	2.721	0.264
1mm	2005-12-20	16:49	225.57	2.712	0.141
1mm	2006-01-06	13:20	225.57	2.794	0.149
1mm	2006-01-07	13:38	225.56	2.827	0.143
1mm	2006-02-06	09:55	216.06	3.218	0.167
1mm	2006-02-16	10:05	233.74	2.801	0.146
1mm	2006-03-06	09:33	225.59	2.415	0.138
1mm	2006-04-14	08:51	225.55	2.595	0.133
1mm	2006-05-09	04:18	225.51	3.349	0.168
1mm	2006-05-20	07:11	225.55	2.669	0.136
1mm	2006-06-07	07:10	235.60	2.682	0.139
1mm	2006-06-15	05:48	225.56	2.435	0.133
1mm	2006-07-21	04:39	225.48	2.555	0.134
1mm	2006-10-06	18:07	225.35	2.920	0.167
1mm	2006-10-23	15:51	225.49	3.263	0.227
1mm	2006-10-24	16:10	224.63	3.198	0.165
1mm	2006-12-06	16:37	271.76	2.387	0.128
1mm	2006-12-13	16:20	220.57	3.102	0.158
1mm	2006-12-15	13:08	225.56	3.181	0.163
1mm	2006-12-15	16:41	220.56	2.516	0.133
1mm	2006-12-20	12:55	225.52	3.244	0.164
1mm	2006-12-20	15:23	225.52	3.244	0.253
1mm	2006-12-22	15:56	220.52	3.167	0.159
1mm	2007-01-03	17:01	225.42	2.589	0.252
1mm	2007-01-12	12:21	221.53	3.372	0.294
1mm	2007-01-26	11:30	227.77	3.290	0.165
1mm	2007-01-30	14:45	220.44	3.107	0.157
1mm	2007-02-03	15:46	225.60	3.133	0.164
1mm	2007-02-04	11:48	225.56	3.207	0.164
1mm	2007-02-06	13:56	240.05	3.064	0.154
1mm	2007-02-13	10:55	239.98	3.342	0.167
1mm	2007-02-13	14:43	239.98	3.317	0.170
1mm	2007-02-14	15:01	239.95	3.448	0.173
1mm	2007-03-06	08:06	262.03	3.170	0.163
1mm	2007-03-31	05:58	226.93	3.105	0.156

Continued on next page.

Table D.7 – continued from previous page

Band	Date	Time	ν	S	σ_s
(1)	YYYY-MM-DD	hh:mm	[GHz]	[Jy]	[Jy]
	(2)	(3)	(4)	(5)	(6)
1mm	2007-04-03	06:41	226.93	3.348	0.168
1mm	2007-04-18	10:36	225.03	3.112	0.158
1mm	2007-04-19	10:21	225.52	3.151	0.159
1mm	2007-04-30	06:55	283.88	3.005	0.153
1mm	2007-05-08	04:48	211.97	3.642	0.187
1mm	2007-05-24	07:58	235.48	2.793	0.147
1mm	2007-06-22	05:50	225.56	2.618	0.157
1mm	2007-06-28	06:28	225.56	3.071	0.171
1mm	2007-11-19	14:44	225.52	3.139	0.160
1mm	2008-01-12	12:56	225.48	2.892	0.146
1mm	2008-01-30	12:23	214.08	2.280	0.119
1mm	2008-03-28	09:38	220.56	2.342	0.119
1mm	2008-04-04	13:00	262.50	2.199	0.260
1mm	2008-04-17	08:13	225.48	2.359	0.125
1mm	2008-04-18	08:06	225.35	2.337	0.120
1mm	2008-05-01	03:39	220.29	2.317	0.123
1mm	2008-05-02	03:51	220.31	2.494	0.169
1mm	2008-05-03	05:04	220.35	2.435	0.124
1mm	2008-10-14	18:48	223.89	2.074	0.104
1mm	2008-11-06	16:22	262.51	1.890	0.097
1mm	2008-11-08	20:58	219.14	2.028	0.111
1mm	2008-12-08	18:46	220.46	2.231	0.112
1mm	2008-12-18	14:40	220.53	2.514	0.127
1mm	2009-02-10	11:40	240.57	2.554	0.286
1mm	2009-02-14	10:59	220.51	2.707	0.146
1mm	2009-02-21	13:50	220.43	2.315	0.160
1mm	2009-02-26	14:37	220.55	2.619	0.153
1mm	2009-03-13	05:55	225.47	2.982	0.188
1mm	2009-04-18	05:56	223.79	2.964	0.198
1mm	2009-10-21	17:28	223.96	2.833	0.156
1mm	2009-10-30	16:32	225.49	3.247	0.165
1mm	2009-11-04	19:35	227.48	2.473	0.128
1mm	2009-11-15	14:12	222.44	3.010	0.165
1mm	2009-12-05	12:44	218.79	3.288	0.165
1mm	2009-12-17	11:13	225.57	2.788	0.142

Continued on next page.

Table D.7 – continued from previous page

Band	Date	Time	ν	S	σ_s
(1)	YYYY-MM-DD	hh:mm	[GHz]	[Jy]	[Jy]
	(2)	(3)	(4)	(5)	(6)
1mm	2010-01-07	18:08	225.52	2.651	0.140
1mm	2010-01-08	18:35	225.52	2.586	0.141
1mm	2010-01-12	18:12	225.47	2.565	0.132
1mm	2010-01-14	15:30	262.53	2.098	0.218
1mm	2010-02-05	13:21	225.52	2.203	0.114
1mm	2010-03-24	09:28	224.75	1.891	0.095
1mm	2010-03-25	09:46	224.78	2.006	0.101
1mm	2010-04-11	06:04	224.54	2.294	0.118
1mm	2010-04-12	06:56	225.74	2.300	0.116
1mm	2010-04-27	06:24	221.87	2.129	0.107
1mm	2010-04-28	06:04	224.89	2.195	0.111
1mm	2010-05-07	06:32	218.93	2.113	0.108
1mm	2010-05-27	08:12	225.56	1.858	0.098
1mm	2010-07-30	21:05	225.52	2.383	0.124
1mm	2010-10-22	19:14	235.55	3.414	0.173
1mm	2010-11-05	17:31	214.11	2.749	0.138
1mm	2010-11-25	13:57	225.49	3.267	0.165
1mm	2010-12-30	13:24	225.48	2.885	0.146
1mm	2010-12-30	17:00	225.48	2.677	0.139
1mm	2011-01-27	10:11	225.49	3.057	0.154
1mm	2011-01-27	14:51	225.49	2.989	0.150
1mm	2011-02-08	14:40	224.81	2.934	0.153
1mm	2011-02-10	08:30	225.49	3.204	0.164
1mm	2011-02-28	08:27	223.40	2.727	0.139
1mm	2011-03-02	08:16	223.98	3.324	0.167
1mm	2011-05-17	03:01	225.51	3.596	0.197
1mm	2011-06-02	07:19	235.52	3.546	0.179
1mm	2011-10-14	17:19	224.69	3.574	0.180
1mm	2011-10-24	17:27	272.06	3.218	0.162
1mm	2011-10-27	19:30	222.68	3.119	0.157
1mm	2011-11-07	17:07	224.91	3.082	0.155
1mm	2011-11-09	14:44	225.60	3.005	0.152
1mm	2011-11-22	17:58	225.24	2.911	0.149
1mm	2011-11-24	14:31	226.14	3.122	0.158
1mm	2012-01-05	16:28	225.44	2.591	0.132

Continued on next page.

Table D.7 – continued from previous page

Band	Date	Time	ν	S	σ_s
(1)	YYYY-MM-DD	hh:mm	[GHz]	[Jy]	[Jy]
(1)	(2)	(3)	(4)	(5)	(6)
1mm	2012-01-17	14:09	215.74	2.655	0.133
1mm	2012-01-20	13:08	224.90	2.708	0.145
1mm	2012-01-21	14:55	224.81	2.672	0.135
1mm	2012-01-27	11:48	225.54	2.818	0.144
1mm	2012-02-09	15:48	224.89	2.481	0.125
1mm	2012-03-12	10:26	220.45	1.956	0.208
1mm	2012-04-05	05:43	225.48	1.702	0.089
1mm	2012-04-16	09:57	225.46	1.926	0.097
1mm	2012-05-22	04:13	225.34	2.138	0.110
1mm	2012-10-13	15:26	225.47	1.549	0.082
1mm	2012-10-17	15:47	224.84	1.564	0.082
1mm	2012-10-18	15:23	225.47	1.597	0.082
1mm	2012-10-25	15:53	225.46	1.565	0.084
1mm	2012-10-27	15:26	225.46	1.588	0.085
1mm	2012-12-19	18:12	225.52	1.469	0.075
1mm	2013-01-24	10:46	225.44	1.545	0.083
1mm	2013-01-24	14:35	225.44	1.437	0.073
1mm	2013-01-31	10:30	225.56	1.417	0.071
1mm	2013-02-08	12:04	225.49	1.385	0.070
1mm	2013-02-08	15:49	225.49	1.390	0.070
1mm	2013-04-26	04:34	225.44	1.116	0.057
1mm	2013-05-01	06:16	225.44	1.082	0.054
1mm	2013-05-02	07:20	225.44	1.107	0.056
1mm	2013-05-04	06:21	225.45	1.093	0.055
1mm	2013-05-05	06:52	225.44	1.079	0.055
1mm	2013-05-07	05:41	225.44	1.060	0.054
1mm	2013-12-05	15:34	225.45	1.716	0.088
1mm	2014-01-14	16:28	225.22	2.128	0.154
1mm	2014-01-16	11:53	225.02	2.203	0.114
1mm	2014-02-01	12:31	225.45	2.188	0.110
1mm	2014-02-03	13:50	225.48	2.290	0.116
1mm	2014-02-07	14:01	224.82	2.301	0.207
1mm	2014-02-08	13:43	224.82	2.393	0.123
1mm	2014-03-17	07:33	225.13	3.678	0.187
1mm	2014-03-18	06:30	224.87	3.373	0.173

Continued on next page.

Table D.7 – continued from previous page

Band	Date	Time	ν	S	σ_s
(1)	YYYY-MM-DD	hh:mm	[GHz]	[Jy]	[Jy]
	(2)	(3)	(4)	(5)	(6)
1mm	2014-03-20	11:04	225.26	3.616	0.182
1mm	2014-03-21	07:35	224.93	3.571	0.179
1mm	2014-04-07	07:45	225.52	2.794	0.140
1mm	2014-04-18	07:41	225.48	2.641	0.132
1mm	2014-04-25	07:37	221.27	2.960	0.148
1mm	2014-06-06	06:03	235.02	3.060	0.157
1mm	2014-06-07	04:13	224.94	3.062	0.154
1mm	2014-11-18	16:47	225.52	3.724	0.386
1mm	2014-12-05	17:14	224.75	3.194	0.166
1mm	2014-12-07	13:51	225.41	3.493	0.175
1mm	2014-12-16	11:45	225.44	3.382	0.182
1mm	2014-12-17	13:23	225.48	3.512	0.188
1mm	2014-12-17	18:22	225.48	3.429	0.175
1mm	2014-12-26	12:01	225.48	3.477	0.188
1mm	2015-01-10	13:08	225.45	3.251	0.164
1mm	2015-01-16	16:29	225.45	3.305	0.170
1mm	2015-01-22	16:52	224.73	3.490	0.177
1mm	2015-01-24	12:26	225.45	3.575	0.179
1mm	2015-01-26	16:09	224.72	3.612	0.186
1mm	2015-01-27	14:56	224.72	3.678	0.185
1mm	2015-01-28	14:06	225.49	3.503	0.176
1mm	2015-01-30	16:00	225.48	3.599	0.183
1mm	2015-01-31	12:45	225.44	3.561	0.178
1mm	2015-03-02	13:16	225.40	4.384	0.490
1mm	2015-04-03	10:35	224.72	4.208	0.213
1mm	2015-04-09	06:18	225.44	4.489	0.225
1mm	2015-04-16	08:00	224.89	4.540	0.227
1mm	2015-10-14	17:00	224.87	3.763	0.191
1mm	2015-10-26	16:19	225.43	4.102	0.205
1mm	2015-11-07	14:52	225.46	4.126	0.208
1mm	2016-01-14	09:45	225.45	3.017	0.166
1mm	2016-01-21	11:03	225.45	3.014	0.160
1mm	2016-02-17	12:43	221.81	2.757	0.139
1mm	2016-03-02	09:34	225.47	2.955	0.153
1mm	2016-03-03	11:36	222.59	2.802	0.140

Continued on next page.

Table D.7 – continued from previous page

Band	Date	Time	ν	S	σ_s
(1)	YYYY-MM-DD	hh:mm	[GHz]	[Jy]	[Jy]
(1)	(2)	(3)	(4)	(5)	(6)
1mm	2016-03-13	07:16	222.58	3.029	0.155
1mm	2016-03-21	07:52	214.53	3.132	0.158
1mm	2016-03-25	07:08	224.99	3.032	0.152
1mm	2016-03-27	08:16	224.92	2.999	0.150
1mm	2016-03-27	12:15	224.92	3.004	0.150
1mm	2016-03-28	08:31	224.90	2.939	0.147
1mm	2016-04-01	07:48	225.44	2.878	0.144
1mm	2016-04-20	05:54	225.27	2.884	0.144
1mm	2016-04-28	06:05	225.53	2.968	0.148
1mm	2016-04-29	05:51	225.53	2.966	0.148
1mm	2016-05-03	05:40	224.89	2.969	0.149
1mm	2016-05-04	07:19	224.89	2.937	0.149
1mm	2016-06-03	04:00	224.70	3.463	0.175
1mm	2016-06-19	05:21	226.08	3.532	0.178
1mm	2016-10-13	16:19	225.54	4.464	0.226
1mm	2017-01-03	19:02	225.52	4.490	0.227
1mm	2017-01-04	13:48	217.66	4.419	0.234
1mm	2017-01-21	10:29	226.26	4.143	0.207
1mm	2017-02-16	08:26	225.51	4.466	0.227
1mm	2017-02-17	15:14	225.55	4.170	0.211
1mm	2017-04-16	10:09	224.98	3.871	0.194
1mm	2017-04-18	08:25	224.98	3.586	0.180
1mm	2017-04-19	05:25	225.18	3.816	0.193
1mm	2017-05-29	06:48	229.02	3.480	0.175
1mm	2017-06-16	06:49	229.51	3.595	0.180
1mm	2017-11-08	14:19	225.54	2.765	0.140
1mm	2018-03-11	07:45	225.55	2.910	0.146
1mm	2018-03-18	07:23	225.52	2.863	0.143
1mm	2018-03-22	07:52	235.56	2.847	0.143
1mm	2018-03-23	06:07	235.56	2.803	0.443
1mm	2018-04-12	07:56	229.53	2.682	0.135
1mm	2018-05-10	07:04	225.54	2.780	0.140
1mm	2018-06-05	06:58	235.56	2.540	0.127

Note: Col.(1): Observation band; Col.(2): UTC observation date; Col.(3): UTC observation time; Col.(4): Observation frequency; Col.(5): Flux density; Col.(6): Uncertainty of the flux density.

Table D.8.: OVRO data, downloaded from www.astro.caltech.edu/ovroblazars/data.php?page=data_return&source=J1058+0133 on 29.10.2018.

Time [MJD] (1)	S [Jy] (2)	σ_S [Jy] (3)
54474.3959954	5.2285684	0.0495742
54476.3906481	5.2349759	0.0733305
54478.3849190	5.1556925	0.0767004
54480.3796991	5.2907223	0.0537424
54484.3694213	5.2561254	0.0652338
54486.3634028	5.2089679	0.0928348
54488.3579630	5.2730150	0.2531890
54494.3414931	4.9618426	0.0465774
54496.3362269	4.9998623	0.0383316
54498.3304977	4.9720102	0.0377435
54502.3218750	4.9732236	0.0302561
54506.3097454	4.9354313	0.0469925
54508.3046528	4.8712598	0.0509637
54548.1937963	4.8287795	0.0570809
54550.1888194	4.7005554	0.0277975
54556.1729167	4.6074361	0.0367743
54558.1665278	4.8135796	0.0399013
54584.1015509	4.6703954	0.0298989
54602.0496644	4.5962889	0.0625577
54604.0446412	4.9031266	0.0394521
54606.0392245	4.8818091	0.0450668
54612.0226505	4.6904485	0.2163557
54619.0033681	4.7051702	0.0347917
54623.9943403	4.7263501	0.0534370
54625.9811921	4.7421836	0.0302669
54629.9714120	4.7076106	0.0522679
54631.9671528	4.6883931	0.0550289
54633.9623032	4.8543488	0.0491508
54634.9594444	4.8722673	0.1136778
54637.9510764	4.8554864	0.0361260
54662.8811921	4.5326119	0.1199661
54664.8776620	4.5276392	0.0277006
54675.8463889	4.6398694	0.1106470
54677.8410995	4.4494580	0.0891714

Continued on next page.

Table D.8 – continued from previous page

Time [MJD] (1)	S [Jy] (2)	σ_s [Jy] (3)
54679.8356713	4.4372270	0.0511039
54683.8248495	4.3534112	0.0259094
54687.8134259	4.3569742	0.0268519
54689.8085995	4.2999061	0.0288406
54693.8084259	4.3870389	0.0257176
54697.7966088	4.4523132	0.0679018
54699.7904398	4.3602437	0.0419773
54701.7856713	4.3465152	0.0723555
54703.7800347	4.4053464	0.0833558
54705.7743634	4.3436334	0.0321080
54762.6341435	4.2838775	0.0252834
54768.6176042	4.2692782	0.0327033
54774.6097917	4.3253125	0.0282456
54776.6041435	4.3556873	0.0404284
54783.5833796	4.5268946	0.0263595
54789.5675231	4.4545920	0.0819714
54793.5564005	4.4675860	0.0330656
54795.5510069	4.4467126	0.0579852
54805.5238310	4.5343466	0.0355899
54809.5129514	4.4966032	0.0304215
54813.5020139	4.4218625	0.0452345
54817.4917361	4.4956977	0.0427438
54819.4856019	4.5868995	0.0386632
54823.4703819	4.6258363	0.0356813
54849.3997106	4.7483124	0.0317101
54853.3913079	4.6865201	0.0425072
54857.3832176	4.7337105	0.0513034
54859.3786111	4.8359591	0.0473516
54861.3724190	4.8255847	0.0399863
54863.3675347	4.8944586	0.0722258
54865.3622917	4.9130407	0.0367417
54871.3449074	4.8341974	0.0585818
54875.3339931	4.9170554	0.0283775
54877.3285185	4.8315044	0.0730342
54879.3231481	4.8659146	0.0283730

Continued on next page.

Table D.8 – continued from previous page

Time [MJD] (1)	S [Jy] (2)	σ_s [Jy] (3)
54881.3194444	4.8764594	0.0343249
54883.3139699	4.8943063	0.0300650
54885.3041319	4.4850120	0.1998346
54887.3032639	4.8939210	0.0341395
54889.2978935	4.8416061	0.0392497
54891.2923611	4.9158882	0.0361163
54899.2705324	4.7871695	0.3769073
54905.2574074	4.8572177	0.0473388
54907.2602199	4.8617019	0.1281238
54910.2650347	4.8597225	0.0679270
54913.2446759	4.6401287	0.0753463
54916.2278704	4.5330468	0.2298863
54919.2188773	4.8427683	0.0656018
54926.1756481	4.6693478	0.0655768
54932.2007755	4.7275048	0.0640135
54935.1828009	4.6464689	0.1898246
54941.1663079	4.6270210	0.0635317
54944.1702199	4.6576970	0.0640153
54960.0969907	4.7167764	0.0887830
54966.0754167	4.5219739	0.1110539
54969.0617708	4.8288437	0.0654970
54972.0603356	4.9320131	0.0820680
54988.0167245	4.8491206	0.0795102
55008.9636690	5.0377992	0.0749789
55018.9265278	5.0098490	0.0683159
55021.9282407	5.1644148	0.0730413
55024.9115278	5.2677246	0.0896480
55027.9142477	5.0520841	0.1116752
55033.8954861	5.0439424	0.0689702
55054.8382755	5.1660967	0.2469032
55057.8307176	5.2442391	0.1114028
55060.8195255	5.0845652	0.0927543
55072.7992361	5.1203397	0.1241822
55099.7235995	5.3058178	0.1109001
55102.7153009	5.4371425	0.0807860

Continued on next page.

Table D.8 – continued from previous page

Time [MJD] (1)	S [Jy] (2)	σ_s [Jy] (3)
55108.6984954	5.4283763	0.1003338
55112.6899306	5.4297396	0.0866784
55115.6880787	5.4760272	0.0759638
55137.6340509	5.5019960	0.0881373
55140.6287037	5.3401528	0.0723097
55150.6044676	5.4529221	0.0746002
55153.6039005	5.3115790	0.0742750
55166.5767708	5.2982781	0.0799809
55172.5579398	5.2931901	0.1058466
55189.5137500	5.2196488	0.1289500
55192.4885532	5.1670512	0.0791458
55199.4794560	5.2832247	0.0974399
55208.4540741	5.2079528	0.0743416
55211.4470949	5.2232525	0.0798946
55214.4400463	5.2177663	0.0756993
55221.4212153	5.0337027	0.0697477
55227.3940741	4.9058134	0.1207375
55230.3974190	4.9879387	0.1250225
55240.3683333	4.8788375	0.0684680
55243.3593634	5.1019389	0.0977815
55246.3527431	4.9701043	0.0868122
55262.3119792	4.7895690	0.1324816
55272.2459259	4.5938644	0.0720275
55276.2324306	4.6723040	0.0701817
55293.3216088	3.6916321	0.2434446
55305.2817824	4.5599957	0.0617714
55308.2721065	4.5583998	0.0787848
55329.2289005	4.6083348	0.0726704
55332.2118634	4.5576889	0.1125198
55335.2093634	4.4366255	0.0683295
55341.1743519	4.5809875	0.0734986
55352.9922685	4.6615754	0.0975300
55368.9503704	4.7546818	0.0748348
55379.9184954	4.6859186	0.0734050
55465.8654514	4.5305828	0.1639616

Continued on next page.

Table D.8 – continued from previous page

Time [MJD] (1)	S [Jy] (2)	σ_s [Jy] (3)
55467.8727894	4.5548067	0.0625725
55491.7947222	4.4539876	0.0887199
55496.7808912	4.6715049	0.0633812
55532.6529630	4.8380475	0.0762520
55577.5234375	5.1633451	0.0881774
55580.5144907	5.1300571	0.0873657
55591.4850463	5.2157003	0.0904511
55603.4620833	5.1574366	0.0752894
55607.4429630	5.1259269	0.0706583
55615.4188773	5.0138292	0.0939570
55622.3865394	5.0910759	0.0690545
55624.3872106	5.1672375	0.0705886
55631.3792708	5.0851786	0.0903681
55653.3116551	5.1576026	0.0787481
55657.2670139	5.0614401	0.1009856
55661.2585880	5.1662506	0.0744899
55662.2563079	5.1702907	0.0706539
55671.2334491	5.1167754	0.0708951
55679.2117130	5.3170640	0.0839842
55682.2073380	5.2622376	0.1124635
55688.1678588	5.3726363	0.0763355
55691.1509606	5.3501687	0.1168901
55729.9975579	5.1593171	0.1380261
55736.9902083	5.2200762	0.0710501
55742.9675694	5.3018549	0.0727426
55752.9457292	5.3423870	0.1293298
55778.9432755	5.3625587	0.1088266
55801.8995949	5.3837825	0.0944545
55833.8110995	5.2665437	0.0755934
55836.7980787	5.5875665	0.1591654
55840.7874769	5.2202953	0.0915461
55844.7572106	5.2799666	0.0748571
55861.7312269	5.3986209	0.0850782
55864.7095833	5.3215258	0.0726942
55871.6951736	5.3457426	0.1172653

Continued on next page.

Table D.8 – continued from previous page

Time [MJD] (1)	S [Jy] (2)	σ_s [Jy] (3)
55882.6766435	5.2688538	0.1182337
55903.6609259	5.3512434	0.0392732
55913.6226505	5.1365779	0.0312551
55923.6138657	5.1478219	0.0351513
55927.5436227	5.1396093	0.0839851
55931.5975463	5.1231762	0.0380627
55941.5297222	4.9583203	0.0759013
55946.4817361	4.9152787	0.0666713
55958.4488310	4.8918965	0.1158400
55990.3707407	4.4911467	0.0918765
55991.4388773	4.4568152	0.0300462
55997.3416435	4.2806875	0.0599511
55998.4144097	4.3909191	0.0365672
56005.3929051	4.3075077	0.0337067
56026.3352546	4.2557885	0.1135871
56033.3090394	4.2123304	0.0459151
56040.3050579	4.2028572	0.0245079
56045.2312384	4.2980343	0.1175464
56056.1568519	4.2600389	0.0616184
56138.9802315	3.9528978	0.0764023
56199.6727662	3.7528390	0.0245329
56200.8222801	3.6811394	0.0779982
56204.8079398	3.7099828	0.0790636
56209.6787384	3.6029398	0.0958717
56210.6735069	3.6272188	0.0751835
56221.6851273	3.5219295	0.1169222
56225.6991551	3.5365901	0.0502635
56231.6910995	3.5550777	0.0824331
56232.5804745	3.6162060	0.0210866
56245.5774769	3.4926975	0.0632384
56249.5921181	3.2385499	0.0549802
56252.6370023	3.3673020	0.0458083
56253.6061574	3.3116416	0.0799627
56256.5823958	3.3863248	0.0530038
56259.5716782	3.3352472	0.0585018

Continued on next page.

Table D.8 – continued from previous page

Time [MJD] (1)	S [Jy] (2)	σ_s [Jy] (3)
56265.5413079	3.2364910	0.0439523
56272.6338542	3.1865415	0.0522019
56273.6147106	3.1432356	0.0670357
56277.5542245	3.1711461	0.0432776
56281.6087731	3.0607299	0.0632540
56301.6057986	2.9634106	0.0198280
56311.4515278	3.0627097	0.0232571
56311.5764005	3.0584951	0.0217168
56336.4499769	3.0262938	0.0609434
56338.4063194	3.0696490	0.0449477
56351.4223148	3.0194899	0.0419431
56358.3468866	3.0507839	0.0473741
56364.2538657	3.1249209	0.0430368
56365.2336111	3.1690888	0.0663830
56378.2054630	3.0655847	0.0433417
56379.3728009	3.0777374	0.0521163
56384.2244444	3.0948228	0.0222429
56386.1896759	3.0826446	0.0261050
56393.2449769	3.0728532	0.0456975
56406.1337153	2.9846196	0.0537488
56417.1264931	2.8941046	0.0644919
56425.1514583	2.8387212	0.0240424
56445.1689120	2.6560733	0.0300194
56446.0886574	2.7221587	0.0576125
56465.0257176	2.6022715	0.0680894
56480.0911690	2.5686680	0.0297168
56562.8466204	2.4329078	0.0352986
56564.7216319	2.5735177	0.0480015
56571.6886921	2.6241424	0.0491103
56579.6790741	2.6286979	0.0358837
56584.6900000	2.7561379	0.0388812
56587.7113079	2.7446517	0.0467712
56593.7077662	2.8109810	0.0333064
56597.6359954	2.7556410	0.0828119
56599.5968750	2.8966154	0.0455927

Continued on next page.

Table D.8 – continued from previous page

Time [MJD] (1)	S [Jy] (2)	σ_s [Jy] (3)
56605.5989005	2.9870904	0.0263675
56611.5995949	2.9943346	0.0377617
56613.5372569	3.0353001	0.0324830
56616.5659259	2.9980409	0.0188455
56625.6185069	3.2221906	0.0444397
56631.5590162	3.1783617	0.0446146
56640.4709954	3.4038161	0.0205740
56652.4452199	3.4731348	0.0478916
56654.4911343	3.4968435	0.0555131
56658.4702083	3.4992789	0.0535010
56674.4946528	3.7180984	0.0514243
56683.4756481	3.8447383	0.0709504
56693.4602546	3.7858923	0.0262558
56707.3487616	4.0566153	0.0568658
56710.4537500	4.0942270	0.0796137
56714.3078356	4.2127923	0.1185730
56735.2355093	4.4236907	0.0754399
56743.2140394	4.6424043	0.0535234
56745.2009722	4.8037520	0.0398064
56749.2984838	4.5869183	0.0268745
56754.2322106	4.4656515	0.1174685
56757.2139699	4.5642425	0.1192396
56758.2045139	4.6368673	0.0656463
56763.1685185	4.6555208	0.0630860
56765.3381944	4.5119423	0.1035632
56779.2866551	4.4919698	0.0690334
56792.1080324	4.8689276	0.0810218
56794.0550463	4.7362554	0.1625810
56886.8174421	4.5151321	0.0472822
56967.7132755	5.3507136	0.0443024
56971.7023843	5.5384673	0.0445259
56987.5419560	5.8888703	0.0503505
57015.5371644	5.8807786	0.0497724
57020.5226157	5.8240298	0.0472056
57029.5409606	5.7721378	0.0463386

Continued on next page.

Table D.8 – continued from previous page

Time [MJD] (1)	S [Jy] (2)	σ_s [Jy] (3)
57041.3942361	5.9756904	0.0536218
57056.3621644	6.1047695	0.0508749
57066.4601505	6.2390435	0.0494636
57076.3668750	6.6582796	0.0538279
57082.3692130	6.1157274	0.0881073
57095.2479745	6.7678792	0.0568644
57107.2140856	6.7249045	0.0576392
57112.2004745	6.6543955	0.0598529
57119.3003125	6.6450626	0.0573959
57125.2775116	6.7238815	0.0536588
57253.8299074	7.2855517	0.1626765
57257.7952199	7.4603132	0.1918426
57260.8224653	7.4575580	0.1249676
57290.7414236	6.5720923	0.0629038
57294.7431134	7.1157875	0.1835910
57320.6271181	7.3596513	0.1873133
57367.5325463	6.4517215	0.0786037
57375.5356597	6.3746122	0.0807580
57379.4725347	6.3130370	0.0769501
57382.4974074	6.2366191	0.0782095
57399.3990972	6.1031800	0.0743143
57404.3855903	6.1125918	0.0778824
57409.3799421	6.1498858	0.0749534
57416.3821991	6.1468732	0.0751141
57431.3634954	5.9489368	0.0727524
57438.3488194	5.9639158	0.0745970
57445.2760880	5.7937238	0.0743572
57449.4240162	6.0767084	0.0536717
57464.2878588	6.0723706	0.0805801
57474.2142477	6.0360610	0.0734831
57540.0198727	6.2787527	0.1622910
57566.0150000	6.5017001	0.0793097
57575.9737616	6.3344698	0.1252701
57592.8609375	6.3159864	0.0575728
57598.8436574	6.2748804	0.0511130

Continued on next page.

Table D.8 – continued from previous page

Time [MJD] (1)	S [Jy] (2)	σ_s [Jy] (3)
57611.8270139	6.3390295	0.0785480
57621.8122569	6.3887805	0.0489551
57627.7978588	6.2240415	0.1073145
57661.7131134	6.5838149	0.0805081
57669.6696065	6.9609717	0.0860549
57688.6576852	6.8193720	0.0945286
57701.5646296	6.9881544	0.0566329
57710.6226273	7.0863797	0.0874724
57715.6511458	7.0618428	0.0834862
57721.5831481	7.3036446	0.1676490
57726.5417593	7.4817068	0.0919606
57730.4989583	7.3029180	0.0548580
57737.4870486	7.4848437	0.0600067
57748.4679398	7.5087059	0.0916206
57750.4945602	7.5587088	0.0996784
57752.4764583	7.3853308	0.1034380
57786.3551736	7.4049304	0.0903227
57809.2781250	7.7687665	0.0954952
57810.3232176	7.6909782	0.1842306
57820.2599884	7.5934210	0.0894578
57873.1382292	6.8270333	0.0906271
57903.0480671	6.7383568	0.1440314
57944.9427199	6.3196736	0.0802824
57985.7923495	6.2765974	0.3941705
57989.8276042	6.1835171	0.1022169
57991.8043634	6.4808783	0.0992045
58024.7244676	6.2780053	0.0773956
58027.7023148	6.1722888	0.2005133
58043.6312847	6.7863974	0.0796587
58060.6144792	6.8033554	0.0855432
58063.5944444	6.6121022	0.0964011
58070.5807407	6.7549542	0.0534849
58076.5842824	6.7346279	0.0822387
58088.5584838	6.6061621	0.0804260
58103.5059491	6.4377024	0.0858540

Continued on next page.

Table D.8 – continued from previous page

Time [MJD] (1)	S [Jy] (2)	σ_S [Jy] (3)
58109.4564352	6.5297727	0.0872335
58111.4690509	6.5783168	0.0761213
58119.4176273	6.3780537	0.1370484
58129.4093056	6.3214149	0.0796058
58132.4077199	6.2337782	0.1216860
58144.3705208	6.6922052	0.0827466
58146.3824537	6.5036080	0.0491140
58153.3714236	6.3205383	0.0956723
58158.3280903	6.2295505	0.0796536
58167.3061227	6.3718885	0.1422747
58171.3020023	6.2731330	0.0766750
58212.1770255	6.0486614	0.0707803
58230.1232292	6.0766207	0.0740755
58233.1532176	6.0025016	0.0847053
58267.0769444	6.3622474	0.0774930
58272.0652083	6.1300757	0.0752626
58293.9607407	6.3357436	0.0779942
58322.9215509	6.2827357	0.1299292

Note: Col.(1): Observation time; Col.(2): Flux density; Col.(3): Uncertainty of the flux density.

Bibliography

- Abdo A. A., Ackermann M., Agudo I., et al., 2010, ApJ 716, 30
- Abdo A. A., Ackermann M., Ajello M., et al., 2009, ApJ 700, 597A
- Aleksić J., Antonelli L. A., Antoranz P., et al., 2011, ApJL 730, L8
- Antonucci R., 1993, ARA&A 31, 473
- Attridge J. M., Roberts D. H., Wardle J. F. C., 1999, ApJ 518, L87
- Atwood W. B., Abdo A. A., Ackermann M., et al., 2009, ApJ 697, 1071
- Beckmann V., Shrader C., 2012, Active Galactic Nuclei, WILEY-VCH Verlag Weinheim
- Blandford R. D., Königl A., 1979, ApJ 232, 34
- Blandford R. D., Payne D. G., 1982, MNRAS 199, 883
- Blandford R. D., Znajek R. L., 1977, MNRAS 179, 433
- Böttcher M., 2010, eprint arXiv: 1006.5048
- Burke B. F., Graham - Smith F., 2010, An Introduction to Radio Astronomy, Cambridge University Press
- Camenzind M., 1993, LNP 421, 109C
- Carroll B. W., Ostlie D. A., 2014, An Introduction to Modern Astrophysics, Pearson Education Limited
- Chodorowski M. J., 2005, AmJPh 73, 639C
- Clark B. G., 1999, ASPC 180, 1C
- Cornwell T. J., 1989, Sci 245, 263C
- Cornwell T., Fomalont E. B., 1999, ASPC 180, 187C
- Costamante L., Cutini S., Tosti G., et al., 2018, MNRAS 477, 4749C
- Cotton W. D., 1995, ASPC 82, 289D

- Dermer C. D., Schlickeiser R., Mastichiadis A., 1992, A&A 256L, 27D
- Diamond P. J., 1995, ASPC 82, 227D
- Donato D., Ghisellini G., Tagliaferri G., Fossati G., 2001, A&A 375, 739
- Edelson R. A., Krolik J. H., 1988, ApJ 333, 646E
- Fuhrmann L., Larsson S., Chiang J., et al., 2014, MNRAS 441, 1899
- Fanaroff B. L., Riley J. M., 1974, MNRAS 167, 31P
- Fossati G., Maraschi L., Celotti A., et al., 1998, MNRAS 299, 433
- Ghisellini G., Righi C., Costamante L., Tavecchio F., 2017, MNRAS 469, 255
- Ghisellini G., Tavecchio F., 2009, MNRAS 397, 985G
- Gravity Collaboration, Sturm E., Dexter J., Pfuhl O., et al., 2018, Nat 563, 657G
- Hada K., Doi A., Kino M., et al., 2011, Nat 477, 185H
- HESS Collaboration, Abramowski A., Acero F., Aharonian F., et al., 2010, A&A 520, A83
- Högbom J. A., 1974, A\$AS 15, 417H
- Houck J. C., DeNicola L. A., 2000, ASPC 216, 591H
- Impey C. D., Tapia S., 1990, ApJ 354, 124I
- Jorstad S. G., Marscher A. P., Lister M. L., et al., 2005, AJ 130, 1418
- Jorstad S. G., Marscher A. P., Mattox J. R., et al., 2001, ApJ 556, 738
- Jorstad S. G., Marscher A. P., Morozova D. A., et al., 2017, ApJ 846, 98
- Jorstad S. G., Marscher A. P., Smith P. S., et al., 2013, ApJ 773, 147
- Kadler M., 2015, Extragalactic jets, Lecture on extragalactic jets held in the summer term
- Kadler M., Ros E., Lobanov A. P., Falcke H., Zensus J. A., 2004, A&A 426, 481
- Kellermann K. I., Pauliny-Toth I. I. K., 1969, ApJ 155, 71
- Kellermann K. I., Sramek R., Schmidt M., et al., 1989, AJ 98, 1195

- Kembhavi A. K., Narlikar J. V., 1999, *Quasars and Active Galactic Nuclei An Introduction*, Cambridge University Press
- Kießling T., 2013, *Auswertung von Messungen und Fehlerrechnung*, Lecture on error analysis held in the winter term
- Königl A., 1981, *ApJ* 243, 700
- Kovalev Y. Y., Kellermann K. I., Lister M. L., et al., 2005, *ApJ* 130, 2473
- Lister M. L., Aller M. F., Aller H. D., et al., 2015, *ApJ* 810L, 9L
- Lister M. L., Aller M. F., Aller H. D., et al., 2018, *ApJS* 234, 12L
- Lister M. L., Cohen M. H., Homan D. C., et al., 2009, *AJ* 138, 1874
- Lister M. L., Homan D. C., Hovatta T., et al., 2019, *ApJ* 874, 43
- Lister M. L., Marscher A. P., Gear W. K., 1998, *ApJ* 504, 702
- Lobanov A. P., 1998, *A&A* 330, 79
- Lobanov A. P., 2005, eprint arXiv: astro-ph/0503225
- MacDonald N. R., Jorstad S. G., Marscher A. P., 2017, *ApJ* 850, 87
- Mannheim K., 1993, *A&A* 269, 67
- Maraschi L., Ghisellini G., Celotti A., 1992, *ApJ* 397L, 5M
- Marscher A. P., 2009, eprint arXiv: 0909.2576
- Max-Moerbeck W., Hovatta T., Richards J. L., et al., 2014, *MNRAS* 445, 428
- Murphy D. W., Browne I. W. A., Perley R. A., 1993, *MNRAS* 264, 298M
- Peterson B. M., Wanders I., Horne K., et al., 1998, *PASP* 110, 660
- Pushkarev A. B., Gabuzda D. C., Vetukhnovskaya Y. N., Yakimov V. E., 2005, *MNRAS* 356, 859
- Pushkarev A. B., Kovalev Y. Y., Lister M. L., Savolainen T., 2009, *A&A* 507, L33
- Readhead A. C. S., 1994, *ApJ* 426, 51
- Richards J. L., Max-Moerbeck W., Pavlidou V., et al., 2011, *ApJS* 194, 29
- Rybicki G. B., Lightman A. P., 1985, *Radiativ Processes in Astrophysics*, WILEY-VCH Verlag Weinheim

- Sbarrato T., Foschini L., Ghisellini G., Tavecchio F., 2011, *AdSpR* 48, 998S
- Schneider P., 2015, *Extragalactic Astronomy and Cosmology An Introduction*, Springer-Verlag Berlin Heidelberg
- Seyfert C. K., 1943, *ApJ*, 97, 28
- Shepherd M. C., 1997, *ASPC* 125, 77S
- Shields G. A., 1999, *PASP* 111, 661
- Sikora M., Begelman M. C., Rees M. J., 1994, *ApJ* 422, 153S
- Sikora M., Stawarz L., Moderski R., et al., 2009, *ApJ* 704, 38S
- Taylor J. R., 1988, *Fehleranalyse Eine Einführung in die Untersuchung von Unsicherheiten in physikalischen Messungen*, VHC Verlagsgesellschaft mbH, Weinheim (Bundesrepublik Deutschland)
- Taylor A. R., Moran J. M., Swenson Jr. G. W., 2017, *Interferometry and Synthesis in Radio Astronomy*, A&A Library, Springer Open
- Urry C. M., Padovani P., 1995, *PASP* 107, 803
- White R. J., Peterson B. M., 1994, *PASP* 106, 879W

List of Figures

2.1. SED of 4C+01.28	8
2.2. Blazar Sequence	9
2.3. Unification Model	10
2.4. Jet Properties	17
2.5. Location of the Radio Core at Different Frequencies	19
2.6. Core Shift of M87	19
2.7. Core Shift Derived by γ -ray/Radio Time Lags	20
2.8. Sketch to Explain Apparent Superluminal Motion	21
2.9. Two-Element Interferometer	27
2.10. (u, v) -Plane Coverage of the MERLIN Array	32
2.11. Very Long Baseline Array	33
3.1. Polarized Flux Density Image of 4C+01.28	40
3.2. Kiloparsec-scale VLA Image of 4C+01.28	41
3.3. Previous Kinematic Analysis of 43 GHz VLBA Observations of 4C+01.28	42
3.4. Previous Kinematic Analysis of 15 GHz VLBA Observations of 4C+01.28	43
4.1. Images of 4C+01.28 with Different Structures.	46
4.2. Newly Calibrated and Cleaned Images of 4C+01.28.	47
4.3. Time Evolution of 4C+01.28 (April 2009 to April 2012).	50
4.4. Time Evolution of 4C+01.28 (July 2012 to April 2015).	51
4.5. Time Evolution of 4C+01.28 (June 2015 to April 2018).	52
4.6. Kinematic Model 1	54
4.7. Kinematic Model 2	56
4.8. Accelerated Kinematic Model for Component J4	58
4.9. Jet Geometry	59
5.1. <i>Fermi</i> /LAT γ -ray and Radio Light Curves	64
5.2. Cross-Correlation Coefficients.	66
6.1. Combined Kinematic and Variability Analysis	70
6.2. Kinematic Analysis Comparison with Jorstad et al. (2017)	71
6.3. Kinematic Analysis Presented by Lister et al. (2019)	73
6.4. Locations of the γ -ray Emitting Region and the Radio Cores within a Jet	76
6.5. Core Shift of 4C+01.28	77

6.6. Comparison between γ -ray Light Curves and Radio Light Curves shifted by the Time Lags	79
6.7. The Overall Picture	84
A.1. (u, v) -Plane Coverages of 4C+01.28 (April 2009 to February 2010)	89
A.2. (u, v) -Plane Coverages of 4C+01.28 (April 2010 to June 2010)	90
A.3. (u, v) -Plane Coverages of 4C+01.28 (August 2011 to August 2013)	91
A.4. (u, v) -Plane Coverages of 4C+01.28 (December 2013 to January 2016)	92
A.5. (u, v) -Plane Coverages of 4C+01.28 (April 2016 to November 2017)	93
A.6. (u, v) -Plane Coverages of 4C+01.28 (February 2018 to April 2018)	94
B.1. Images of 4C+01.28 (April 2009 to February 2010)	95
B.2. Images of 4C+01.28 (April 2010 to April 2011)	96
B.3. Images of 4C+01.28 (June 2011 to April 2013)	97
B.4. Images of 4C+01.28 (June 2013 to June 2015)	98
B.5. Images of 4C+01.28 (August 2015 to February 2017)	99
B.6. Images of 4C+01.28 (April 2017 to April 2018)	100

List of Tables

2.1. AGN Classes	12
3.1. Previous Kinematic Analysis of 43 GHz VLBA Observations of 4C+01.28	43
3.2. Previous Kinematic Analysis of 15 GHz VLBA Observations of 4C+01.28 (Vector Motion Fit)	44
3.3. Previous Kinematic Analysis of 15 GHz VLBA Observations of 4C+01.28 (Acceleration Fit)	44
4.1. Apparent Speeds of Kinematic Model 1	53
4.2. Apparent Speeds of Kinematic Model 2	57
4.3. Apparent Speeds of the Accelerated Kinematic Model for Component J4	58
5.1. Cross-Correlation Coefficients and Time Lags	68
6.1. Apparent Location of the γ -ray Emitting Region	80
6.2. Apparent Locations of the Radio Cores at Different Frequencies	82
6.3. Crossing Times	83
D.1. Image Parameters	107
D.2. Modelfit Parameters	110
D.3. 14-day Binned <i>Fermi</i> /LAT γ -ray Data	117
D.4. ALMA-Band 3 Data	125
D.5. ALMA-Band 6 Data	133
D.6. ALMA-Band 7 Data	134
D.7. SMA Data	138
D.8. OVRO Data	145

Danksagung

An dieser Stelle möchte ich mich bei allen bedanken, die zum Gelingen dieser Arbeit beigetragen haben.

Als erstes möchte ich mich bei Prof. Dr. Matthias Kadler dafür bedanken, dass er mir die Möglichkeit gegeben hat dieses interessante Projekt zu bearbeiten. Bei aufkommenden Problemen unterstützte er mich durch viele aufschlussreiche Diskussionen und hilfreiche Ratschläge. Darüber hinaus möchte ich ihm auch dafür danken, dass er durch seine sehr interessanten Vorlesungen mein Interesse für die Arbeit in der Astronomie geweckt hat.

Ebenfalls möchte ich mich bei Prof. Dr. Eduardo Ros für die Übernahme des Zweitgutachtens bedanken. Auch er hat mit hilfreichen Hinweisen zum Gelingen dieser Arbeit beigetragen.

Außerdem möchte ich mich bei Dr. Michael Kreter für die Berechnung und Bereitstellung der *Fermi*/LAT-Lichtkurve und die vielen anregenden Diskussionen bedanken.

Auch bei Andrea Gokus möchte ich mich für ihre Unterstützung bei der Korrelationsanalyse bedanken.

Des Weiteren möchte ich mich bei Rosamunde Pare für die vielen hilfreichen Diskussionen und für das Korrekturlesen dieser Arbeit bedanken. Besonders ihre Hinweise zur Zeichensetzung halfen mir sehr dabei die Arbeit zu verbessern. Hier bedanke ich mich auch bei Stefan Lindeholz, dessen Hinweise ebenfalls zum Gelingen dieser Arbeit beigetragen haben.

Zudem möchte ich mich bei allen Mitarbeitern des Lehrstuhls für Astronomie, unter der Leitung von Prof. Dr. Karl Mannheim, für die herzliche Aufnahme und für die Unterstützung bedanken. Besonders bei meinen Bürokollegen Michael Blank, Manuel Dörr, Stefan Lindeholz und Lukas Schrenk möchte ich mich hier für die angenehme Arbeitsatmosphäre und für die vielen interessanten Diskussionen bedanken.

Ganz besonders möchte ich mich auch bei meinen Eltern bedanken, die mich während meines Studiums immer unterstützt haben.

Acknowledgements

This research has made use of NASA's Astrophysics Data System.

This research has made use of the NASA/IPAC Extragalactic Database (NED), which is operated by the Jet Propulsion Laboratory, California Institute of Technology, under contract with the National Aeronautics and Space Administration.

This research has made use of ISIS functions (ISISscripts) provided by ECAP/Remeis observatory and MIT (<http://www.sternwarte.uni-erlangen.de/isis/>).

This study makes use of the following ALMA data: ADS/JAO.ALMA#2011.0.00001.CAL. ALMA is a partnership of ESO (representing its member states), NSF (USA) and NINS (Japan), together with NRC (Canada), MOST and ASIAA (Taiwan), and KASI (Republic of Korea), in cooperation with the Republic of Chile. The Joint ALMA Observatory is operated by ESO, AUI/NRAO and NAOJ.

The Submillimeter Array is a joint project between the Smithsonian Astrophysical Observatory and the Academia Sinica Institute of Astronomy and Astrophysics and is funded by the Smithsonian Institution and the Academia Sinica.

This research has made use of data from the OVRO 40-m monitoring program (Richards, J. L. et al. 2011, *ApJS*, 194, 29) which is supported in part by NASA grants NNX08AW31G, NNX11A043G, and NNX14AQ89G and NSF grants AST-0808050 and AST-1109911.

This research has made use of data from the MOJAVE database that is maintained by the MOJAVE team (Lister et al., 2018, *ApJS*, 232, 12).

This study makes use of 43 GHz VLBA data from the VLBA-BU Blazar Monitoring Program (VLBA-BU-BLAZAR; <http://www.bu.edu/blazars/VLBAproject.html>), funded by NASA through the Fermi Guest Investigator Program. The VLBA is an instrument of the National Radio Astronomy Observatory. The National Radio Astronomy Observatory is a facility of the National Science Foundation operated by Associated Universities, Inc.

Selbstständigkeitserklärung

Hiermit erkläre ich, dass die vorliegende Arbeit nach allgemeiner Studien- und Prüfungsordnung für die Bachelor- und Masterstudiengänge (ASPO) an der Julius-Maximilians-Universität Würzburg selbstständig und nur unter Benutzung der angegebenen Quellen und Hilfsmittel angefertigt wurde. Des Weiteren wurde die Arbeit noch keiner anderen Prüfungsbehörde zur Erlangung eines akademischen Grades vorgelegt.

Würzburg, 27. September 2019

Florian Rösch